

Performance of Load-Bearing
Cold-Formed Steel Wall Systems with
Web-Perforated Studs
Subjected to Standard Fire

by

Shijun Yang

A thesis

presented to the University of Waterloo

in fulfillment of the

thesis requirement for the degree of

Doctor of Philosophy

in

Civil Engineering

Waterloo, Ontario, Canada, 2017

© Shijun Yang 2017

AUTHOR'S DECLARATION

I hereby declare that I am the sole author of this thesis. This is a true copy of the thesis, including any required final revisions, as accepted by my examiners.

I understand that my thesis may be made electronically available to the public.

Abstract

Load-bearing cold-formed steel (CFS) wall systems are commonly constructed with CFS C-shape studs with one or two layers of fire-rated sheathing attached to both sides. In practice, perforations are placed in stud webs to accommodate the passage of utilities or installation of intermediate braces. These walls may fail by local buckling at the web perforations, combined with studs bending towards the furnace, as demonstrated by several full-scale fire tests. Current understanding of fire performance of such walls with web-perforated studs remains relatively limited, and the effect of web perforations on the fire resistance have not yet been accounted for in current design methods.

Finite element analysis (FEA) using the software ABAQUS, an alternative to full-scale fire tests, was employed to investigate the heat transfer and structural responses of CFS walls. Three-dimensional heat transfer models were developed and validated with full-scale fire tests. Parametric studies demonstrate that for insulated CFS walls, web perforations induce a larger temperature gradient in perforated cross sections than in the solid ones along the stud length; however, for non-insulated CFS walls, the effect of web perforations on the temperature distributions in stud cross sections is negligible.

Sequentially uncoupled 3D FE thermal-stress models were developed to evaluate the fire performance of load-bearing CFS walls with web-perforated studs. These walls were partially insulated, sheathed by double layers of MgO board or Type C gypsum board, and by mixed Type X and MgO board. Unlike in previous studies, temperature distributions incorporated into the structural model were obtained from heat transfer analysis so as to include the difference in temperature distributions caused by web perforations. Three models were developed: (1) a CFS wall stud model, as in previous studies. The predicted failure time is acceptable when compared with that of full-scale fire testing. (2) a CFS wall frame model. Stiffness and force interactions among the CFS wall studs were considered. The middle few studs of the wall frame may bear higher loads than that applied to a single stud, demonstrating that the single stud model may overestimate fire resistance. Thus, the stiffness and force interactions should be considered in the FEA to achieve better accuracy. (3) a CFS wall system model. Sheathing, attached to CFS wall framing, may enhance the load carrying capacity of walls. Such an increase in load carrying capacity is permitted and can be evaluated in the design of CFS walls at ambient temperature. However, the effect of using sheathing to brace to wall studs has not been investigated at elevated temperature. Modelling sheathing using shell element, in addition to the CFS

wall frame, provides more realistic prediction of the structural response of full-scale fire tests than the above-mentioned two models.

A simplified design method is extended for CFS web-perforated studs in walls, subjected to standard fire, based on effective width method as stated in the North American Specification for the Design of Cold-Formed Steel Structural Members (AISI S100). CFS wall studs are subjected to combined compression and bending due to neutral axis shift, thermal bowing and their magnification effects. A plate buckling coefficient, accounting for the web perforation length and width, is introduced to characterize the nominal axial strength. The effect of web perforations on the nominal flexural bending is ignored, as is consistent with AISI S100 (2012) at room temperature and parametric study results at elevated temperature. The limit of web perforation length is extended from the 114 mm, specified in AISI S100 at room temperature, to 130 mm at both room and elevated temperatures. The accuracy of the proposed design equations is acceptable when considering the complexity of the problem being dealt with and the simplicity of the calculation.

Acknowledgements

Many wonderful people have supported me these four years. Bofu made the journey more purpose-driven, joyful, and passionate. He always had confidence in me and encouraged me to challenge myself. My parents and brother are consistently my greatest support, deepest love. I would achieve nothing if they were not behind me.

I would like to express my sincere gratitude to my supervisor, Professor Lei Xu, for his guidance, encouragement, continuous support, and unselfish investment of time to discuss my research progress. This study would not have been successful to this level without such assistance. I also appreciate the opportunity he gave me to study at the University of Waterloo.

I would like to extend my gratitude to Professors Elizabeth Weckman, John Straube and Mahesh Pandey, for serving as my thesis committee members, and for their comments and constructive suggestions on my research. Special thanks to Professor Ben Schafer of John Hopkins University for serving as the external examiner.

Professor Elizabeth Weckman played an important role in my first-year PhD program. Courses taught by her and others organized by her research group contributed greatly to my research background in fire. Other than her brilliant expertise in fire, her devotion to work, generosity and genuine desire to help has inspired me and will remain in my memories.

Ms. Mary McPherson of the Writing Centre is such an excellent writing specialist, who has helped with my thesis, reports and publications throughout my PhD program. Working with her is always a pleasure.

My fellow graduate students in Waterloo and dear friends both in Canada and overseas helped me adapt to the new life and survive the negative feelings. I feel grateful to be around all these lovely people.

TO

My family and Bofu

Table of Contents

AUTHOR'S DECLARATION	ii
Abstract	iii
Acknowledgements	v
Table of Contents	vii
List of Tables.....	x
List of Figures	xi
Chapter 1 Introduction.....	1
1.1 Background.....	1
1.2 Research objective and scope	3
1.3 Thesis organization.....	3
Chapter 2 Literature Review	5
2.1 Experimental research	5
2.2 Thermal modelling	7
2.2.1 Analytical thermal modelling.....	7
2.2.2 Finite element heat transfer analysis	8
2.3 Finite element structural modelling.....	9
Chapter 3 Behaviour of Web-Perforated CFS C-shape Studs at Ambient and Elevated Temperatures	12
3.1 Introduction	12
3.2 Behaviour of CFS C-shape stub columns at ambient temperature	13
3.2.1 Stub column tests.....	13
3.2.2 Comparison with DSM approach	18
3.3 Finite element modelling of CFS C-shape columns at ambient and uniform elevated temperatures	21
3.3.1 Stub column tests.....	21
3.3.2 Finite element modelling and analysis	24
3.4 Behaviour of web-perforated CFS wall studs subjected to non-uniform cross-sectional elevated temperature.....	28
3.4.1 Non-uniform cross-sectional temperature distribution.....	29

3.4.2 Finite element structural analysis.....	31
3.4.3 Results and discussions.....	34
3.5 Conclusions.....	38
Chapter 4 Thermal Modelling and Analysis of CFS Walls with Web-Perforated Studs Subjected to Standard Fire.....	39
4.1 Introduction.....	39
4.2 Thermal modelling.....	40
4.2.1 Full-scale fire tests.....	40
4.2.2 Assumptions.....	42
4.2.3 Finite element type and mesh.....	42
4.2.4 Thermal boundary conditions.....	44
4.2.5 Thermal properties.....	46
4.3 Comparison with test results.....	48
4.4 Effect of web perforations.....	51
4.4.1 Parameters.....	51
4.4.2 Results and discussions.....	52
4.5 Conclusions.....	60
Chapter 5 Structural Modelling and Analysis of CFS Walls with Web-Perforated Studs Subjected to Standard Fire.....	61
5.1 Introduction.....	61
5.2 Full-scale fire tests.....	62
5.3 Sequentially uncoupled thermal-stress analysis.....	67
5.3.1 Finite element thermal model.....	67
5.3.2 Thermal properties.....	69
5.4 Finite element structural model of CFS wall stud.....	74
5.4.1 Mechanical properties.....	75
5.4.2 Residual stresses and initial geometric imperfection.....	77
5.4.3 Results and discussion.....	78
5.5 Finite element structural model of CFS wall frame.....	84

5.5.1 Results and discussions	88
5.6 Finite element structural model of CFS wall system.....	96
5.6.1 FEA results and discussions	99
5.7 Conclusions	105
Chapter 6 Extended Design Method Based on AISI S100.....	107
6.1 Introduction	107
6.2 Parametric study	107
6.2.1 Parameters of single CFS stud model.....	108
6.2.2 Results and discussions	108
6.3 Extended design equations based on AISI S100	112
6.3.1 Nominal axial strength	112
6.3.2 Nominal flexural strength.....	113
6.3.3 Combined compression and bending.....	116
6.4 Comparison of results between extended design method and FEA.....	119
6.5 Conclusions	122
Chapter 7 Conclusions and Future Research.....	123
7.1 Conclusions	123
7.1.1 Web-perforated CFS C-shape studs at ambient and elevated temperatures	123
7.1.2 Finite element thermal modelling and analysis	124
7.1.3 Finite element structural modelling and analysis	124
7.1.4 Extended design method based on AISI S100.....	125
7.2 Future research	126
Bibliography	128
Appendices	134
Appendix A Comparison of gypsum board surface temperature on the ambient side between FEA and full-scale fire tests.....	134
Appendix B FEA results for parametric study (section 6.2)	138
Appendix C Design example using extended design method	142
Appendix D Calculation results using extended design method	155

List of Tables

Table 3.1 Specimen dimensions (Xu, 2014)	15
Table 3.2 Mechanical properties from tensile coupon tests (Xu, 2014)	15
Table 3.3 Comparison of test results with DSM approach	21
Table 3.4 Nominal cross-section dimensions of specimens without perforations (Feng et al., 2003d).....	22
Table 3.5 Nominal cross-section dimensions of specimens with perforations (Feng et al., 2003d)....	22
Table 3.6 Mechanical properties at ambient temperature	23
Table 3.7 Sensitivity study of element sizes	25
Table 3.8 Comparison of compressive strength between FEA and test results	27
Table 3.9 Applied load at ambient temperature (Step-1).....	32
Table 4.1 Full-scale fire tests (Kolarkar, 2010)	41
Table 4.2 Thermal properties (Gunawan, 2011)	46
Table 4.3 CFS walls with web-perforated studs in parametric study.....	52
Table 5.1 Load-bearing CFS wall fire tests (Xu, 2011).....	64
Table 5.2 Thermal properties of gypsum board at ambient temperature (Clancy, 1999)	70
Table 5.3 Coefficients for thermal properties of MgO board	72
Table 5.4 Reduction factor for cold-formed steel based on EC 3 Part 1.2 (2005).....	76
Table 5.5 Comparison of failure time between FEA and test results.....	83
Table 6.1 Failure criteria for calculating nominal flexural strength (Feng &Wang, 2005)	115

List of Figures

Figure 1.1 Behaviour of CFS wall studs exposed to fire from one side	2
Figure 2.1 CFS wall systems with exterior insulation (Kolarkar, 2010)	6
Figure 2.2 CFS wall systems with exterior insulation (Chen & Ye, 2013)	7
Figure 2.3 Non-uniform temperature distributions in CFS wall studs for FE modelling	10
Figure 3.1 Specimen profiles (Xu, 2014)	14
Figure 3.2 Experimental setup (Xu, 2014)	16
Figure 3.3 Specimen failure modes (Xu, 2014).....	17
Figure 3.4 Load-displacement relationships (Xu, 2014)	18
Figure 3.5 Stress-strain relationship of steel at ambient temperature.....	23
Figure 3.6 Stress-strain relationship of steel at elevated temperature	24
Figure 3.7 FE mesh and boundary conditions for specimen 100×54×15×1.2.....	25
Figure 3.8 Failure modes of columns without perforations.....	26
Figure 3.9 Failure modes of columns with perforations.....	26
Figure 3.10 Comparison of compressive strength between FEA and test results.....	27
Figure 3.11 Configuration of CFS wall section.....	29
Figure 3.12 Temperature contour ($L_h=380$ mm): (a) CFS wall and (b) C-shape column.....	30
Figure 3.13 Stress-strain relationship of cold-formed steel at elevated temperature.....	32
Figure 3.14 Load and boundary conditions in structural analysis	33
Figure 3.15 Initial global geometric imperfection ($L/1000$).....	33
Figure 3.16 Time-end reaction force curve ($L_h=380$ mm, $R=0.9$)	34
Figure 3.17 Time-axial deformation curve ($L_h=380$ mm, $R=0.9$)	35
Figure 3.18 Failure mode ($L_h=380$ mm, $R=0.9$)	36
Figure 3.19 Effect of web perforation lengths on failure time	37

Figure 3.20 Effect of web perforation lengths on temperature distribution.....	37
Figure 4.1 Temperature simplifications in CFS wall stud without web perforations	40
Figure 4.2 Experimental set-up (Kolarkar, 2010)	41
Figure 4.3 Equivalent wall width for determining temperature distribution.....	42
Figure 4.4 Finite element meshes of CFS wall segments	43
Figure 4.5 Heat transfer mechanism in CFS walls.....	45
Figure 4.6 Thermal properties of gypsum board (Gunawan, 2011).....	47
Figure 4.7 Thermal properties of cold-formed steel (Gunawan, 2011)	48
Figure 4.8 Thermal conductivity of glass fibre (Gunawan, 2011)	48
Figure 4.9 Comparison of time-temperature profiles between FEA and tests by Kolarkar (2010)	50
Figure 4.10 Configuration of CFS walls with web-perforated studs	51
Figure 4.11 Temperature contour of insulated CFS walls at mid-height cross section.....	53
Figure 4.12 Temperature contour of insulated CFS wall frames at 104 minutes.....	53
Figure 4.13 Temperature contour of non-insulated CFS walls at mid-height cross section	54
Figure 4.14 Non-uniform temperature distributions in insulated CFS wall studs at 104 minutes	55
Figure 4.15 Non-uniform temperature distributions in non-insulated CFS wall studs at 120 minutes	55
Figure 4.16 Stud depth-temperature profiles	56
Figure 4.17 Comparison of stud temperatures for insulated CFS walls ($L_h=530$ mm).....	58
Figure 4.18 Comparison of stud temperatures for insulated CFS walls ($L_h=130$ mm).....	58
Figure 4.19 Comparison of stud temperatures for non-insulated CFS walls ($L_h=530$ mm).....	59
Figure 4.20 Comparison of stud temperatures for non-insulated CFS walls ($L_h=130$ mm).....	59
Figure 5.1. Configuration of load-bearing CFS wall specimens (Xu, 2011)	66
Figure 5.2. Experimental setup (Xu, 2011).....	67
Figure 5.3. Finite element mesh of CFS walls	68

Figure 5.4 Thermal properties of Type C and X gypsum board (Mehaffey et al., 1994).....	71
Figure 5.5 Thermal properties of MgO board (Chen et al., 2013).....	73
Figure 5.6 Loading and boundary conditions of single CFS stud model	74
Figure 5.7 True stress-strain relationship of CFS stud at elevated temperature.....	77
Figure 5.8 Reduction factor of CFS stud at elevated temperature.....	77
Figure 5.9 Time-reaction force curve (LBW-E1(a))	79
Figure 5.10 Time-axial deformation curve (LBW-E1(a))	79
Figure 5.11 Mises stress contour of FEA results for single stud model (LBW-E1(a))	80
Figure 5.12 U3 of FEA results for single stud model (LBW-E1(a)).....	80
Figure 5.13 Temperature contour of Stud 4 at failure time (LBW-E1(a))	81
Figure 5.14 Cross-sectional temperature contours of Stud 4 for all specimens at failure time	83
Figure 5.15 FE mesh of CFS wall frame model.....	85
Figure 5.16 Interactions and constraints of CFS wall frame model	86
Figure 5.17 Boundary and loading conditions of CFS wall frame model.....	87
Figure 5.18 Failure mode of CFS wall frame model (LBW-E1(a))	89
Figure 5.19 Failure mode of CFS wall frame model (LBW-3)	90
Figure 5.20 Time-average axial displacement relationships at stud top end.....	91
Figure 5.21 Time-reaction force relationships at stud bottom end.....	93
Figure 5.22 Failure mode of CFS wall frame model (LBW-3) (friction coefficient=0.3)	95
Figure 5.23 Time-reaction force relationships at stud bottom support (friction coefficient=0.3)	96
Figure 5.24 Sheathing modelled using shell element S4R.....	97
Figure 5.25 Interaction and constraint between sheathing and studs	98
Figure 5.26. Stress-strain relationship of sheathing	99
Figure 5.27. Structural response of CFS frame at 60 minutes.....	101

Figure 5.28. Temperature distribution within CFS frames at 60 minutes.....	101
Figure 5.29. Out-of-plane deformation (UZ) versus time (min) curve	102
Figure 5.30. Stress distributions within gypsum boards at 60 minutes.....	104
Figure 6.1 Cross-sectional temperature profiles of studs with different perforation lengths.....	109
Figure 6.2 Time-temperature curve of stud flange-web junctions	110
Figure 6.3 Comparison of normalized cross-sectional yield strength.....	110
Figure 6.4 Comparison of normalized cross-sectional elastic modulus.....	111
Figure 6.5 Failure time-applied load relationship predicted by FEA.....	111
Figure 6.6 Neutral axis shift, thermal bowing and magnification effects	118
Figure 6.7 Calculated ultimate compression strength at mid-height and at support	120
Figure 6.8 Comparison of interaction of compression and bending	120
Figure 6.9 Comparison of axial strength based on extended design method.....	121

Chapter 1 Introduction

1.1 Background

Cold-formed steel (CFS) wall systems are increasingly being used in low- and mid-rise building structures. CFS wall systems are commonly constructed by CFS C-shape wall studs lined with one or two layers of sheathing on both sides, often with interior insulation. During fire events, load-bearing CFS wall systems serve as fire-resistant barriers that play an important role in sustaining applied loads, maintaining structural integrity, and controlling the spread of fire from the room of origin to adjacent compartments. Normally, the CFS C-shape wall studs are under concentrically compressive loads at ambient temperature. When exposed to fire attack, usually from one side, the CFS C-shape studs are subjected to highly non-uniform elevated temperature distributions on their cross sections, as shown in Figure 1.1(a). There is a steep temperature gradient from the fire-exposed side to the unexposed side along the web, and also a temperature gradient along the flanges since heat is dissipated rapidly from the thin-walled steel studs to the surrounding material. Such non-uniform temperature distributions induce bending in the studs. Consequently, the axially loaded CFS wall studs are subjected to a combination action of axial compression and flexural bending, which complicates the evaluation of their structural performance. Firstly, the neutral axis of the stud cross-section shifts from its original position, due to the non-uniform distribution of strength and stiffness throughout the stud, as shown in Figure 1.1(a). Secondly, thermal bowing (e_{AT}) and magnification effects (e_{pAT}) are induced due to the elevated temperatures, as shown in Figure 1.1(b) (Alfawakhiri, Sultan, & MacKinnon, 1999). The foregoing effects caused by non-uniform temperature distributions will compound the already complex structural behaviour of CFS studs, which are already vulnerable to local buckling, distortional buckling, global buckling, as well as complex boundary conditions.

In practice, CFS C-shape studs are perforated to allow electrical, plumbing, and heating passages through walls and ceilings. During fire, the non-uniform temperature distribution and structural behaviour of web-perforated CFS wall studs are more complicated than those of unperforated steel studs. Alfawakhiri's (2001) experimental study on laterally braced load-bearing CFS wall systems with web-perforated studs under standard fire found that CFS wall studs failed by local buckling at the web-perforated regions.

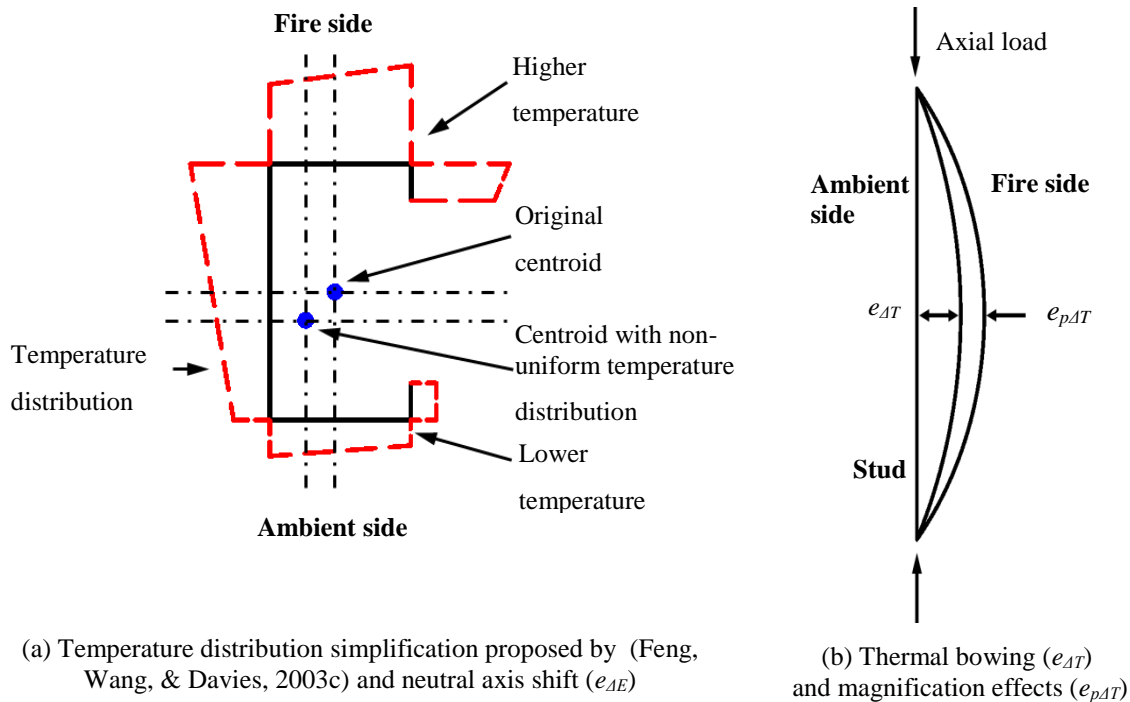


Figure 1.1 Behaviour of CFS wall studs exposed to fire from one side

Two approaches may be used to demonstrate structural fire safety of CFS walls: (1) prescriptive approach, in which fire resistance rating of CFS walls (45 min., 1 hr., 1.5 hr. or 2 hr., etc.) is primarily based on specifying the number of layers and thickness in each layer of fire protection sheathing, and the percent of design load. (2) performance-based approach; that is, the behaviour of the CFS walls in fire is explicitly assessed. But challenges exist in the latter one, such as more realistic fire models; more accurate thermal properties; three-dimensional heat transfer models including detailed wall components; verified coupled thermo-mechanical models at system level; performance-based design method; etc. (Abreu, Vieira, Abu-Hamd, & Schafer, 2014).

Although the performance-based fire resistance design guidelines for hot-rolled steel members are well-established, they are not applicable to CFS wall studs that are susceptible to various buckling. Several fire design recommendations based on effective width method (EWM) are proposed for CFS wall studs without web perforations, subjected to non-uniform temperature distributions under standard fire. These recommendations have been adopted for the American Iron and Steel Institute (AISI) design provisions (Gerlich, Collier, & Buchanan, 1996; Klippstein, 1980), Eurocode 3 (Feng & Wang, 2005; Kaitila, 2002; Ranby, 1999; Zhao et al., 2005) and Canadian cold-formed steel design rules

(Alfawakhiri, 2002). Unlike the abovementioned design method, Shahbazian's (2013) equations is based on direct strength method (DSM). However, little research has been undertaken to investigate the performance of load-bearing CFS walls with web-perforated studs subjected to standard fire. In addition, only limited research is exploring the behaviour of perforated CFS wall studs at both ambient and elevated temperatures.

1.2 Research objective and scope

The research described in this thesis is undertaken to clarify the thermal and structural performance of CFS walls with web-perforated studs under standard fire. The ultimate goal is to propose a simplified design method to evaluate the fire resistance of steel studs with web perforations in CFS walls exposed to standard fire from one side. The scopes of this research are as follows:

- investigating the effect of web perforations on the compressive strength of C-shape CFS stub columns at ambient temperature, and accessing the applicability of DSM for calculating the ultimate strength of CFS studs with web perforations;
- evaluating the effect of web perforation length and load ratio on the failure time of steel studs in CFS wall segment exposed to standard fire from one side using finite element analysis;
- investigating the temperature distributions of steel studs with varying web perforation length in CFS wall segment exposed to standard fire from one side using finite element analysis;
- developing sequentially uncoupled thermal-stress finite element models, featuring heat transfer and stress analysis, for load-bearing CFS walls with web-perforated studs under standard fire; three models, i.e., single CFS stud mode, CFS wall frame model and CFS wall system model, are discussed;
- proposing design equations, accounting for the presence of web perforations, for evaluating the fire resistance of web-perforated studs in CFS walls exposed to standard fire from one side.

1.3 Thesis organization

This thesis includes the development of sequentially uncoupled finite element thermal and structural analysis and proposes design equations for evaluating the behaviour of CFS walls with web-perforated studs subjected to standard fire. The thesis is organized into seven chapters as follows:

- Chapter 2 reviews selected previous studies on the performance of CFS wall systems subjected to standard fire.
- Chapter 3 investigates the effect of web perforations on the behaviour of C-shape studs at ambient temperature, and uniform and non-uniform cross-sectional elevated temperatures.
- Chapter 4 conducts a three-dimensional finite element analysis to trace the heat transfer process of CFS walls with web-perforated CFS studs subjected to standard fire. The thermal models of CFS walls are validated using data from full-scale fire tests. The temperature distribution within CFS studs of varying web perforation lengths are investigated.
- Chapter 5 investigates the thermal and structural performance of CFS load-bearing walls with C-shape studs with web perforations subjected to standard fire. Sequentially uncoupled 3D FE thermal-stress analysis is carried out, in which the heat transfer analysis is conducted to obtain the temperature distribution of an entire CFS wall. In the subsequent structural analysis, a CFS wall frame rather than a single stud is modeled to achieve system-level structural responses. Additionally, sheathing, modelled using both shell element and in-plane lateral restraint, is discussed. The finite element analysis results are compared with those from full-scale fire tests.
- Chapter 6 develops a simple method for quantifying thermal performance and proposes design equations based on AISI S100 to evaluate the fire resistance of web-perforated studs in fully insulated CFS walls exposed to standard fire;
- Chapter 7 concludes the thesis, and provides recommendations for future research.

Chapter 2 Literature Review

Presented in this chapter is a literature review that covers a range of the must-relevant research papers, reports and theses on the fire performance of CFS wall systems.

2.1 Experimental research

In this section, some of previous experimental studies of full-scale load-bearing CFS walls under standard fire conditions are presented in chronological order.

Gerlich (1995), Gerlich, Collier, and Buchanan (1996) conducted three tests on non-insulated load-bearing CFS wall specimens exposed to ISO 834 fire (1975). All the test specimens generally failed by buckling of the compression flange of steel studs on the ambient side of the wall systems. A model to predict the failure time was proposed. The process of the prediction consisted of a heat transfer analysis of using computer software TASEF (Sterner & Wickstorm, 1990) and a structural analysis using self-developed spreadsheets.

Kodur and Sultan (2001) studied the effect of various factors influencing fire resistance of laterally braced load-bearing CFS wall systems with 14 full-scale CFS wall specimens. All the tests were performed based on the standard procedures stipulated in CAN/ULC S101-M89 (1989). The results showed that CFS wall specimens failed structurally as a result of local or overall buckling, and the insulation type and stud-spacing significantly influence the fire resistance of steel stud wall systems.

Alfawakhiri (2002) conducted three standard fire resistance tests of laterally braced load-bearing CFS wall specimens. The effects of cavity insulation, resilient channels, and stud spacing on the fire resistance of CFS wall systems were investigated. All the CFS wall specimens exhibited structural failure as a result of overall buckling of wall studs at elevated temperature. The dominant failure mode of the studs for non-insulated walls was the buckling of the flange exposed to ambient temperature near mid-height and bending towards the furnace, while the failure of studs for insulated walls was the buckling of the flange exposed to elevated temperature at the location of the bottom web perforation and bending away from the furnace for insulated walls. This was because the existence of cavity insulation changed the temperature gradient across the stud sections in the wall thickness direction. Similar to that was found by Kodur and Sultan (2001), Alfawakhiri also concluded that the cavity insulation was detrimental to the fire resistance of load-bearing CFS walls. In Alfawakhiri's study, each

stud had four web perforations, and the studs failed by local buckling at the locations of web perforations.

Feng (2004) carried out eight full-scale tests of load-bearing CFS wall systems, of which two were at ambient temperature and six were exposed to the standard fire condition from one side. Load ratios of 0.2, 0.4, and 0.7 were considered in this study. The temperature development in the steel studs was found to be independent on the applied loads in the CFS wall systems. The failure mode of the CFS wall studs for all the tests was global buckling about the major axis with some torsion on the fire-exposed side, except for one test failed by local buckling at the top. This was mainly because the unexposed gypsum boards were able to prevent lateral restraint for CFS wall studs about the minor axis during the whole fire tests. The failure times of CFS wall systems with thinner thickness of steel studs was found to be less than those of wall systems with thicker studs.

Sultan (2010) conducted 41 full-scale wall fire resistance tests in accordance with ULC-S101 standard fire exposure at the National Research Council of Canada. These tests, including CFS stud walls and timber stud walls, aimed to determine the gypsum board fall-off temperature criterion, which was based on the sudden temperature rise measured on the back side of the fire-exposed gypsum board caused by its falling-off or sagging. Little difference in the fall-off temperatures was observed for wall systems with a single layer or double layers of gypsum boards, with and without insulation in wall cavity and with different screw spacing.

Kolarkar (2010) and Gunalan (2011) conducted a total of 12 full-scale fire tests of non-laterally braced load-bearing LFS walls with cavity insulation or external insulation subjected to ASTM E119 fire (2002). Glass fibre, rock wool and cellulosic fibre were used as the insulation materials. Test results showed that CFS wall systems with external insulation, as shown in Figure 2.1, provided considerably increased failure time and smaller lateral deformations than those with cavity insulation. Similar to that was found by Feng (2004), the temperature gradient in the steel studs was found to be independent on the applied loads in the CFS wall systems.

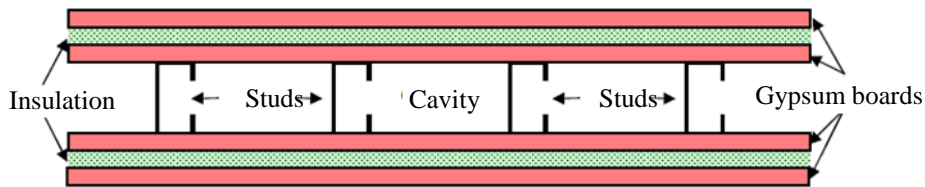


Figure 2.1 CFS wall systems with exterior insulation (Kolarkar, 2010)

Xu (2011) conducted 16 full-scale tests of laterally braced load-bearing CFS wall systems with perforated studs subjected to ISO 834 fire (1999). The objective of these tests was to investigate for the application of laterally braced load-bearing CFS walls with web-perforated studs in mid-rise buildings. The effects of various lining materials, such as MgO boards and gypsum boards (Type C and Type X), on the fire resistance were also studied. In particular, fire test specimens with lining material mainly composed of MgO board, diamon lath and stucco with wine mesh on the fire-exposed side or both sides were investigated.

Chen and Ye (2013) carried out six full-scale CFS wall specimens with double layers of lining materials on both sides, of which the insulation material of Aluminum silicate wool was used as external insulation on the fire-exposed side while no external insulation was used on the ambient side. Five types of lining materials were used in the experiments, including gypsum board, bolivian magnesium board, oriented standard board (OSB), autoclaved light weight concrete (ALC) board, and rock wool board. Similar to Kolarkar (2010) and Gunalan (2011), test results showed that the failure time of load-bearing CFS wall systems was greatly increased due to external insulation. Results also demonstrated that the CFS walls attached with bolivian magnesium boards or ALC boards had superior fire performance to those attached with gypsum boards or OSB boards in mid-rise buildings.

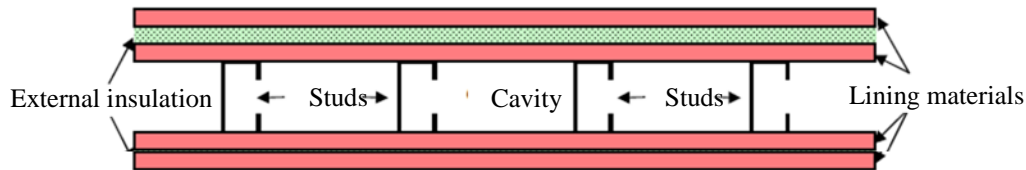


Figure 2.2 CFS wall systems with exterior insulation (Chen & Ye, 2013)

2.2 Thermal modelling

Since the temperature distributions in the steel studs are independent with the applied axial loads; thus, the developed analytical and finite element heat transfer models can be used to predict the temperature distributions of both non-load-bearing and load-bearing CFS wall systems.

2.2.1 Analytical thermal modelling

Klippstein (1978, 1980) first proposed an analytical method to predict the time of structural failure for load-bearing CFS walls subjected to standard fire. One-dimensional heat transfer models were developed to predict the temperature distribution across the steel studs of CFS wall systems without

cavity insulation (Collier, 1996; Sultan, 1996) and with cavity insulation (Kodur & Sultan, 2001; Shahbazian & Wang, 2014). Chen and Ye (2013) improved the convergence of the one-dimensional thermal response models by using the Gauss-Seidel method to solve the governing equation. In all the above proposed models, except for Shahbazian and Wang's model (2014), the presence of the thin-walled CFS steel frame was neglected because the argument that the CFS frame plays a minor role in the heat transfer mechanism.

2.2.2 Finite element heat transfer analysis

Gerlich (1995), Alfawakhiri (2001) and Gunawan (2011) performed heat transfer analyses to predict the temperature distributions associated with time variation for CFS wall systems exposed to standard fire conditions using computer programs TASEF (Sternier & Wickstrom, 1990), TRACE (Alfawakhiri, 2001) and SAFIR (2004). Good accuracy was reported based on the results obtained from the programs. Jones (2001) investigated the performance of CFS and light timber frame wall assemblies lined with gypsum boards subjected to real building fires using SAFIR.

Feng et al. (2003c) conducted heat transfer analyses of non-load-bearing small-scale CFS stud wall systems by using the finite element software ABAQUS. A parametric study was also carried out to examine the thermal performance of different steel stud systems. This study assumed a uniform temperature distribution along the stud length and perfect contact between the interior insulation and the steel sections. Feng, et al. (2003c) concluded that ABAQUS could be used to simulate the temperature distributions in CFS wall systems under standard fire conditions provided there was no integrity failure of the gypsum boards, including cavity radiation, by adopting appropriate thermal boundary conditions and thermal properties. It was also found that the temperature profiles of steel stud wall systems were not affected much by the shape of the CFS cross section. The effect of lips on temperature distribution can be ignored when the flange width is small. It was found that the thermal performance of CFS wall system was not significantly affected by the types of interior insulation and the shape of the CFS cross section. Temperatures of the steel section of a CFS stud panel system depend primarily on insulation panels on the fire-exposed side. However, it was noticed that cavity insulation was beneficial to the fire resistance of load-bearing CFS walls, which contradicted the conclusion that is found by Kodur and Sultan (2001) and Alfawakhiri (2001).

Zhao et al. (2001) investigated the validity of different computer programs such as ABAQUS, ANSYS, FLUENT. The results obtained from the programs are in consistency with a good accuracy.

It was concluded that all the computer programs were capable for heat transfer analysis once one of them is validated against tests. In this investigation, it was assumed that conduction is the primary heat transfer mechanism in the steel studs and gypsum boards. Convection and radiation acted essentially for heat transfer from fire to gypsum boards. For the reason of simplicity, radiation effects within the gypsum boards were neglected. In numerical models, nonlinearity due to temperature dependency of material properties and boundary conditions were taken into account. The height and the cross-section size of the stud were considered as parameters affecting the thermal behaviour. However, the mass transfer in materials such as moisture movement was not simulated.

2.3 Finite element structural modelling

Finite element analysis has been carried out to investigate the structural behaviour of load-bearing CFS wall systems under fire conditions and to determine their fire resistance rating using ABAQUS by many researchers. The FEAs of CFS wall studs under fire conditions were conducted under two conditions, namely steady state condition (Feng et al., 2003c; Gunalan & Mahendran, 2013) and transient state condition (Feng et al., 2003c; Gunalan & Mahendran, 2013; Kaitila, 2002; Zhao et al., 2005). In modelling steady state, the non-uniform temperature distributions in CFS cross section were raised to the target levels and maintained. An external axial load was then applied to the stud in increments until failure. In modelling transient state, the target load was first applied based on the specified load ratio, after that the measured time-dependent non-uniform temperature distributions in the stud were incorporated.

Kaitila (2002), Feng et al. (2003c), and Gunalan and Mahendran (2013) used a rigid plate at each end of the stud to simulate pinned support conditions. The reference point for the rigid plate was the original centroid of the gross cross section. Zhao et al. (2005) considered two support conditions. In the first case pinned support condition was assumed for both ends, whereas in the second case fixed support condition was used in one end while pinned support condition was used at the other end. The connection of CFS stud to gypsum boards was simulated by restraining the lateral displacement of both flanges at screw spacing intervals along the length of the stud. That is, gypsum boards on both sides of the CFS wall stud were assumed to be effective in restraining the stud from flexural buckling about the minor axis and torsional buckling until failure. This assumption was adopted by other researchers as well (Feng et al., 2003c; Gunalan & Mahendran, 2013; Kaitila, 2002; Zhao et al., 2005).

Three simplifications of non-uniform temperature distributions in CFS wall stud were adopted by the foregoing researchers in the FEAs as shown in Figure 2.3. In the first simplification, the lip and flange elements had the uniformly distributed temperature with same magnitude whereas the temperature distribution associated with the web is linear. In the second simplification, linear temperature distributions were assigned to all the three elements. In the final simplification, the lip temperature was taken as equal to that of the web at the corresponding height, the flange temperature was assumed to be a constant while the web temperature distribution was bilinear which decreased linearly from hot flange to the center of the web, and then further reduced linearly from the center of the web to the cold flange at a lower rate. The foregoing simplifications of non-uniform temperature distributions were adopted to develop manual- based methods to evaluate ultimate strength of CFS wall studs under fire, since the real temperature distribution in different elements of a CFS stud was highly non-uniform as shown from fire tests. Based on Feng et al. (2003c) and Gunalan and Mahendran (2013), the first simplification can yield the results with good accuracy in FEAs.

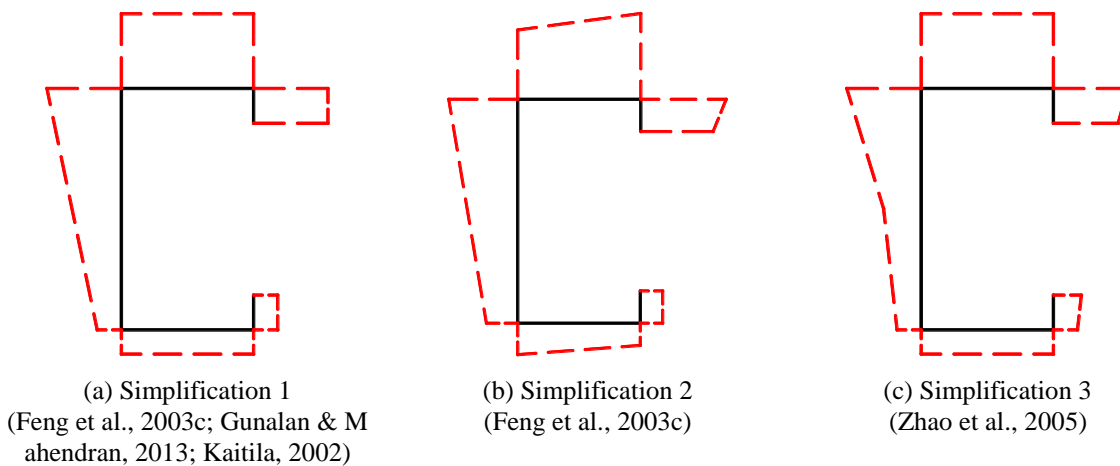


Figure 2.3 Non-uniform temperature distributions in CFS wall studs for FE modelling

In Zhao et al.'s (2005) study, the average measured temperatures at the mid-height of all the studs were used in the numerical simulations. In Gunalan and Mahendran's (2013) investigation, the studs that had a vertical joint of gypsum boards were modeled as the studs were subjected to higher temperature due to the opening of gypsum board joints which could initiate the failure of the CFS wall systems during the fire test. Also, Gunalan and Mahendran's (2013) research adopted the average

measured temperatures at three different height locations (top, mid and bottom) of each single critical stud. This could eliminate the sharp rise and fall in deformation-time curves of the stud.

The initial geometrical imperfection does not have any noticeable effect on the behaviour of studs due to the dominance of thermal bowing according to Feng et al. (2003c), and Gunalan and Mahendran (2013). The residual stresses in steel studs were found to be unimportant in the FEAs under fire conditions by all the researchers (Feng et al., 2003c; Gunalan & Mahendran, 2013; Kaitila, 2002; Zhao et al., 2005).

The FE models of CFS wall studs developed by Zhao et al. (2005), and Gunalan and Mahendran (2013) were validated with test results and shown a good accuracy. However, Kaitila (2002) and Feng et al.'s (2003c) models for CFS wall studs under transient conditions were not validated against relevant experimental results. Though the accuracy of these two models could not be validated, the failure time and deformation curves obtained from these FEAs were found to be in a good consistency with the FEA results obtained by Zhao et al. (2005) and Gunalan and Mahendran (2013).

Chapter 3 Behaviour of Web-Perforated CFS C-shape Studs at Ambient and Elevated Temperatures

3.1 Introduction

For ambient temperature, load-bearing CFS wall stud design in the North American is generally based on AISI S100 (2012) provisions. In the main specification of AISI S100 (2012), the width and length of a perforation are limited to be no more than 63.5 mm and 114 mm, respectively; and the strength determination of a stiffened element (e.g., the web of a C-section) with noncircular perforations is based on the traditional effective-width based method, that is, considering members as assemblages of individual elements often subject to local buckling. In Appendix 1 of AISI S100 (2012), the Direct Strength Method (DSM) provides an alternative procedure for determining the strength of CFS members, and extends the limits on the perforation size, shape and spacing. The DSM based approach utilizes finite strip analysis which accounts for the influence of perforations on predicting the elastic buckling loads of a stud, and then substitutes the obtained elastic buckling loads into a set of compressive strength prediction equations to determine the stud strength. However, only a limited number of tests have been carried out to validate the accuracy and generality of the DSM equations in AISI S100 (2012).

Used as wall studs, cold-formed steel (CFS) C-shape studs are often enclosed with insulation in the wall cavity and protected by gypsum boards on both sides. Pre-punched web perforations in studs accommodate the passage of utilities and installation of intermediate braces in practice. A CFS C-shape stud in a CFS wall is subjected to non-uniform cross-sectional distribution of elevated temperature when the wall assembly is exposed to fire attack from one side. Consequently, the stud fail by a combination of axial compression and bending actions due to thermal bowing, magnification effects and neutral axis shift. Due to the existence of web perforations, the non-uniform temperature distributions and structural behaviour of CFS wall studs become more complicated than those of steel studs without perforations at elevated temperatures during fire events. The complexity associated with perforation shape, size, and spacing has created a challenge in determining the compressive strength of CFS C-shape studs with web perforations. Currently, research on the behaviour of web-perforated CFS wall studs at elevated temperatures is limited.

Presented in this chapter are experimental and finite element studies on web-perforated CFS wall studs under various conditions. First, at ambient temperature, the experimental investigation of CFS C-shape stub columns with web perforations at varying lengths (Xu, 2014) are reported. The efficiency and accuracy of DSM in predicting the ultimate compressive strength of such columns is verified through a comparison with test data (Xu, 2014). Second, finite element analysis (FEA) is carried out to investigate the behaviour of CFS C-shape stub columns with web perforations at uniform cross-sectional distribution of elevated temperatures, and the applicability of FEA is validated by tests (Feng, Wang, & Davies, 2003d). Finally, finite element analysis is performed to investigate the effect of web perforations on the behaviour of CFS C-shape wall studs subjected to non-uniform cross-sectional distribution of elevated temperatures. Sequentially uncoupled thermal-stress analysis is carried out under transient state condition. The non-uniform cross-sectional distributions of elevated temperature are obtained from the thermal analysis of insulated CFS walls. CFS C-shape wall studs subjected to the concentrically axial load with different ratios are investigated.

3.2 Behaviour of CFS C-shape stub columns at ambient temperature

This section aims to investigate the effect of the length of web perforations on the behaviour of CFS C-shape columns. The compressive strength from CFS C-shape stub column tests (Xu, 2014) are compared with that calculated using the DSM approach.

3.2.1 Stub column tests

3.2.1.1 Stub column specimens

To study the effect of web perforations on the compressive strength of CFS C-shape columns, a total of 18 stub columns were tested, six being solid sections without a web perforation, and 12 having pre-punched web perforations. The parameters investigated were the nominal thickness of steel, t , and the length of web perforation, L_w . The nominal thicknesses of steel were 1.2 mm and 1.5 mm, and the lengths of the web perforations ranged from 0 to 130 mm. The details of specimens and perforation dimensions are shown in Figure 3.1 and Table 3.1, in which the first number of the designation denotes the length of web perforation, the second and third digits represent the steel thickness, and the number of the specimen in a column group, respectively.

The specimens were fabricated with cold-formed galvanized steel. The length for all the specimens was selected as 490 mm for the following reasons: (i) to minimize the influence of global buckling; and

(ii) to ensure enough clear distance from the perforation to the end of the specimen, avoiding possible end effects. Both ends of the specimen were milled flat to ensure full contact between the specimen and the steel bearing plates. A slotted perforation, located in the center of the web, had a constant width, d_h of 38 mm. The lengths of the perforations, L_h , were 0, 75, 114 and 130 mm. The nominal thickness of the specimen, t , were 1.2 and 1.5 mm. For each column group, three identical specimens were tested.

Mechanical properties for the specimens were based on the tensile coupon tests as per the Chinese standard (GB/T228, 2010), which were tested at the Chang'an University, China. Three tensile coupons were cut longitudinally from the web of a randomly selected C-shape CFS specimen for each thickness. The average material properties are listed in Table 3.2, where f_y , f_u , E_s and ν are the steel yield stress, tensile strength, Young's modulus of elasticity and Poisson's ratio, respectively.

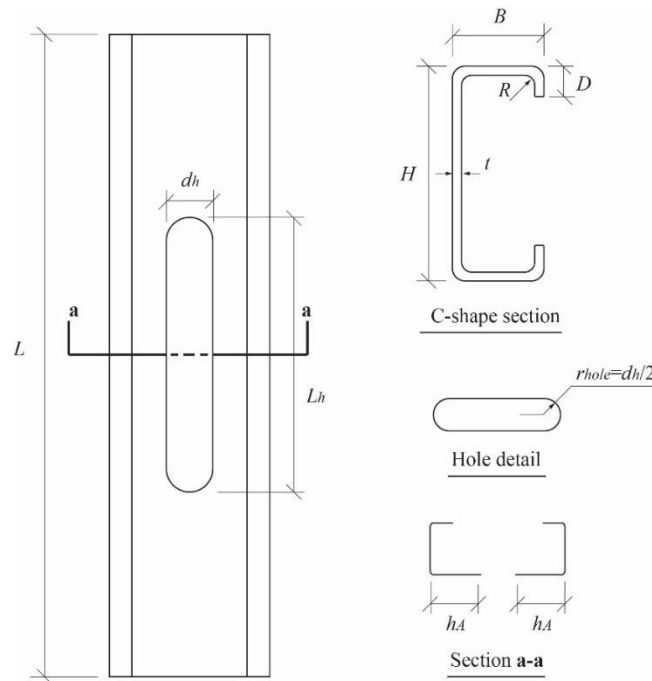


Figure 3.1 Specimen profiles (Xu, 2014)

Table 3.1 Specimen dimensions (Xu, 2014)

Specimen No.	L (mm)	H (mm)	B (mm)	D (mm)	t (mm)	R (mm)	d_h (mm)	L_h (mm)
0-1.5-1	490	150	40	15	1.5	3.0	38	0
0-1.5-2								
0-1.5-3								
75-1.5-1	490	150	40	15	1.5	3.0	38	75
75-1.5-2								
75-1.5-3								
114-1.5-1	490	150	40	15	1.5	3.0	38	114
114-1.5-2								
114-1.5-3								
130-1.5-1	490	150	40	15	1.5	3.0	38	130
130-1.5-2								
130-1.5-3								
114-1.2-1	490	150	40	15	1.2	2.4	38	114
114-1.2-2								
114-1.2-3								
130-1.2-1	490	150	40	15	1.2	2.4	38	130
130-1.2-2								
130-1.2-3								

Table 3.2 Mechanical properties from tensile coupon tests (Xu, 2014)

t (mm)	E_s (N/mm ²)	f_y (N/mm ²)	f_u (N/mm ²)	ν
1.2	2.03×10^5	235	400	0.3
1.5	2.03×10^5	385	510	0.3

3.2.1.2 Experimental setup

Shown in Figure 3.2 is the setup of the experimental investigation. The compressive tests were conducted on a hydraulic compressive test frame system with a loading capacity of 2,000 kN. The load was applied uniformly and concentrically to each specimen through two bearing plates. The column cross section was restrained from lateral movement at ends by the friction-bearing conditions. The axial deformation of each specimen was measured with a dial gauge, and the longitudinal strains were recorded by four uniaxial strain gauges placed at the mid-height of the specimen. The axial load was applied with an increment of one-tenth of the estimated compressive strength of each specimen, and the smaller load increments were adopted when the specimen approached failure.

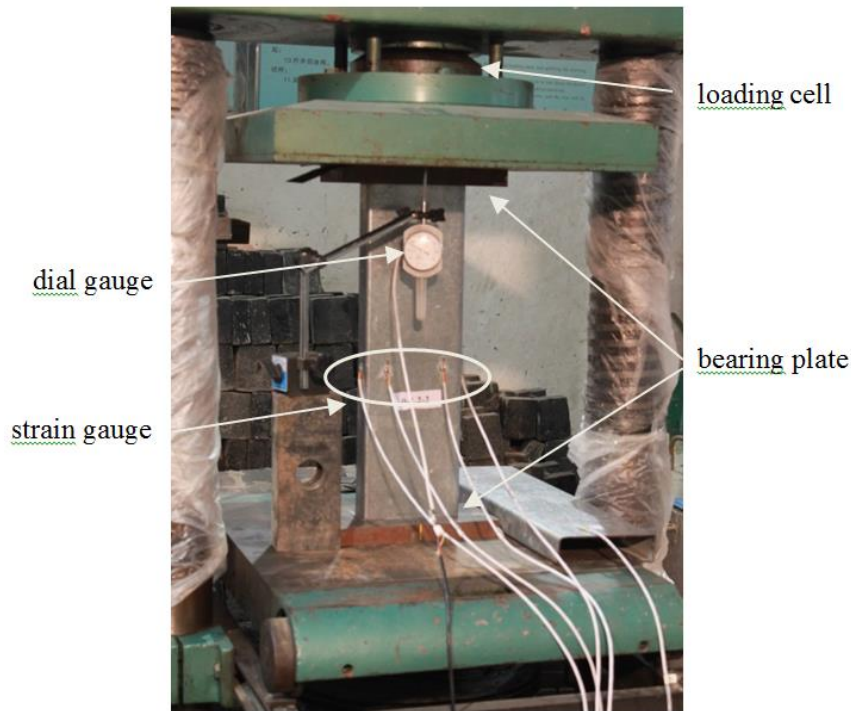


Figure 3.2 Experimental setup (Xu, 2014)

3.2.1.3 Experimental results

Shown in Figure 3.3 are the failure modes of the specimens. The typical failure mode observed was local buckling in the web near both column ends, together with inward distortional buckling with only one half-wave located longitudinally between the two ends. For the specimens showing a smooth half sine wave in the web near the perforation, there occurred larger out-of-plane deflection at the center of the web, and more localized deformation in both flanges at the mid-height of the column when compared to the specimens without perforation.

The existence of the perforation degrades the transverse plate stiffness of the web, which in turn deteriorates the rotation restraint provided by the web to the flange. Consequently, both the web and flange deformations around the perforation are increased. However, owing to the possible presences of initial geometrical imperfections and minor misalignments in the specimens, local buckling concentrated in flanges and unstiffened strips adjacent to web perforations were observed in a few specimens, such as specimen 130-1.5-3.

The typical load-displacement curves for each specimen group obtained from the tests are shown in Figure 3.4. The differences in the ultimate strength, P_{test} , among the three identical specimens for each group are found to be less than 7%. The length of web perforation has little influence on the ultimate strength.



a) Group 0-1.5



b) Group 75-1.5



c) Group 114-1.5



d) Group 130-1.5



e) Group 114-1.2



f) Group 130-1.2

Figure 3.3 Specimen failure modes (Xu, 2014)

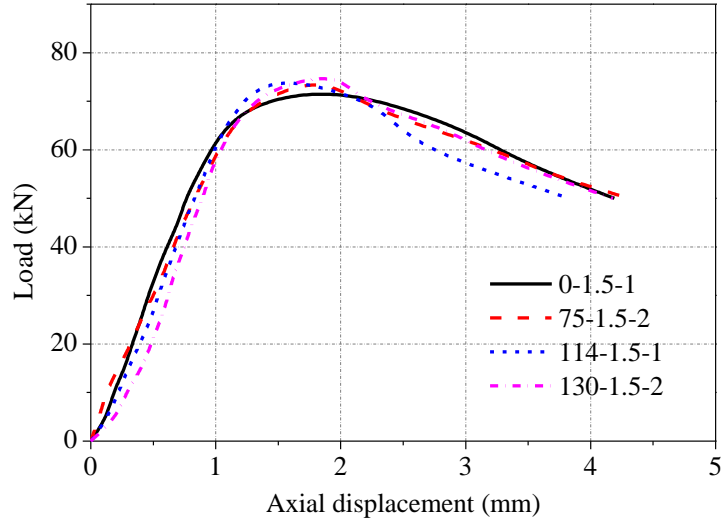


Figure 3.4 Load-displacement relationships (Xu, 2014)

3.2.2 Comparison with DSM approach

According to the DSM approach, the nominal axial strength, P_n , is calculated as the minimum strength from the local, distortional, and global buckling, i.e., $P_n = \min(P_{nl}, P_{nd}, P_{ne})$. The limit state strengths, P_{nl} , P_{nd} , and P_{ne} , are determined from Eqs. (3.1)-(3.9) for members without web perforations, and from Eqs. (3.1)-(3.6) and (3.10)-(3.16) for members with web perforations (AISI-S100, 2012).

(a) Flexural, torsional, or flexural-torsional buckling

$$\text{for } \lambda_c \leq 1.5, \quad P_{ne} = (0.658^{\lambda_c^2}) P_y, \quad (3.1)$$

$$\text{for } \lambda_c > 1.5, \quad P_{ne} = \left(\frac{0.877}{\lambda_c^2} \right) P_y, \quad (3.2)$$

where

$$\lambda_c = \left(P_y / P_{cre} \right)^{0.5}. \quad (3.3)$$

(b) Local buckling or local-global buckling interaction

The nominal axial strength, P_{nl} , is calculated as the following:

$$\text{for } \lambda_l \leq 0.776, \quad P_{nl} = P_{ne}, \quad (3.4)$$

$$\text{for } \lambda_l > 0.776, P_{nl} = \left[1 - 0.15 \left(\frac{P_{crl}}{P_{ne}} \right)^{0.4} \right] \left(\frac{P_{crl}}{P_{ne}} \right)^{0.4} P_{ne}, \quad (3.5)$$

where

$$\lambda_l = (P_{ne} / P_{crl})^{0.5}. \quad (3.6)$$

(c) Distortional buckling

For columns without web perforations,

$$\text{for } \lambda_d \leq 0.561, P_{nd} = P_y, \quad (3.7)$$

$$\text{for } \lambda_d > 0.561, P_{nd} = \left[1 - 0.25 \left(\frac{P_{crl}}{P_y} \right)^{0.6} \right] \left(\frac{P_{crl}}{P_y} \right)^{0.6} P_y, \quad (3.8)$$

where

$$\lambda_d = (P_y / P_{crl})^{0.5}. \quad (3.9)$$

For columns with web perforations,

$$\text{for } \lambda_d < \lambda_{d1}, P_{nd} = P_{ynet}, \quad (3.10)$$

$$\text{for } \lambda_{d1} < \lambda_d \leq \lambda_{d2}, P_{nd} = P_{ynet} - \left(\frac{P_{ynet} - P_{d2}}{\lambda_{d2} - \lambda_{d1}} \right) (\lambda_d - \lambda_{d1}), \quad (3.11)$$

$$\text{for } \lambda_d > \lambda_{d2}, P_{nd} = \left(1 - 0.25 \left(\frac{P_{crl}}{P_y} \right)^{0.6} \right) \left(\frac{P_{crl}}{P_y} \right)^{0.6} P_y, \quad (3.12)$$

where

$$\lambda_d = (P_y / P_{crl})^{0.5}, \quad (3.13)$$

$$\lambda_{d1} = 0.561 (P_{ynet} / P_y), \quad (3.14)$$

$$\lambda_{d2} = 0.561 \left[14 (P_y / P_{ynet})^{0.4} - 13 \right], \quad (3.15)$$

$$P_{d2} = \left(1 - 0.25 \left(\frac{1}{\lambda_{d2}} \right)^{1.2} \right) \left(\frac{1}{\lambda_{d2}} \right)^{1.2} P_y. \quad (3.16)$$

In the foregoing equations, λ_c , λ_l and λ_d are the slenderness ratios; P_y and P_{net} are the column squash loads associated with gross and net sections, respectively; and P_{cre} , P_{crl} and P_{crd} are the elastic global, local and distortional buckling loads, respectively.

Due to the relatively short length of the specimens, global buckling (i.e., flexural, torsional, or flexural-torsional buckling) does not occur; thus, only the elastic buckling loads associated with local and distortional buckling modes, P_{crl} and P_{crd} , were investigated by finite strip analysis with CUFSM software (Schafer & Ádány, 2006). For members without web perforations, P_{crl} and P_{crd} are obtained from the two local minimums of the elastic buckling curve (Li & Schafer, 2010). For members with web perforations, P_{crl} and P_{crd} can be determined based on the method of Moen and Schafer (2009), which accounts for the influence of web perforations.

The compressive strength of the 18 specimens obtained from the stub column tests (Xu, 2014) are used to assess the accuracy of the DSM approach. Shown in Table 3.3 is a comparison of the compressive strength obtained from the test results and predicted by the DSM approach. Among all the buckling limit states, local buckling loads P_{nl} are lowest, signifying that all the specimens were governed by local buckling. The ratio of local and distortional buckling loads P_{nl}/P_{nd} ranges from 0.89 to 0.96. As the length of the perforation increases, the ratio P_{nl}/P_{nd} approaches 1.0, representing the intensive interaction between local and distortional buckling. When $L_h=130$ mm, ratio P_{nl}/P_{nd} approaches to 0.93 and 0.96 for specimens with thickness of 1.5 and 1.2 mm, respectively; which indicates sections with thinner thickness is more likely involved with the interaction of local and distortional buckling.

From Table 3.3, it can also be seen that the nominal strengths of the specimens with web perforations evaluated by the DSM are in good agreement with those of the tests. The nominal strength P_n evaluated by DSM are slightly greater than the tested ultimate strength, P_{test} , except in one case. The differences between the two are less than 9%. Thus, the DSM approach is accurate in determining the compressive strength of CFS C-shape stub columns with non-circular web perforations, and L_h is up to 130 mm.

Table 3.3 Comparison of test results with DSM approach

Specimen No.	A_g (mm ²)	A_{net} (mm ²)	P_{test} (kN)	P_{ne} (kN)	P_{nt} (kN)	P_{nd} (kN)	P_n (kN)	P_n/P_{test}
0-1.5-1			76.0					1.06
0-1.5-2	374	317	73.0	131.40	71.52	80.64	71.52	1.02
0-1.5-3			74.0					1.03
75-1.5-1			70.0					0.98
75-1.5-2	374	317	75.0	131.34	71.50	78.80	71.50	1.05
75-1.5-3			74.0					1.03
114-1.5-1			75.0					1.05
114-1.5-2	374	317	76.0	131.26	71.47	77.60	71.47	1.06
114-1.5-3			73.0					1.02
130-1.5-1			73.0					1.02
130-1.5-2	374	317	76.0	131.23	71.46	77.10	71.46	1.06
130-1.5-3			78.0					1.09
114-1.2-1			42.0					1.07
114-1.2-2	299	254	40.0	66.48	39.43	41.09	39.43	1.01
114-1.2-3			40.0					1.01
130-1.2-1			43.0					1.09
130-1.2-2	299	254	43.0	66.46	39.43	40.87	39.43	1.09
130-1.2-3			43.0					1.09

3.3 Finite element modelling of CFS C-shape columns at ambient and uniform elevated temperatures

Finite element analysis is performed to simulate the behaviour of CFS C-shape columns with and without web perforations at both ambient and elevated temperatures using ABAQUS (2012). In total, 52 steady-state tests on CFS C-shape columns both at ambient and uniform elevated temperatures were conducted by Feng, Wang, & Davies (2003d). In this current study, 11 of those 52 specimens, from the Lipped channel 100×54×15×1.2 series (CFS C-shape sections), are used to develop and verify the finite element model. The temperature distribution of CFS columns is considered to be uniform in the cross section at a given temperature.

3.3.1 Stub column tests

Shown in Table 3.4 and Table 3.5 are the measured dimensions of the specimens exposed to different uniform temperatures throughout the tests. The notations included in these two tables and the specimen profiles are presented in Figure 3.1. The uniform temperatures range from 22 °C to 700 °C. The nominal length of the specimens is 400 mm. The d_h and L_h are 40 mm and 100 mm, respectively.

Table 3.4 Nominal cross-section dimensions of specimens without perforations (Feng et al., 2003d)

Temp.(°C)	Specimen No.	<i>H</i> (mm)	<i>B</i> (mm)	<i>D</i> (mm)	<i>t</i> (mm)	<i>L</i> (mm)
Amb.	Lip12a1	100.05	53.64	17.09	1.23	400.2
250	Lip12b325	100.27	53.64	17.21	1.19	400
400	Lip12c140	99.31	52.31	16.25	1.18	398
550	Lip12c355	99.96	52.32	16.56	1.18	399
700	Lip12d670	100.31	52.44	15.75	1.2	402

Table 3.5 Nominal cross-section dimensions of specimens with perforations (Feng et al., 2003d)

Temp.(°C)	Specimen No.	<i>H</i> (mm)	<i>B</i> (mm)	<i>D</i> (mm)	<i>t</i> (mm)	<i>L</i> (mm)
Amb.	Lip12a3	100.05	53.64	17.09	1.19	400.8
	Lip12a4	100.05	53.64	17.09	1.19	400.4
400	Lp12ch140	100.76	53.23	15.64	1.24	398
	Lp12ch240	99.31	52.08	16.16	1.203	398.5
550	Lp12bh155	99.43	51.92	16.15	1.188	399
	Lp12bh255	99.87	51.04	16.17	1.19	399

Tensile coupon tests for S350GD+Z steel at ambient temperature were conducted by Feng et al. (2003d). The material properties are shown in Table 3.6. The measured stress-strain relationship indicates that cold-formed steel exhibits a gradual yielding behaviour followed by a considerable period of strain hardening, which is quite different from that of hot-rolled steel. Plotted in Figure 3.5 is the stress-strain curve at ambient temperature. The elastic stress-strain behaviour is represented by a linear segment up to a limit stress $f_p = 0.7f_y$, where f_y is the 0.2% proof stress. The slope of this linear segment equals the measured elastic modulus. The gradual yield behaviour is idealised by using a bilinear representation with the tangent moduli E_1 and E_2 between the proportional limit f_p and the yield strength f_y with an intermediate point at a stress of $0.875f_y$. The strain-hardening behaviour is represented by a linear segment with a tangent modulus E_3 . The value of E_1 , E_2 and E_3 are 80000 N/mm^2 , 20000 N/mm^2 and $1/200E_1$. The stress-strain relationship at elevated temperatures is derived based on Eurocode 3 Part 1.2 (BS EN 1993-1-2, 2005) as shown in Figure 3.6.

Table 3.6 Mechanical properties at ambient temperature

Cross-section	f_y (N/mm ²)	f_u (N/mm ²)	E (N/mm ²)
100×54×15×1.2	410.58	526.02	186950

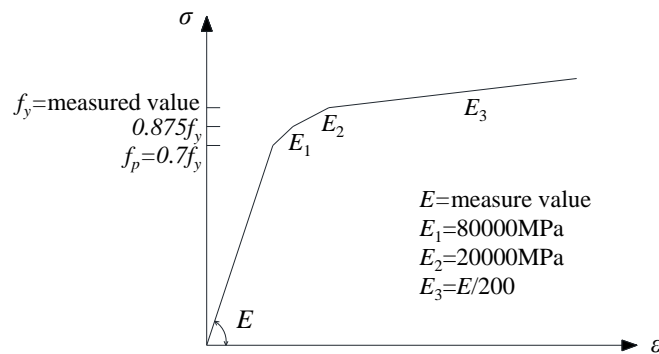


Figure 3.5 Stress-strain relationship of steel at ambient temperature

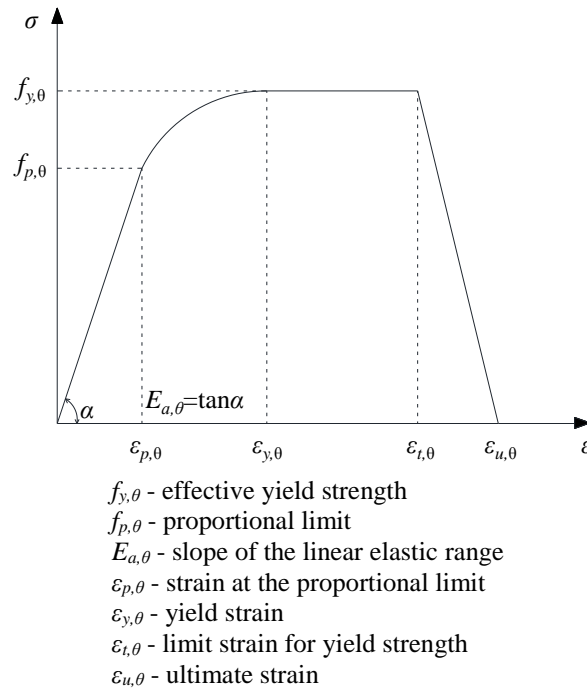


Figure 3.6 Stress-strain relationship of steel at elevated temperature

3.3.2 Finite element modelling and analysis

Each finite element analysis is carried out in two steps. First, apply a linear eigenvalue buckling analysis to obtain the buckling modes. Then, the lowest buckling mode derived is incorporated into the second step to conduct a nonlinear analysis. Feng, Wang, & Davies (2003a) demonstrated that the compressive strength of CFS C-shape columns would have not been noticeably affected by initial geometric imperfection and the maximum initial local imperfection can be taken as the thickness of the cross section. Due to the test specimens are stub columns, the influence of global imperfection can be ignored. The round corners of the C-shape columns were simplified as rectangular ones, in which cold work of forming and residual stresses were ignored.

3.3.2.1 Finite element type and mesh

The four-node shell element with reduced integration and hourglass control (S4R) can be used in this study which was demonstrated by Feng et al. (2004). To study the sensitivity to mesh sensitivity, five mesh sizes are examined for the specimen without web perforation Lip12c355. The compressive strength predicted using different element sizes are provided in Table 3.7. The mesh control around web perforations is adopted as quad-dominated for element shape, free for technique, and media axis

for algorithm. The element size of 7.5 mm×7.5 mm (length by width) ratio (Figure 3.7(a)) provides adequate accuracy with minimum computational time. For C-shape columns with web perforation, a finer mesh size of 5 mm×5mm (Figure 3.7(b)) is required to guarantee the accuracy.

Table 3.7 Sensitivity study of element sizes

Mesh size	Lip12c355 Compressive strength $P_{test}=23$ kN				
	2.5mm	5mm×5mm	7.5mm×7.5mm	10mm×10mm	15mm×15mm
F_{FEA} (kN)	25.53	25.73	25.90	26.61	26.75
$(F_{FEA}-P_{test})/P_{test}$	0.11	0.12	0.13	0.16	0.16

3.3.2.2 Boundary conditions and displacement application

The ends of the columns were fixed against all degrees of freedom except for the axial displacement at the loaded end (Z direction), and the displacement was applied at each node of the loaded end to simulate the experimental boundary conditions (Figure 3.7(c)). The RIKS method is used to predict the post-buckling behaviour.

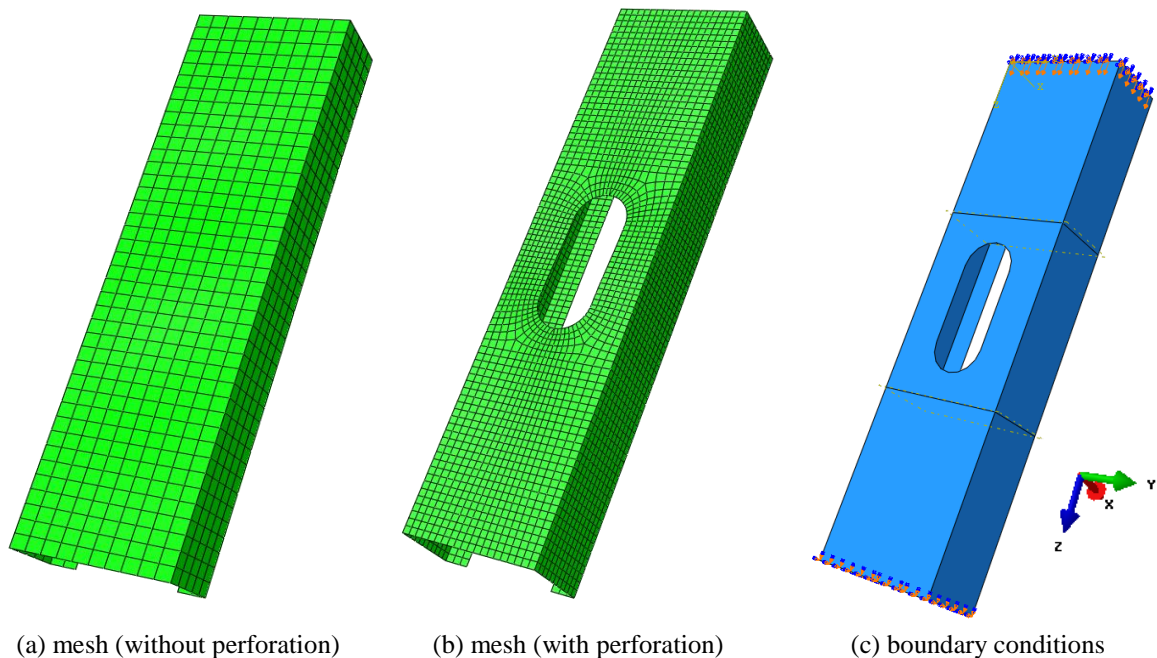


Figure 3.7 FE mesh and boundary conditions for specimen 100×54×15×1.2

3.3.2.3 Validation of finite element model

The finite element model is validated by the experiments conducted by Feng et al. (2003d). Compared in Figure 3.8 and Figure 3.9 are the failure modes of specimens without and with web perforation between test and FEA results, respectively. The FEA results show that the specimens failed with a combination of local buckling and distortional buckling, which agrees well with the tests.

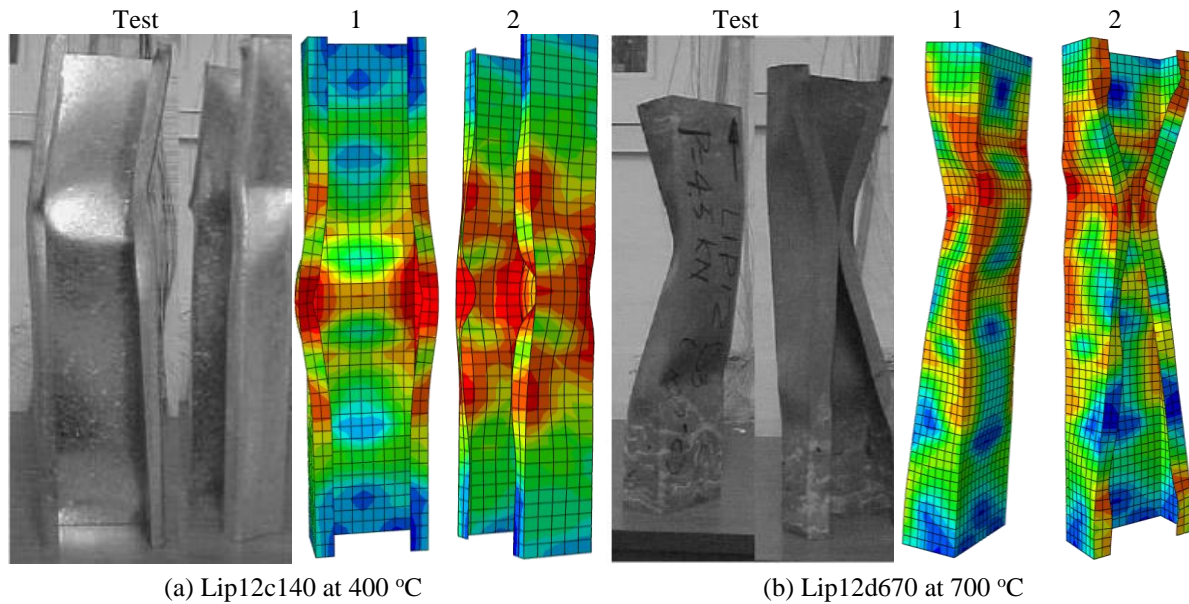


Figure 3.8 Failure modes of columns without perforations

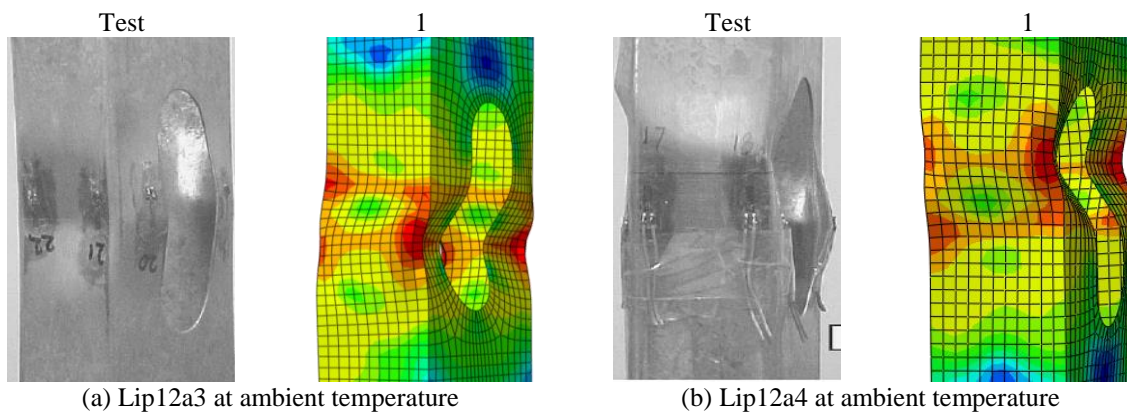


Figure 3.9 Failure modes of columns with perforations

Presented in Table 3.8 and Figure 3.10 are the comparison between test compressive strength and FEA results. The mean values of the P_{test}/P_{FEA} ratio are 0.91 and 0.95 for CFS C-shape columns without perforation and with perforation, and the standard deviations of the P_{test}/P_{FEA} ratio are 0.09 and 0.07,

respectively. It shows that the predicted compressive strengths are close to the test compressive strength below 550 °C while has a deviation of 36% at 700 °C. Since the test result at 700 °C is unreliable due to high temperature effect on load cell (Feng et al., 2003d), the FEA compressive strength can also be considered to be accurate. Thus, this comparison indicates that the FEA predicts credible compressive strength of CFS columns at uniform elevated temperatures.

Table 3.8 Comparison of compressive strength between FEA and test results

without perforations					with perforations				
Temp. (°C)	Specimen	P_{test} (kN)	P_{FEA} (kN)	$\frac{P_{test}}{P_{FEA}}$	Temp. (°C)	Specimen	P_{test} (kN)	P_{FEA} (kN)	$\frac{P_{test}}{P_{FEA}}$
Amb.	Lip12a1	55.99	67.13	0.83	Amb.	Lip12a3	54.86	60.79	0.90
250	Lip12b325	53.16	59.64	0.89	Amb.	Lip12a4	53.48	60.31	0.89
400	Lip12c140	45.75	43.77	1.05	400	Lp12ch140	39.93	42.53	0.94
550	Lip12c355	23.00	26.61	0.86	400	Lp12ch240	43.02	40.36	1.07
700	Lip12d670	5.70	8.85	0.64	550	Lp12bh155	22.64	25.03	0.90
					550	Lp12bh255	25.17	25.10	1.00
			Mean	0.91					0.95
			COV	0.09			(Lip12d670 at 700 °C is not included.)		0.07

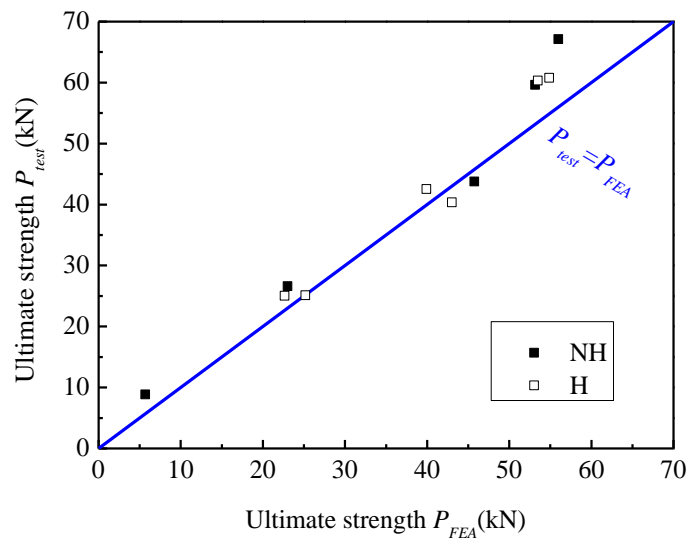


Figure 3.10 Comparison of compressive strength between FEA and test results

3.4 Behaviour of web-perforated CFS wall studs subjected to non-uniform cross-sectional elevated temperature

Presented in this section is an FEA on the effect of web perforations on the behaviour of cold-formed steel C-shape studs subjected to non-uniform cross-sectional distribution of elevated temperature with use of finite element analysis. The length of web perforations investigated varies from 0 mm to 630 mm (25 in.). The non-uniform cross-sectional distributions of elevated temperature obtained from finite element thermal analysis of insulated CFS walls in standard fire for up to 105 minutes were employed. Sequentially uncoupled thermal-stress analyses were carried out under a transient state condition. Concentrically loaded cold-formed steel C-shape studs with load ratios of 0.6, 0.7, 0.8 and 0.9 are investigated.

Using ABAQUS (2012), the FEA procedure commenced a thermal analysis to obtain the non-uniform cross-sectional distributions of elevated temperature of a CFS column from a 600mm wide CFS wall section, followed by a structural analysis to investigate the behaviour of the column at elevated temperature. The nodal temperature at the elevated temperature obtained from the thermal analysis were applied as a predefined boundary condition of the FE model in the structural analysis.

Illustrated in Figure 3.11 are the cross-section of the CFS wall segment modelled in FEA and the nominal cross-sectional dimensions of the CFS C-shape column at the location of web perforation. The modelled CFS wall segment, 600 mm in width and 3200 mm in height, consists of a CFS C-shape column (150 mm \times 40 mm \times 15 mm \times 1.5 mm) sheathed with a double layer of 12 mm thick gypsum board on both sides. The 150 mm deep wall cavities are filled with glass fibre. Five web perforations are evenly spaced 640 mm o.c. along the height of the column. The L_h varies from 0 mm to 630 mm, whereas d_h remains constant at 38 mm (1.5 in.). Six different L_h , i.e., 0 mm (0 in.), 130 mm (5 in.), 250 mm (10 in.), 380 mm (15 in.), 510 mm (20 in.) and 630 mm (25 in.) are investigated. The ambient temperature is defined as 20 °C. The CFS walls are exposed to the standard fire curve defined by ISO 834 (1999) for up to 105 minutes.

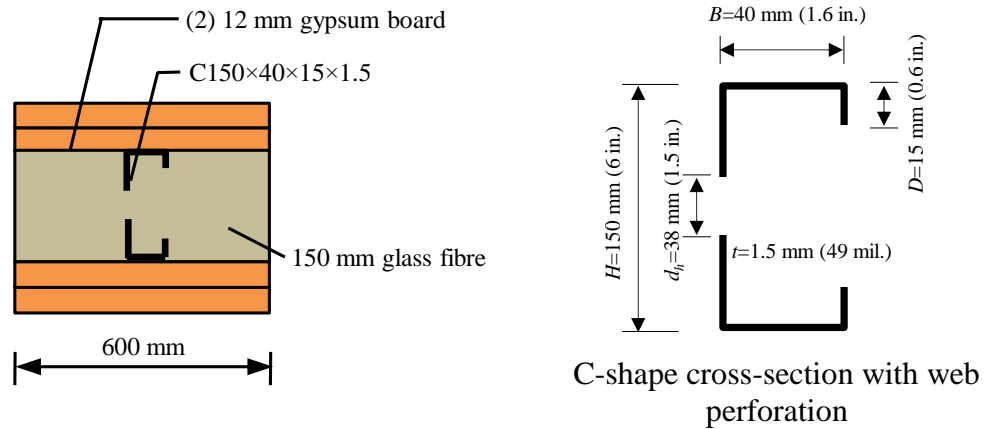
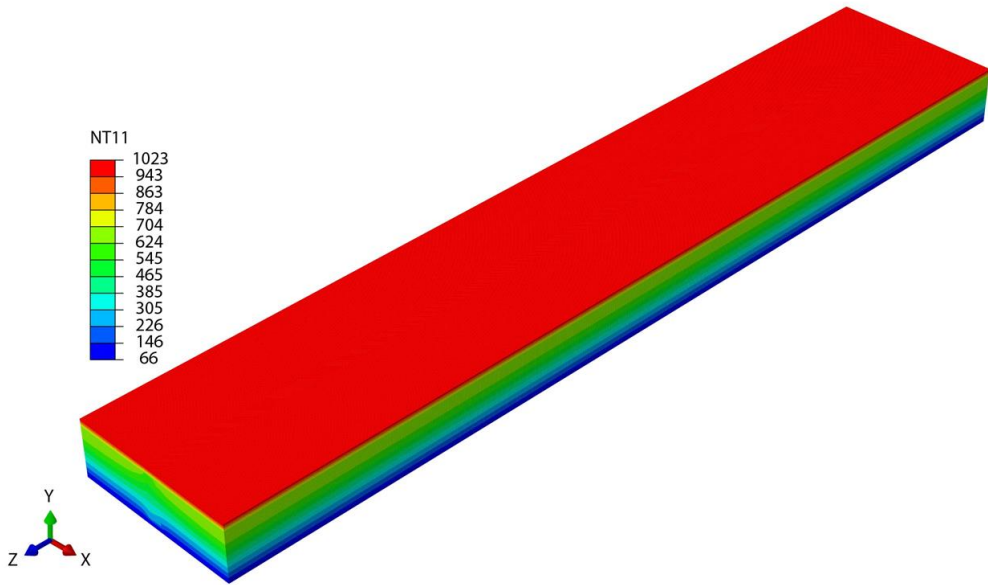


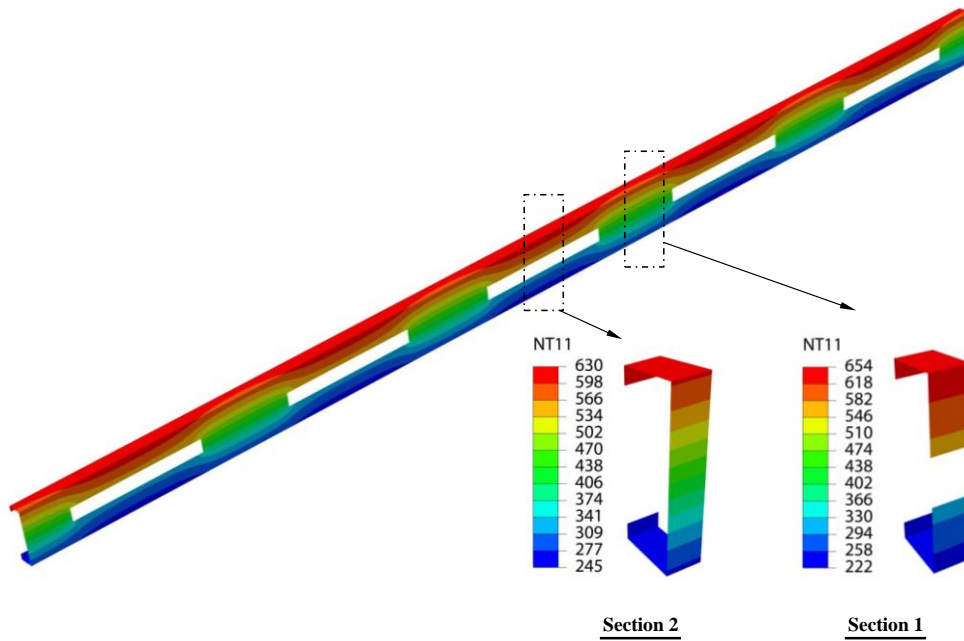
Figure 3.11 Configuration of CFS wall section

3.4.1 Non-uniform cross-sectional temperature distribution

Finite element thermal analysis was performed for insulated CFS walls subjected to standard fire. The method used to develop the FE thermal model in this study is similar to that from Section 4.4 in Chapter 4, which was verified and calibrated with experimental tests. Shown in Figure 3.12(a) and (b) are the predicted temperature distribution in the CFS wall and C-shape column at 105 minutes' fire exposure, respectively. The temperature of the gypsum board surface is 1023 °C on the fire-exposed side (ES), and 66 °C on the unexposed side (UES). The non-uniform cross-sectional temperature distribution in the CFS C-shape column also varies along the column height. The maximum temperature in the column is 654 °C. The cross-sectional views in Section 1 and 2 illustrate the temperature contours at the location with and without web perforation, respectively. It is observed that the temperature of Section 1 is higher on the hot flange and lower on the cold flange compared with the corresponding temperatures of Section 2. The temperature distribution in the web of Section 1 also differs from that of Section 2 due to the presence of the perforation.



(a) CFS wall



(b) C-shape column

Figure 3.12 Temperature contour ($L_h = 380$ mm): (a) CFS wall and (b) C-shape column

3.4.2 Finite element structural analysis

The FE structural analysis was performed under a transient state condition in two steps. First, a pre-determined axial compression load was applied as Step 1. After that, the temperature distributions obtained from the heat transfer analysis were incorporated in the analysis as Step-2.

In the structural analysis, the CFS C-shape column is modeled with a rigid plate (150 mm×40 mm) attached to each end as shown in Figure 3.14. The reference point of the rigid plate coincides with the centroid of the cross section of the column. The element type and mesh of the CFS C-shape column are the same as those of the heat transfer model, for which correlations are required to import the temperature from the heat transfer analysis. A global mesh size of 15 mm is used to discretize the rigid plate. The time period of Step 2 is specified as 6300, which corresponds to 105 minutes. In the Step 2, the maximum number of time increments is 500; the initial increment size is 30; and the minimum and maximum increment sizes are 1×10^{-9} and 300, respectively. The CFS column and rigid plate are modeled with a 4-node shell element with reduced integration (S4R) and rigid bilinear quadrilateral elements (R3D4), respectively.

When it is exposed to elevated temperature, the mechanical properties of steel deteriorate rapidly, consequently reducing the stiffness and strength of CFS columns. The yield strength, elastic modulus and Poisson's ratio of steel at ambient temperature are taken as 345 MPa, 203 GPa and 0.3, respectively. Presented in Figure 3.13 is the nominal stress-strain relationship of cold-formed steel at elevated temperatures, which is derived base on EC 3 Part 1.2 (2005). Steel expands considerably when exposed to elevated temperature. Therefore, thermal bowing will be developed due to the presence of non-uniform temperature distributions across the cross section. Hence, the thermal expansion coefficient, α_T , of CFS at different temperatures needs to be determined for the structural analysis of CFS wall systems at elevated temperature. In this study, α_T of CFS stipulated in Eurocode 3 Part 1.2 (2005) is adopted, and is the same as that of hot-rolled steel.

Illustrated in Figure 3.14 is the load and boundary condition of the modelled CFS column. The column is simply supported by translational displacements; i.e., UX, UY and UZ at the lower end and UX and UY at the upper end are restrained. Twisting about the Z axis (URZ) is restrained at both ends. A target axial load is applied first via the reference node of the rigid plate at the upper end. The load ratio (R), i.e., the ratio of the applied load at the fire limit state and the ultimate compressive strength of the CFS column at ambient temperature, ranges from 0.6 to 0.9. Shown in Table 3.9 is the applied

axial load of CFS C-shape studs in the FE structural model. At ambient temperature, the ultimate compressive strength drops gradually as the perforation length increases. For example, with length of wen perforation $L_h=630$ mm, the ultimate strength of the CFS C-shape column is only about 60% that of a column without perforations. Initial global geometrical imperfection is accounted for through eigenvalue buckling analysis. The first mode shape and a magnitude of one thousandth of the column length ($L/1000$) is adopted (Figure 3.15). The time dependent nodal temperature obtained from the thermal analysis (Figure 3.12(b)) are incorporated into the structural model as a predefined boundary condition. The ambient temperature is assumed to be 20 °C.

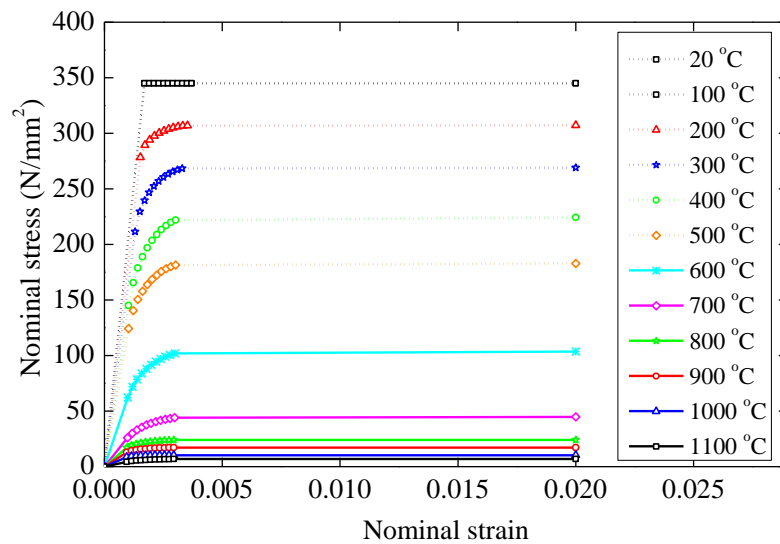


Figure 3.13 Stress-strain relationship of cold-formed steel at elevated temperature

Table 3.9 Applied load at ambient temperature (Step-1)

L_h (mm)	Applied load (kN)				
	$R=0.9$	$R=0.8$	$R=0.7$	$R=0.6$	$R=0.5$
0	14.8	13.2	11.5	9.9	8.2
130	13.3	11.8	10.3	8.9	7.4
250	12.4	11.1	9.7	8.3	6.9
380	12.1	10.7	9.4	8.0	6.7
510	11.2	10.0	8.7	7.5	6.2
630	9.0	8.0	7.0	6.0	5.0

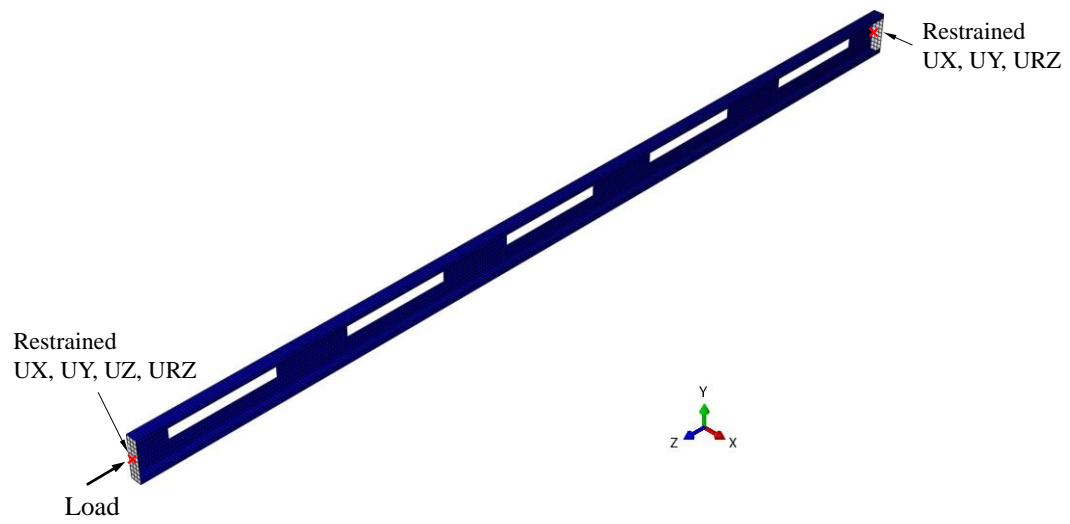


Figure 3.14 Load and boundary conditions in structural analysis

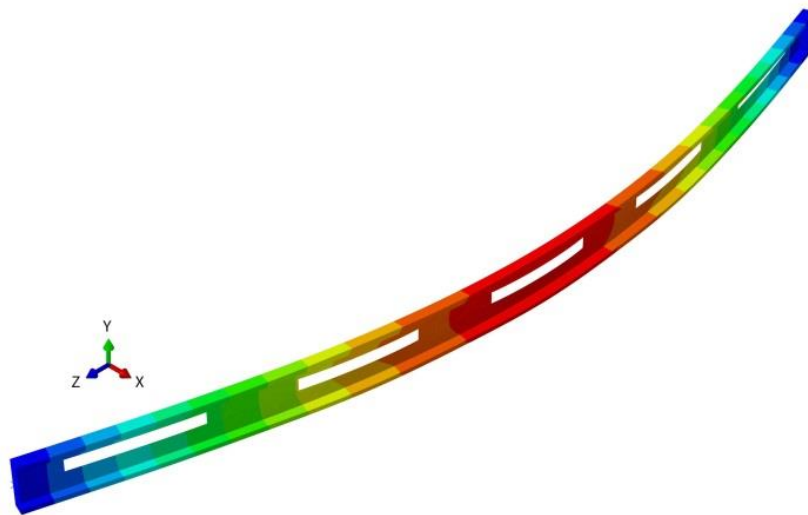


Figure 3.15 Initial global geometric imperfection ($L/1000$)

3.4.3 Results and discussions

Respectively shown in Figure 3.16 and Figure 3.17 are the predicted external reaction force at the lower end and axial deformation of the column at the upper end for a CFS C-shape column with a web perforation $L_h=380$ mm (15 in.) and a load ratio $R=0.9$. As shown in Figure 3.17, the column shortens initially due to the applied axial load at ambient temperature, and then gradually expands as the temperature increases. However, the magnitude of the external reaction force at the lower end stay the same as that of the applied load until column failure occurs at 48.9 minutes. This failure is evidenced by the rapid increase of column deformation and sudden decrease of the reaction force at the lower end of the column. The corresponding end reaction force and axial deformation of the column at the failure is about 85% of the initially applied load and 54 mm, respectively.

Presented in Figure 3.18 is the predicted failure mode of the CFS C-shape column with $L_h=380$ mm (15 in.) and a load ratio of 0.9. Global buckling about the Y-axis together with local failure around the perforation at mid-height is observed. No torsional buckling about the Z-axis occurs since the rotation URZ is assumed to be restrained by the presence of gypsum board on both flanges of the CFS C-shape studs. Thermal bowing is towards the fire-exposed side. The flange of the column on the fire-exposed side buckles first due to the higher temperature, and results in rapid degradation of both the stiffness and strength of the flange. The flange on the fire-unexposed side bears an increasing load and fails as a consequence.

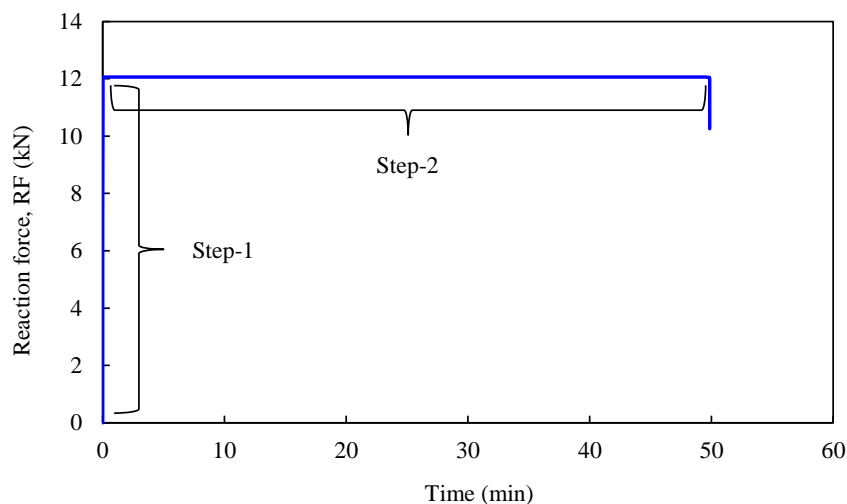


Figure 3.16 Time-end reaction force curve ($L_h=380$ mm, $R=0.9$)

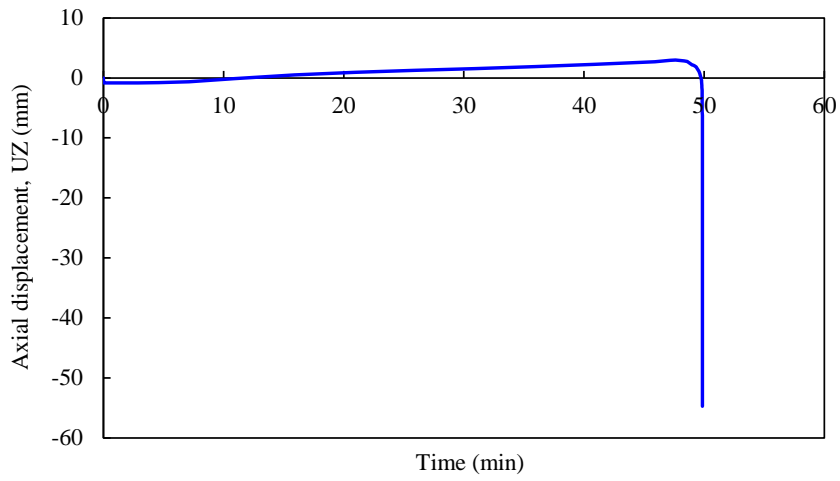
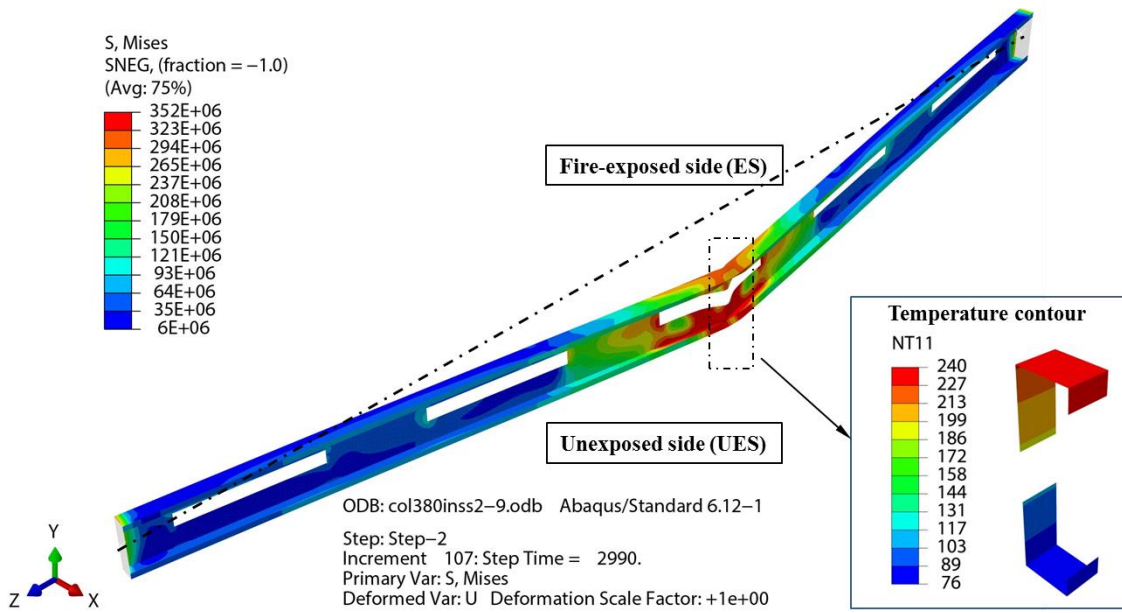
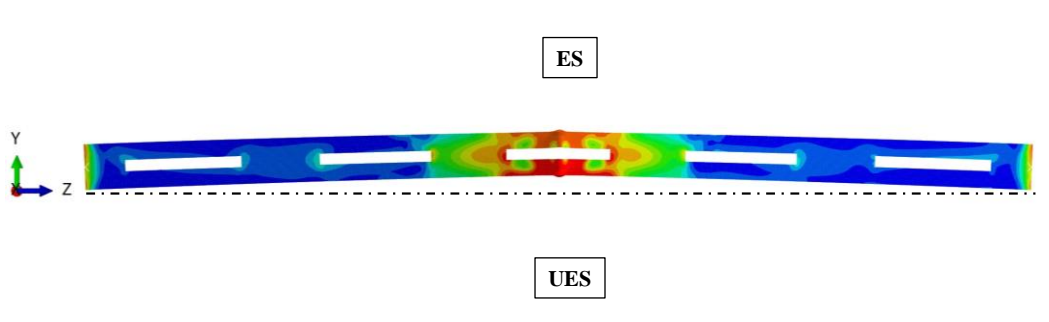


Figure 3.17 Time-axial deformation curve ($L_h=380$ mm, $R=0.9$)



(a) Elevation view



(b) YZ plane view

Figure 3.18 Failure mode ($L_h=380$ mm, $R=0.9$)

Compared in Figure 3.19 is the effect of perforation length on the predicted failure time. At a given perforation length, the failure time decreases rapidly as the load ratio increases. For the case of no web perforations i.e., $L_h=0$ mm, the corresponding failure time is 90.2 minutes for $R=0.6$, and 48.7 minutes when $R=0.9$. The failure time of the latter case is about 46% less than that of the former one. It is found in this investigation that for a given load ratio, the variation among failure times for studs with different L_h is within 10%.

In addition, for a CFS C-shape column with a specified load ratio, the ultimate compressive strength of the columns at elevated temperature is significantly influenced by degradation of material properties of steel and fire exposure time. In contrast, the distribution of non-uniform cross-sectional temperature has a minor influence on the capacity of the column. Compared in Figure 3.20 are the temperature contours of CFS C-shape studs with different web perforation lengths of $L_h=0$ mm, 380 mm and 630 mm in the region of mid-height of the studs at the exact failure time. As can be seen from the figure, there is a minor variation in temperature distributions among these cross sections, which further explains the results presented in Figure 3.19. The web perforation width investigated in this study maintains a constant of 38 mm (1.5 in.), that is, $\frac{1}{4}$ of the web depth of 150 mm (6 in.). If the perforation width increases, a larger temperature gradient is expected, which may more strongly influence the behaviour of the CFS C-shape studs.

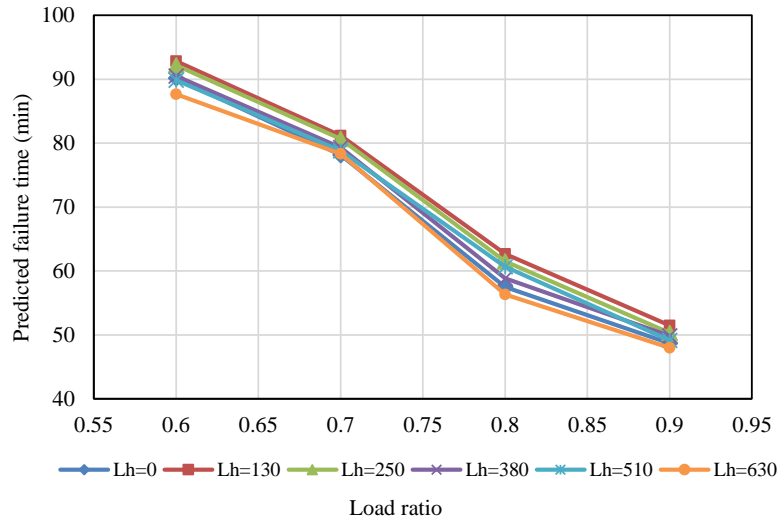


Figure 3.19 Effect of web perforation lengths on failure time

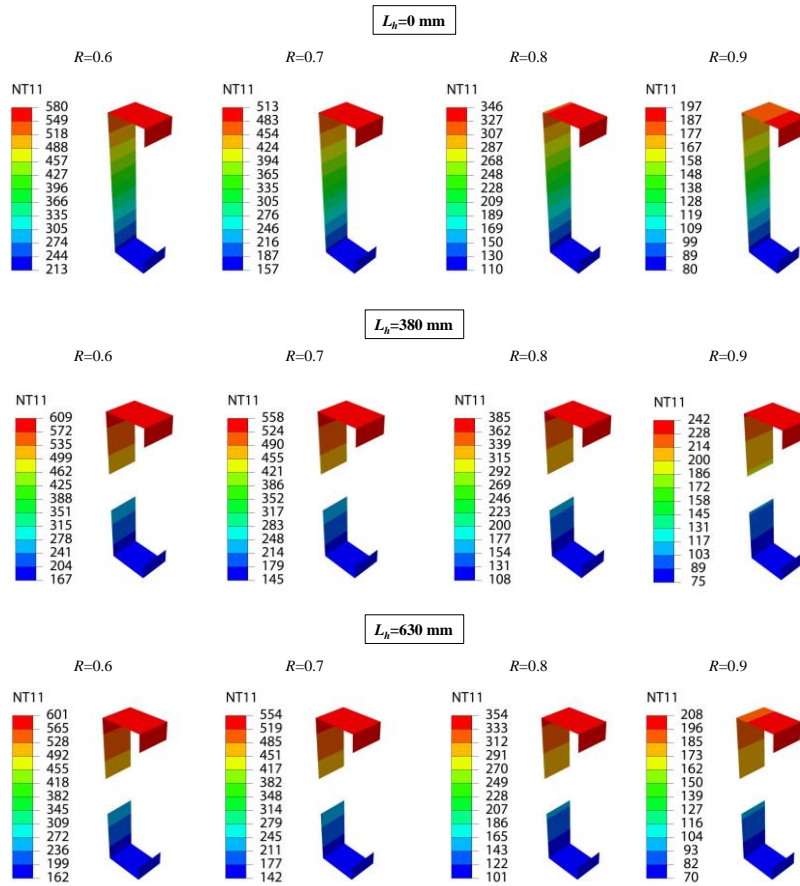


Figure 3.20 Effect of web perforation lengths on temperature distribution

3.5 Conclusions

In this chapter, the behaviour of CFS C-shape stub columns at both ambient and uniform elevated temperatures are investigated. Based on the heat transfer analysis in Chapter 4, the structural analysis of CFS C-shape wall studs subjected to non-uniform cross-sectional distributions of elevated temperature is also carried out. The following conclusions can be drawn:

- Stub column tests (Xu, 2014) found that the length of web perforations has slight effect on the ultimate compressive strength of CFS C-shape stub columns at ambient temperature. In this study, the comparison of the ultimate strength obtained from the tests and predicted by the DSM approach demonstrates that the DSM approach accurately assesses the compressive strength of C-shape CFS stub columns with web perforations.
- Finite element structural model is developed using ABAQUS to investigate the behaviour of CFS C-shape columns at ambient temperature and uniform cross-sectional distribution of elevated temperature ranging from 22 °C to 700 °C. The accuracy of this model is validated based on the stub column tests with web perforations (Feng et al., 2003d).
- The effects of web perforations on the behaviour of CFS C-shape slender columns subjected to non-uniform cross-sectional distribution of elevated temperatures are also investigated. The FEA results demonstrate that the web perforation can affect the temperature distribution in the stud cross sections, but the temperature gradient within a cross section is hardly associated with the web perforation length. The differences in failure times among the CFS C-shape studs with different web perforation lengths at a given load ratio are within 10%.

Chapter 4 Thermal Modelling and Analysis of CFS Walls with Web-Perforated Studs Subjected to Standard Fire

4.1 Introduction

As growing interest in performance-based fire safety design, engineering professionals and researchers are increasingly exploring verified fire resistance models. The temperature distributions in CFS walls under fire have been investigated numerically using 1D and 2D models by other researchers. Several 1D numerical models were proposed to estimate the temperature history through the cross sections of non-insulated CFS walls (Chen, Ye, Bai, & Zhao, 2013; Collier, 1996; Sultan, 1996) and insulated CFS walls (Shahbazian & Wang, 2013; Shahbazian & Wang, 2014; Sultan, Alfawakhiri, & Benichou, 2001). The thermal gradients along the length and width of the CFS walls were ignored. The quantity of heat transfer via conduction or radiation by the CFS steel frame was neglected, except in Shahbazian and Wang's model (Shahbazian & Wang, 2013; Shahbazian & Wang, 2014; Sultan et al., 2001). Moreover, 2D finite element (FE) thermal modelling was established for CFS walls, in which uniform temperature distribution along the stud length was assumed (Feng, Wang, & Davies, 2003b; Gunawan, 2011; Keerthan & Mahendran, 2012; Keerthan & Mahendran, 2013; Shahbazian & Wang, 2013). To develop manual-based methods for evaluating the ultimate strength of CFS wall studs under fire, simplified non-uniform temperature distributions through stud cross sections, as shown in Figure 4.1, were adopted (Feng et al., 2003c; Gunalan & Mahendran, 2013; Shahbazian & Wang, 2011). For example, it is found that it is acceptable to assume that the temperature varies linearly throughout the web while remaining constant in the flanges and lips (Shahbazian & Wang, 2011). However, neither 1D nor 2D models can be used to investigate the effect of web perforation of CFS stud on temperature distributions in the wall assemblies.

Presented in this chapter are the FE thermal analyses to trace the heat transfer process of CFS wall systems under standard fire conditions. The FE models were developed for both the CFS walls with or without cavity insulation. These models were first validated by the standard fire resistance tests of CFS wall systems conducted at the Queensland University of Technology (Kolarkar, 2010), and then a parametric study was carried out to investigate the effects of stud perforations on the thermal performance of CFS wall systems.

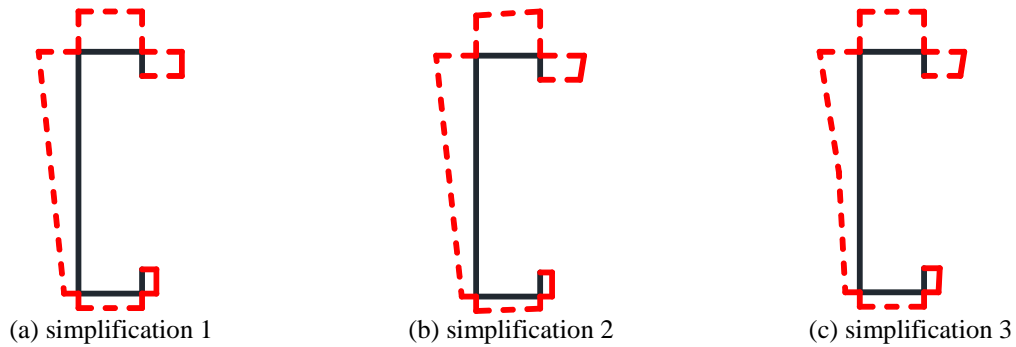


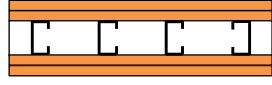
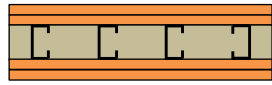
Figure 4.1 Temperature simplifications in CFS wall stud without web perforations

4.2 Thermal modelling

4.2.1 Full-scale fire tests

Shown in Table 4.1 are information of two fire tests conducted by Kolarkar (2010), representing non-insulated and insulated CFS walls, which were designated as test specimen 3 and 4, respectively. The test specimens were lined with double layers of 16 mm thick Type X gypsum board. The CFS frames, with overall dimensions of 2400 mm by 2400 mm, were not laterally braced with either cross bracing or horizontal bridging. The CFS studs and tracks were fabricated from G500 galvanized steel sheets with a nominal base metal thickness of 1.15 mm. The C-shape section steel studs (90 mm×40 mm×15 mm) were evenly spaced 600 mm o.c.. Shown in Figure 4.2 is the experimental set-up of the fire tests. The test specimens were not restrained at their perimeters. A constant axial compression load of 15 kN/stud was first applied and maintained throughout the test based on a load ratio of 0.2, that is, 0.2 times the unfactored ultimate compressive capacity of each steel stud at ambient temperature. A custom designed gas furnace was then used to expose one side of the wall to the standard temperature-time fire curve AS 1530.4 (Australian Standard, 2005). K type thermocouple wires were installed to measure the temperature history during testing. The tests were stopped when one or more of the steel studs could no longer sustain the applied load. The specimen 3 and 4 failed after 111 and 101 minutes' fire exposure, respectively, due to structural instability. Further details of the fire tests can be found in (Kolarkar, 2010).

Table 4.1 Full-scale fire tests (Kolarkar, 2010)

Test Specimen	Configuration	Insulation	Failure time	Failure mode
3		None	111 min.	Structural failure
4		Glass Fibre	101 min.	

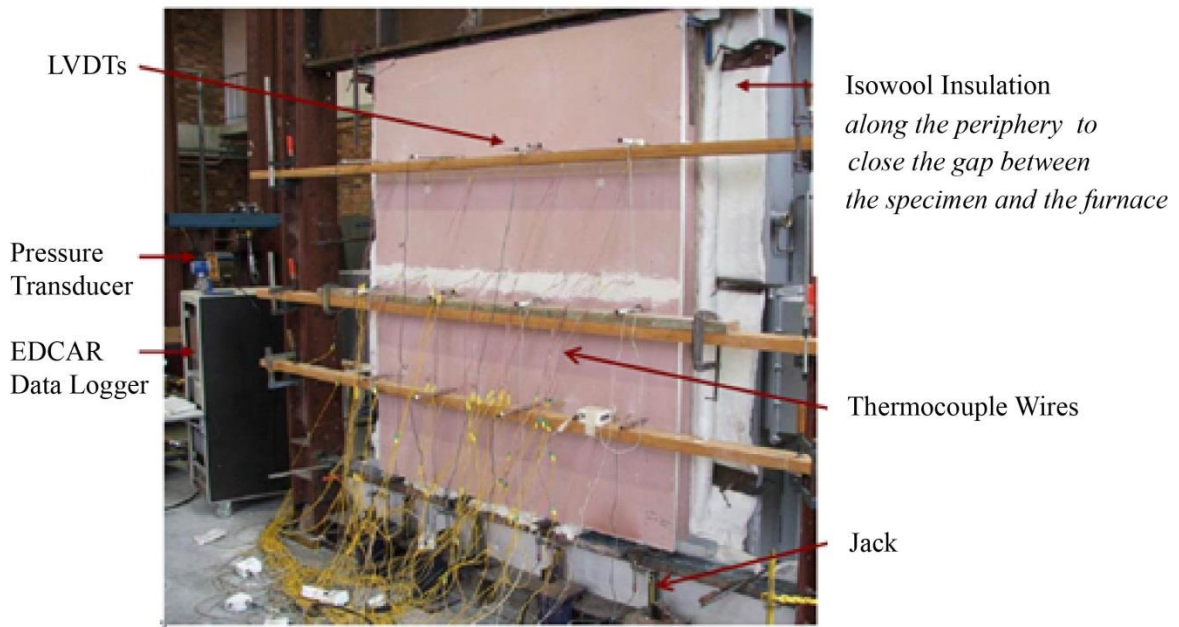


Figure 4.2 Experimental set-up (Kolarkar, 2010)

In this study, as shown in Figure 4.3, 600 mm wide CFS wall sections of the specimen 3 and 4 were modeled to validate proposed 3D finite element analyses (FEAs). Such modelling was viable for two reasons. First, the heat transfer from the fire to the exposed surface at any point was assumed to be uniform, since minor temperature variation associated with the ventilation and heat sink characteristics of the furnace were negligible; second, the heat transfer is extensive between the steel flanges and the adjacent materials within the equivalent wall width, W_e , which can be expressed as

$$W_e = 45 + 0.85b_f \text{ (mm)} \quad (4.1)$$

where b_f is the width of the stud flange. The equivalent wall width is largely affected by the flange

width and no greater than 300 mm based on (Shahbazian & Wang, 2013). Outside the equivalent wall width, the temperature distribution within CFS walls becomes uniform.

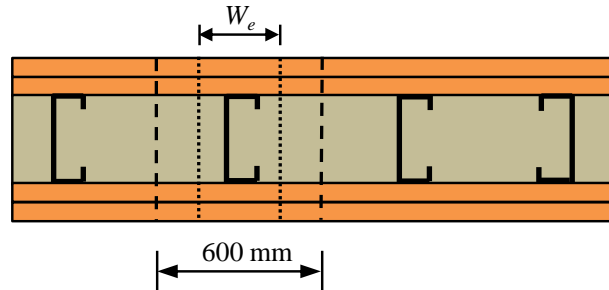


Figure 4.3 Equivalent wall width for determining temperature distribution

4.2.2 Assumptions

In this study, similar to that of the other researchers (Feng et al., 2003b; Gunawan, 2011; Keerthan & Mahendran, 2012; Keerthan & Mahendran, 2013; Shahbazian & Wang, 2013), no thermal contact resistance between adjacent elements was assumed. In addition, the effects of ablation, shrinkage and cracking of gypsum board were taken into account through the modification of thermal properties of materials as shown in Table 4.2 (Gunawan, 2011). The heat loss to the cavity was neglected. Moisture migration across the cavity and gypsum boards, which is highly dependent on the moisture content of the gypsum board, was neglected due to its complexity. However, moisture migration through the gypsum boards was considered by the specific heat of the material. The gypsum boards on both fire-exposed and unexposed sides remained in place until failure during the fire tests (Kolarkar, 2010). Thus, the gypsum board fall-off was not included in the models. The foregoing assumptions yield smaller temperature gradient within CFS walls than that in the fire tests.

4.2.3 Finite element type and mesh

When modelling the wall assembly with software ABAQUS, the gypsum boards and insulation were modeled using 8-node continuum solid elements (DC3D8). The steel studs were simulated with 4-node shell elements (DS4). The geometry of 16 mm thick gypsum board, 90 mm thick Type X insulation, and CFS stud (90 mm×40 mm×15 mm) were defined by creating parts in the software. The part instance (a usage of a part within the assembly) of gypsum board was patterned four times to simulate the four layers of gypsum boards. All the part instances (gypsum boards, insulation, CFS studs) were positioned accurately to model the CFS wall. The part instances for double layers of gypsum boards on both sides

and insulation within the cavity were merged into a single part instance but the intersecting boundaries were retained. Merging the gypsum board and insulation part instances avoids a large number of computationally expensive tie constraints between the intersecting boundaries. Since the intersecting boundaries were retained, material properties can be assigned to gypsum board and insulation individually. The temperature degree of freedom for the elements between all the contact surfaces is tied. Shown in Figure 4.4 are the FE meshes of the test specimens. A global mesh size of 30 mm was first selected for the specimen, and local seed number of six and fours were then assigned to the web and flange of the CFS stud by six and four nodes, respectively. It was subsequently found that such type of mesh scheme could ensure both computational accuracy and efficiency.

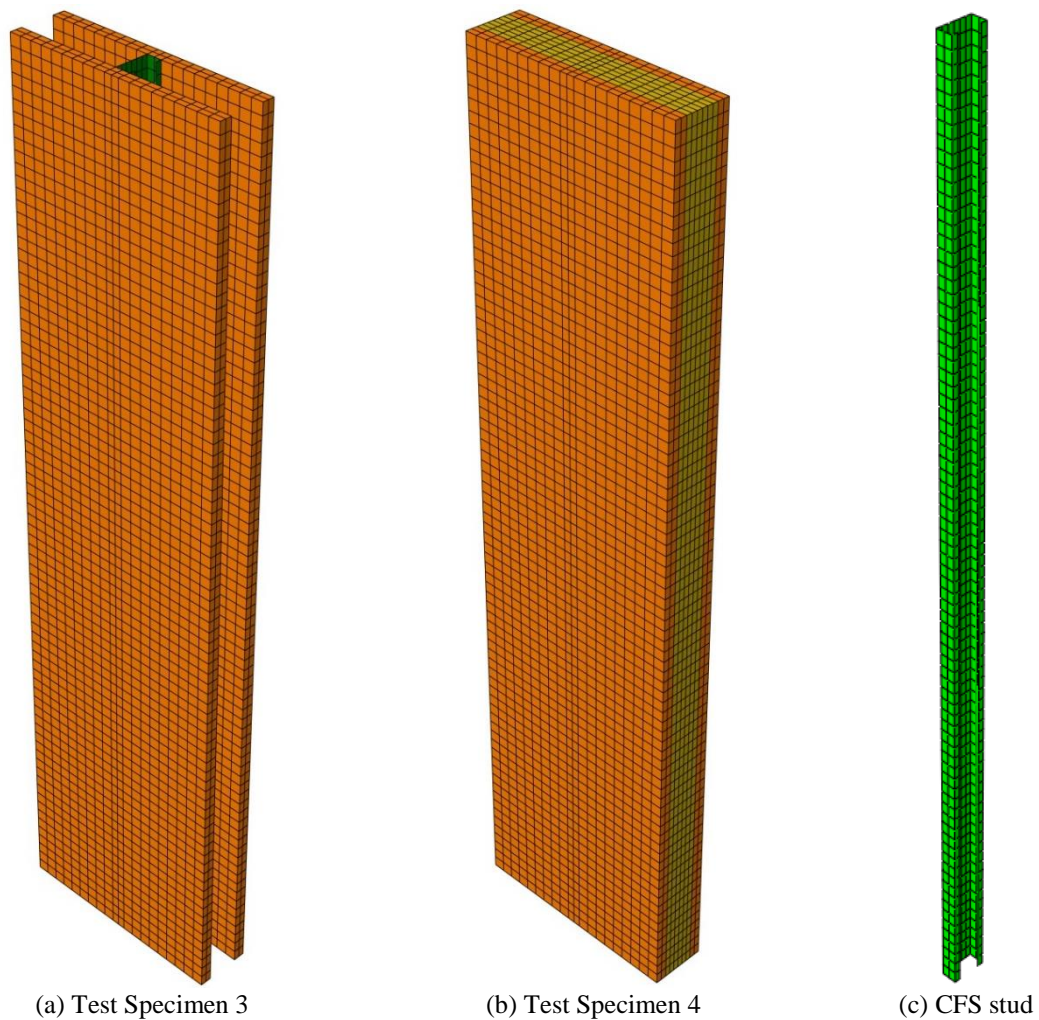


Figure 4.4 Finite element meshes of CFS wall segments

4.2.4 Thermal boundary conditions

Heat is transferred via conduction, convection and radiation between physical systems. Shown in Figure 4.5 are the heat transfer mechanisms from the fire side to the ambient side through the CFS wall systems, where Gb denotes the gypsum board. For instance, the heat transfer modes for Test Specimen 3 shown in Figure 4.5 (a) can be illustrated as follows:

- heat transfer from the fire to the exposed surface by radiation and convection;
- heat transfer through the gypsum boards on the exposed side by conduction;
- heat transfer from exposed side gypsum board surface to the wall cavity by radiation and convection;
- heat transfer through the steel studs within the wall cavity by conduction;
- heat transfer from the wall cavity to the unexposed side gypsum surface by radiation and convection;
- heat transfer through the gypsum boards on the unexposed side by conduction;
- heat transfer from the unexposed surface to ambient by radiation and convection.

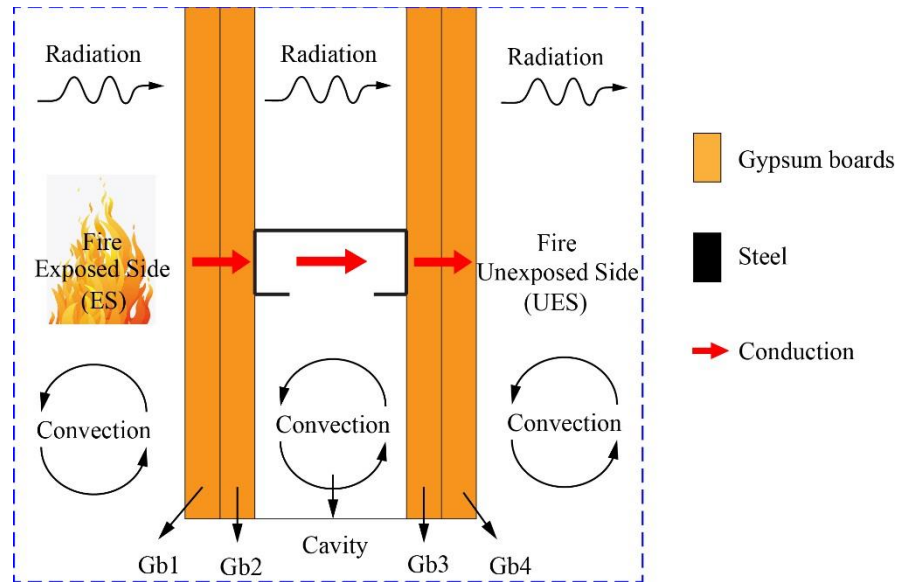
The heat flux at the boundary on the fire-exposed and unexposed sides is represented by:

$$q = \sigma \varepsilon \left[(\theta - \theta^z)^4 - (\theta^0 - \theta^z)^4 \right] + h(\theta - \theta^0) \quad (4.2)$$

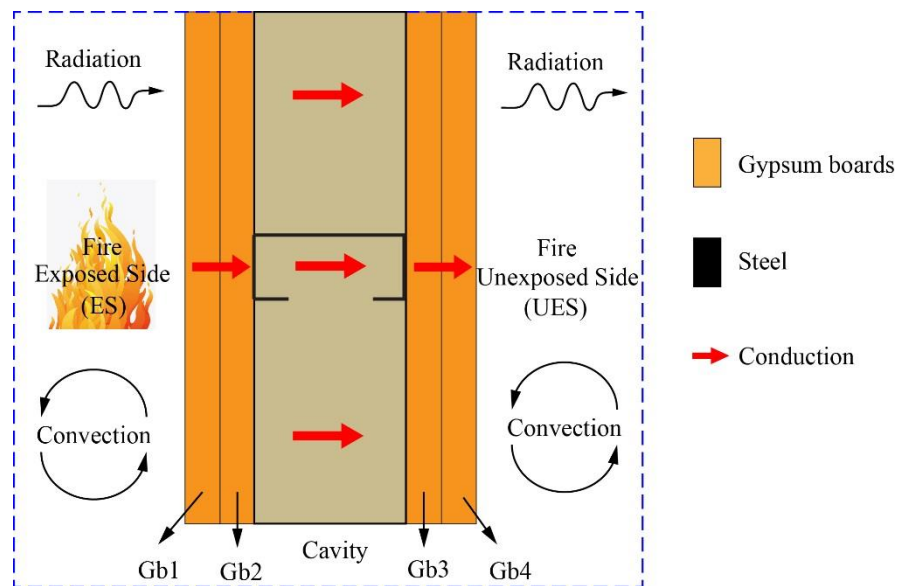
where q is the heat flux to the unit surface area (W/m^2), σ is the Stefan-Boltzmann constant ($5.67 \times 10^{-8} \text{ W}/\text{m}^2/\text{K}^4$), and ε is the relative emissivity, which is the relative ability of its surface to gain from or lose energy by radiation. In general, it depends on the emissivity of the combustion gas and the wall surface. Both the exposed and unexposed surfaces were regarded as a gray body and $\varepsilon = 0.9$. θ is the measured temperature at the point on the surface, θ^z is the absolute zero temperature (273.16 K) and θ^0 is a reference sink temperature. θ^0 was taken as the gas temperature according to the standard cellulosic curve on the exposed side and 20 °C on the ambient side. h is the convective heat transfer coefficient ($\text{W}/\text{m}^2\text{K}$), and 25 $\text{W}/\text{m}^2\text{K}$ and 10 $\text{W}/\text{m}^2\text{K}$ were adopted on the fire-exposed side and the unexposed side respectively.

The existence of cavities induced a complex problem of cavity radiation. In the cavity, the conduction in the steel studs was taken into account; for simplicity, the radiation was considered and the grey body

radiation was assumed in the cavity, while the convection within the gypsum boards was neglected (Mecozzi & Zhao, 2005). The emissivity was taken as 0.9 for gypsum board and 0.6 for steel studs on the wall cavity surfaces (Gunawan, 2011).



(a) Test specimen 3 (non cavity insulation)



(b) Test specimen 4 (glass fibre as cavity insulation)

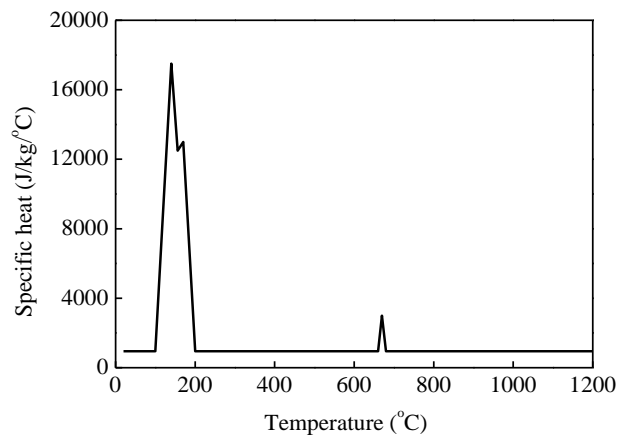
Figure 4.5 Heat transfer mechanism in CFS walls

4.2.5 Thermal properties

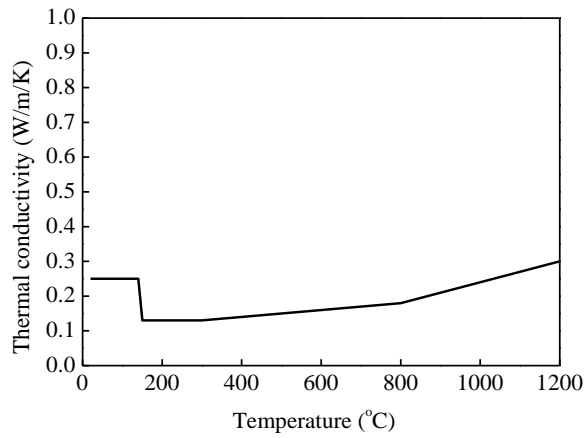
Thermal properties govern heat transfer and thermal deformations. The latter is ignored in the uncoupled thermal analysis. The measured thermal properties reported by (Kolarkar, 2010) were used in the FEAs, as shown in Table 4.2 and from Figure 4.6 to Figure 4.8. The parameters, including thermal conductivity k , specific heat C_p , and density D , vary as functions of temperature T are defined.

Table 4.2 Thermal properties (Gunawan, 2011)

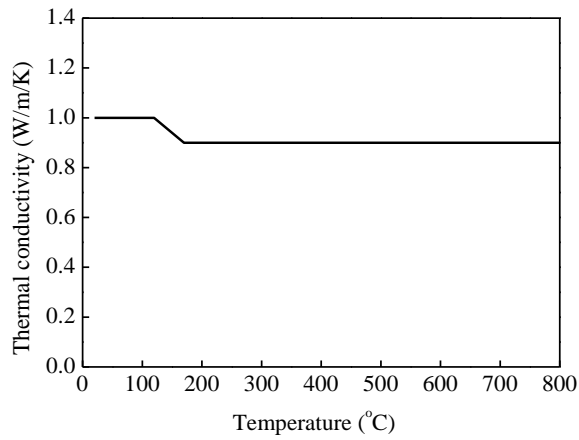
Material	T (°C)	C_p (J/kg°C)	T (°C)	k (W/m/K)	T (°C)	D (kg/m ³)
Gypsum board	0-20	950	0-140	0.25	0-120	729
	20-100	950	140-150	$1.93-0.012T$	120-170	$904-1.458T$
	100-140	$413.75T-40425$	150-300	0.13	170-1500	656
	140-156	$-312.5T+61250$	300-800	$0.1+0.0001T$		
	156-170	$35.714T+6928.6$				
	170-200	$-401.67T+81283$				
	200-660	950				
	660-670	$205T-134350$				
	670-680	$-205T+140350$				
	≥ 680	950				
Steel	20-600	$425+7.73 \times 10^{-1}T-1.69 \times 10^{-3}T^2+2.22 \times 10^{-6}T^3$	20-800	$54-3.33 \times 10^{-2}T$	0-1200	7850
	600-735	$666+13002/(738-T)$	800-1200	27.3		
	735-900	$545+17820/(T-731)$				
	900-1200	650				
Glass fibre	0-800	1200	0-600	$0.5+0.0002T$	0-800	15.42
			600-700	$-7.8+0.014T$		
			700-800	$99.98T-69984$		



(a) Specific heat of gypsum boards

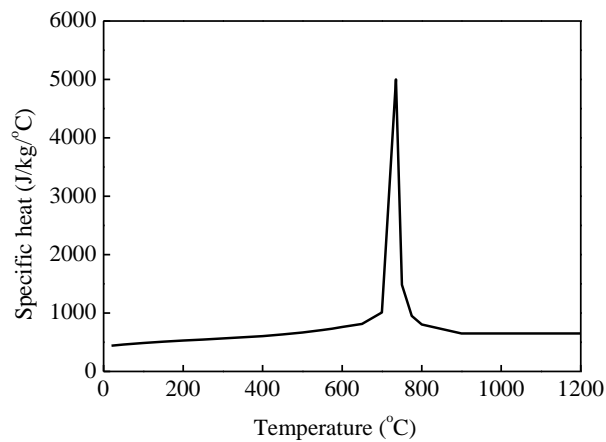


(b) Thermal conductivity of gypsum boards

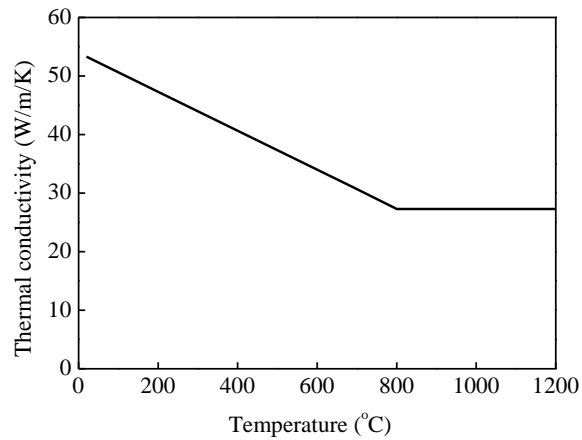


(c) Relative density of gypsum boards

Figure 4.6 Thermal properties of gypsum board (Gunawan, 2011)



(a) Specific heat of steel



(b) Thermal conductivity of cold-formed steel

Figure 4.7 Thermal properties of cold-formed steel (Gunawan, 2011)

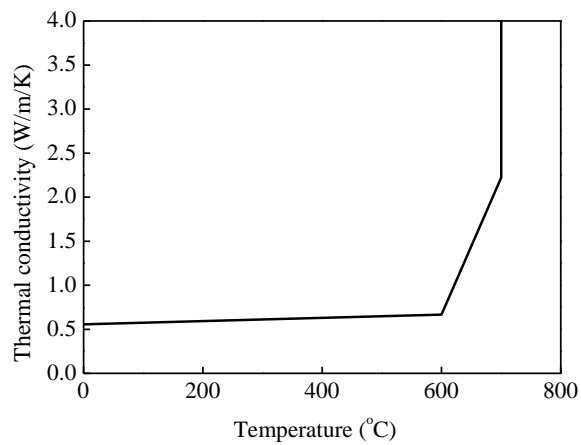


Figure 4.8 Thermal conductivity of glass fibre (Gunawan, 2011)

4.3 Comparison with test results

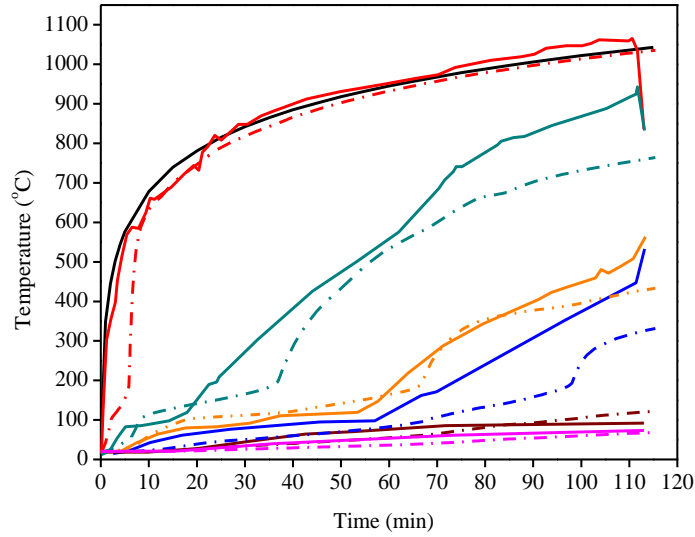
The measured time-temperature profiles from the tests are used for validation of the proposed 3D FE modelling. Compared in Figure 4.9 are the time-temperature profiles of the gypsum boards at different surfaces obtained from the FEAs in this study with those reported by (Kolarkar, 2010). The symbols ES, Gb1, Gb2, Gb3, Gb4 and UES are defined in Figure 4.5.

4.3.1.1 Test specimen 3

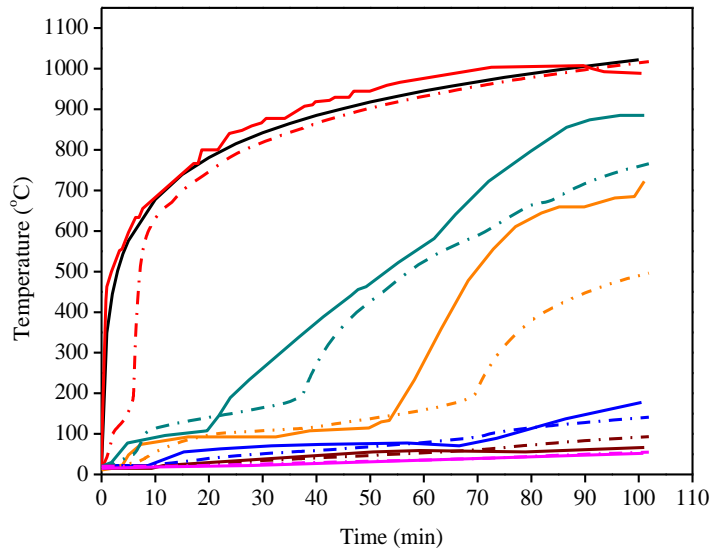
As shown in Figure 4.9(a), the time-temperature profiles obtained from the FEA and the fire test followed the same general trends on each surface. Both the temperature profiles for the interface Gb1 and Gb2 showed three phases. Initially, the temperature at the interface rose rapidly from the ambient temperature to approximately 100 °C within 10 minutes of starting the test. After that, the interface temperature increased gradually, and the heat in this phase was primarily consumed in the physical and chemical process of the gypsum board, that is, the process of free water evaporation and chemically bound water release. In the final phase, the temperature abruptly rose first and then increased slowly until the end of the test. The temperature profiles for the interfaces at the cavity surfaces Gb2-Cav and Cav-Gb3 from FEA coincided well but were slightly larger than those from the test results, which was probably resulted from that the radiation could not be simulated accurately in FEAs. The temperature profiles for interfaces Gb3-Gb4 and Gb4-UES obtained from FEAs and the tests were in good agreement which almost overlapped.

4.3.1.2 Test specimen 4

As shown in Figure 4.9(b), the temperature profiles of the FEA and the fire test for each interface also matched well, except for the interface Cav-Gb3. The temperature profile of the interface Cav-Gb3 obtained from FEA was considerably lower than that measured from the test. This might be resulted from that the glass fibre had gradually melted and the insulation in the cavity almost burnt out on the exposed surface in the test. The melting and burning of the insulation eventually resulted in the heat transferring faster across the cavity. Unfortunately, the melting and burning process of glass fibre could not be accounted for in the FEAs.



(a) Test Specimen 3 (non-insulated CFS wall)



(b) Test Specimen 4 (insulated CFS wall)

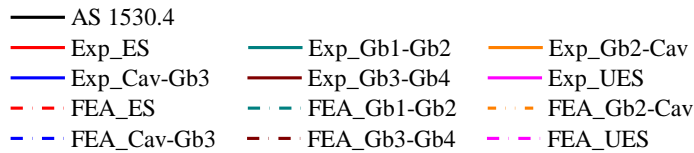


Figure 4.9 Comparison of time-temperature profiles between FEA and tests by Kolarkar (2010)

4.4 Effect of web perforations

4.4.1 Parameters

To investigate the effect of stud web perforation on time-dependent temperature distributions for CFS walls under fire, extensive FEAs were carried out based on the previously validated 3D FE models. Shown in Figure 4.10 and Table 4.3 are the CFS walls investigated in the parametric study. The CFS walls are lined with double layers of 12 mm Type X gypsum board on both sides. The CFS frame fabricated from G500 galvanized steel C-shape and track sections is built to a height of 3200 mm and a width of 3550 mm. Seven CFS C-shaped studs are evenly spaced 600 mm o.c. All the CFS studs (150 mm×40 mm×1.5 mm) are connected to the top and bottom CFS tracks (150 mm×50 mm×1.5 mm). Five slotted web perforations are evenly spaced 640 mm o.c. along the length of each steel stud. The length of web perforations, L_h , varies from 130 mm to 530 mm as shown in Table 4.3 and Figure 4.12, whereas the width of web perforations remains at 38 mm. For the purpose of comparison, two CFS walls without web perforations, with and without insulation, are also investigated.

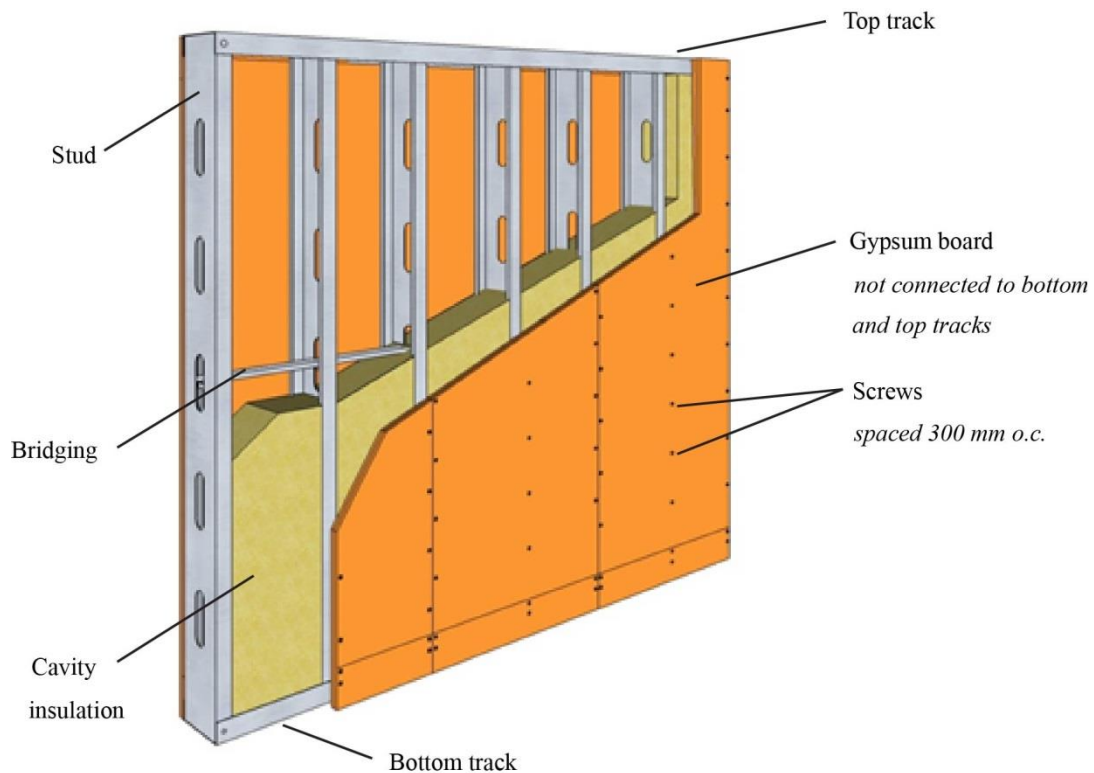
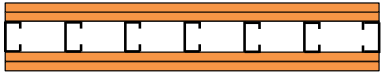
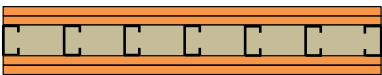


Figure 4.10 Configuration of CFS walls with web-perforated studs

Table 4.3 CFS walls with web-perforated studs in parametric study

CFS wall No.	Configuration	Insulation	Perforation length, L_h (mm)
1		None	0
2			130
3			330
4			530
5		Glass Fibre	0
6			130
7			330
8			530

The 600 mm-wide CFS wall section taken from the center of the wall was modeled in the FEAs. The time period of the step specified was 7200 (120 minutes). The maximum number of increments was 1000. The initial increment size was 30 and the minimum and maximum increment size was 7.2×10^{-9} and 720, respectively. The FEAs for both insulated and non-insulated CFS walls stopped at the increment number of 1000. The FEAs for the insulated CFS walls terminated at about 104 minutes resulted from severe element distortion around the slotted web perforation in both the CFS studs and the insulation. However, the FEAs for the non-insulated CFS walls were carried out smoothly up to the specified time limit of 120 minutes.

4.4.2 Results and discussions

4.4.2.1 Temperature contour

Shown in Figure 4.11 and Figure 4.13 are the temperature contour at 104 minutes for the horizontal cross section at the mid-height and the CFS wall studs of insulated CFS walls with different lengths of web perforations, respectively. It can be seen that the existence of web perforation together with perforation length may affect the temperature distributions of the CFS wall studs in the insulated walls, whereas the web perforations have little influence on the temperatures of gypsum surfaces on both the exposed and unexposed sides. Shown in Figure 4.13 is the temperature contour of the horizontal cross section at the mid-height of non-insulated CFS walls at 120 minutes. Similar temperature distribution is observed among CFS walls with or without web perforations.

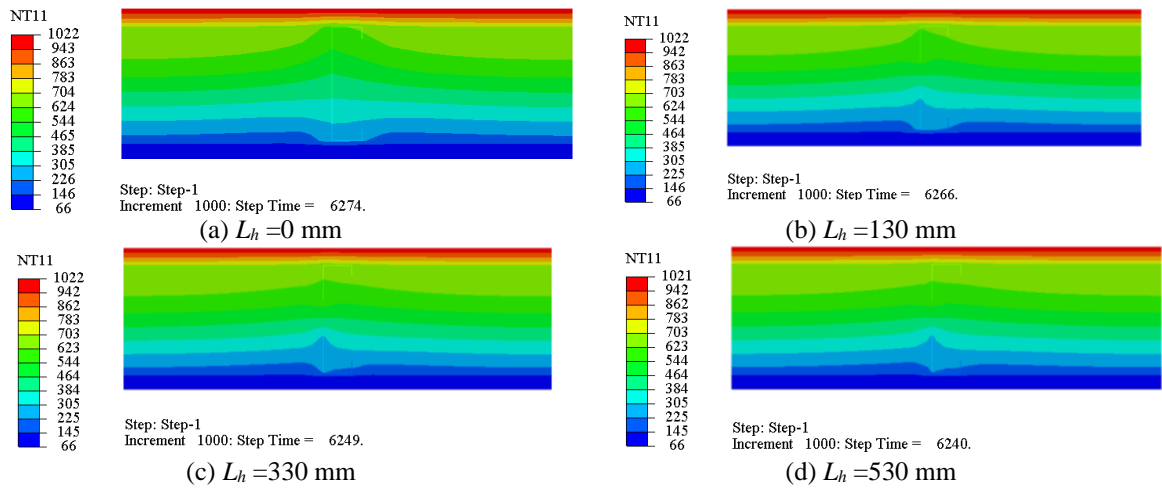


Figure 4.11 Temperature contour of insulated CFS walls at mid-height cross section

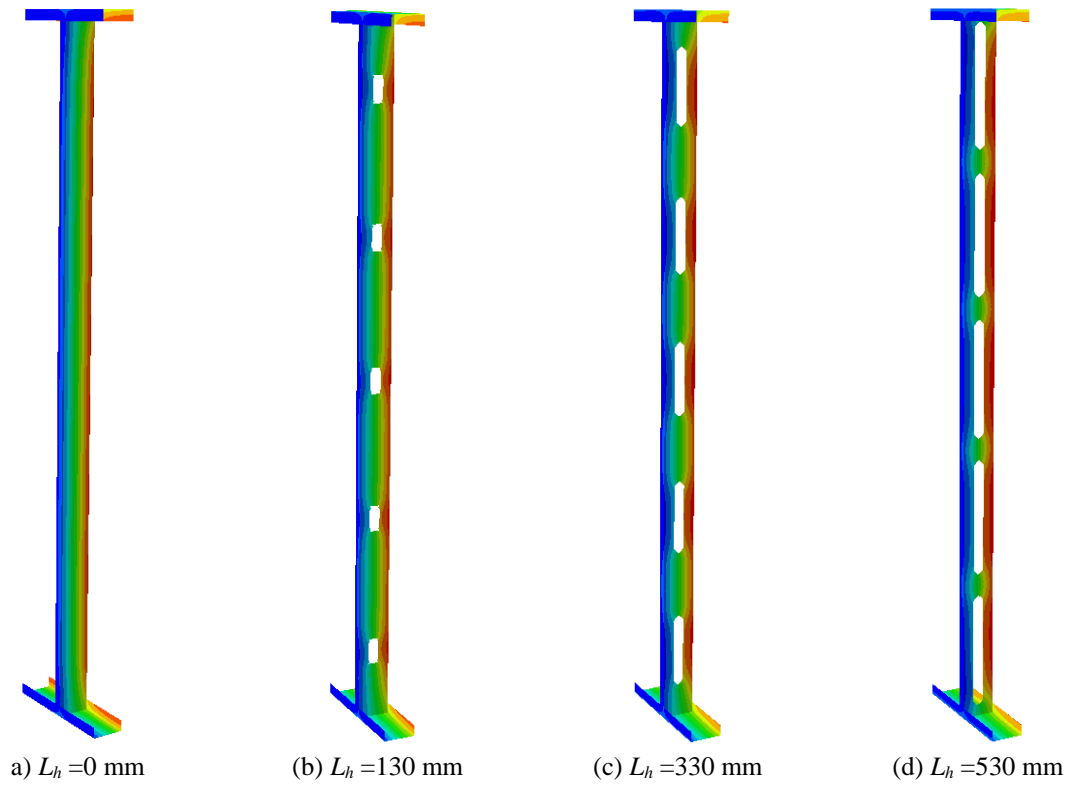


Figure 4.12 Temperature contour of insulated CFS wall frames at 104 minutes

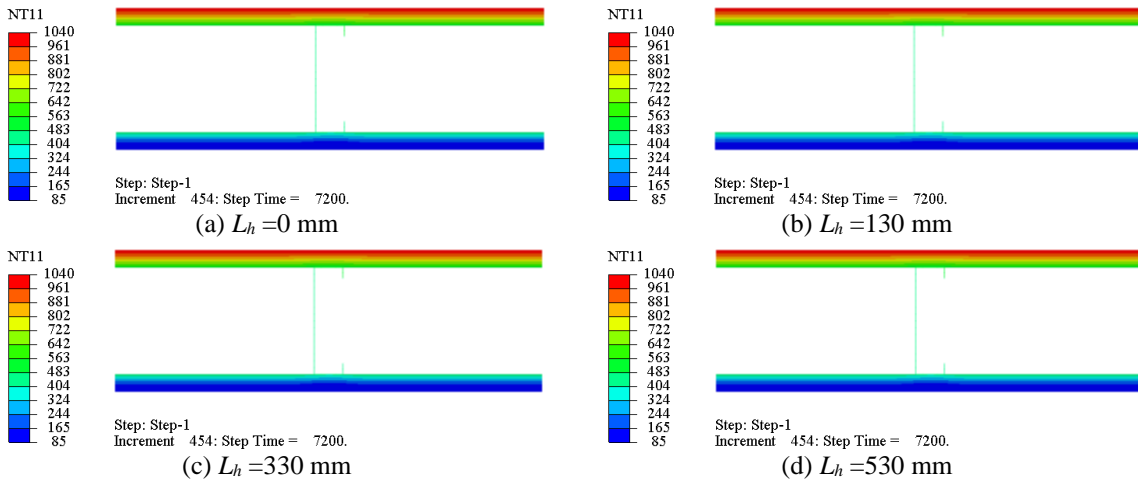


Figure 4.13 Temperature contour of non-insulated CFS walls at mid-height cross section

4.4.2.2 Temperature profiles at mid-height cross section of studs

Shown in Figure 4.14 are the temperature profiles at the mid-height cross section of steel studs of insulated CFS walls at 104 minutes. All the lip and flange elements have close linearly distributed temperature. When the web is not perforated, temperature distribution of the web is almost linear. However, in the case that the web is perforated, the temperature distribution becomes bilinear. The temperature distributions of the web portion which connects the hot and cold flange are almost linear but decrease from the hot flange toward the cold one with different slopes as shown in Figure 4.14(b)-(d). The perforations block the heat transfer by conduction along the web. As the perforation length increases, the web temperature becomes higher on the hot side and lower on the cold side than those of studs without perforations as shown in Figure 4.14 and Figure 4.16(a). The large temperature difference between the stud flanges on the exposed and unexposed sides would result in more severe bending the CFS studs.

Shown in Figure 4.15 are the temperature profiles at the mid-height cross section of steel studs for non-insulated CFS walls at 120 minutes. In this case, the web perforation has little influence on the temperature distribution across the section. From Figure 4.16(b), the web temperature distributions are almost linear with the same slope for both portions of the web separated by the perforation. As the perforation length increases, the web temperature becomes slightly higher than in the studs without web perforations.

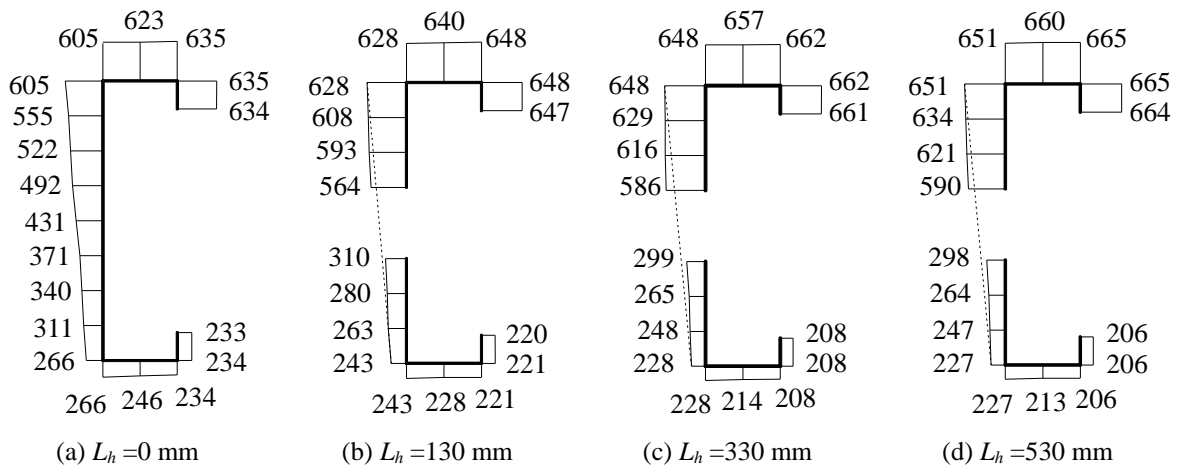


Figure 4.14 Non-uniform temperature distributions in insulated CFS wall studs at 104 minutes

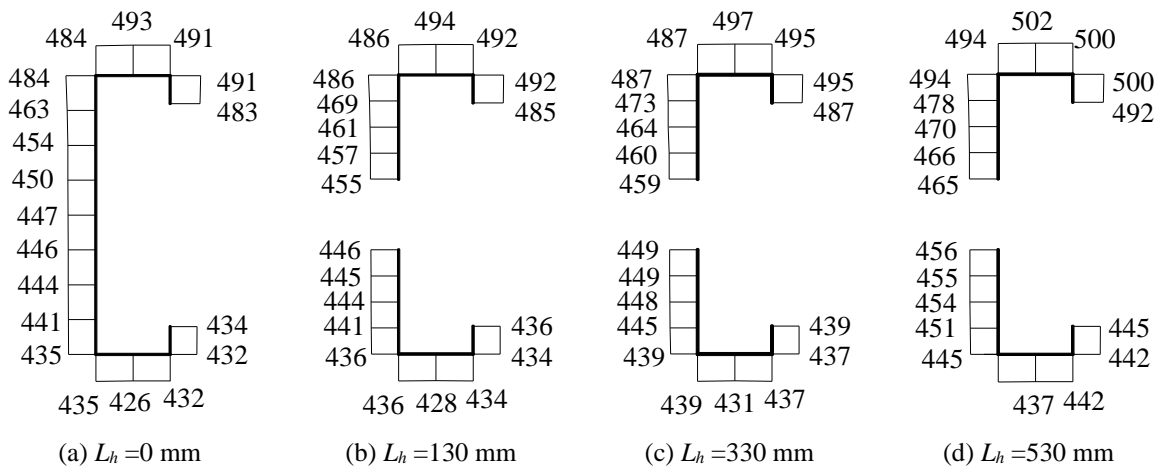
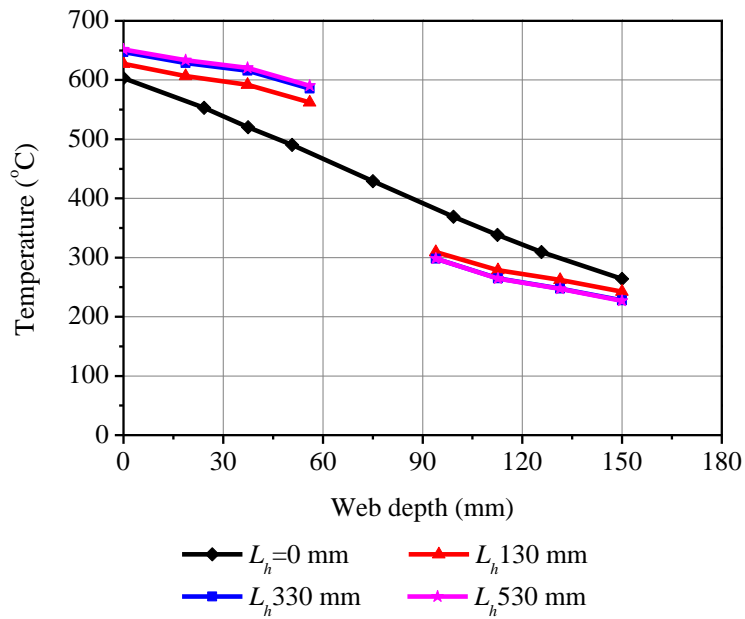
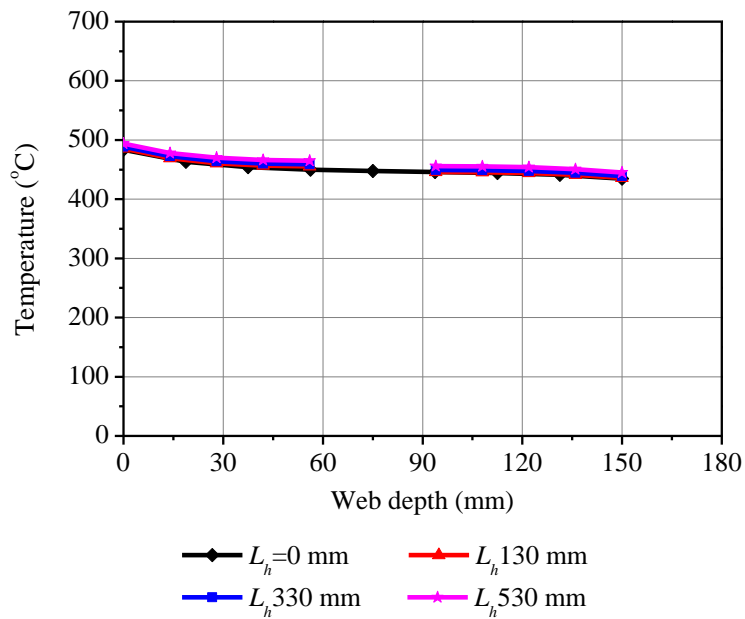


Figure 4.15 Non-uniform temperature distributions in non-insulated CFS wall studs at 120 minutes



(a) Insulated CFS wall studs at 104 minutes



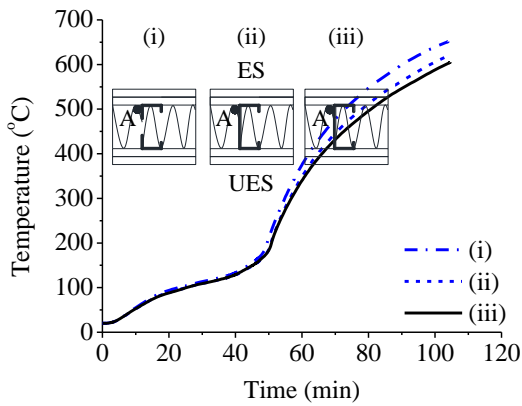
(b) Non-insulated CFS wall studs at 120 minutes

Figure 4.16 Stud depth-temperature profiles

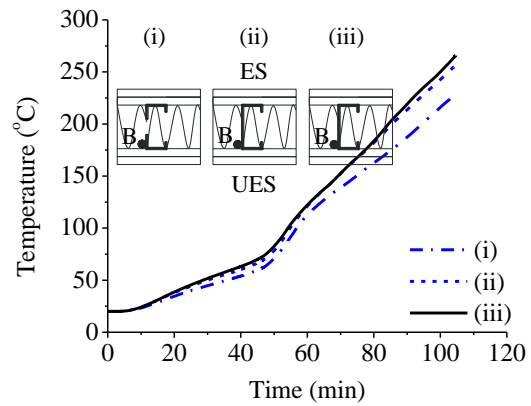
4.4.2.3 Temperatures at flange-web junctions of studs

Compared in Figure 4.17 are the temperatures at location A of the flange-web junction of steel studs inside the insulated CFS walls with 530 mm long web perforations and without web perforations, respectively. Sections (i) and (ii) are the horizontal cross sections of CFS studs corresponding to the center of the stud web perforations and at the center between the two web perforations. Section (iii) represents the horizontal cross section at mid height for CFS walls without stud web perforations. At fire exposure of 104 minutes, it is found that the temperatures at section (i) are 8% higher on the exposed side (ES) and 15% lower on the unexposed side (UES) than those at section (iii). However, the temperatures at section (ii) are only 2% higher on the exposed side and 4% lower on the unexposed side than those at section (iii). Thus, the temperature gradient between two perforations decreases gradually along the stud. Similar trend can be also found for the case $L_h = 130 \text{ mm}$ as shown in Figure 4.18. From Figure 4.17, it can be seen that as the perforation length decreases from 530 mm to 130 mm, the temperature differences between sections (i) and (iii) reduce to 4% from 8% on the exposed side and to 8% from 15% on the unexposed side; the temperature-time curves for sections (ii) and (iii) are almost the same on both sides. The results indicate that the temperature distribution between two perforations in the studs changes gradually. The temperature gradient in the studs reaches to the highest value at the center of the perforations, resulting in that the strength and stiffness at this cross section could be the lowest along the stud length. Thus, local buckling may be induced around the web perforations, which is detrimental to the stability of CFS studs and consequently to the integrity of the walls. Therefore, it may be non-conservative and inappropriate to neglect the existence of web perforations in CFS wall studs while evaluating the wall performance at elevated temperatures.

Compared in Figure 4.19 are the temperatures at location B of the flange-web junction of steel studs inside the non-insulated CFS walls with 530 mm long web perforations and without web perforations, respectively. In this case, the temperature at section (i) is slightly higher than that at section (iii) on the exposed sides. The temperature at section (ii) becomes slightly lower first and then higher than that at section (iii) on the unexposed sides due to cavity radiation. When the perforation length reduces to 130 mm, as shown in Figure 4.20, the temperature curves of all the three sections are almost overlapped. From Figure 4.19 and Figure 4.20, it can be seen that the temperature distribution along steel studs is much more uniform for the non-insulated CFS walls than that for insulated CFS walls. The absence of insulation in the cavity equalizes the temperatures across the stud cross sections more rapidly through radiation than that of the insulated CFS walls.

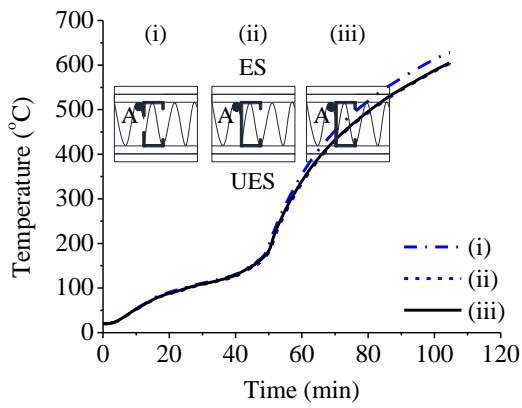


(a) flange-web junction on the exposed side

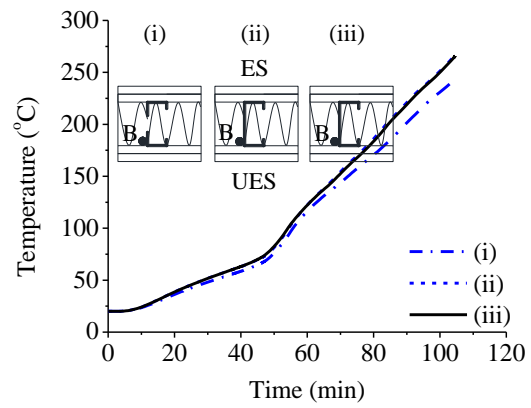


(b) flange-web junction on the unexposed side

Figure 4.17 Comparison of stud temperatures for insulated CFS walls ($L_h=530$ mm)

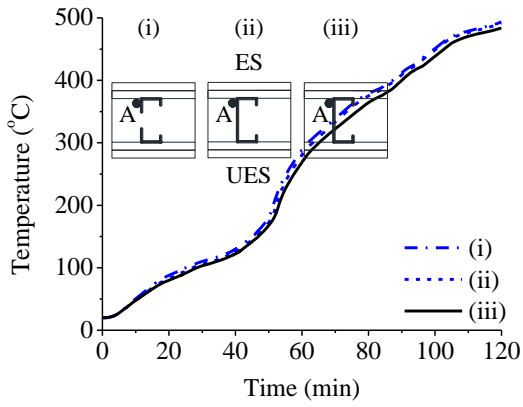


(a) flange-web junction on the exposed side

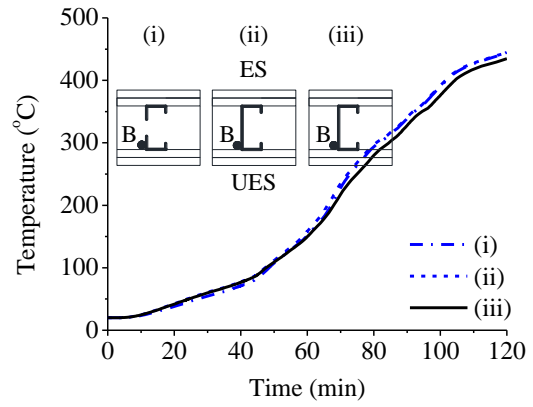


(b) flange-web junction on the unexposed side

Figure 4.18 Comparison of stud temperatures for insulated CFS walls ($L_h=130$ mm)

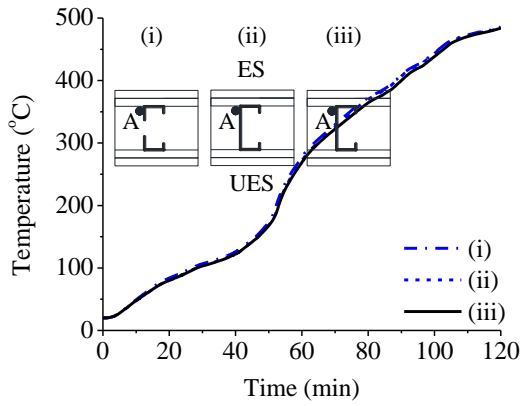


(a) flange-web junction on the exposed side

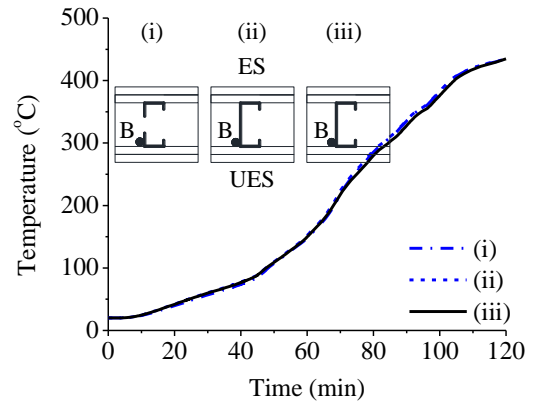


(b) flange-web junction on the unexposed side

Figure 4.19 Comparison of stud temperatures for non-insulated CFS walls ($L_h=530$ mm)



(a) flange-web junction on the exposed side



(b) flange-web junction on the unexposed side

Figure 4.20 Comparison of stud temperatures for non-insulated CFS walls ($L_h=130$ mm)

4.5 Conclusions

Presented in this chapter is a numerical investigation on thermal performance of CFS load-bearing walls subjected to standard fire conditions. 3D FE thermal models of CFS walls with perforated studs were proposed and validated with the results from fire tests (Kolarkar, 2010). Parametric studies were carried out to evaluate the effect of web perforations on the temperature distribution within CFS walls. The following conclusions can be drawn based on the investigation:

- 3D FE thermal models of CFS walls have been developed and validated using full-scale fire tests on CFS load-bearing walls. The 3D models can be used to investigate the effect of stud web perforations on the temperature distributions of studs in CFS walls subjected to standard fire. Such investigation cannot be accomplished using the 1D and 2D FE models.
- For non-insulated and insulated CFS walls, the web perforations in CFS studs have little influence on the temperature distributions for gypsum board surfaces on both fire-exposed and unexposed sides.
- For non-insulated CFS walls, the stud web perforation has negligible influence on the temperature distribution through the cross sections and as well as along the stud length. The heat transfer via radiation within the cavity far outweighs that blocked by conduction via web perforations.
- For insulated CFS walls with web perforations, the temperature distribution is no longer linear but almost bilinear along the web depth. The largest temperature gradient in the CFS studs occurs at the cross section located in the center of the web perforation along the stud length, perhaps induce local bending at web perforations. Therefore, it may be non-conservative if the web perforations in CFS studs are neglected when evaluating the fire resistance of CFS walls.

Chapter 5 Structural Modelling and Analysis of CFS Walls with Web-Perforated Studs Subjected to Standard Fire

5.1 Introduction

Fire resistance rating of load-bearing CFS walls under standard fire conditions is often governed by the structural failure of one or more studs. In order to understand the structural behaviour of CFS walls under fire conditions, it is important to simulate the complete loading history based on transient-state fire conditions. FE structural modelling of CFS walls under fire has been successfully developed by (Feng & Wang, 2005; Gunalan & Mahendran, 2013; Kaitila, 2002). In the foregoing studies, simplified temperature distributions across the CFS wall studs were obtained first based on the measured average time-temperature curves of CFS wall studs from the fire tests. Then the temperature distributions were input into the FE structural models as thermal boundary conditions. However, the simplified temperature distribution method is not applicable for modelling the CFS wall tests conducted by Xu (2011) for the following two reasons. First, the time-temperature curves of CFS wall studs were not measured during the fire tests. Second, the temperature distributions across and along the studs cannot be represented by the simplified temperature distribution shown in Figure 4.1 due to the existence of web perforations. The temperatures of the studs for FEAs, obtained by the uncoupled heat transfer analysis discussed in Chapter 4, were input into the sequential stress analysis as a predefined field.

The use of finite element modelling to characterize the structural responses of CFS load-bearing walls with non-perforated C-shape studs has been validated by full-scale fire tests (Gunalan & Mahendran, 2013; Zhao et al., 2005). The CFS walls were simplified using a single stud model for stress analysis, and the temperature distributions used in the analysis were obtained from tests. Although the structural responses obtained from the single stud model appeared to be acceptable, the system effect, such as the possible redistribution of loading among studs was not considered. It is also noted that the above-mentioned investigations assumed temperature distributions to be bilinear or linear along the web depth, as shown in Figure 4.1. For CFS walls with web-perforated C-shape studs, the validity of such simplification is yet to be investigated.

Also, it is well known that the sheathing which is fastened to the CFS wall framing may enhance the load carrying capacity of the wall by providing lateral braces to the wall studs. Such increase of load carrying capacity is permitted and can be evaluated in the design of the wall at ambient temperature.

However, the effect of sheathing bracing on the wall studs has not been investigated in the case of elevated temperature. As it is difficult to identify the effect of sheathing bracing in a fire test, a numerical investigation is carried out using FEA. The investigation results are presented in this section. The modelling of FEA to simulate the CFS wall framing employed in this investigation has been validated in previous investigations (Xu, 2011; Yang & Xu, 2016). The effect of sheathing bracing on the fire performance of load-bearing CFS walls was investigated by incorporating the sheathing into the FE model of stress analysis, accounting for different sheathing stiffnesses at elevated temperature. With the growing demand for more-accurate assessment of CFS building safety under fire, the outcomes of this investigation would certainly benefit design practitioners by providing better understanding of sheathing's effect on the behaviour of load-bearing CFS walls subjected to elevated temperature.

In this chapter, three finite element models, including CFS single stud model, CFS wall frame model and CFS wall system model, are developed to investigate the fire performance of load-bearing CFS walls with web-perforated studs subjected to standard fire. Sequentially uncoupled 3D FE thermal-stress analysis is carried out in which heat transfer analysis is conducted to obtain the temperature distribution of an entire CFS wall. In the subsequent structural analysis, a CFS wall frame assembly rather than a single stud is modelled, to achieve system-level structural responses. The FEA results are compared with those from full-scale fire tests.

5.2 Full-scale fire tests

Shown in Table 5.1 are the configuration details and test results of the full-scale fire tests on seven load-bearing CFS walls conducted by Xu (2011). The test results, including the fire duration, temperature and failure mode, are also summarized in this table.

Illustrated in Figure 5.1 are the specimen configurations. The overall dimension is 3,550 mm by 3,000 mm for specimens 1-5 and 3,550 mm by 3,200 mm for specimens 6-7. The specimens are sheathed with one or two layers of Type X, Type C gypsum board or MgO board on both sides. The 150 mm deep wall cavities are filled with 90 mm thick glass fibre on the fire side. Seven C-shape CFS studs (150 mm×40 mm×15 mm×1.5 mm) are evenly spaced 600 mm o.c., except for the rightmost stud which is spaced 550 mm o.c. Three slotted web perforations ($L_h=75$ mm, $d_h=38$ mm) and five slotted web perforations ($L_h=130$ mm, $d_h=38$ mm) are along the length of each stud for specimens 1-5 and specimens 6-7, respectively. An additional CFS stud is placed on each end of the CFS frame to eliminate

the gap between the specimen and the test frame in which the specimen is mounted so as to prevent lateral sway. The top and bottom ends of these studs are connected with U-shape CFS track (150 mm×50 mm×1.5 mm). The CFS frames are laterally braced with a horizontal bridge (38 mm×13 mm×1.5 mm) at mid-height. The CFS studs, tracks and bridging are fabricated from cold-formed galvanized steel sheets. The yield stress of the CFS studs and tracks are 345 N/mm², and of the bridging, 228 N/mm².

Shown in Figure 5.2 is the experimental setup. The target load was applied first and maintained throughout the fire test. A target load was applied axially to the specimens through ten jacks and maintained throughout the testing. The applied load ratio varied from 0.8 to 1.0. These jacks were connected to the same hydraulic pump and were spaced 310 mm along a 3470 mm long loading beam. A propane-fired gas furnace was used to expose one side of the wall to the ISO 834 time-temperature fire curve (1999). Eight type K thermocouples were installed to measure the temperature development of the sheathing surface on the ambient side. A comparison of the gypsum board surface temperature on the ambient side between FEA and test are shown in Appendix A.

Table 5.1 Load-bearing CFS wall fire tests (Xu, 2011)

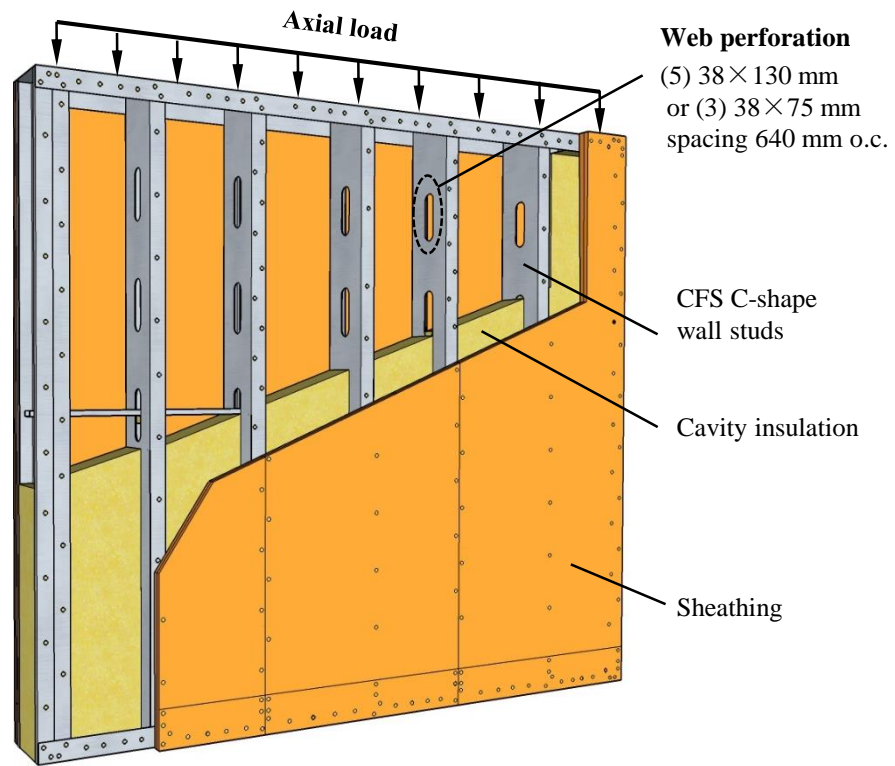
No.	Specimen	Wall systems (Wall height=3.0 m)			Load (kN/m)		Result	Temperature		Comment
		Fire-exposed side Sheathing	Wall stud	Fire-unexposed Side Sheathing	Calculated	Applied	Fire Duration (minute)	Initial (°C)	Max (°C)	Failure mode
1	LBW-E1(a)	(2) 12 mm MgO board	150×40×15×1.5mm stud at 600 mm o.c. w/ three 75×38 punched holes	(2) 12 mm MgO board	33.02	28.07 @ 85%	155	13	79.6 @ #2	Failed at cracked vertical joint at center line
2	LBW-E1a(b)	(2) 12 mm MgO board	150×40×15×1.5mm stud at 600 mm o.c. w/ three 75×38 punched holes	(2) 12 mm MgO board	33.02	33.02 @ 100%	153	15	136.8 @ #4	Failed at cracked vertical joint at center line, multiple horizontal cracks also shown at mid-up per location
3	LBW-G1(a)	(2) 12 mm Type C Gypsum Board	150×40×15×1.5mm stud at 600 mm o.c. w/ three 75×38 punched holes	(2) 12 mm Type C Gypsum Board	33.06	29.75 @ 90%	100	15	93.8 @ #4	Failed at cracked vertical joint at center line
4	LBW-E2	(1) 12 mm MgO board + (1) 9 mm MgO Board	150×40×15×1.5mm stud at 600 mm o.c. w/ three 75×38 punched holes	(1) 12 mm MgO board + (1) 9 mm MgO Board	33.19	33.19 @ 100%	117	8.5	78.5 @ #2	Failed by structural integrity caused by a horizontal crack
5	LBW-E5	(1) 12 mm MgO board + 12 mm Type X Gypsum Board	150×40×15×1.5mm stud at 600 mm o.c. w/ three 75x38 punched holes	(1) 12 mm MgO board + (1) 12 mm Type X Gypsum Board	33.13	31.47 @ 95%	100	8.6	83.2 @ # 10	Failed by fire escaped from a rear crack

Table 5.1 Load-bearing CFS wall fire tests (Xu, 2011)

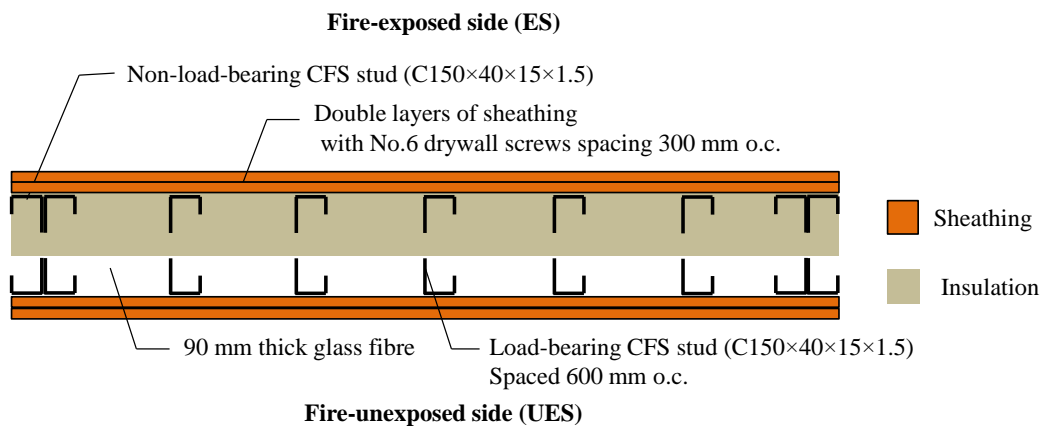
No.	Specimen	Wall systems (Wall height=3.2 m)			Load (kN/m)		Result	Temperature		Comment
		Fire-exposed side Sheathing	Wall stud	Fire-unexposed Side Sheathing	Calculated	Applied	Fire Duration (minute)	Initial (°C)	Max (°C)	Failure mode
6	LBW-2	(1) 12 mm MgO board + (1) 12 mm Type X Gypsum Board	150×40×15×1.5mm stud at 600 mm o.c. w/ five 130×38 punched holes	(1) 12 mm MgO board + (1) 12 mm Type X Gypsum Board	33.02	26.5 @ 80%	68	23	82.3 @ #5	Structural failure associated with 130×38 punched holes
7	LBW-3	(2) 12 mm Type C Gypsum Board	150×40×15×1.5m stud at 600 mm o.c. w/ five 130×38 punched holes	(2) 12 mm Type C Gypsum Board	33.06	26.5 @ 80%	83	21	136.8 @ #4	Structural failure associated with 130×38 punched holes

Note:

1. For Specimen 1-5: wall height=3.0 m; for Specimen 6-7: wall height=3.2 m.
2. Cavity was filled with 90 mm fibre glass.
3. Initial temperature: ambient temperature; max temperature: maximum temperature measured by thermocouple as shown in Figure 5.2.



(a) Elevation view



(b) Plan view

Figure 5.1. Configuration of load-bearing CFS wall specimens (Xu, 2011)

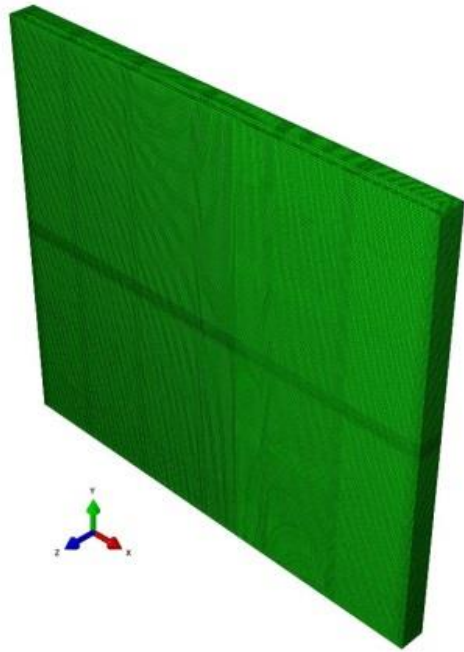


Figure 5.2. Experimental setup (Xu, 2011)

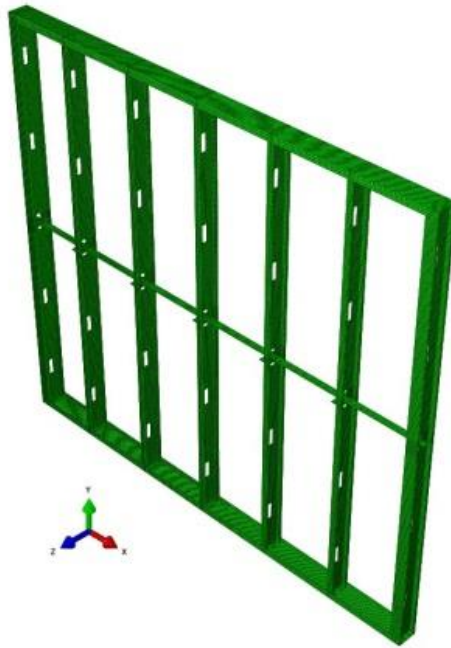
5.3 Sequentially uncoupled thermal-stress analysis

5.3.1 Finite element thermal model

The method used to develop the FE thermal model is the same as that described in Chapter 4. The CFS walls are exposed to the standard fire curve defined by ISO 834 (1999) for up to 240 minutes.



(a) sheathing and glass fibre



(b) CFS frame

Figure 5.3. Finite element mesh of CFS walls

5.3.2 Thermal properties

The thermal properties of materials are critical for heat transfer analysis, and indirectly influence the structural response of the wall system. The parameters, including thermal conductivity, specific heat, and density, vary as functions of temperature are defined.

The thermal properties of cold-formed steel and glass fibre reported by Keerthan & Mahendran (2012) are adopted, as shown in Table 4.2 and from Figure 4.6 to Figure 4.8. The density of the cold-formed steel remains $7,850 \text{ kg/m}^3$ at elevated temperatures.

5.3.2.1 Type C and X Gypsum board

Gypsum board consists of a noncombustible core, covered with thick sheets of paper. The sheets of paper, before burning out, maintain the integrity of the core. The core is primarily gypsum ($\text{CaSO}_4 \cdot 2\text{H}_2\text{O}$), containing about 21% by weight of chemically bound water and a small amount of free water. Type X gypsum board is generic fire-rated to provide 45 or 60 minutes protection to a load-bearing wood or steel frame with a lining thickness of 12.7 or 15.9 mm, respectively. Type X contains glass fibres in the core for enhanced fire performance and may have other additives to improve fire performance. Type C is manufactured to provide better fire resistance or to meet other performance needs, and meets all the requirements of the Type X board and is further enhanced with additional glass fibres, more core ingredients and greater gypsum core density.

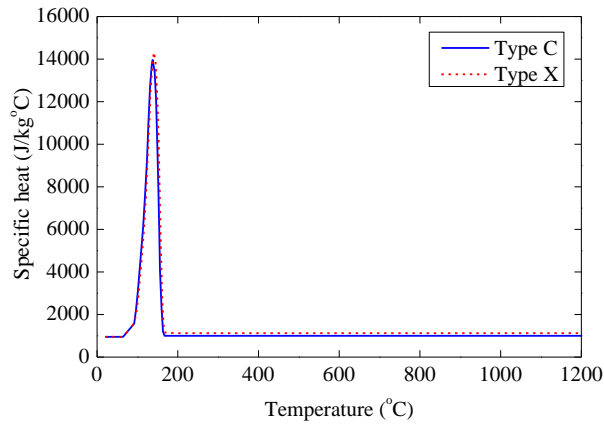
Different gypsum boards may have scattered thermal properties, perhaps resulting from chemical composition and testing conditions. Shown in Table 5.2, from Clancy (1999), are the thermal properties at ambient temperature published by gypsum board manufacturers around the world. The thermal properties of Type X have been reported by Sultan (1996) and Mehaffey (1994), and those of Type C only by Mehaffey (1994). To ensure Type C has relatively higher fire performance than Type X, the data obtained from (Mehaffey et al., 1994) are selected for the FEA in this study. At ambient temperature, the densities of the Type C and Type X gypsum boards are 732 kg/m^3 and 648 kg/m^3 , respectively; and the thermal conductivity of both types is approximately $0.24 \text{ W/m}\cdot^\circ\text{C}$.

The thermal properties of gypsum board at elevated temperature reported by Mehaffey et al. (1994) are plotted in Figure 5.4. The dehydration (removal of free water) initiates at about 80°C . The calcination of chemically bound water is complete at about 200°C . During the dehydration and calcination processes, the temperature rise through gypsum board is effectively delayed. The density and thermal conductivity of gypsum board drop considerably, and the specific heat rises to a peak and

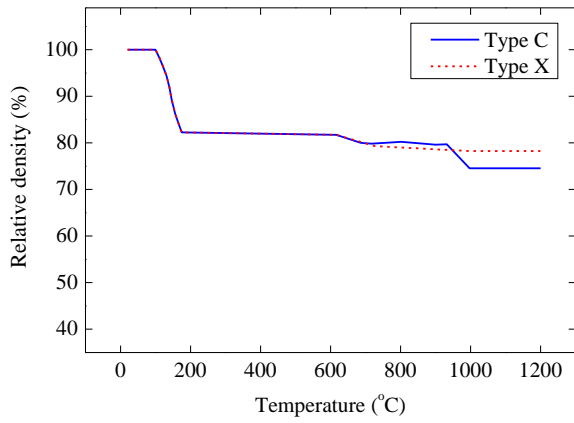
then decreases. After the completion of calcination, the paper sheets outside of the noncombustible core burn out, causing an increase of the thermal conductivity until 800 °C. After that, a higher thermal conductivity is used to include the effect of ablation and cracking.

Table 5.2 Thermal properties of gypsum board at ambient temperature (Clancy, 1999)

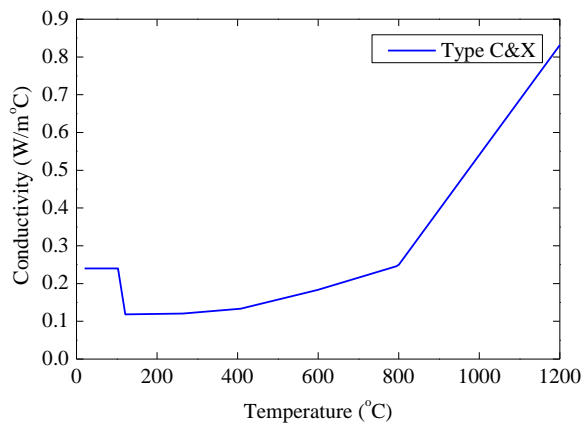
Country	Reference	Density (kg/m ³)	Specific Heat (J/kg·°C)	Conductivity (W/m·°C)
Canada	Mehaffey (1994)-Type C	732	950	0.24
	-Type X	648	950	0.24
Canada	Westrock heavy, regular	578	600	0.2
Canada	Sultan (1996) -Type X	698	1500	0.25
United states	Gypsum Assoc. (1993)			0.16
Europe	Konig et al (2000)			
	Nordic-Type F	825		0.25
	-Type GN (regular)	700		0.25
United Kingdom	British Gypsum Glasroc	1000		0.288
United Kingdom	British Gypsum Fireline	800		0.2
United Kingdom	Knauf Plasterboards	800		0.2
Australia	Boral (1997) Firestop	810		0.17
Australia	CSR Gyprock (1997)			
New Zealand	Winstone Wallboards ltd			
	-GIB® Fyreline	730-880		
	-Standard	690		



(a) Specific heat (J/kg°C)



(b) Relative density (%)



(c) Thermal conductivity (W/m°C)

Figure 5.4 Thermal properties of Type C and X gypsum board (Mehaffey et al., 1994)

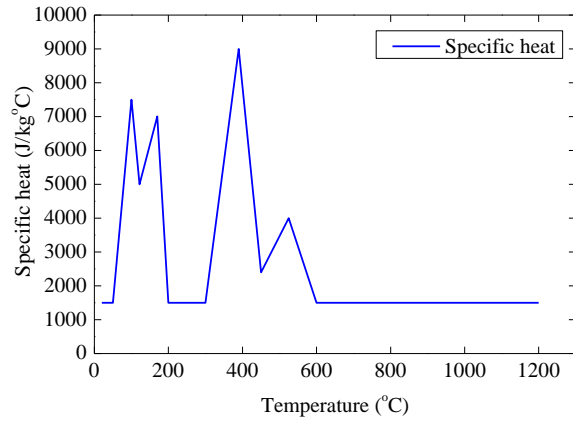
5.3.2.2 MgO board

MgO board, an alternative to gypsum board, has been found to show better fire resistance (Chen, Ye, Bai, & Zhao, 2012), but is more costly. The thermal properties of MgO board measured by (Chen, Ye, Bai, & Zhao, 2013), as shown in Figure 5.5, are adopted. Eq. (5.1) is used to fit the thermal properties; the relevant coefficients (A and B) are given in Table 5.3.

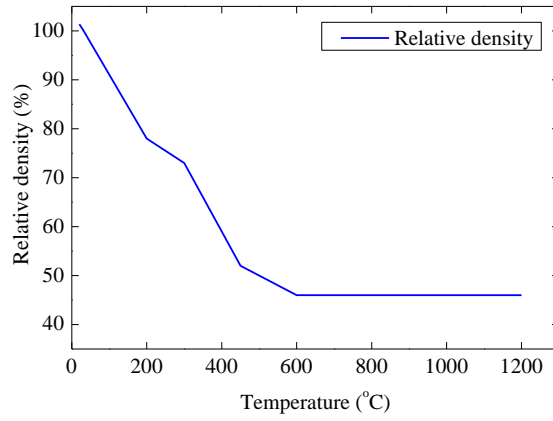
$$y = A \cdot T + B \quad (5.1)$$

Table 5.3 Coefficients for thermal properties of MgO board

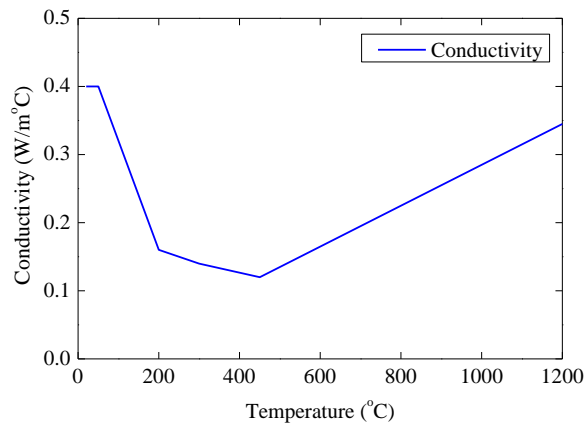
y	T (°C)	A	B
Specific heat (J/kg·°C)	0-50	0	1,500
	50-100	120	-4,500
	100-122	-113.63	18,863
	122-170	41.67	-83.33
	170-200	-183.3	38.167
	200-300	0	1,500
	300-390	83.33	-23,500
	390-450	-110	51,900
	450-525	21.33	-7,200
	525-600	-33.33	21,500
	≥600	0	1,500
Relative density (%)	30-200	-1.294×10 ⁻¹	103.8
	200-300	-5×10 ⁻²	88
	300-450	-1.4×10 ⁻¹	115
	450-600	-4×10 ⁻²	70
	≥600	0	46
Conductivity (W/m·°C)	0-50	0	0.4
	50-200	-1.6×10 ⁻³	0.48
	200-300	-2×10 ⁻⁴	0.2
	300-450	-1.333×10 ⁻⁴	0.18
	≥450	-3×10 ⁻⁴	-0.015



(a) Specific heat (J/kg°C)



(b) Relative density (%)



(c) Thermal conductivity (W/m°C)

Figure 5.5 Thermal properties of MgO board (Chen et al., 2013)

5.4 Finite element structural model of CFS wall stud

For structural analysis, CFS wall stud model was developed using a single CFS C-shape wall stud from the wall specimens described in section 5.2. The temperature distribution within the CFS stud was incorporated from the heat transfer analysis, which requires the FE mesh in the structural model to be identical to that used in the heat transfer analysis such that the predefined nodal temperatures can be applied. The element type S4R was used to model the perforated CFS wall studs. Rigid plates made of R3D4 elements were attached to each end of the stud, as shown in Figure 5.6. Pinned support conditions were assumed for both ends. Axial load was applied at the centroid of the section, at the upper end. The sheathing restraint was simulated by restraining the appropriate horizontal displacement (UX) every 300 mm along the length of the stud. No temperature deterioration for screws is considered. The in-plane lateral restraint provided by the gypsum boards was considered on both fire-exposed and unexposed sides. It was assumed that the gypsum board on the hot flange side also provided sufficient lateral restraint until the stud failed. This assumption is consistent with that adopted by Kaitila (2002), Feng et al. (2003d), Zhao et al. (2005) and Gunalan (2011) in their FE models.

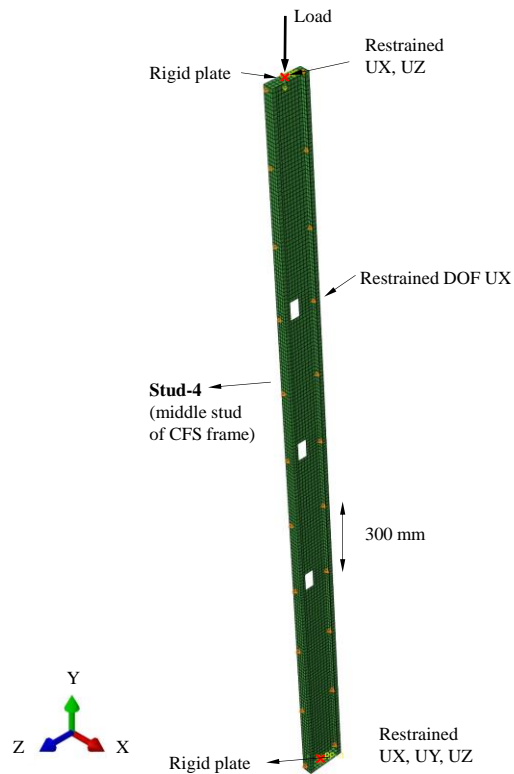


Figure 5.6 Loading and boundary conditions of single CFS stud model

5.4.1 Mechanical properties

The mechanical properties of cold-formed steel at elevated temperature are obtained based on Eurocode 3 Part 1.2 (2005). The nominal stress-strain relationship at elevated temperature is shown in Figure 3.13. For ABAQUS, the true stress-plastic strain relationship is used as input, as shown in Figure 5.7, and can be obtained using Eqs.(5.2) and (5.3). Listed in Table 5.4 are the reduction factors for the elastic modulus, proportional limit and yield strength at elevated temperature. For instance, the reduction factor for the elastic modulus versus temperature curve is plotted in Figure 5.8. According to (Xu, 2011), the elastic modulus and yield strength at room temperature are 2.03×10^5 N/mm² and 345 N/mm², respectively.

$$\sigma_{true} = \sigma_{nom} (1 + \varepsilon_{nom}) \quad (5.2)$$

$$\varepsilon_{true}^{pl} = \ln(1 + \varepsilon_{nom}) - \frac{\sigma_{true}}{E} \quad (5.3)$$

where σ_{true} , σ_{nom} , ε_{nom} , ε_{true}^{pl} and E are the true stress, nominal stress, nominal strain, true plastic strain and elastic modulus of steel at a given temperature.

Steel expands considerably when exposed to high temperatures, inducing thermal bowing due to the presence of non-uniform temperatures across the stud section. Hence, the thermal expansion coefficient is necessary in the analysis of CFS wall systems at elevated temperature. The thermal elongation $\Delta l/l$ of cold-formed steel at elevated temperature is also assumed to follow those specified in Eurocode 3 Part 1.2 (2005), and can be determined from the following:

$$\Delta l/l = \begin{cases} 1.2 \times 10^{-5} T + 0.4 \times 10^{-8} T^2 - 2.416 \times 10^{-4} & 20^\circ C \leq T < 750^\circ C \\ 1.1 \times 10^{-2} & 750^\circ C \leq T \leq 860^\circ C \\ 2 \times 10^{-5} T - 6.2 \times 10^{-3} & 860^\circ C < T \leq 1200^\circ C \end{cases} \quad (5.4)$$

where:

l is the length at 20 °C;

$\Delta l/l$ is the temperature induced elongation;

T is the steel temperature (°C).

Taking a derivative of Δ/l with respect to temperature,

$$\alpha_s = \begin{cases} 1.2 \times 10^{-5} + 0.8 \times 10^{-8} (T - 20) & 20^\circ C \leq T < 750^\circ C \\ 0 & 750^\circ C \leq T \leq 860^\circ C \\ 2 \times 10^{-5} & 860^\circ C < T \leq 1200^\circ C \end{cases} \quad (5.5)$$

Table 5.4 Reduction factor for cold-formed steel based on EC 3 Part 1.2 (2005)

T (°C)	$k_{E,T} = E_T/E$	$k_{p,T} = f_{p,T}/f_y$	$k_{p0.2,T} = f_{p0.2,T}/f_y$
20	1	1	1
100	1	1	1
200	0.9	0.807	0.89
300	0.8	0.613	0.78
400	0.7	0.42	0.65
500	0.6	0.36	0.53
600	0.31	0.18	0.3
700	0.13	0.075	0.13
800	0.09	0.05	0.07
900	0.0675	0.0375	0.05
1000	0.045	0.025	0.03
1100	0.0225	0.0125	0.02

where:

$k_{E,T}$: Reduction factor (relative to E) for the slope of the linear elastic range

$k_{p,T}$: reduction factor (relative to f_y) for proportional limit

$k_{p0.2,T}$: reduction factor (relative to f_y) for effective yield strength

E_T : slope of linear elastic range at elevated temperature T

$f_{p,T}$: proportional limit at elevated temperature T

$f_{p0.2,T}$: effective yield strength at elevated temperature T

E : elastic modulus at 20 °C

F_y : yield strength at 20 °C

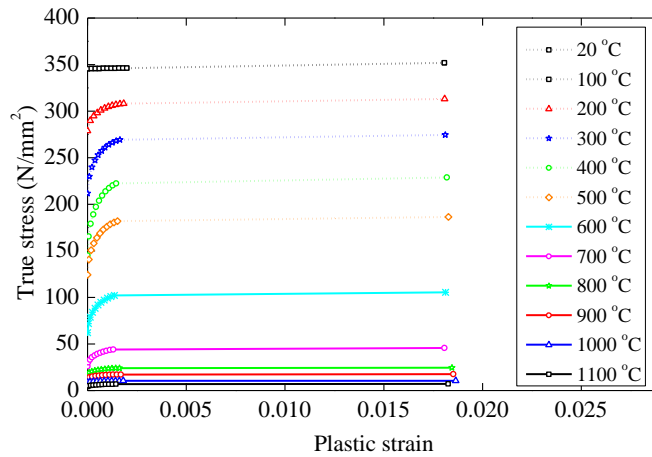


Figure 5.7 True stress-strain relationship of CFS stud at elevated temperature

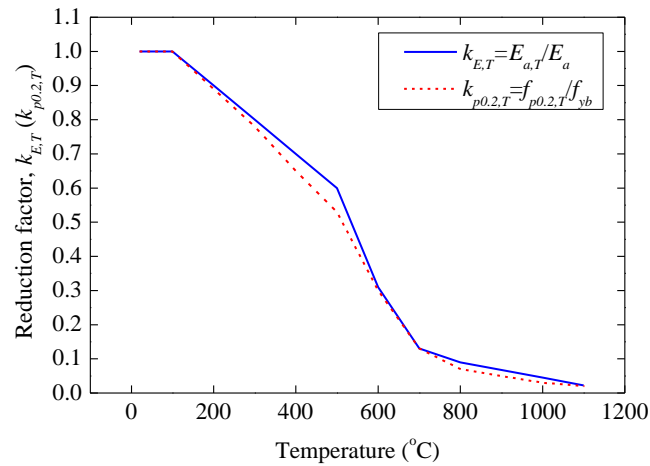


Figure 5.8 Reduction factor of CFS stud at elevated temperature

5.4.2 Residual stresses and initial geometric imperfection

With increasing temperatures, the residual stresses in studs decrease rapidly (Lee, 2004). Therefore, the residual stresses were not considered in this study, an omission in line with that of other researchers (Feng et al., 2003d; Gunalan & Mahendran, 2013; Kaitila, 2002). Due to the thermal bowing effect, the initial geometric imperfection becomes insignificant on the ultimate strength of CFS wall studs subjected to non-uniform elevated temperature distributions (Gunalan & Mahendran, 2013); hence, initial geometric imperfection was also not considered in this study.

5.4.3 Results and discussion

The results obtained from the FE structural model based on a single stud model for the seven tested specimens, shown in Table 5.1, are analyzed. All the studs fails in a similar way. The failure mode of studs is found to have little difference associated with the web perforation length ($L_h=75$ mm or 130 mm). Detailed FEA results, for instance, Stud-4 of specimen LBW-E1(a) are discussed below.

Shown in Figure 5.9 is the predicted time-reaction force (RF2) curve at the bottom end of the CFS stud. For the single stud, RF2 equals the applied load at the top end. At point A, the target load is applied at room temperature. At point B, the applied load starts to decrease. At point C, the applied load reduces to 85% of the applied load. The RF2 of Stud-4 of specimen LBW-E1(a) remains constant until failure occurs at about 96 minutes.

Plotted in Figure 5.10 is the time-axial deformation curve at the top end. The stud shortens initially, due to the applied axial load at room temperature; then gradually expands as temperature increases; and finally shortens again since the stud can no longer sustain the applied load. The failure of the stud is evidenced by the rapid increase of column deformation and sudden decrease of the reaction force at the lower end of the column.

Presented in Figure 5.11 and Figure 5.12 are respectively the predicted stress contour (Mises) and out-of-plane movement (U3) with respect to the phase designated as point A, B and C. Global bending about the X-axis, combed with local failure at the top end, can be observed. However, no failure associated with the web perforation is observed. Thermal bowing is observed as the stud bends towards the fire-exposed side. The flange of the column on the fire-exposed side buckles first due to the higher temperature, and results in rapid degradation of both the stiffness and strength of the flange. The flange on the fire-unexposed side bears an increasing load and fails as a consequence.

Illustrated in Figure 5.13 is the temperature contour at phase Point C. Section 1 and 2 represent the cross section located at the center of a web perforation region and between two web perforations, respectively. The temperature within the stud ranging from 363 °C to 721 °C. According to Table 5.4, at 363 °C, the elastic modulus and yield stress of cold-formed steel decreases to approximately 75% and 70% of those at room temperature, respectively; and at 721 °C, the elastic modulus and yield stress both drop to about 13% that at room temperature. As a result, a large stress gradient exists in the stud. Plotted in Figure 5.14 are the cross-sectional temperature distributions at Section 1 and 2 for all the specimens at failure time, obtained from the heat transfer analysis.

Presented in Table 5.5 is a comparison of failure times between FEA and test results. According to (Xu, 2011), specimen LBW-2 failed prematurely due to the failure of the specimen's sheathing joints in the fire test. The difference in failure time between the predicted FEA and test results, excluding specimen LWB-2, is within 11%, which illustrates that the single CFS stud model provides results with good accuracy and can be used for parametric study to investigate the effect of web perforation.

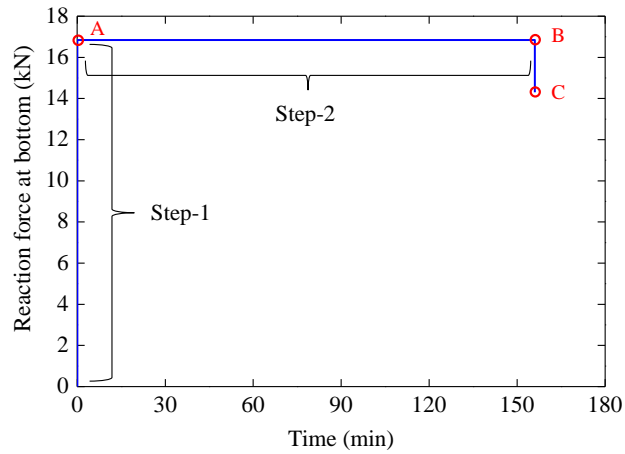


Figure 5.9 Time-reaction force curve (LBW-E1(a))

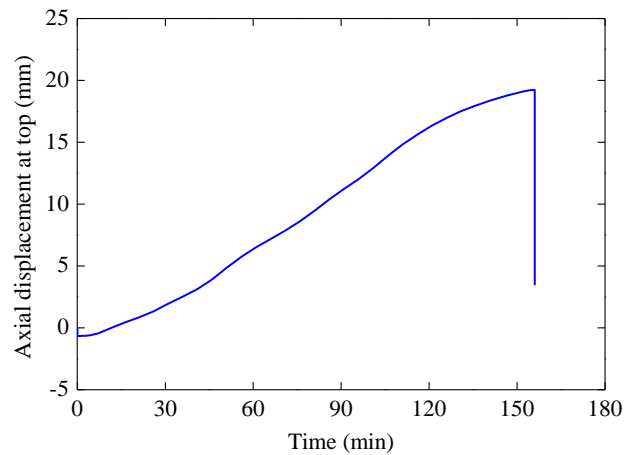


Figure 5.10 Time-axial deformation curve (LBW-E1(a))

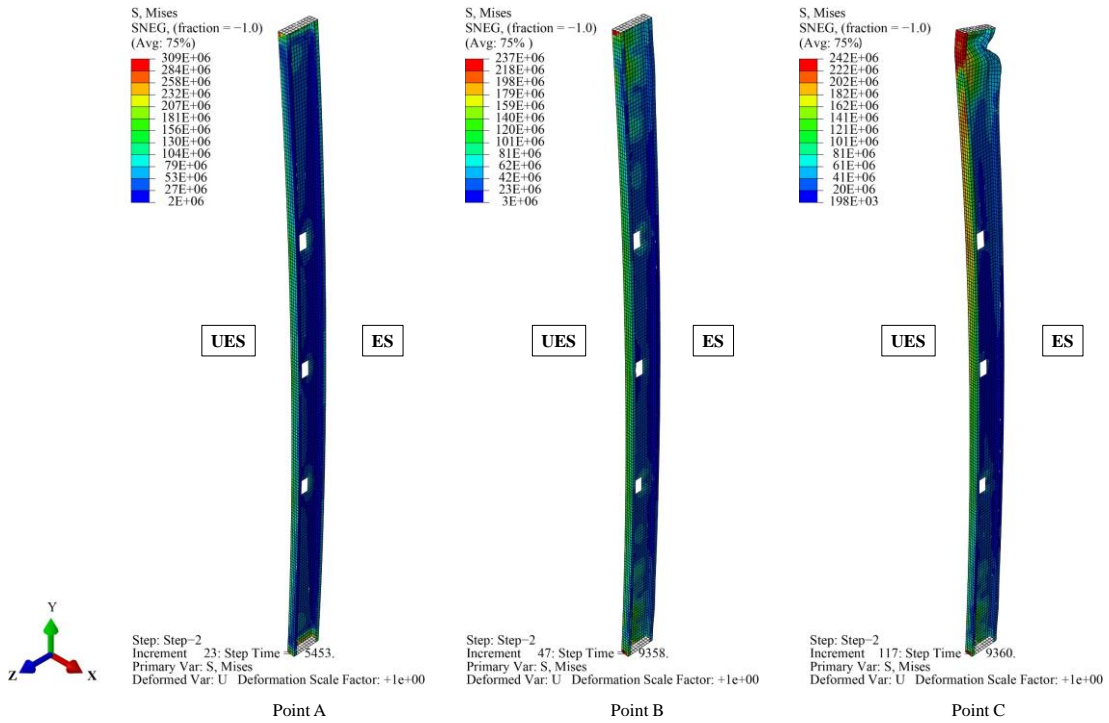


Figure 5.11 Mises stress contour of FEA results for single stud model (LBW-E1(a))

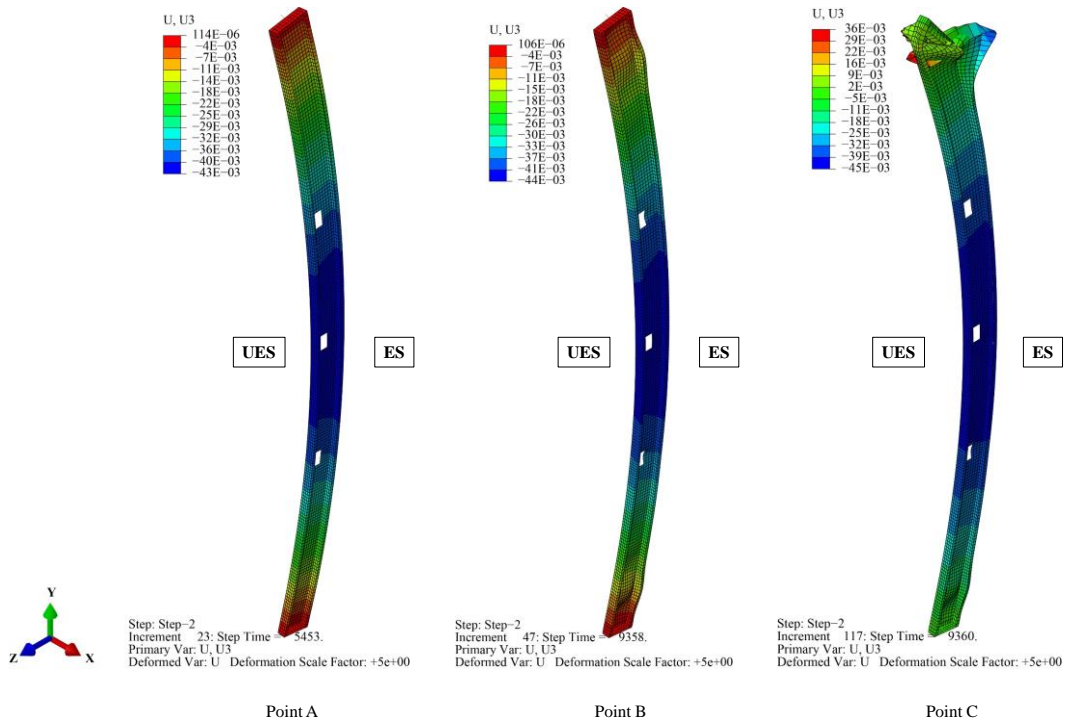


Figure 5.12 U3 of FEA results for single stud model (LBW-E1(a))

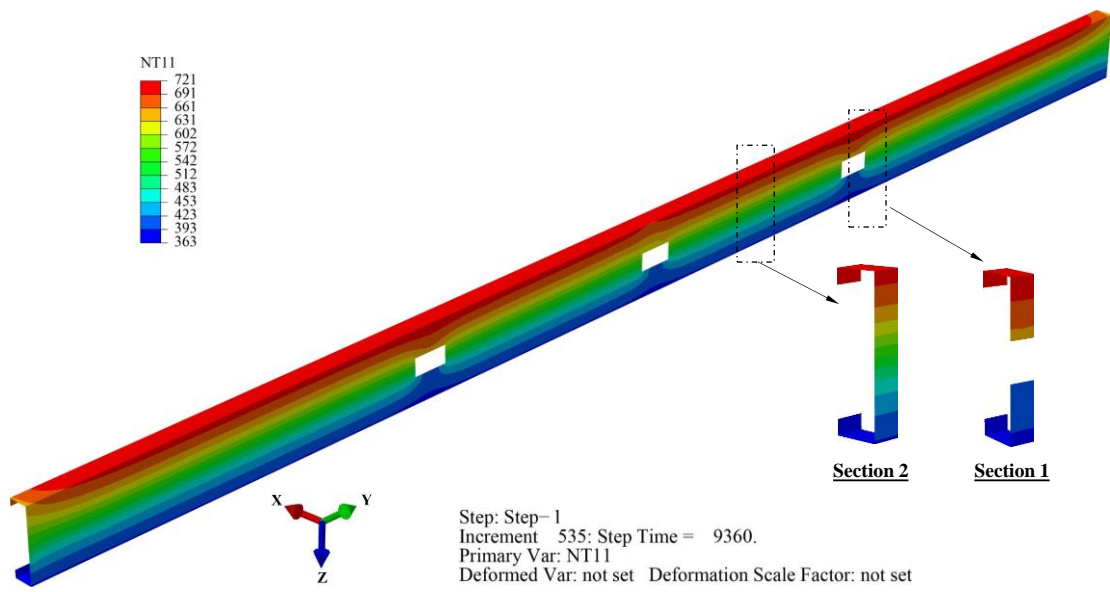
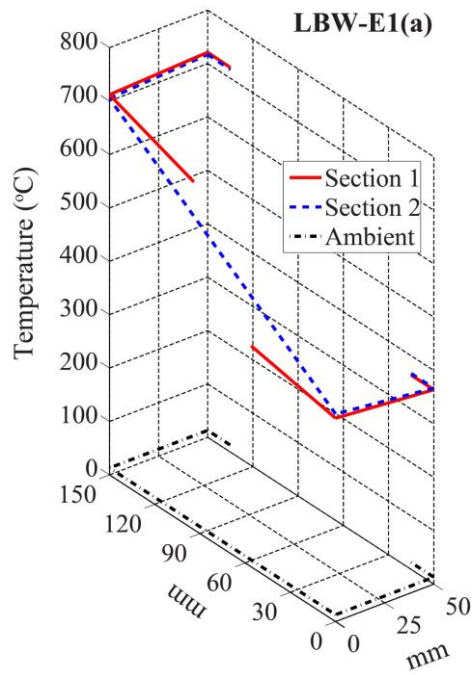
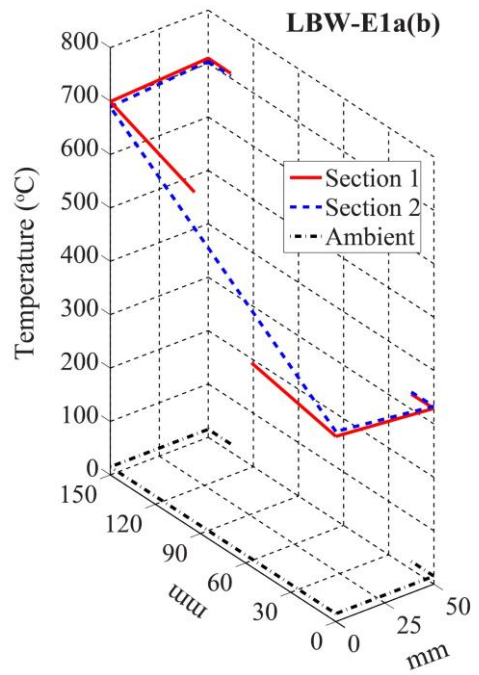


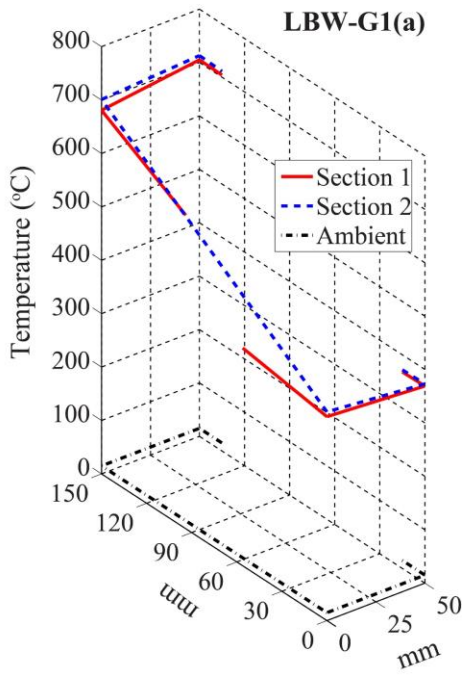
Figure 5.13 Temperature contour of Stud 4 at failure time (LBW-E1(a))



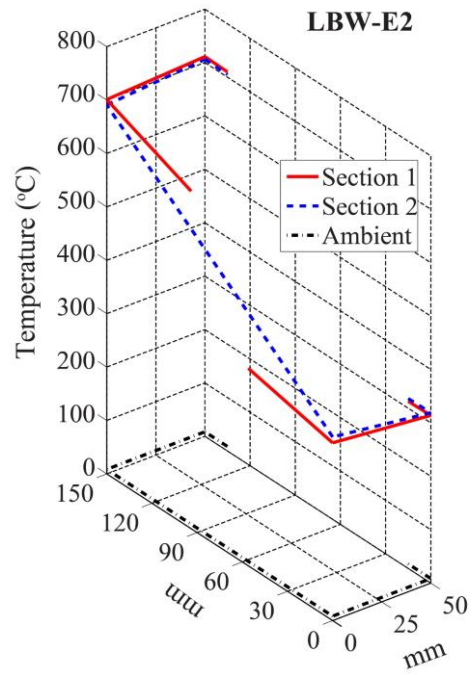
(a) LBW-E1(a)



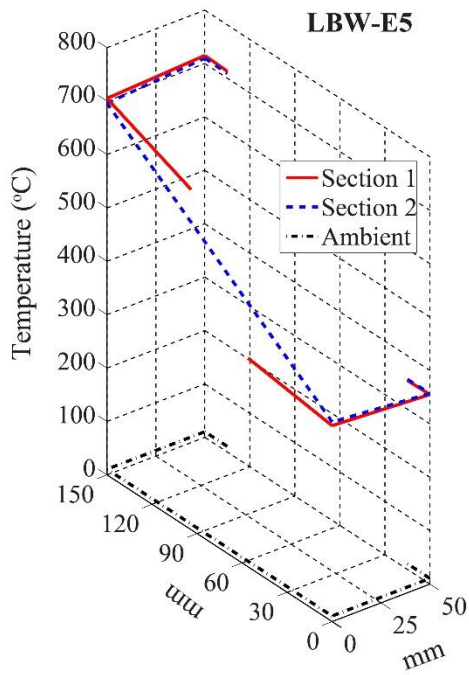
(b) LBW-E1a(b)



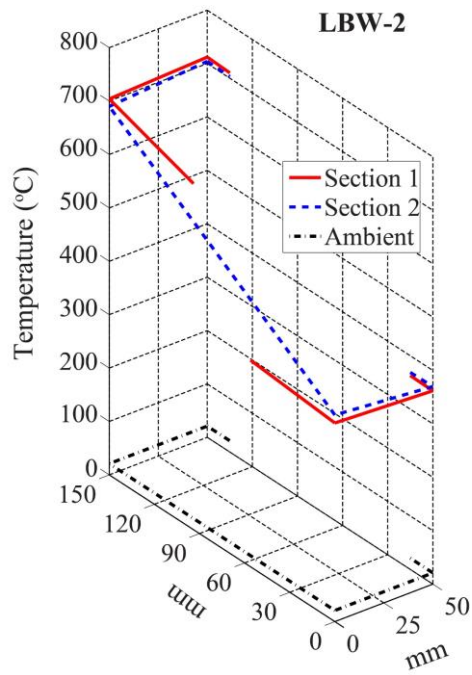
(c) LBW-G1(a)



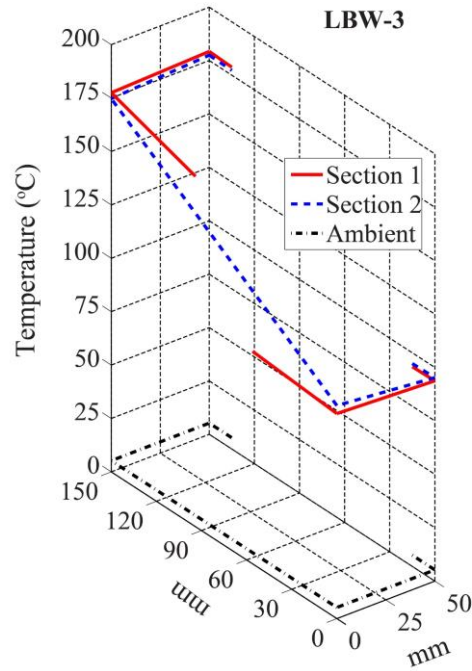
(d) LBW-E2



(e) LBW-E5



(f) LBW-2



(g) LBW-3

Figure 5.14 Cross-sectional temperature contours of Stud 4 for all specimens at failure time

Table 5.5 Comparison of failure time between FEA and test results

No.	Specimen	t_{FEA} (min)	t_{Test} (min)	$(t_{FEA}-t_{Test})/t_{Test} \times 100\%$
1	LBW-E1(a)	156.01	155	0.65%
2	LBW-E1a(b)	139.28	153	-8.97%
3	LBW-G1(a)	89.19	100	-10.81%
4	LBW-E2	118.21	117	1.03%
5	LBW-E5	108.82	100	8.82%
6	LBW-2	108.10	68	58.97% (premature failure)
7	LBW-3	92.86	83	11.88%
Average				4%
Standard Deviation (STDEV) (excluding LBW-2)				0.091

5.5 Finite element structural model of CFS wall frame

Unlike the FE modelling using a single CFS stud discussed in Section 5.4, the system-level FE model of the CFS wall frame developed in this study is presented in this section. Modelling of the tested wall frames can simulate possible stress redistribution within the CFS studs. The FE model includes all the steel components of a CFS frame except for the bottom track, as shown in Figure 5.15. By excluding the bottom track, the reaction force at the bottom end of each stud, a key parameter in the FE result analysis, can be extracted from the output database (.odb) file of ABAQUS. Similar to that of the single CFS stud model, the restraints associated with sheathing are modelled by restraining the horizontal displacement (UX) at the locations of screws. As to interior glass fibre insulation, its contribution of delay to the temperature rise is modeled in the thermal analysis, but the effect of glass fibre swelling is disregarded in the stress analysis. In this study, swelling of glass fibre does not have much effect on CFS studs of the tested wall frames as there is about 50 mm space in the wall cavities since the stud depth is 150 mm but the thickness of glass fibre is only 90 mm. In addition, swelling of glass fibre was not observed in the tests.

The CFS frame is modelled using S4R element. To incorporate nodal temperature into sequential stress analysis, the location of each node in the FE mesh should be consistent with that of the thermal analysis. The finite element meshes of the structural model are the same as those of the heat transfer model, for which correlation is required to import the heat transfer results. The time period of the step specified is 14400 (240 minutes). The maximum number of increments is 200. The initial increment size is 30, whereas the minimum and maximum increment sizes are 1×10^{-9} and 300, respectively.

Shown in Figure 5.16 are the interactions and constraints between all the components of the CFS wall frame. The contact interaction between the webs of the two studs on each end of the CFS frame is hypothesized to be frictionless, and the hard contact is selected for the normal direction behaviour. The tie interaction is defined to model the contacted surfaces between the loading beam and top track of the CFS frame, and the locations of nodes are where screws are placed. The spring/dashpots are defined to simulate the contact relationship between the track web and stud ends.

Presented in Figure 5.17 are the boundary and loading conditions. All three translational displacements associated with the bottom end of the stud, i.e. UX, UY and UZ, are restrained. The horizontal displacements of the web of the top track, UZ, are restrained. The axial loads are applied

evenly to eight nodes at the locations of the ten jacks to prevent the composed loading beam failing locally.

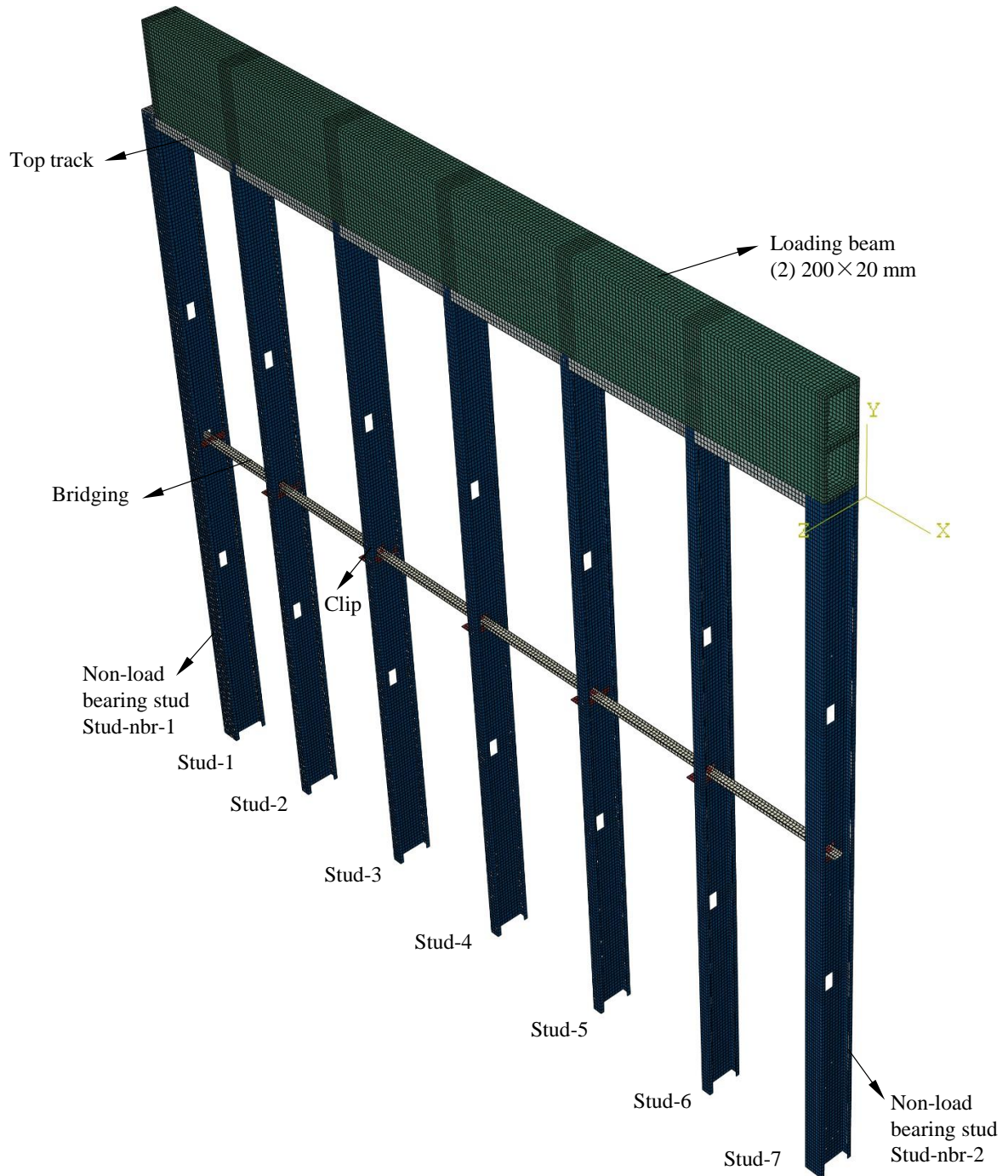


Figure 5.15 FE mesh of CFS wall frame model

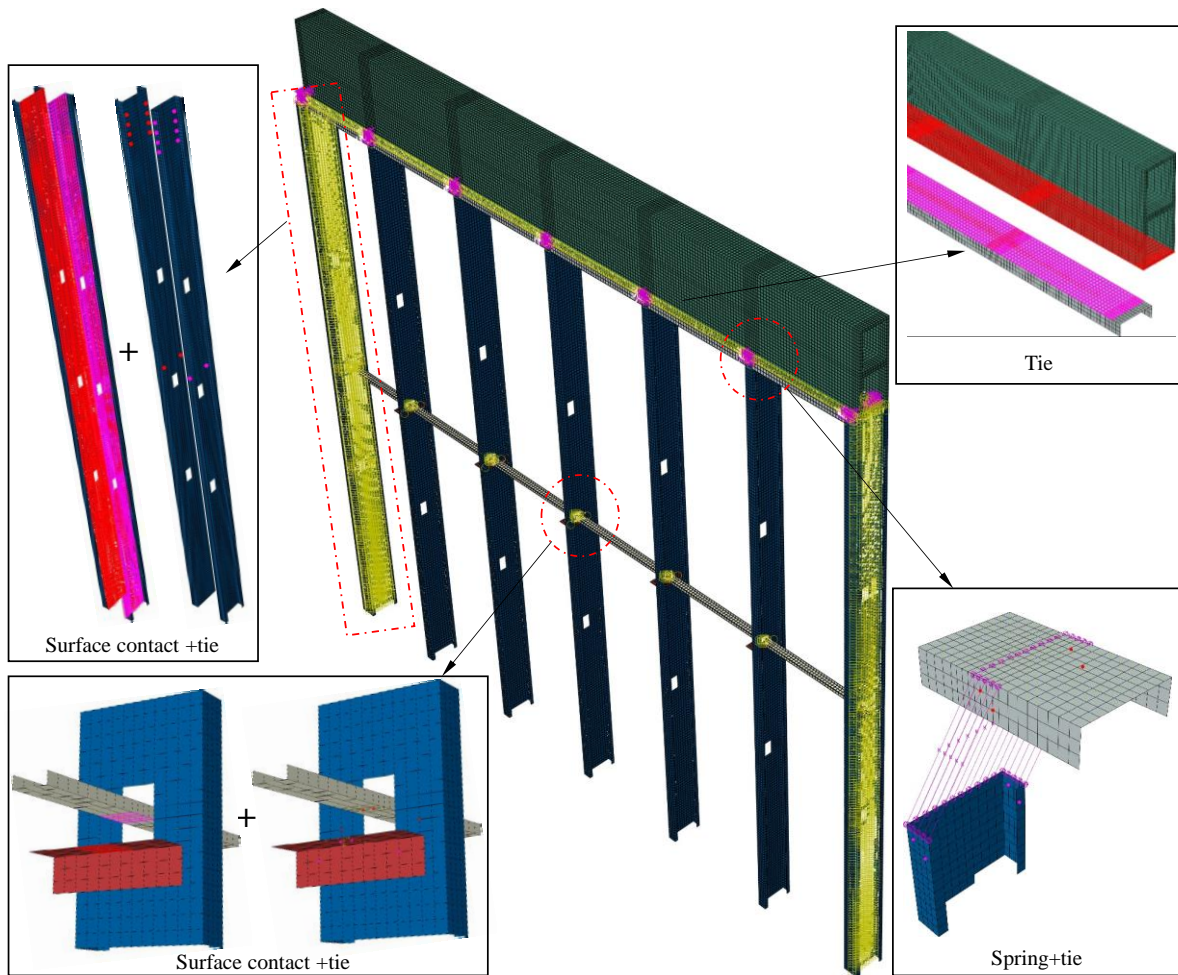


Figure 5.16 Interactions and constraints of CFS wall frame model

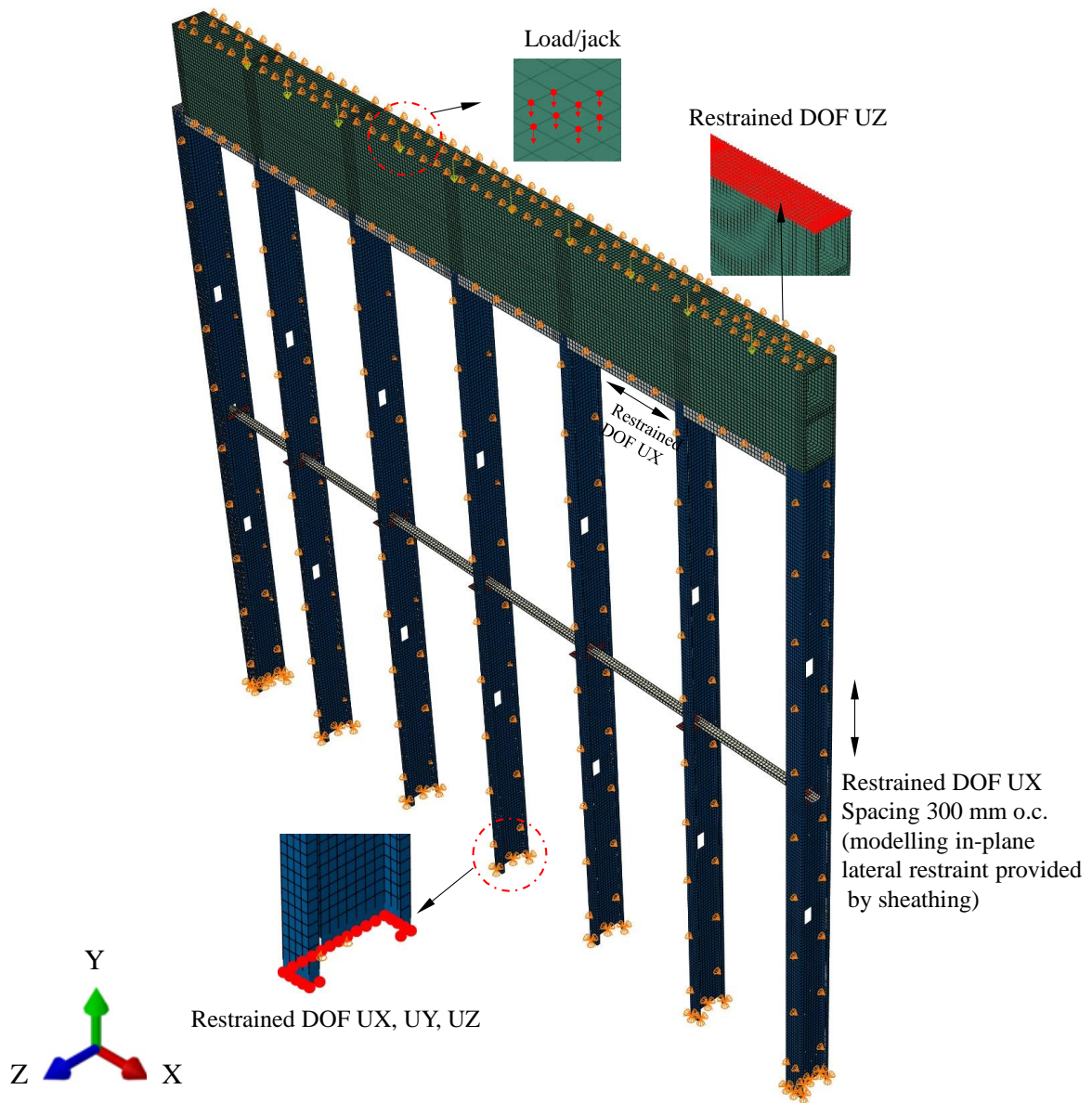


Figure 5.17 Boundary and loading conditions of CFS wall frame model

5.5.1 Results and discussions

The results obtained from the FE structural model based on the CFS wall frame model are analyzed. The failure mode of the CFS walls with a wall height of 3.0 m and 3.2 m are illustrated using specimens LBW-E1(a) and LBW-3, respectively. Shown in Figure 5.18 and Figure 5.19 are the failure modes of the two specimens obtained from the CFS wall frame model. Both CFS studs of the specimens bend towards the furnace and both ends of the studs deform considerably, corresponding to local failure at the ends. The wall height for specimens LBW-E1(a) and LBW-3 are 3.0 m and 3.2 m, respectively. In addition, the length and number of web perforations are different, as shown in Table 5.1. Local failure is associated with the web perforation near ends of the studs for specimen LBW-3, but not for specimen LBW-E1(a), perhaps because the web perforation length is greater and the bearing height associated with the perforation at the end is much shorter than that of specimen LBW-E1(a).

Shown in Figure 5.20 is the time-average axial displacement curve. The average axial displacement is obtained based on all the loaded nodes of the loading beam. The frame is shortened at ambient temperature when the load is applied but subsequently elongated at elevated temperature due to thermal expansion. But unlike shown in Figure 5.10 for the single CFS stud model, there is no abrupt axial shortening is observed at the time of failure and after failure for both specimens. Due to the local failures at the web perforation and ends of the studs, the computer program terminates when the local failures occurred.

Presented in Figure 5.21 are the time-reaction force relationships at the bottom ends of the studs for all the specimens. Unlike a sudden drop in reaction force and axial deformation for single CFS stud model as illustrated in Figure 5.9 and Figure 5.10, there are force and stiffness interactions among the CFS studs. For all seven specimens, at the first phase, the loads in the interior studs initially increase as the temperature increases but the loads in end studs are reduced. This may be caused by the deformation of the loading beam. However, as the further increase of the temperature, the loads in the interior studs reached to their peak values. The loads were started to shift to the end studs. In the second phase, the loads in the interior studs decreases as the increase of the temperature. At the meantime, the loads in the end studs increase considerably. For the CFS wall frame model, the failure time of the specimens cannot be identified.

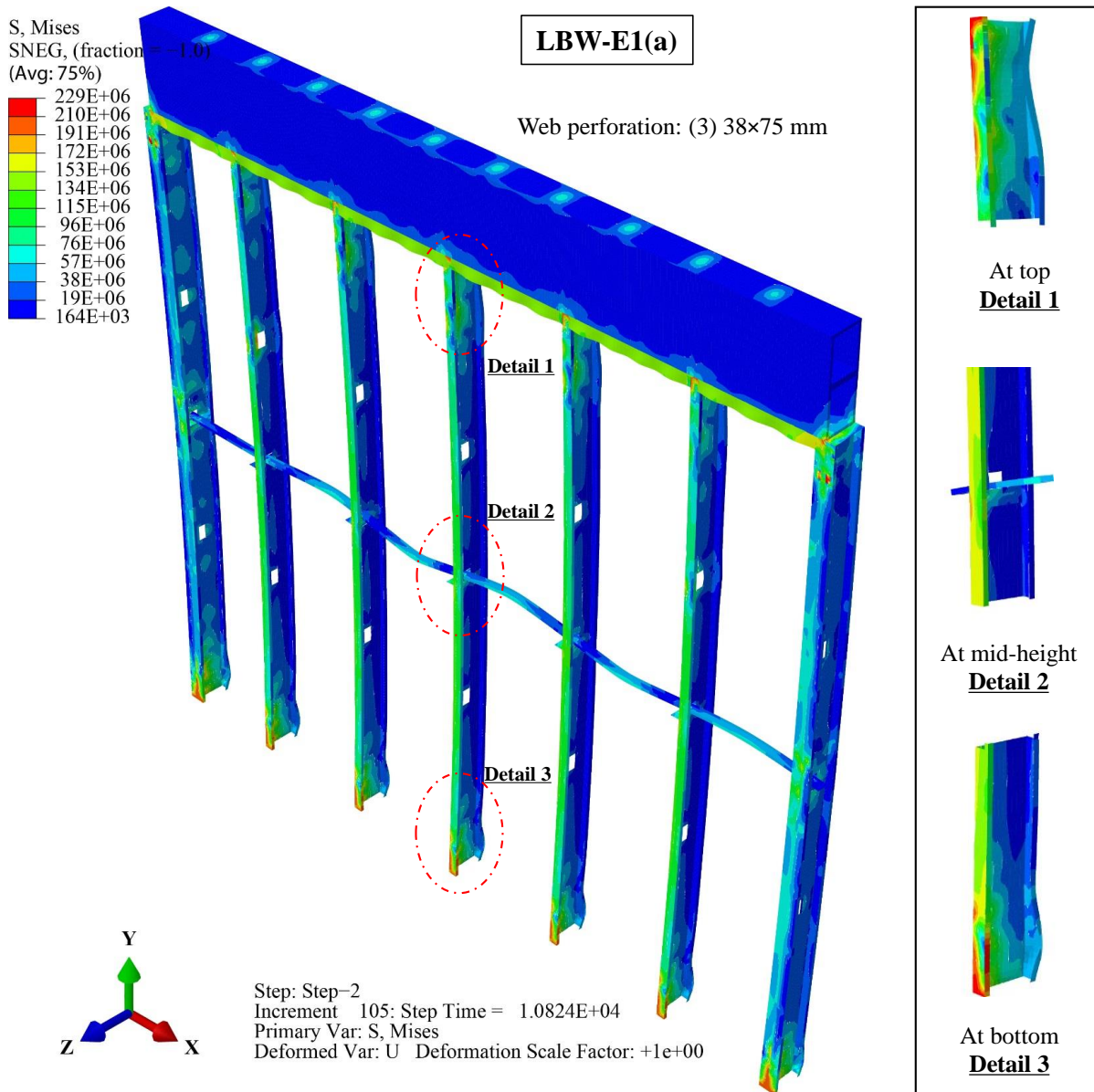


Figure 5.18 Failure mode of CFS wall frame model (LBW-E1(a))

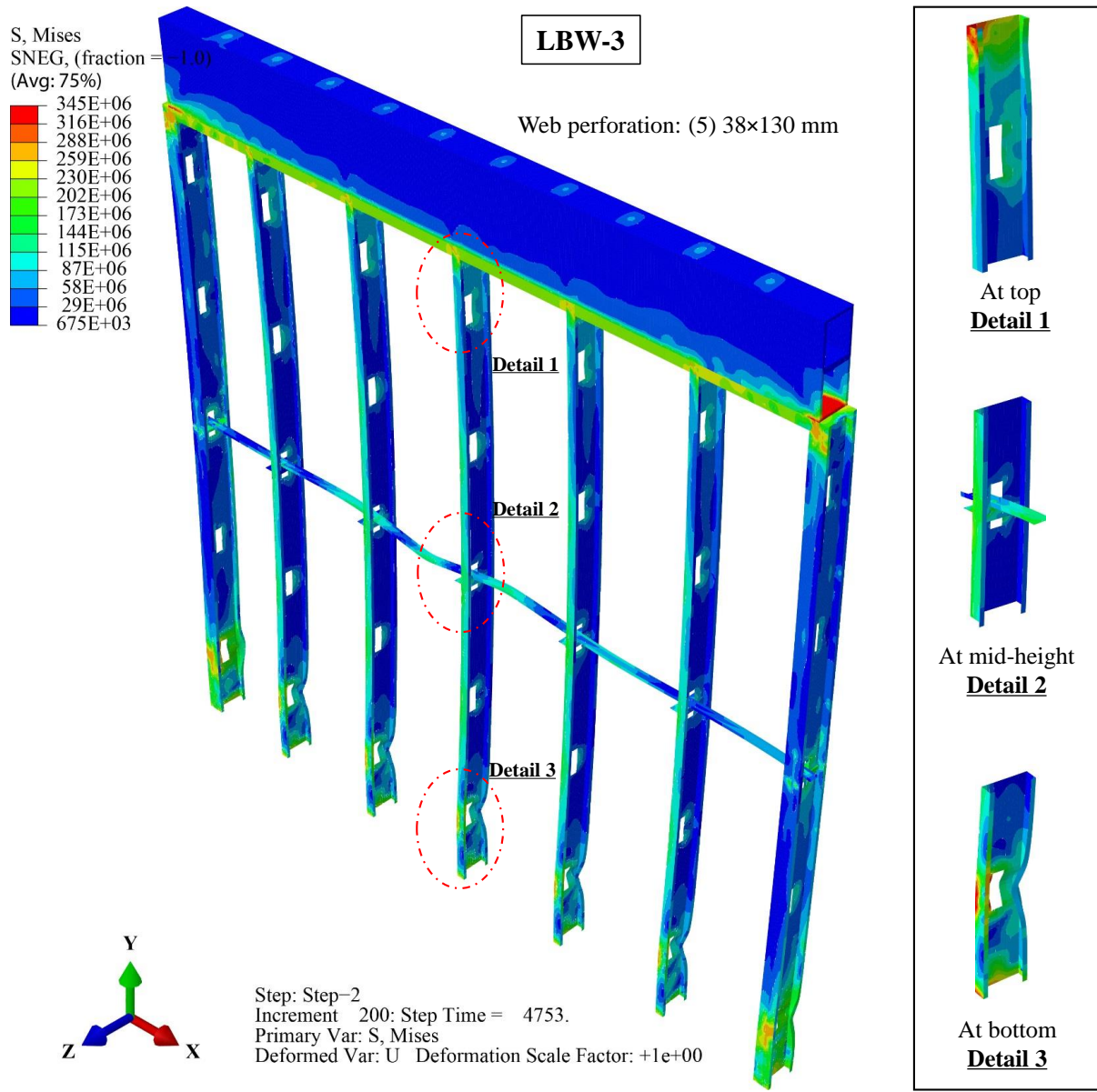


Figure 5.19 Failure mode of CFS wall frame model (LBW-3)

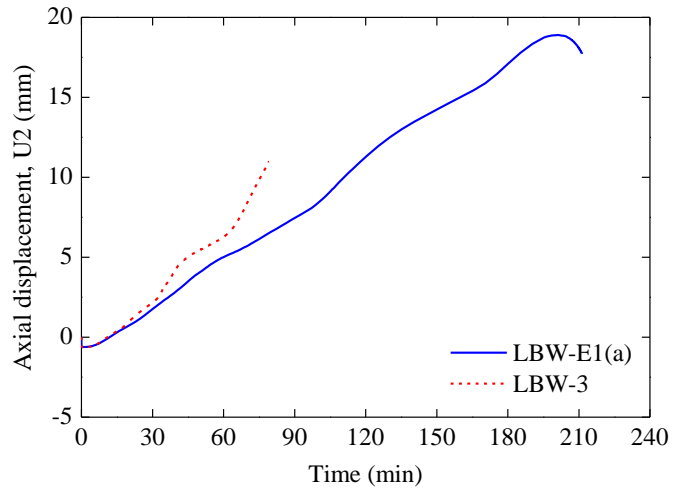


Figure 5.20 Time-average axial displacement relationships at stud top end

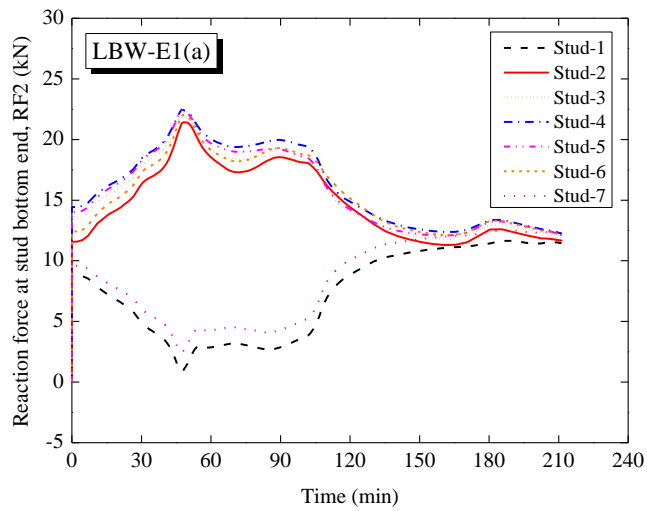


Figure 5.21 Time-reaction force relationships at stud bottom end

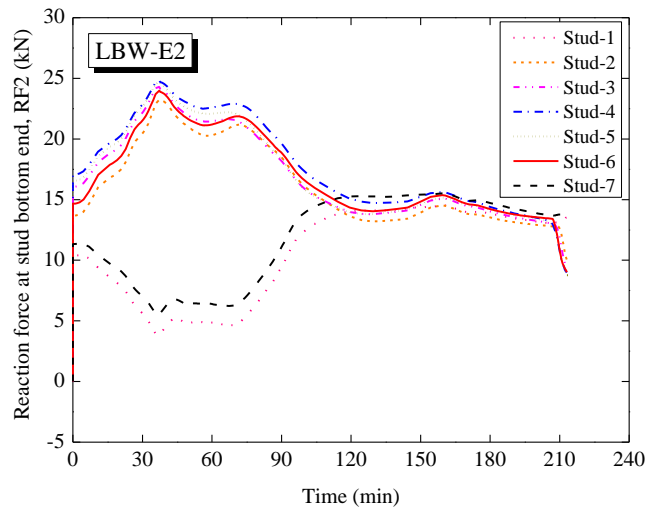
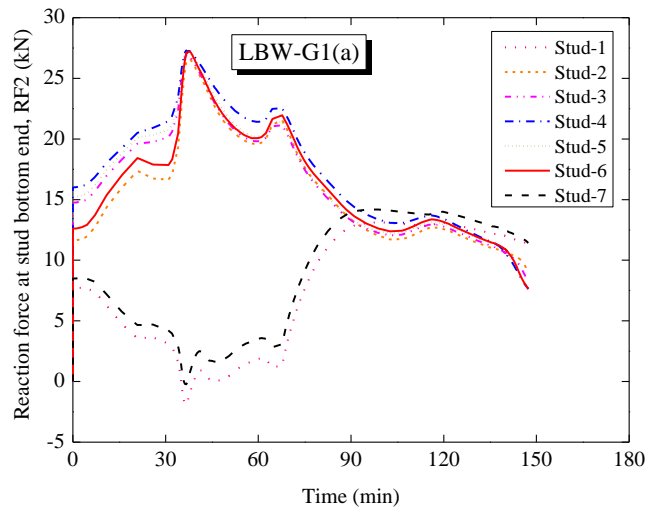
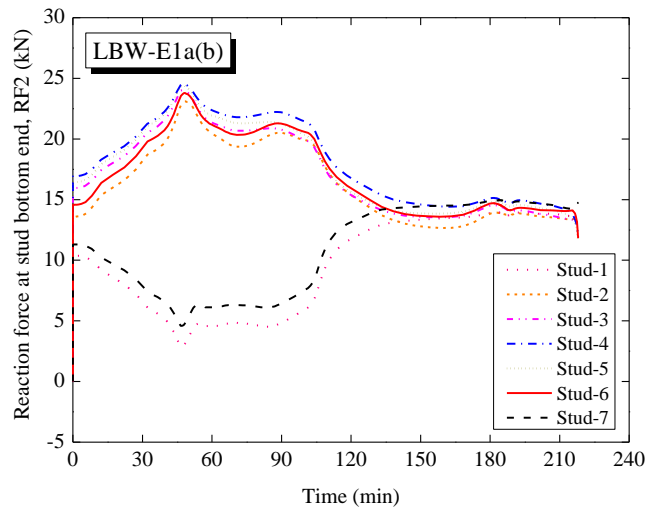


Figure 5.21 Time-reaction force relationships at stud bottom end

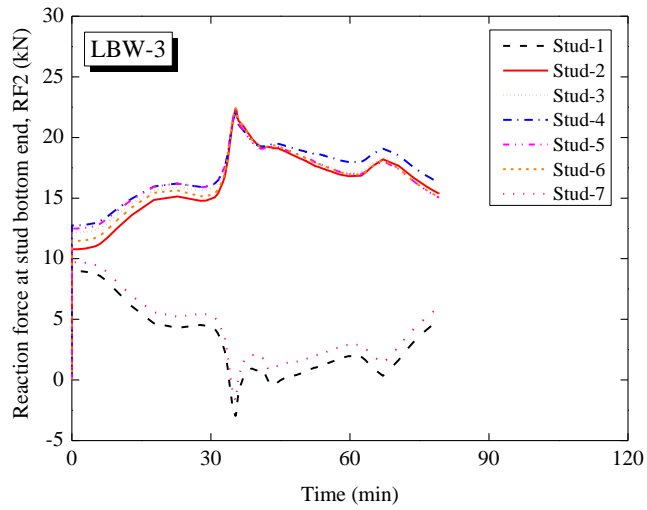
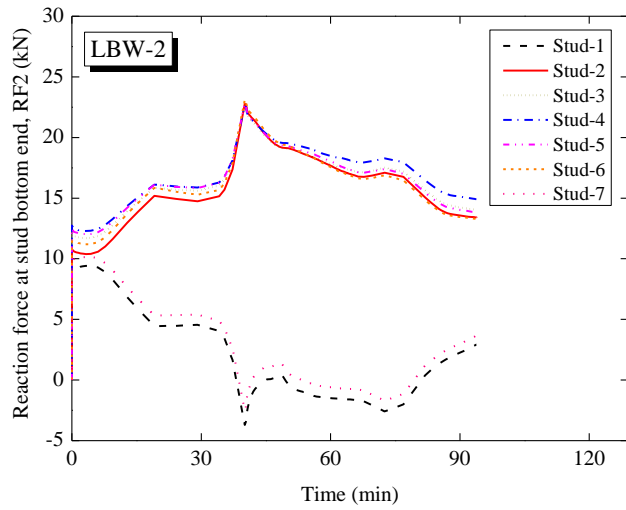
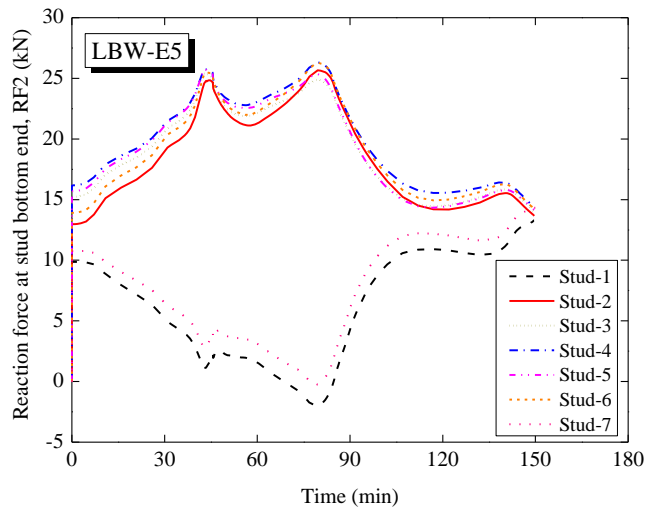


Figure 5.21 Time-reaction force relationships at stud bottom end

From Figure 5.21, it is found that axial forces in end studs, Stud-1 and Stud-7, are in tension for a certain period of time in all the modelled specimens. Intuitively, it is expected that all the studs of the CFS wall frame are in compression due to the applied load and elevated temperature. A thorough examination on modelling of CFS wall frame was conducted, and it was found that the tension forces in the end studs was resulted from adopting the tie interaction to simulate the surface contact condition between the hot-rolled structural loading beam and the top track of CFS wall frame. In the FE model of CFS wall frame, the loading beam is assumed to be remained at ambient temperature throughout the fire event. Thus, there is no thermal expansion in the loading beam. Due to the compatibility of deformation, the possible thermal expansion of the top track of the CFS wall frame is restrained by the loading beam when tie interaction is specified, which results in tension forces in Stud-1 and Stud-7. Evidently, when the tie interaction between the loading beam and the top track of CFS wall frame is replaced with friction interaction, the end studs are no longer in tension in any time during the fire duration.

Presented in Figure 5.22 is the failure mode of a CFS wall frame (LBW-3) with the height of 3.2 m and web perforations of 38 mm \times 130 mm, in which the surface contact condition between the loading beam and the top track of CFS wall frame was simulated with friction interaction. Considering there is no available information on the friction coefficient between hot-rolled structural steel and galvanized cold-formed steel at elevated temperature, the friction coefficient of 0.3 was adopted in the investigation. The CFS wall frame, shown Figure 5.22, failed in a similar way to the case when the tie interaction was specified (Figure 5.19). The FE simulation associated with Figure 5.22 terminated early at 75.5 minutes instead of 79.2 minutes as that of Figure 5.19. Differential horizontal movement at the contact surface between the loading beam and the top track of CFS wall frame was also observed, as illustrated in Figure 5.22.

Shown in Figure 5.23 is the time-reaction force relationships of stud bottom support corresponding to the frame shown in Figure 5.22. It can be seen from Figure 5.23 that all the wall studs of the frame are in compression throughout the fire duration. Therefore, it appears that the friction interaction is more realistic than the tie interaction. However, convergence issues were encountered when adopting the friction interaction for simulating the wall specimens with height of 3.0 m and shorter web perforation length. Thus, there is a need in future research to further explore appropriate boundary conditions between the loading beam and the top track of CFS wall frame at elevated temperature to achieve more realistic and accurate simulations.

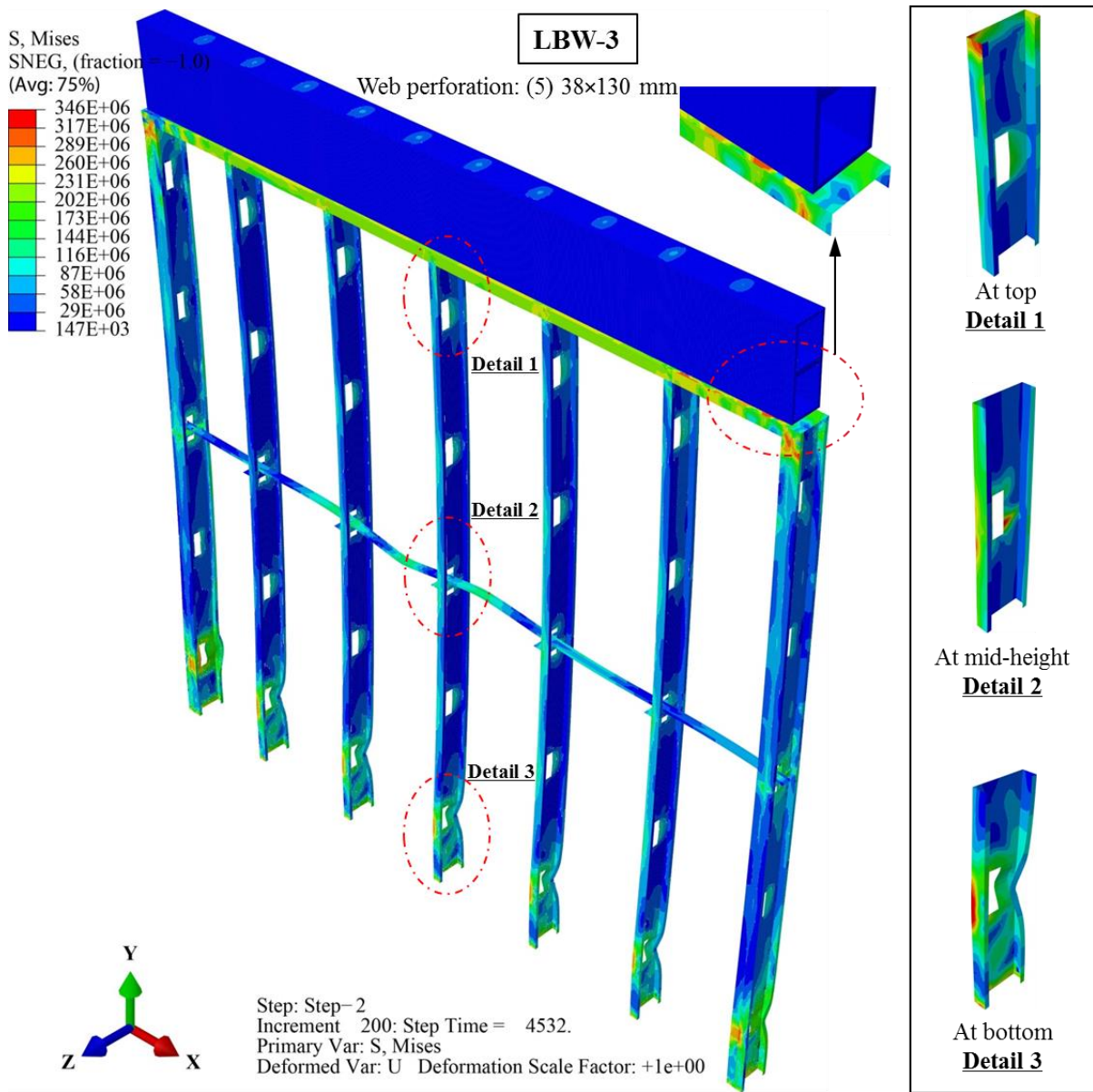


Figure 5.22 Failure mode of CFS wall frame model (LBW-3) (friction coefficient=0.3)

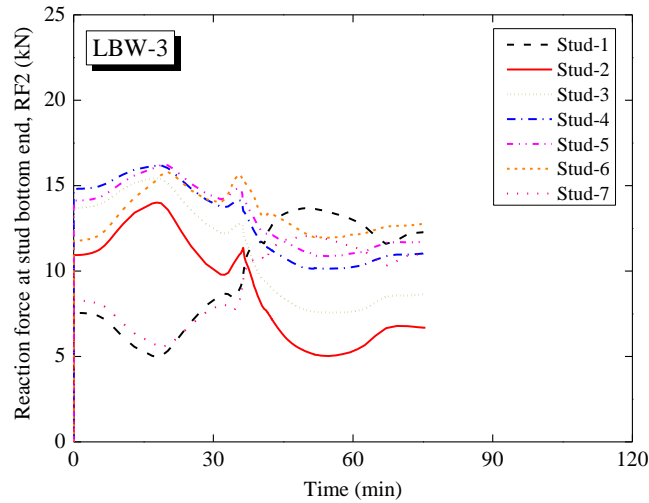


Figure 5.23 Time-reaction force relationships at stud bottom support (friction coefficient=0.3)

5.6 Finite element structural model of CFS wall system

To investigate the effect of sheathing bracing on the behaviour of CFS walls at elevated temperature, sheathing is modelled with shell element in this model in addition to the CFS wall frame. The mechanical properties, i.e., elastic modulus and yield stress is very limited for gypsum board and they are not available for MgO board. A parametrical study is conducted to study the effect of different sheathing stiffnesses on the structural performance of the wall systems. The FE model is developed according to the configuration of the 3.0 m tall CFS wall with three web perforations (38×75 mm). Shown in Figure 5.24 is the FE model where sheathing is modelled using shell element S4R. Presented in Figure 5.25(a) and (b) are the interaction and constraint between the sheathing and stud, respectively. The temperature is applied only to the CFS wall frame, as shown in Figure 5.25(c). The sheathing on both sides of the wall are modelled with different stiffness in order to simulate the corresponding elevated temperature difference.

The mechanical properties of gypsum board on the fire-unexposed side are constants with elastic modulus, E_{s-Uexp} , of $2.0 \times 10^4 \text{ N/mm}^2$ and yield stress, f_{y-Uexp} , of 3.2 N/mm^2 . Due to lack of the mechanical properties of gypsum board at elevated temperature, four reduced mechanical properties (E_{s-Exp} and f_{y-Exp}) are investigated for that of the sheathing on the fire-exposed side. The four reduced material properties for E_{s-Exp} and f_{y-Exp} are 1.0, 0.5, 0.25 and 0.125 times of that of E_{s-Uexp} and f_{y-Uexp} at ambient temperature, as shown in Figure 5.26. In addition, the investigation is also conducted for the case in

which the effect of the sheathing is not directly simulated by the shell element in the FE model of stress analysis; instead, the effect of sheathing is simplified by restraining the horizontal displacement (UX) of the wall studs at the locations of screws as that discussed in section 5.5 for CFS wall frame model.

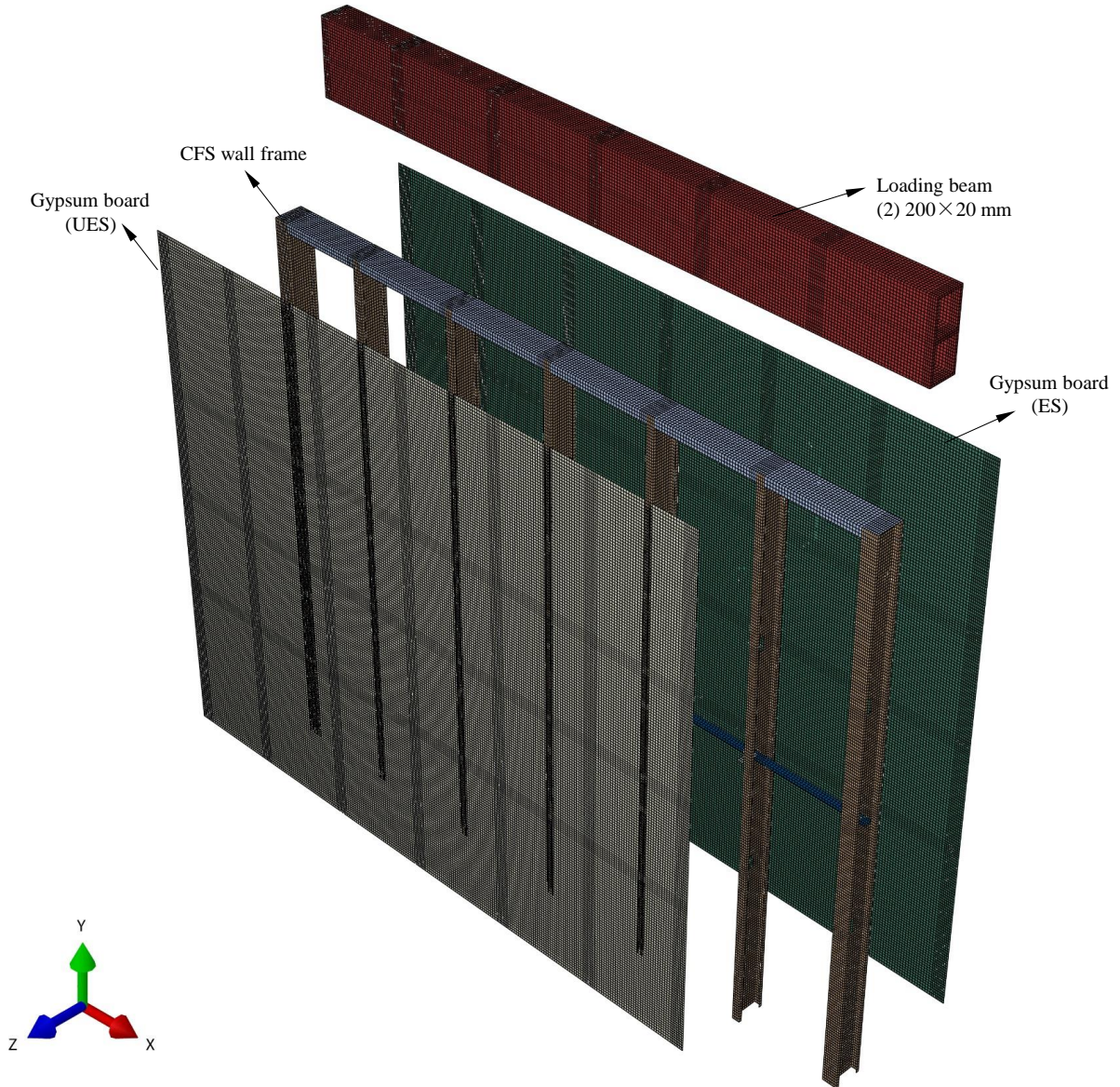
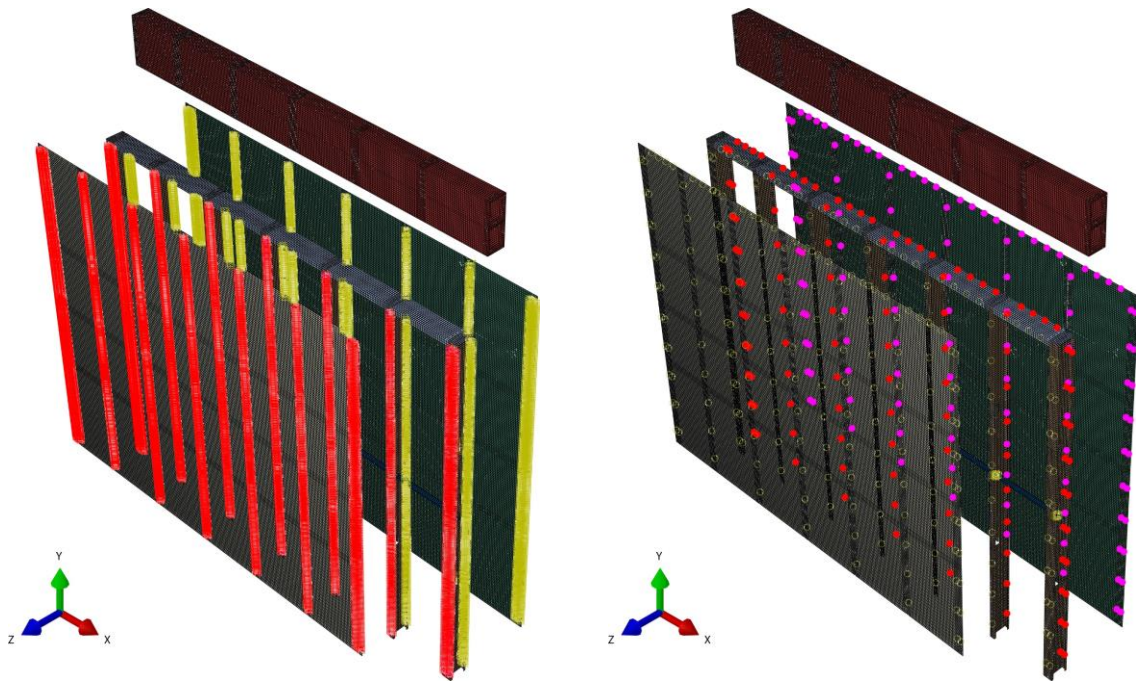
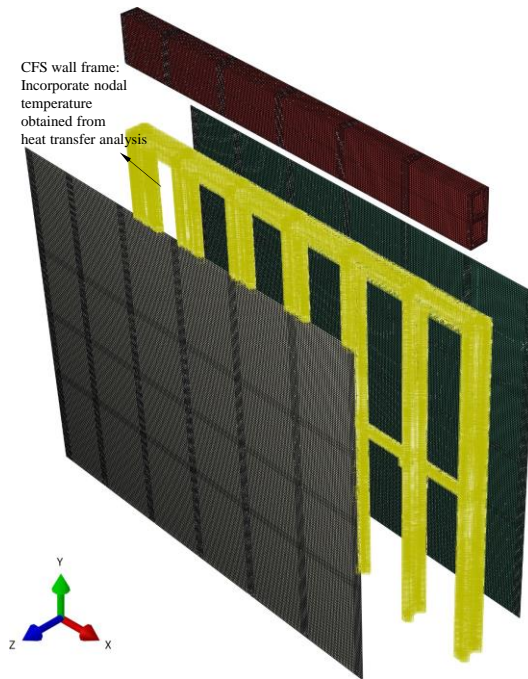


Figure 5.24 Sheathing modelled using shell element S4R



(a) Surface contact

(b) Tie interaction



(c) Incorporate nodal temperature

Figure 5.25 Interaction and constraint between sheathing and studs

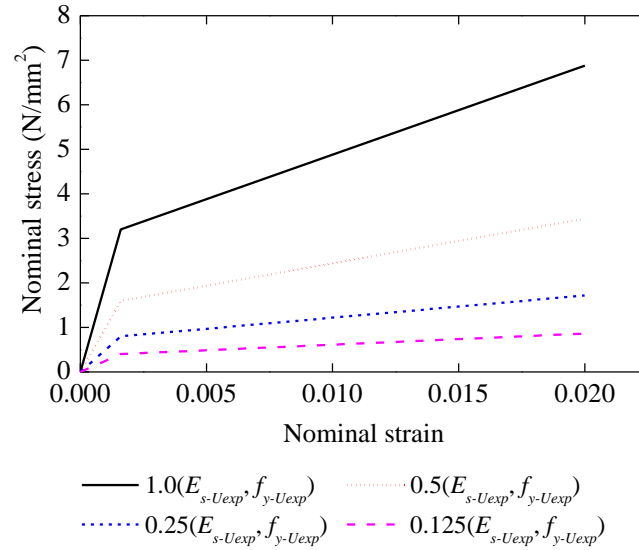
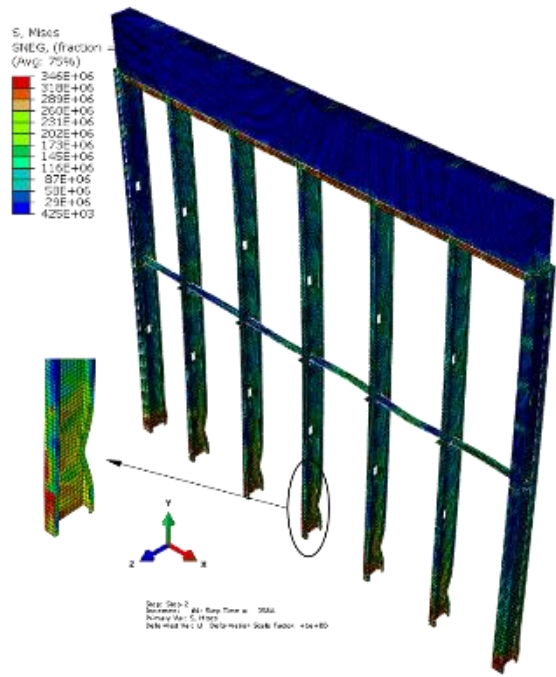


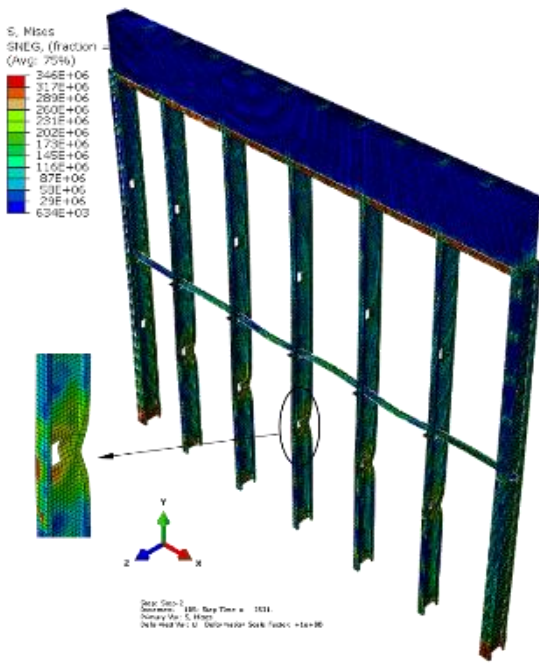
Figure 5.26. Stress-strain relationship of sheathing

5.6.1 FEA results and discussions

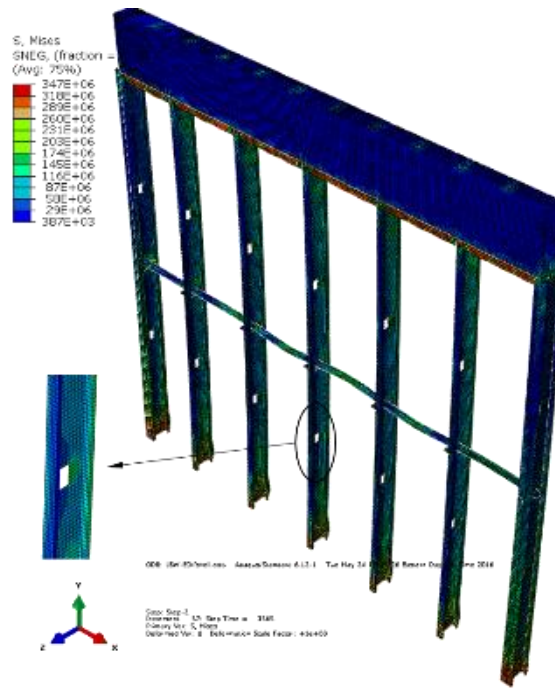
Illustrated in Figure 5.27 is the structural response of the CFS wall system at 60 minutes. For the CFS walls with different mechanical properties of gypsum boards on the fire-exposed side, buckling failure occurs at the bottom end of CFS wall studs for the case $f_{y-Exp}=0.125f_{y-Uexp}$ and $E_{y-Exp}=0.125E_{y-Uexp}$. However, for the other three cases, i.e. $f_{y-Exp}=0.25f_{y-Uexp}$ and $E_{y-Exp}=0.25E_{y-Uexp}$, $f_{y-Exp}=0.5f_{y-Uexp}$ and $E_{y-Exp}=0.5E_{y-Uexp}$, and $f_{y-Exp}=f_{y-Uexp}$ and $E_{y-Exp}=E_{y-Uexp}$, the failures occur at the web perforation near the bottom end of CFS studs. At 60 minutes, the furnace temperature is 945.3 °C, and the temperature within the CFS frame varies from 512 °C to 112 °C as shown in Figure 5.28. Based on Eurocode 3 Part 1.2 (2005), the reduction factors for elastic modulus and yield strength of CFS vary from 0.6 to 1 and from 0.53 to 1, respectively. The stress reaches the yield strength first on the fire-exposed side, shown in Figure 5.27(a)-(c). For the case in which sheathing is not directly modelled by shell elements, i.e. in CFS wall frame model (Figure 5.27(c)), buckling failure is not observed at 60 minutes, but buckling failure occurs at web perforations near the bottom stud ends for the cases of Figure 5.27(a) and (b). Therefore, it may indicate that the simulating effect of sheathing by restraining the horizontal displacements of CFS studs at the location of screws of without directly modelling sheathing with shell elements in stress analysis may overestimate the failure time of the wall.



(a) CFS frame ($f_{y-Exp}=0.125f_{y-Uexp}$)



(b) CFS frame ($f_{y-Exp}=0.25f_{y-Uexp}$)



(c) CFS frame (restrain UX at screw locations)

Figure 5.27. Structural response of CFS frame at 60 minutes

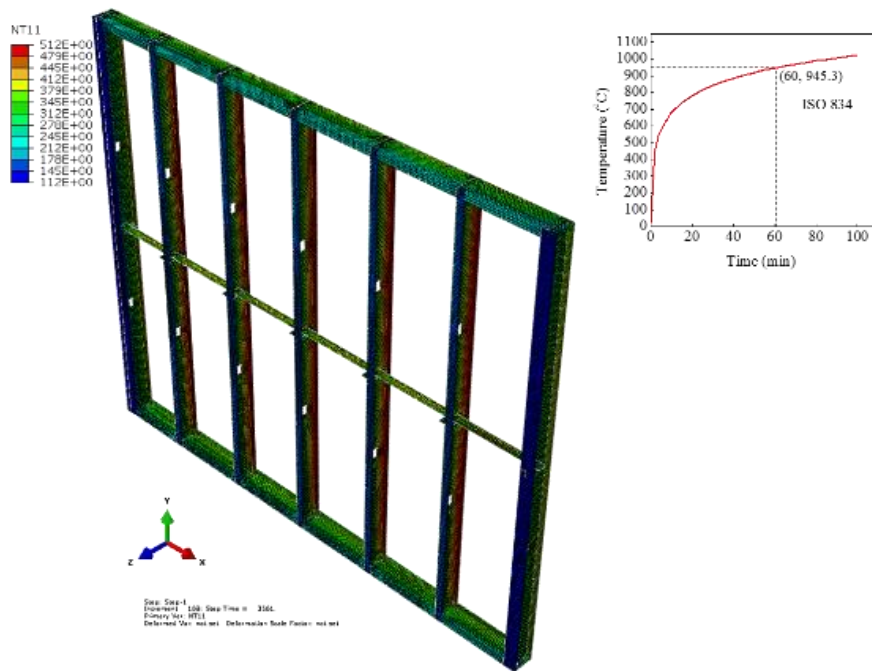


Figure 5.28. Temperature distribution within CFS frames at 60 minutes

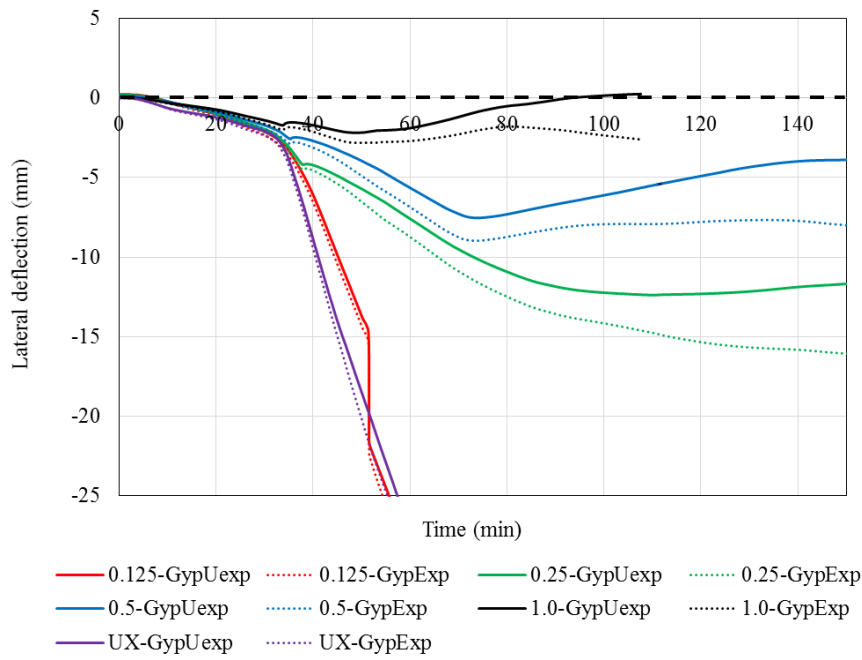
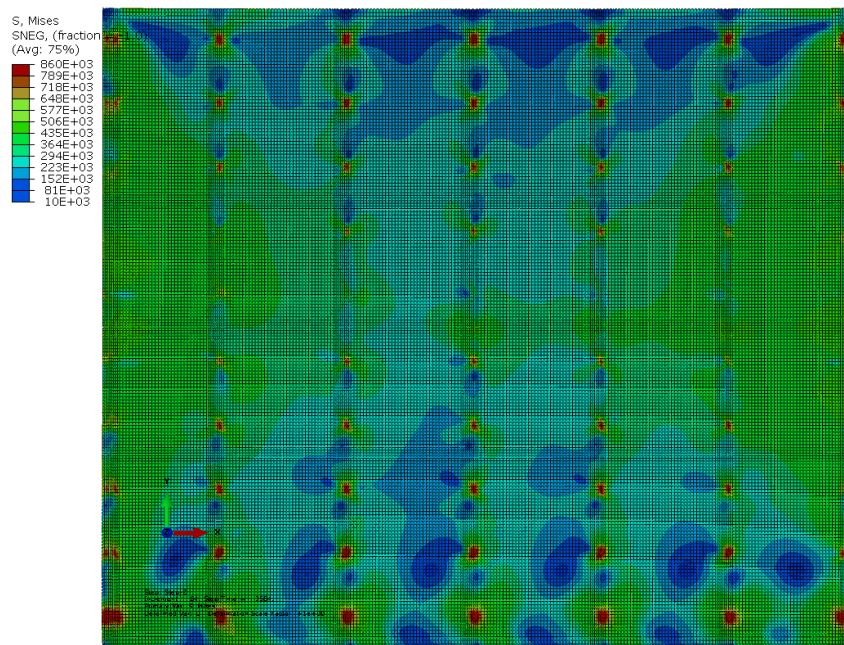
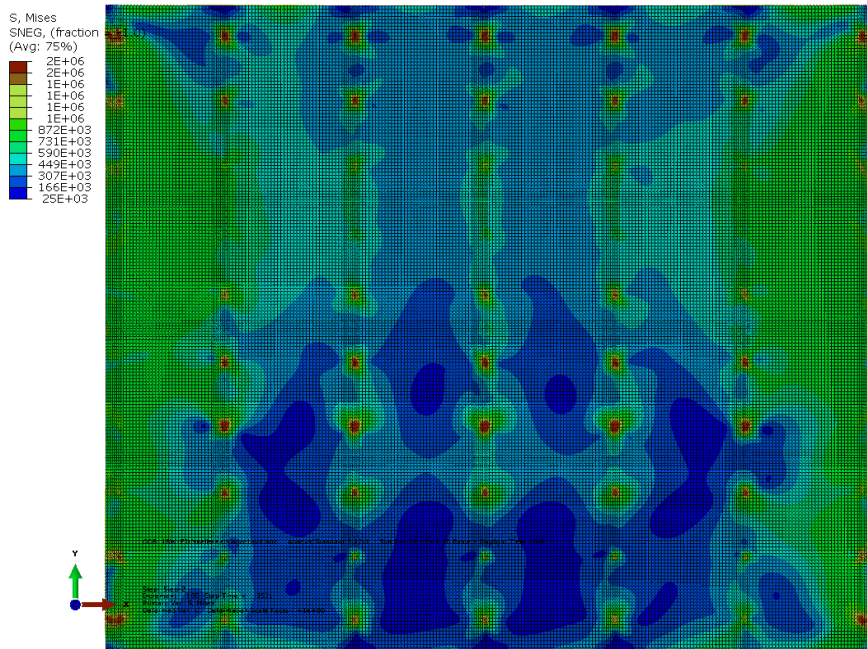


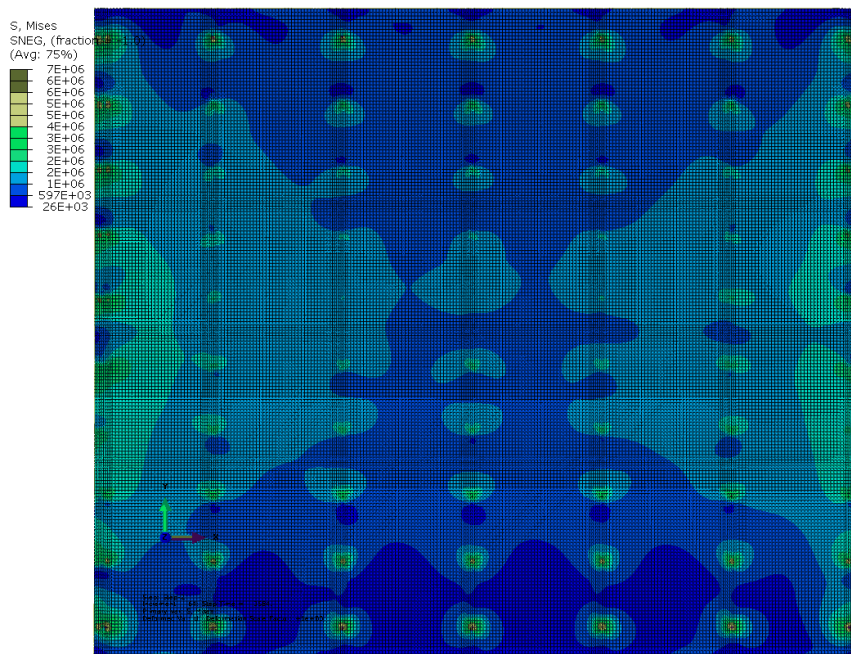
Figure 5.29. Out-of-plane deformation (UZ) versus time (min) curve



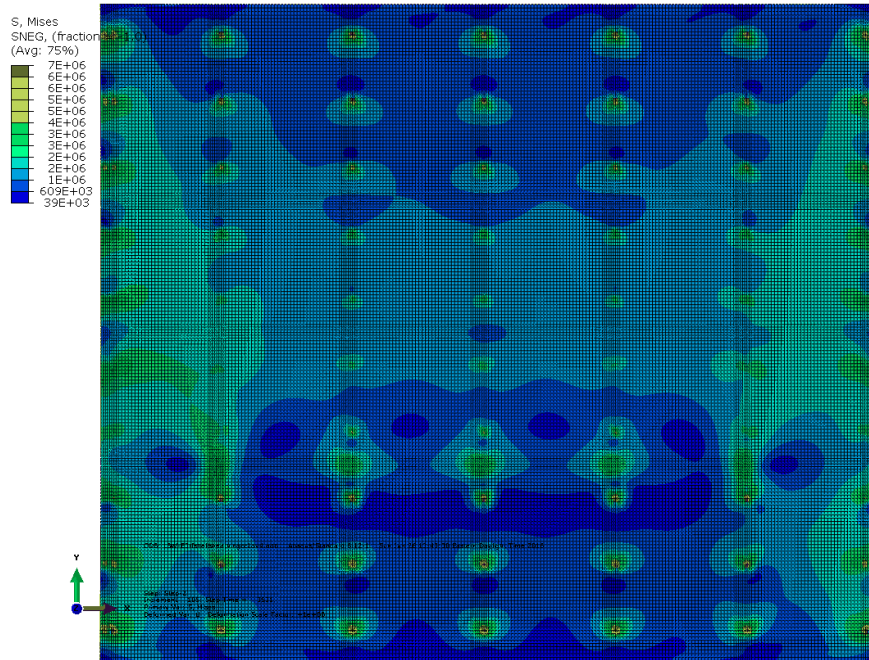
(a) GypExp ($f_{y-Exp} = 0.125 f_{y-Uexp}$)



(b) GypExp ($f_{y-Exp}=0.25f_{y-Uexp}$)



(c) GypUexp ($f_{y-Exp}=0.125f_{y-Uexp}$)



(d) GypUexp ($f_{y-Exp}=0.25f_{y-Uexp}$)

Figure 5.30. Stress distributions within gypsum boards at 60 minutes

As shown in Figure 5.28, temperature distributions are non-uniform through the wall cross sections and along the length of web-perforated CFS studs, inducing bending in the studs due to effects of neutral axis shifting and thermal bowing. Plotted in Figure 5.29 is the relationship between the lateral deflection (UZ), that is, out-of-plane deformation and exposing time in minute at mid-height on both sides of the wall for the cases ($f_{y-Exp}=0.125, 0.25, 0.5$ and $1.0f_{y-Uexp}$). The lateral deflection of stud flange on the fire-exposed side is greater than that on the fire-unexposed side for each case. As the increase of temperature, the difference of the lateral deflections between the two flanges increase except for the case ($f_{y-Exp}=0.125f_{y-Uexp}$) because of early failure of the wall assembly. Also observed from Figure 5.29, the magnitude of mechanical property on the fire-exposed side, i.e., E_{y-Exp} , has the considerable effect on the out-of-plane deformation of the wall which can be critical to the fire performance of the wall. Taking the case of CFS wall with $f_{y-Exp}=0.125f_{y-Uexp}$ and $E_{y-Exp}=0.125E_{y-Uexp}$, the lateral deflection reaches 8.3 mm at about 43.1 minutes, which is $L/360$ (L =wall height). Then, the lateral deflection further increases to 25 mm at 55.5 minutes, which reaches the limit of $L/120$. For CFS walls with gypsum board finishes, the deflection limit of $L/360$ is normally used for preventing cracking at ambient temperature in practice. Therefore, in this case cracking of the gypsum boards may already occur as early as at 43.1 minute.

Once cracks developed in the sheathing, the fire may penetrate from the fire-exposed side to the fire-unexposed side, the failure of the wall can system be imminent. It is also observed the lateral deflection of the case without directly modelling sheathing (i.e., CFS wall frame model) in stress analysis and case $f_{y-Exp}=0.125f_{y-Uexp}$ and $E_{y-Exp}=0.125E_{y-Uexp}$ are similar and they are considerably different from that of other cases, which illustrates that the effect of sheathing is not realistically simulated in the CFS wall frame model.

Shown in Figure 5.30 are the stress distributions within the gypsum boards on the fire-exposed side (GypExp) and unexposed side (GypExp) at 60 minutes. In the horizontal direction, the stress on the left and right sides of the sheathing are higher than that at the central region. This is because the wall is similar to a four edges simply-supported one-way plate subjected to a uniformly distributed load in which the left and right sides are experienced the larger curvature gradients. Additionally, from Figure 5.30, due to the stiffness of the wall system in the transverse direction of the studs is considerably less than that of the longitudinal direction, the stress with the sheathing is higher in the region near buckling failure than that in the other regions on the fire-exposed side due to large deformation of CFS studs, whereas the stress has a small difference on the fire-unexposed side.

5.7 Conclusions

A sequentially uncoupled 3D FE thermal-stress analysis is proposed for evaluating the performance of load-bearing CFS walls with C-shape web-perforated studs subjected to the standard fire. The predicted temperature profiles and the failure time are compared with the tests. It can be concluded in the following:

- Simulating CFS wall fire tests using a single stud model is acceptable. The difference in the failure time predicted by the single stud model and seven fire tests is within 11%. The nodal temperature obtained from the heat transfer analysis is critical to the structural response.
- Modelling the load-bearing fire wall tests using CFS wall frame can obtained the system-level response; however, the failure criteria are yet to be determined. From the FEA results obtained from the CFS wall frame model, it is found that the middle few studs may bear higher loads than that applied to a single stud and then there are stiffness and force interactions among the CFS wall studs. Consequently, the single stud model may overestimate the failure time. Thus, the stiffness and force interactions should be considered in FEA in order to achieve better accuracy.

- For laterally braced CFS walls, modelling the restraint provided by sheathing by restraining in-plane lateral displacement is acceptable in case no credible mechanical properties of specific sheathing materials at elevated temperature. However, in case the mechanical properties are available, modelling the sheathing using shell element provides more realistic prediction on the structural response demonstrated in load-bearing wall fire tests. The interaction of force and stiffness among wall studs found in CFS wall frame model are verified by the CFS wall system model. Moreover, the failure time cannot be identified in the CFS wall system model.

Chapter 6 Extended Design Method Based on AISI S100

6.1 Introduction

Presented in this chapter is a design method to account for the effect of web perforation length on the fire resistance of studs in load-bearing CFS walls. At elevated temperature, CFS wall studs are subjected to combined compression and bending. Design calculations should check both cross sections at the mid-height and at the support of the column. At the mid-height of the column, the bending moment about the major axis (x-x) is a result of the thermal bowing, neutral axis shift and magnification effect ($P-\Delta$ effect). At the support, the bending moment about the strong axis is caused by a neutral axis shift only. In previous studies, investigation of the effect of web perforations on the ultimate strength and failure time of CFS studs at non-uniform temperature is very limited.

The following are included in this chapter:

- Investigating the effect of web perforation on the ultimate strength of studs using FEA;
- Determining an applicable and simple non-uniform cross-sectional temperature distribution for CFS studs with web-perforated studs for design purposes;
- Proposing a design method based on AISI S100 (2012) that accounts for the effect of web perforation;
- Presenting a design example;
- Comparing results between extended design method and FEA.

6.2 Parametric study

A parametric study has been performed to investigate the effect of web perforation length on the ultimate strength of CFS studs with web perforations in walls subjected to standard fire from one side. The temperature distribution of CFS wall studs are obtained from heat transfer analysis based on a 600 mm wide CFS wall segment. The segment is sheathed by double layers of 12 mm MgO board on both sides, and fully insulated by 150 mm thick glass fibre in the cavity. The development of the heat transfer model and structural model are similar to those in sections 3.4 and 5.4, respectively. The material properties, including thermal and mechanical properties are the same as in sections 5.3.2 and 5.4.1.

6.2.1 Parameters of single CFS stud model

The parameters adopted in this FE study are:

- Stud section: C-shape section (150×40×15×1.5);
- Length of studs: 3000 mm;
- Web perforations: three web perforations spaced 600 mm o.c. along the stud length;
 $d_h=38$ mm, $L_h = 0, 75, 114, 130, 250, \text{ and } 380$ mm;
- Screw spacing: 300 mm o.c.;
- Applied axial load: varying from 12 kN to 82 kN

6.2.2 Results and discussions

Shown in Figure 6.1 are the cross-sectional temperature profiles of studs with varying perforation lengths. The effect of web perforation length on the temperature profiles is consistent with that discussed in section 4.4.2. Small temperature variations exist within the flange and lip on both hot and cold sides, but can be assumed to be uniform. The temperature distributions of cross-sections with web perforations are slightly higher on the hot side and lower on the cold side when compared with solid sections. As L_h increases, the temperature distribution on the cold side reduces slightly. Plotted in Figure 6.2 is the time dependent temperature curve of the flange-web junctions of the studs ($L_h=0$ mm). The temperature gradient within the stud cross section increases with the fire-exposure time.

Illustrated in Figure 6.3 and Figure 6.4 are the comparisons of the cross-sectional yield strength and elastic modulus for the stud ($L_h=0$ mm) at elevated temperatures, respectively. The symbols $F_{y,HF}$ and $F_{y,CF}$ are the yield strength of the hot flange and cold flange at elevated temperature; E_{HF} and E_{CF} are the elastic modulus of the hot flange and cold flange at elevated temperature.

Presented in Figure 6.5 is the fire-exposure time-applied load relationship predicted by the FEA. The detailed failure times corresponding to the applied axial load can be seen in Appendix B. At a given applied axial load, the failure time of studs decreases as L_h increases. For studs with $L_h=250$ and 380 mm, the drop in failure time is much larger when compared with the cases when $L_h \leq 130$ mm. For all the studs with varying L_h , as the applied load reduces, the difference in failure time caused by L_h drops gradually and eventually diminishes. For instance, when $0 \text{ mm} < L_h \leq 130 \text{ mm}$, the following can be drawn according to Figure 6.5:

First phase: $T_{HF} = 20\text{ }^{\circ}\text{C}$, $T_{CF} = 20\text{ }^{\circ}\text{C}$, there are no reductions in $F_{y,20}$ and E_{20} , and $e = 0$. The failure time of the stud depends on the compression strength at room temperature only.

Second phase: $T_{HF} > 20\text{ }^{\circ}\text{C}$, $T_{CF} = 20\text{ }^{\circ}\text{C}$, there are no reductions in $F_{y,20}$ and E_{20} , and $e = e_{AT} \neq 0$. The failure time of studs is dominated by compression; and failure occurs at the mid-height.

Third phase: $T_{HF} > 100\text{ }^{\circ}\text{C}$, $20\text{ }^{\circ}\text{C} < T_{CF} \leq 100\text{ }^{\circ}\text{C}$, there are reductions in $F_{y,HF}$ and E_{HF} and $e = (e_{AT} - e_{AE}) / \alpha_x$ where e_{AE} is small, e_{AT} dominates failure. Bending moment increases in the studs; the failure time of studs is dominated by compression; and failure occurs at the mid-height.

Fourth phase: $T_{HF} > 100\text{ }^{\circ}\text{C}$, $T_{CF} > 100\text{ }^{\circ}\text{C}$, there are reductions in $F_{y,HF}$, $F_{y,CF}$, E_{HF} and E_{CF} . $e = (e_{AT} - e_{AE}) / \alpha_x$ where e_{AT} and e_{AE} increased rapidly. Bending moment increases further in the studs. Below about 102 minutes' fire exposure, the effect of e_{AE} is beneficial; failure occurs at mid-height. After that, failure occurs at supports, and $F_{y,HF}$ and E_{HF} are relatively low when compared with E_{HF} and E_{CF} .

The symbols e is the eccentricity caused by thermal bowing (e_{AT}) and central axis shift (e_{AE}); α_x is the moment amplification factor related to e .

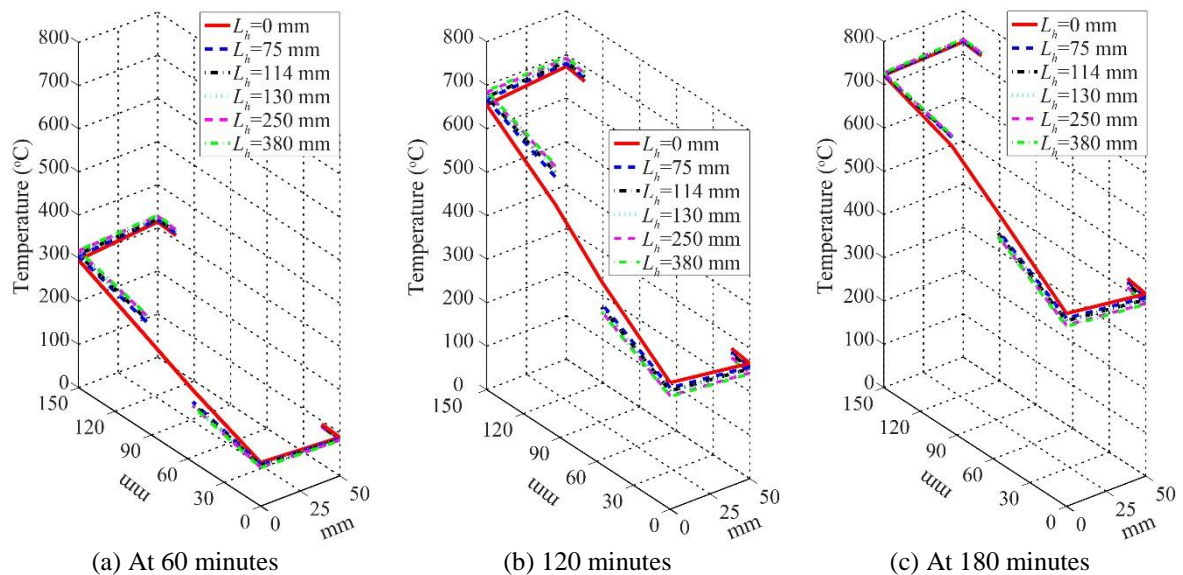


Figure 6.1 Cross-sectional temperature profiles of studs with different perforation lengths

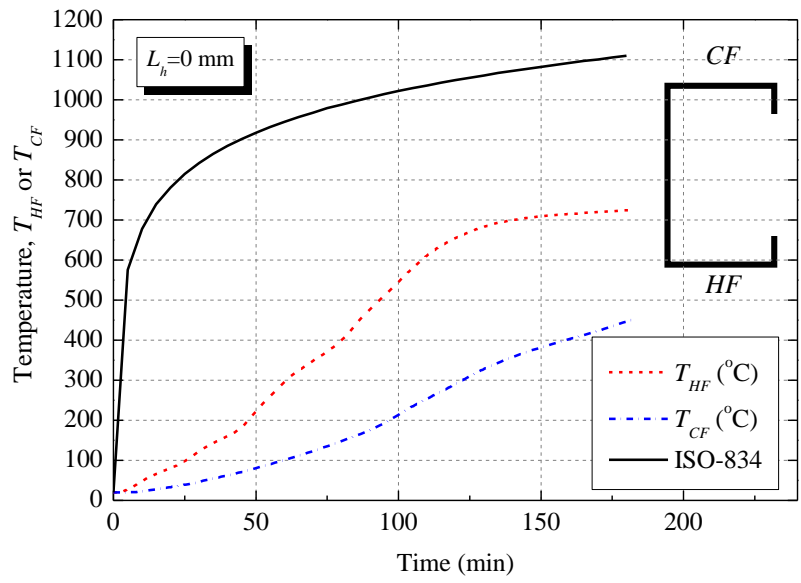


Figure 6.2 Time-temperature curve of stud flange-web junctions

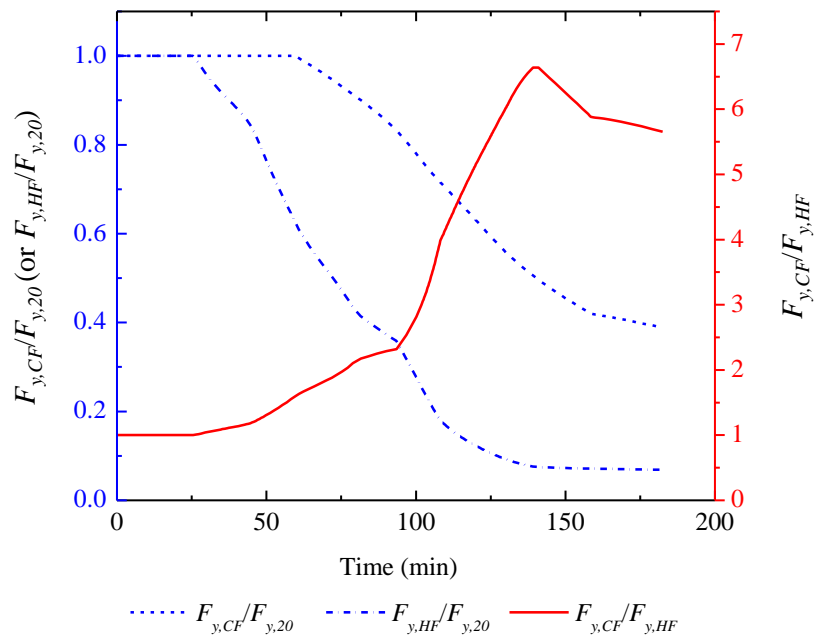


Figure 6.3 Comparison of normalized cross-sectional yield strength

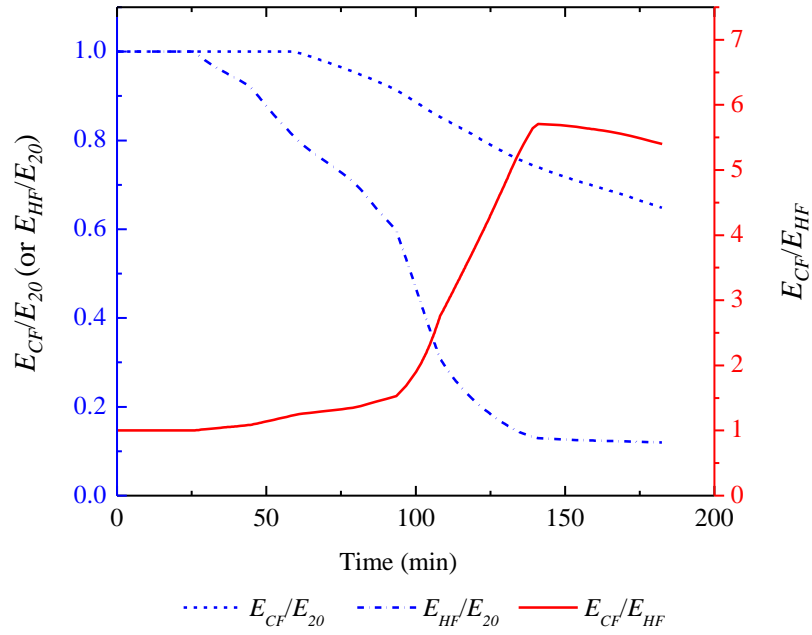


Figure 6.4 Comparison of normalized cross-sectional elastic modulus

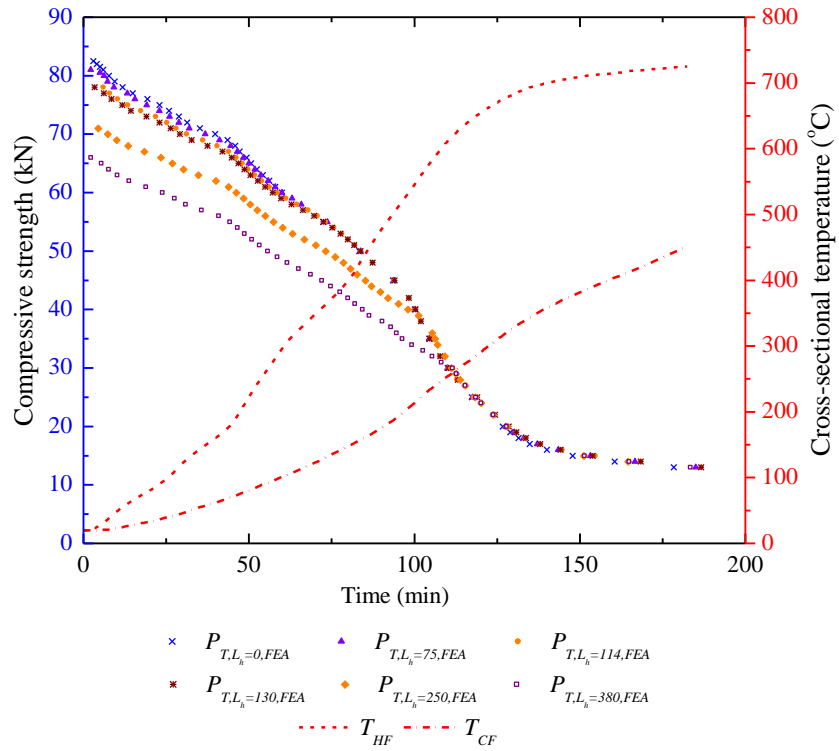


Figure 6.5 Failure time-applied load relationship predicted by FEA

6.3 Extended design equations based on AISI S100

6.3.1 Nominal axial strength

Using the same type of approach as in AISI S100 (2012) for cold-formed steel members at room temperature, the nominal axial strength, P_n , is calculated in accordance with Eq. (6.1).

$$P_n = A_e F_n \quad (6.1)$$

The symbol A_e is the effective area assuming uniform compression at elevated temperature and calculated at buckling stress F_n . The value A_e is the summation of the effective width of all compression elements calculated at buckling stress F_n , in accordance with Clauses B1 to B4. The average yield stress for each element at elevated temperature is used to calculate the effective width. For cross sections without web perforation, the web is considered as a uniformly compressed stiffened element, and the plate buckling coefficient, k , is taken to be 4 (Clause B2.1(a)). For cross sections with web perforation, the web is assumed to consist of two unstiffened strips A and B, adjacent to the perforations. The effective width of each unstiffened strip are determined in accordance with B2.1(a), except that plate buckling coefficient, k , is be taken to be 0.43, regardless of web perforation length. However, the presence of web perforations can either decrease or increase the critical buckling stress (El-Sawy & Nazmy, 2001; Komur & Sonmez, 2008; Maiorana, Pellegrino, & Modena, 2009). The influence of the length of web perforation and width of the unstiffened strip on k are accounted for in (Moen & Schafer, 2009). The value k_i for unstiffened strips A and B are approximated by Eqs. (6.2) and (6.3). The value k_i varies from 0.425 to 0.925. At a given unstiffened strip width, k increases as web perforation length decreases.

$$\text{for } L_n / h_i \geq 1, k_i = 0.425 + \frac{0.2}{(L_n / h_i)^{0.95} - 0.6} \quad (6.2)$$

$$\text{for } L_n / h_i < 1, k_i = 0.925, \text{ and } i = A \text{ or } B. \quad (6.3)$$

To better fit the FE results in section 6.2, Eq. (6.2) is modified as in Eq. (6.4).

$$\text{for } L_n / h_i \geq 1, k_i = 0.425 + \frac{0.2}{(L_n / (h_i - 2.5t))^{0.95} - 0.6} \quad (6.4)$$

where t is the thickness of the web.

Correspondingly, the effective width of the unstiffened strip on each side is calculated using Eq.(6.5).

$$d_{effi} = \rho h_i + 2.5t; \quad i = A \text{ or } B \quad (6.5)$$

The buckling stress F_n is calculated as below:

$$\text{For } \lambda_c \leq 1.5 \quad (6.6)$$

$$F_n = (0.658^{\lambda_c^2}) \bar{F}_{y,T} \quad (6.7)$$

$$\text{For } \lambda_c > 1.5 \quad (6.8)$$

$$F_n = \left[\frac{0.877}{\lambda_c^2} \right] \bar{F}_{y,T} \quad (6.9)$$

where

$$\lambda_c = \sqrt{\frac{\bar{F}_{y,T}}{F_e}} \quad (6.10)$$

F_e = minimum of flexural and flexural-torsional buckling stresses calculated in accordance with Clauses C4.1.1 and C4.1.2, using the weighted average mechanical properties ($\bar{F}_{y,T}$, \bar{E}_T and \bar{G}_T) at elevated temperatures.

$\bar{F}_{y,T}$ = weighted average yield stress of cross section at elevated temperature.

6.3.2 Nominal flexural strength

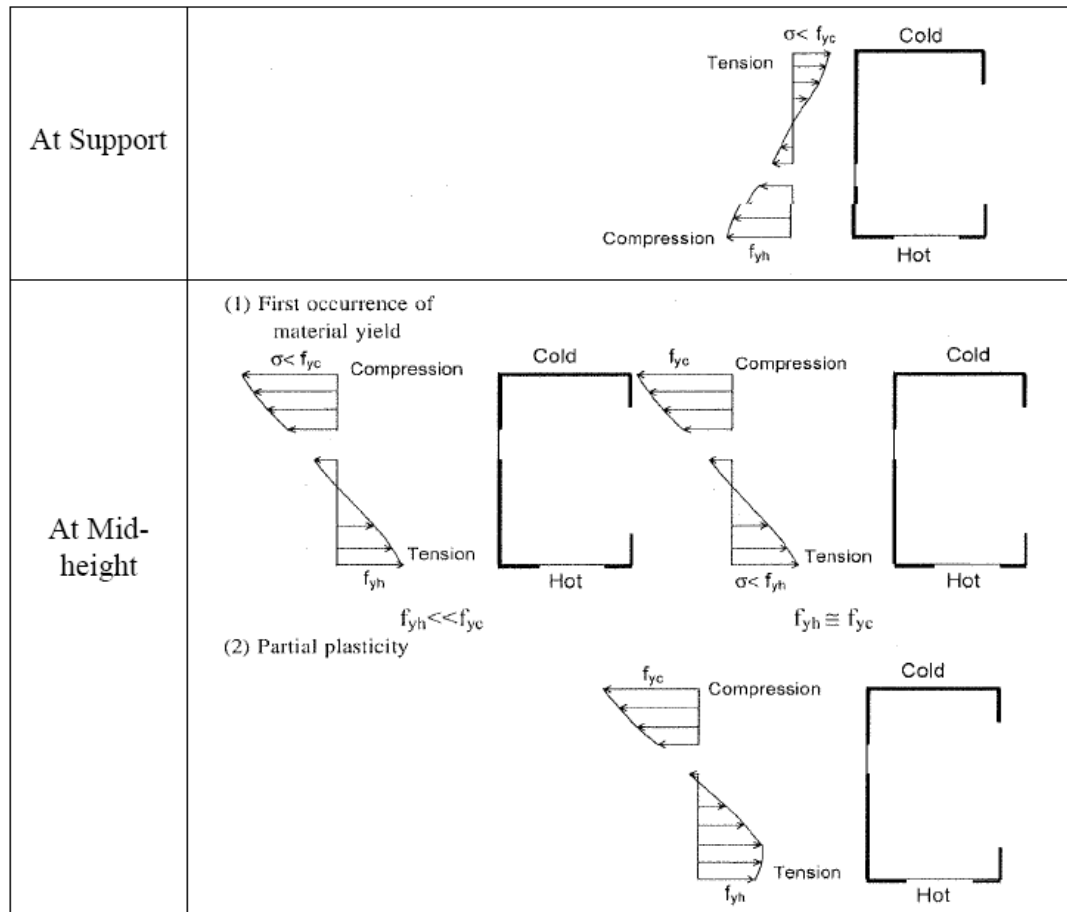
In accordance with Clause B2.4, C-Section webs with perforations under stress gradient at room temperature ignores the effect of L_h and only accounts for d_h/h (h =web depth). The effective width of web can be determined as below:

- When $d_h/h < 0.38$, the effective widths shall be determined in accordance with Section B2.3(a) by assuming no hole exists in the web.
- When $d_h/h \geq 0.38$, the effective width shall be determined in accordance with Clause B3.1(a), assuming the compression portion of the web consists of an unstiffened element adjacent to the hole.

However, at elevated temperature, the bending strength for a cross section with perforations is associated with both d_h and L_h . As discussed in section 6.2.2, for $L_h \leq 130$ mm, the effect of web perforation on the fire resistance of the CFS studs weakens as the cross-sectional temperature increases. At higher temperature, the bending moment caused by thermal bowing, central axis shift and magnification effect increase, which relatively reduces the weight of nominal axial strength. However, for $L_h = 250$ and 380 mm, the fire resistance is largely reduced by the presence of web perforations; thus, the effect of web perforation should be accounted for. In this study, the extended design equations deal with $L_h \leq 130$ mm only. To simplify calculations, the CFS cross section is assumed to be solid, neglecting the effect of web perforation.

The CFS wall studs are subjected to combined compression and bending at non-uniform elevated temperature. The effect on strength of bending moment about the minor axis (y-y axis) caused by neutral axis shift (e_{AE}) is small (Zhao et al., 2005), and ignored, as in (Klippstein, 1980; Gerlich et al., 1996; Ranby, 1999; Kaitila, 2002; Zhao et al., 2005, Gunalan, 2013). Thus, the bending moment about major axis (x-x axis) is considered only.

Table 6.1 Failure criteria for calculating nominal flexural strength (Feng & Wang, 2005)



Design calculations should check both cross sections. At the mid-height, compression is on the cold side. When calculating the moment strength of the cross section, partial plasticity is considered, as shown in Table 6.1 (Feng & Wang, 2005; Zhao et al., 2005). Yielding occurs on both flanges with bi-linear stress distribution in the web on the hot side. However, the calculation is very complicated because of the need to determine the stress distribution on the hot side. A simpler calculation method extended by (Gunalan, 2013) is used in this study, and the nominal moment strength, $M_{nx,eff}$, is calculated in accordance with Eq. (6.11) as follows:

$$M_{nx,eff} = \bar{S}_{eff,T} \bar{F}_{y,T} \quad (6.11)$$

At the supports, the hot flange is in compression whereby the first yield of the compression flange is adopted (Feng and Wang, 2005; Zhao et al., 2005; Gunalan, 2013). $M_{nx,eff}$ is calculated in accordance with Eq. (6.12) as follows:

$$M_{nx,eff} = \bar{S}_{eff,T} F_{y,HF} \quad (6.12)$$

where $\bar{F}_{y,T}$ is the weighted average yield stress of the cross section; $F_{y,HF}$ is the yield stress of the hot flange; and $\bar{S}_{eff,T}$ is the weighted elastic section modulus of the effective section calculated based on pure bending in accordance with Eq. (6.13), in which $\bar{I}_{eff,T}$ and y_{max} are the weighted average moment of inertia and maximum distance from the extreme fibre of the flange to the centroid of the cross section.

$$\bar{S}_{eff,T} = \frac{\bar{I}_{eff,T}}{y_{max}} \quad (6.13)$$

6.3.3 Combined compression and bending

At elevated temperature, the CFS wall studs are subjected to combined compression and bending. The bending moment about the major axis (x-x axis) is considered only. Based on AISI S100 (2012) for cold-formed steel structural members at room temperature, the required strengths (factored force and moments) \bar{P} and \bar{M}_x are determined using second-order analysis and must satisfy the following interaction Eq.(6.14):

$$\frac{\bar{P}}{\phi_c P_n} + \frac{C_{mx} \bar{M}_x}{\phi_b M_{nx,eff} \alpha_x} \leq 1.0 \quad (6.14)$$

where

\bar{P} = required compressive axial strength;

P_n = nominal axial resistance;

\bar{M}_x = required flexural strength with respect to centroidal axis;

$M_{nx,eff}$ = nominal flexural resistance about centroidal axis;

ϕ_c, ϕ_b = resistance factors whose values are taken to be 1 in this case;

α_x = moment amplification factor and can be calculated using $\alpha_x = 1 - \frac{\bar{P}}{P_{Ex}}$ at elevated temperature,

in which P_{Ex} is the elastic buckling load $P_{Ex} = \frac{\pi^2 EI_x}{(K_x L_x)^2}$, where I_x is the moment of inertia of full unreduced cross section about the x-x axis, L_x is the unbraced length for bending about x-axis, and K_x is the effective length factor for buckling about the x-x axis; and the detailed calculation for α_x can be seen in Appendix C;

C_{mx} is the coefficient for unequal end moments; for members whose ends are unrestrained, $C_{mx}=1.0$.

Design calculations should check both cross sections at the mid-height and at the support of the column. At the mid-height of the column, the bending moment about the major axis (x-x) is a result of the thermal bowing, neutral axis shift and magnification effect ($P-\Delta$ effect). At the supports, the bending moment about the strong axis is caused by a neutral axis shift only. The total moment strength \bar{M}_x , due to thermal bowing, neutral axis shift and their magnification effects, is given by Eqs. (6.15) and (6.16).

At the mid-height:
$$\bar{M}_x = \frac{C_{mx} \bar{P} e}{\alpha_x} = \frac{C_{mx} \bar{P} (e_{\Delta T} - e_{\Delta E})}{\left(1 - \frac{\bar{P}}{P_{Ex}}\right)} \quad (6.15)$$

At the supports:
$$\bar{M}_x = \frac{C_{mx} \bar{P} e}{\alpha_x} = \frac{C_{mx} \bar{P} e_{\Delta E}}{\left(1 - \frac{\bar{P}}{P_{Ex}}\right)} \quad (6.16)$$

where e is the total eccentricity due to neutral axis shift, thermal bowing and their magnification effects; $e_{\Delta E}$ is the neutral axis shift in the x-x axis, and $e_{\Delta T}$ is the thermal bowing at the mid-height (shown in Figure 6.6). For a simply supported column, $e_{\Delta T}$ is calculated in accordance with Eq.(6.17) as follows:

$$e_{\Delta T} = \frac{\alpha_s (T_{HF} - T_{CF}) L^2}{8b_w} \quad (6.17)$$

where L is the column length; T_{HF} and T_{CF} are the average temperatures of the hot and cold sides of the cross section, respectively; α_s is the thermal expansion coefficient of steel, taken as in Eurocode 3 Part 1.2 (2005); and b_w is the overall depth of the cross section.

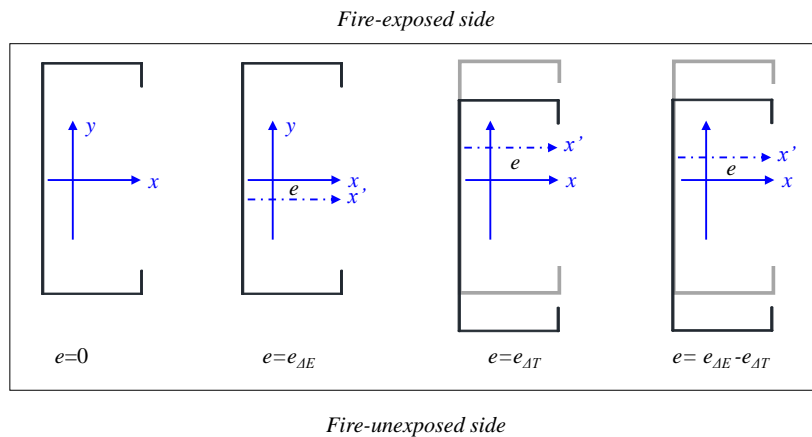
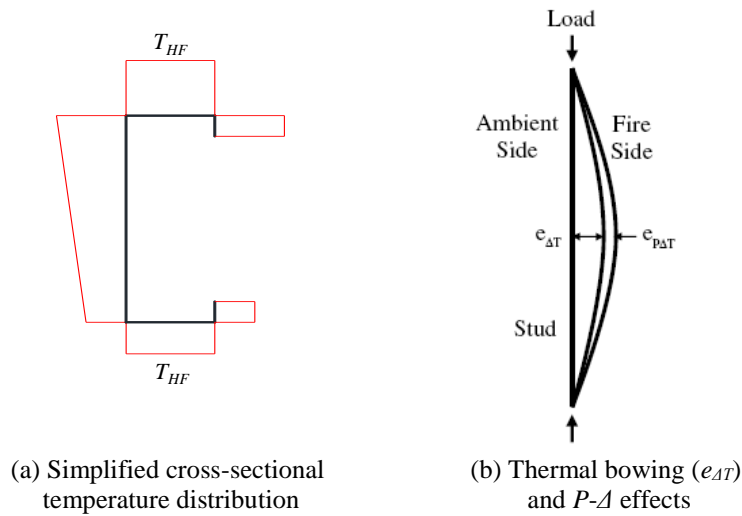


Figure 6.6 Neutral axis shift, thermal bowing and magnification effects

To simplify the calculation of the combined compression and bending, the cross-sectional elevated temperature distribution is shown in Figure 6.6(a), and is the same as in (Feng et al., 2003c; Gunalan & Mahendran, 2013; Kaitila, 2002).

6.4 Comparison of results between extended design method and FEA

When applying the extended calculation method, the compressive strength is calculated based on a given cross-sectional temperature distribution. This temperature distribution can be determined using the hot and cold flange temperatures of CFS studs without web perforations, obtained from heat transfer analysis. A detailed design example is presented in Appendix C, and detailed calculation results obtained from using the extended design method can be seen in Appendix D. Shown in Figure 6.7 is an example of the calculated axial strength of the studs at the mid-height and at the support, using the extended design method. The calculated axial strength equals the minimum of these two values. The intersection point in this figure separates the studs failing at the mid-height and at the support.

Shown in Figure 6.8 is a comparison of the interaction of compression and bending for the studs obtained using the extended design method. $\bar{P} / P_n - L_h = i$ is the ratio of the calculated ultimate axial strength over the nominal compression strength for the studs with $L_h = i$ mm, $i = 0, 75, 114$ and 130 mm; and $(\bar{M}_x / \alpha_x) / M_{nx,eff} - L_h = i$ is the ratio of calculated ultimate flexural strength, considering magnification effects, over the nominal flexural strength for studs with $L_h = i$ mm. The trend for the interaction of compression and bending is consistent with that discussed in section 6.2.2. The effect of web perforation length on the calculated ultimate strength also agrees well with that predicted by the FEA, as shown in Figure 6.5.

Presented in Figure 6.9 are the stud normalized compressive strengths calculated using the extended design method with the applied axial loads used in the FEA to obtain the stud failure times. The symbols $\bar{P}_{T,L_h=i,proposed}$ and $\bar{P}_{T,L_h=i,FEA}$ represent the calculated nominal axial strength or the applied axial load in the FEA for studs without or with web perforations ($i = 0, 75, 114$ and 130 mm) at 20°C or elevated temperature. $\bar{P}_{20,L_h=0,AISI}$ is the nominal axial strength of the studs without web perforations at 20°C , calculated using AISI S100 (2012). $\bar{P}_{20,L_h=0,AISI} (= 73.1N)$ is about 9% times lower than $\bar{P}_{20,L_h=0,FEA} (= 82.7N)$, since the former has included the effect of initial geometric imperfection, eccentricity, residual stress, etc. Thus, the calculated or predicted axial strength is normalized using $\bar{P}_{20,L_h=0,AISI}$ and $\bar{P}_{20,L_h=0,FEA}$, respectively. By doing this, the trends for calculated and predicted results are comparable. By accounting for the reduction caused by web perforation length in the extended method, the calculated ultimate strength for studs with perforations is always lower than that for studs

without web perforations. For design purposes, this level of accuracy is considered acceptable by accounting for the complexity of the problem being dealt with and the simplicity of the extended design method.

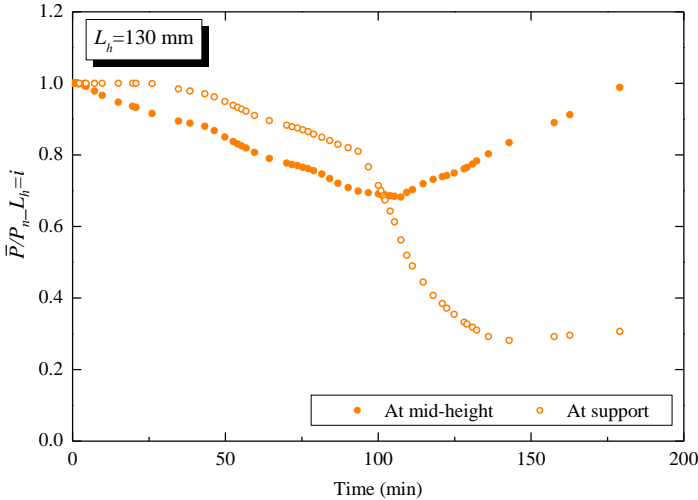


Figure 6.7 Calculated ultimate compression strength at mid-height and at support

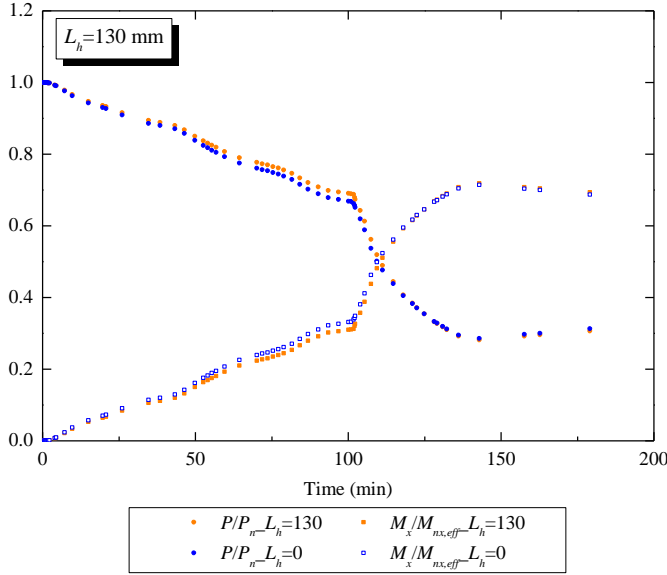


Figure 6.8 Comparison of interaction of compression and bending

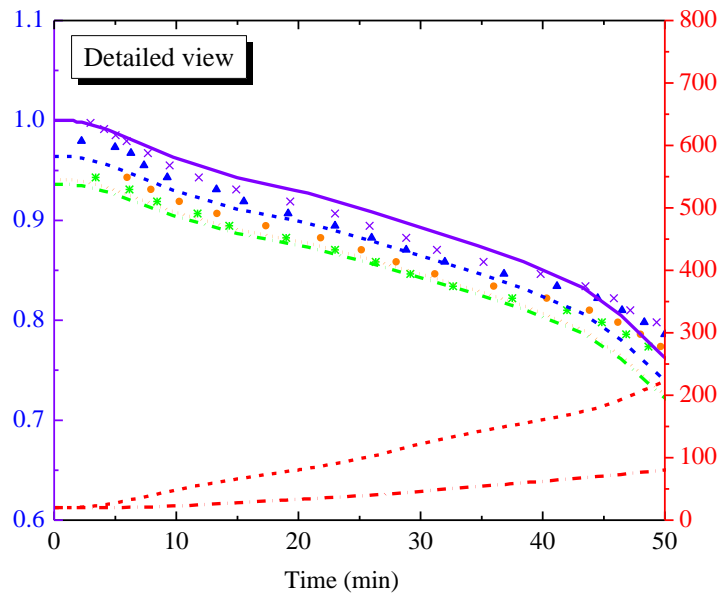
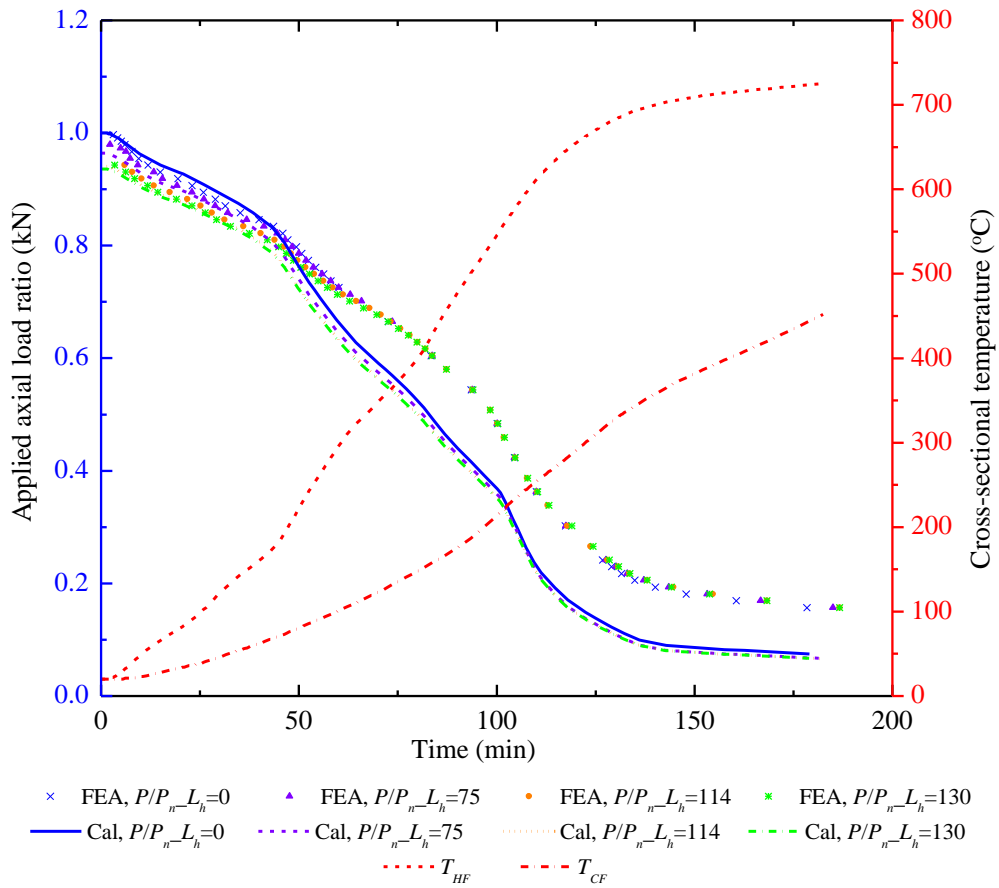


Figure 6.9 Comparison of axial strength based on extended design method

6.5 Conclusions

In this chapter, a design method is extended based on AISI S100 (2012) to evaluate the ultimate strength for CFS studs in walls subjected to standard fire. Conclusions can be drawn as follows:

- The reduction caused by web perforation length is accounted for in the extended method, which ensures that the calculated ultimate strength for studs with perforations is always lower than that for studs without web perforations. A plate buckling coefficient, accounting for the web perforation length and width is introduced to characterize the nominal axial strength. The effect of web perforation on the nominal flexural bending at elevated temperature is ignored, as is consistent with AISI S100 (2012) at room temperature. The accuracy is acceptable considering the complexity of the problem being dealt with and the simplicity of the calculation.
- In the extended design equations, the limit of web perforation length is extended from the 114 mm, specified in AISI S100 at room temperature, to 130 mm at non-uniform cross-sectional elevated temperature. For $L_h \leq 130$ mm, the non-uniform cross-sectional temperature distribution of studs can be adopted as the case of studs without web perforations. The temperature in the stud web can be assumed to be linear and to have the same slope for the unstiffened strips on both hot and cold sides. For L_h larger than 250 mm, the effect of web perforation on the ultimate strength of studs at elevated temperature is amplified when compared with that for studs with $L_h \leq 130$ mm.

Chapter 7 Conclusions and Future Research

7.1 Conclusions

Cold-formed steel (CFS) load-bearing wall systems are commonly constructed with CFS studs, have a CFS track connecting their top and bottom, and are lined with one or two layers of sheathing on both sides. In practice, the CFS studs are perforated in the web to install intermediate braces, or to allow the passage of electrical, plumbing, and heating service. With the growing interest in performance-based fire safety design, coupled with the costly and time consuming nature of full-scale testing, engineering professionals and researchers are increasingly exploring validated fire resistance models and simple design equations. Several contributions have been made in this study:

7.1.1 Web-perforated CFS C-shape studs at ambient and elevated temperatures

The behaviour of CFS C-shape stub columns at both ambient, uniform and non-uniform elevated temperatures have been investigated.

The effects of web perforations on the failure mode and ultimate strength of CFS C-shape stub columns were investigated at ambient temperature. The results show that a web perforation length of less than 130 mm has negligible effect on the ultimate compressive strength. Thus, the limitation on the length of web perforations not to exceed 114 mm stated in the effective width method in AISI-S100 (2012) may be extended to 130 mm. Additionally, the DSM approach in AISI S100 (2012) accurately assesses the compressive strength of the stub column specimens.

- Finite element structural models for web-perforated CFS C-shape columns at ambient and uniform elevated temperature (22 °C to 700 °C) have been developed, with validity of this model validated by stub columns tests. A parametric study of CFS C-shape slender columns with non-uniform cross-sectional temperatures distribution found that the length of web perforations has small effect on failure time.

7.1.2 Finite element thermal modelling and analysis

Heat transfer analysis has been conducted to investigate the thermal performance of CFS walls with web-perforated CFS studs under standard fire. Both cavity insulated and non-insulated CFS walls were considered. The extended 3D finite element thermal models were validated using data from full-scale fire tests. Unlike 1D and 2D models adopted by previous studies, the 3D models can simulate the temperature variation within the stud cross section and along the stud length caused by web perforations.

- For non-insulated CFS walls, web perforations in the CFS studs have negligible influence on the temperature distribution through the cross sections and along the stud length. The heat transfer within the cavity dominates by radiation, far outweighing that by conduction, and is blocked by web perforations.
- For insulated CFS walls with web perforations, the temperature distribution is no longer linear but almost bilinear along the web depth. The largest temperature gradient in the CFS studs occurs at the cross section located in the center of the web perforation along the stud length. The larger temperature gradient may induce local bending around web perforations, which can be detrimental to the stability of the studs and integrity of the CFS walls. Therefore, it may be non-conservative to neglect the web perforations in CFS wall studs when evaluating wall performance at elevated temperature.

7.1.3 Finite element structural modelling and analysis

A sequentially uncoupled 3D FE thermal-stress analysis has been extended for evaluating the performance of load-bearing CFS walls with C-shape web-perforated studs subjected to the standard fire.

- Simulating CFS wall fire tests using a single stud model is acceptable. The difference in the failure time predicted by the single stud model and seven fire tests is within 11%. The nodal temperature obtained from the heat transfer analysis is critical to the structural response. Modelling the load-bearing fire wall tests using a CFS wall frame can obtain a system-level response; however, the failure criteria are yet to be determined. From the FEA results obtained from the CFS wall frame model, it is found that the middle few studs may bear much higher loads than that applied to a single stud, due to stiffness and force interactions among the CFS

wall studs. Consequently, the single stud model may overestimate the failure time. Thus, stiffness and force interactions should be considered in FEA so as to achieve better accuracy. For laterally braced CFS walls, modelling the restraint provided by sheathing by restraining in-plane lateral displacement is acceptable, if no credible mechanical properties exist for specific sheathing materials at elevated temperature. However, if the mechanical properties are available, modelling the sheathing using shell element provides more realistic prediction of the structural response demonstrated in load-bearing wall fire tests. The interaction of force and stiffness among wall studs found in the CFS wall frame model have been verified by the CFS wall system model. The failure time cannot be identified in this model.

7.1.4 Extended design method based on AISI S100

Design calculations should check both cross sections at mid-height and at supports of the column. At the mid-height of the column, the bending moment about the major axis (x-x) is a result of the thermal bowing, neutral axis shift and magnification effect ($P-\Delta$ effect). At the support, the bending moment about the strong axis is caused by neutral axis shift only.

- A parametric study using FEA is conducted to investigate the effect of web perforation on the ultimate strength of studs. The effect of web perforations longer than 250 mm on the ultimate strength of studs at elevated temperature is amplified when compared with that for studs of $L_h \leq 130$ mm.
- For design purposes, when $L_h \leq 130$ mm, the non-uniform cross-sectional temperature distribution of studs can be adopted, just as in the case of studs without web perforations. The temperature in the stud web can be assumed to be linear and have the same slope for the unstiffened strips on both hot and cold sides.
- The reduction caused by web perforation length is accounted for in the extended method, which ensures that the calculated ultimate strength for studs with perforations is always lower than that for studs without web perforations. A design method has been extended based on the effective width method in AISI S100 (2012) to evaluate the ultimate strength of CFS studs in walls subjected to standard fire. A plate buckling coefficient, associated with web perforation length and width, has been introduced to characterize the nominal axial strength. The effect of web perforation on the nominal flexural bending at elevated temperature is ignored, an approach consistent with that stipulated in AISI S100 (2012) at room temperature. The accuracy is

acceptable considering the complexity of the problem being dealt with and the simplicity of the calculation. In the extended design equations, the limit of web perforation length is extended from 114 mm, specified in AISI S100 at room temperature, to 130 mm at non-uniform cross-sectional elevated temperature.

7.2 Future research

Several interesting future research topics arose from the experiments, sequentially uncoupled finite element thermal-stress analysis, and design method extended in this thesis. The major points for future study, organized by research topic, are listed below.

Web-perforated CFS C-shape studs at ambient and elevated temperatures (Chapter 3)

- Conducting experimental studies of web-perforated C-shape studs at uniform and non-uniform elevated temperatures to study their structural responses.

Thermal modelling and analysis (Chapter 4)

- Improving the accuracy of heat transfer analysis by quantifying the thermal properties of sheathing materials, i.e., gypsum board (Type X and Type C) and MgO board via lab testing;
- Improving accuracy by simulating the effect of screws, sheathing joints, gypsum board cracking and spalling on temperature distributions of CFS walls;
- Investigating how a variety of web perforation sizes (widths, lengths), shapes, arrangements, etc., in CFS studs affect the structural performance of load-bearing CFS walls;
- Developing a simplified numerical heat transfer model to predict the cross-sectional temperature distribution of studs in CFS walls for engineering practice.

Finite element structural modelling and analysis (Chapter 5)

- Performing additional validation of the CFS wall stud model, CFS wall frame model and CFS wall system model using academically oriented full-scale fire tests on load-bearing CFS walls with web-perforated studs;
- Determining the failure criteria of the CFS wall frame model and CFS wall system model by further investigating the stiffness and force interactions among the CFS wall studs;
- Improving the accuracy of the CFS wall system model by quantifying the mechanical properties of sheathing materials, i.e., gypsum board (Type X and Type C) and MgO board via lab testing;
- Improving the accuracy of the CFS wall system model by modelling the effects of screws, sheathing joints, gypsum board cracking and spalling, and boundary conditions between loading beam and top track on the structural response of CFS walls;
- Investigating how a variety of web perforation sizes (widths, lengths), shapes, arrangements, etc., in CFS studs affect the structural performance of load-bearing CFS walls.

Extended design method based on AISI S100 (Chapter 6)

- Validating the extended design method in this study with a variety of full-scale fire test results;
- Extending the extended design method to account for a variety of web perforation sizes, both by width and length;
- Incorporating a coefficient into the extended equations by considering how stiffness and force interactions among the CFS wall studs affect the ultimate strength and failure time of CFS walls;
- Proposing a design method based on DSM approach, in addition to EWM method in this study, for CFS studs with non-uniform cross-sectional elevated temperature distribution.

Bibliography

- ABAQUS (2012). *ABAQUS/standard (Version 6.12 ed.)*, ABAQUS Inc., <http://www.simulia.com/>, Providence, RI.
- AISI-S100. (2012). *North American Specification for the Design of Cold-formed Steel Structural Members*, American Iron and Steel Institute, Washington, D.C., United States.
- Alfawakhiri, F. (2002). *Behaviour of cold-formed-steel-framed walls and floors in standard fire resistance tests* (Doctoral dissertation), Carleton University, Ottawa, Canada.
- Alfawakhiri, F., Sultan, M. A., & MacKinnon, D. H. (1999). Fire resistance of loadbearing steel-stud walls protected with gypsum board: A review. *Fire Technology*, 35(4), 308-335.
- Abreu, J. C. B., Vieira, L. M., Abu-Hamd, M. H., & Schafer, B. W. (2014). Review: Development of performance-based fire design for cold-formed steel. *Fire Science Reviews*, 3(1).
- AS 1530.4. (2005). *Methods for fire tests on building materials, components and structures. Part 4: Fire-resistance test of elements of construction*, Australian Standard, Sydney, Australia.
- BS EN 1993-1-2. (2005). *Design of steel structures - Part 1-2: General rules - Structural fire design*, European Committee for Standardization, Brussels, Belgium.
- Chen, W., Ye, J., Bai, Y., & Zhao, X. L. (2013). Thermal and mechanical modeling of load-bearing cold-formed steel wall systems in fire. *Journal of Structural Engineering*, 140(8), A4013002-1-A4013002-13.

- Chen, W., Ye, J., Bai, Y., & Zhao, X. (2012). Full-scale fire experiments on load-bearing cold-formed steel walls lined with different panels. *Journal of Constructional Steel Research*, 79, 242-254.
- Clancy, P. (1999). *Time and probability of failure of timber framed walls in fire* (Doctoral dissertation), Victoria University of Technology, Melbourne, Australia.
- Collier, P. (1996). A model for predicting the fire-resisting performance of small-scale cavity walls in realistic fires. *Fire Technology*, 32(2), 120-136.
- El-Sawy, K. M., & Nazmy, A. S. (2001). Effect of aspect ratio on the elastic buckling of uniaxially loaded plates with eccentric holes. *Thin-Walled Structures*, 39(12), 983-998.
- Feng, M., Wang, Y. C., & Davies, J. M. (2003a). Structural behaviour of cold-formed thin-walled short steel channel columns at elevated temperatures. Part 2: Design calculations and numerical analysis. *Thin-Walled Structures*, 41(6), 571-594.
- Feng, M., Wang, Y. C., & Davies, J. M. (2003b). Thermal performance of cold-formed thin-walled steel panel systems in fire. *Fire Safety Journal*, 38(4), 365-394.
- Feng, M., Wang, Y. C., & Davies, J. M. (2003c). Axial strength of cold-formed thin-walled steel channels under non-uniform temperatures in fire. *Fire Safety Journal*, 38(8), 679-707.
- Feng, M., Wang, Y., & Davies, J. (2003d). Structural behaviour of cold-formed thin-walled short steel channel columns at elevated temperatures. Part 1: Experiments. *Thin-Walled Structures*, 41(6), 543-570.

- Feng, M., Wang, Y. C., & Davies, J. M. (2004). A numerical imperfection sensitivity study of cold-formed thin-walled tubular steel columns at uniform elevated temperatures. *Thin-Walled Structures*, 42(4), 533-555.
- Feng, M., & Wang, Y. C. (2005). An analysis of the structural behaviour of axially loaded full-scale cold-formed thin-walled steel structural panels tested under fire conditions. *Thin-Walled Structures*, 43(2), 291-332.
- GB/T228. (2010). *Metallic materials. Tensile testing. Part 1: Method of test at room temperature*, Standardization Administration of the People's Republic of China, Beijing, China.
- Gerlich, J. T., Collier, P. C. R., & Buchanan, A. H. (1996). Design of light steel-framed walls for fire resistance. *Fire and Materials*, 20(2), 79-96.
- Gunalan, S., & Mahendran, M. (2013). Finite element modelling of load bearing cold-formed steel wall systems under fire conditions. *Engineering Structures*, 56, 1007-1027.
- Gunawan, L. (2011). *Numerical models to simulate the thermal performance of LSF wall panels* (Master's thesis), Queensland University of Technology, Brisbane, Australia.
- ISO 834-1 (1999). *Fire-resistance tests - Elements of building construction - Part 1: General requirements*, International Standard Organization.
- Kaitila, O. (2002). *Finite element modelling of cold-formed steel members at high temperatures* (Licentiate thesis), Helsinki University of Technology, Espoo, Finland.

- Keerthan, P., & Mahendran, M. (2012). Numerical modelling of non-load-bearing light gauge cold-formed steel frame walls under fire conditions. *Journal of Fire Sciences*, 0(0), 1-29.
- Keerthan, P., & Mahendran, M. (2013). Thermal performance of composite panels under fire conditions using numerical studies: Plasterboards, rockwool, glass fibre and cellulose insulations. *Fire Technology*, 49(2), 329-356.
- Klippstein, K. H. (1980). *Behavior of cold-formed steel studs in fire tests*, American Iron and Steel Institute, Washington, D.C., United States.
- Kodur, V. R., & Sultan, M. A. (2001). Factors governing fire resistance of loadbearing steel stud walls. *Proceedings of 5th AOSFST International Conference*, Newcastle, Australia, 1-2.
- Kolarkar, P. (2010). *Structural and thermal performance of cold-formed steel stud wall systems under fire conditions* (Doctoral dissertation), Queensland University of Technology, Brisbane, Australia.
- Komur, M. A., & Sonmez, M. (2008). Elastic buckling of rectangular plates under linearly varying in-plane normal load with a circular cutout. *Mechanics Research Communications*, 35(6), 361-371.
- Li, Z., & Schafer, B. (2010). Application of the finite strip method in cold-formed steel member design. *Journal of Constructional Steel Research*, 66(8), 971-980.
- Maiorana, E., Pellegrino, C., & Modena, C. (2009). Elastic stability of plates with circular and rectangular holes subjected to axial compression and bending moment. *Thin-Walled Structures*, 47(3), 241-255.

- Mecozzi, E., & Zhao, B. (2005). Development of stress-strain relationships of cold-formed lightweight steel at elevated temperatures. *Proceedings of the Eurosteel Conference*, Maastricht, The Netherlands, 41-49.
- Mehaffey, J., Cuerrier, P., & Carisse, G. (1994). A model for predicting heat transfer through gypsum-board/wood-stud walls exposed to fire. *Fire and Materials*, 18(5), 297-305.
- Moen, C. D., & Schafer, B. W. (2009). Elastic buckling of cold-formed steel columns and beams with holes. *Engineering Structures*, 31(12), 2812-2824.
- Ranby, A. (1999). *Structural fire design of thin walled steel sections* (Licentiate thesis), Lulea University of Technology, Stockholm, Sweden.
- Schafer, B., & Ádány, S. (2006). Buckling analysis of cold-formed steel members using CUFSM: Conventional and constrained finite strip methods. *Eighteenth International Specialty Conference on Cold-Formed Steel Structures*, Orlando, Florida, United States. 39-54.
- Shahbazian, A., & Wang, Y. C. (2011). Calculating the global buckling resistance of thin-walled steel members with uniform and non-uniform elevated temperatures under axial compression. *Thin-Walled Structures*, 49(11), 1415-1428.
- Shahbazian, A., & Wang, Y. C. (2013). A simplified approach for calculating temperatures in axially loaded cold-formed thin-walled steel studs in wall panel assemblies exposed to fire from one side. *Thin-Walled Structures*, 64, 60-72.
- Shahbazian, A., & Wang, Y. C. (2014). A fire resistance design method for thin-walled steel studs in wall panel constructions exposed to parametric fires. *Thin-Walled Structures*, 77, 67-76.

- Sultan, M. A. (1996). A model for predicting heat transfer through noninsulated unloaded steel-stud gypsum board wall assemblies exposed to fire. *Fire Technology*, 32(3), 239-259.
- Sultan, M. A., Alfawakhiri, F., & Benichou, N. (2001). A model for predicting heat transfer through insulated steel-stud wall assemblies exposed to fire. *Fire and Materials 2001 International Conference*, San Francisco, 495-506.
- Xu, L. (2011). *Internal report of W-IBS system load bearing wall fire test*, Worthington construction group, Cleveland, United States.
- Xu, L., Shi, Y., & Yang, S. (2014). Compressive Strength of Cold-formed Steel C-shape Columns with Slotted Holes. *Proceedings of 22nd Specialty Conference on Cold-Formed Steel Structures*, St Louis, United States.
- Yang, S., & Xu, L. (2016). 3D FEA of load-bearing cold-formed steel wall systems with web-perforated studs subjected to standard fire. *Proceeding of 9th International Conference on Structures in Fire*, Princeton, New Jersey, United States, 400-407.
- Yu, C., & Schafer, B. W. (2007). Effect of longitudinal stress gradients on elastic buckling of thin plates. *Journal of Engineering Mechanics*, 133(4), 452-463.
- Moen, C. D., & Schafer, B. W. (2009). Elastic buckling of thin plates with holes in compression or bending. *Thin-Walled Structures*, 47(12), 1597-1607.
- Zhao, B., Kruppa, J., Renaud, C., O'Connor, M., Mecozzi, E., Apiazu, W., . . . Salmi, P. (2005). *Calculation rules of lightweight steel sections in fire situations* (No. 21426), European Commission, Luxembourg.

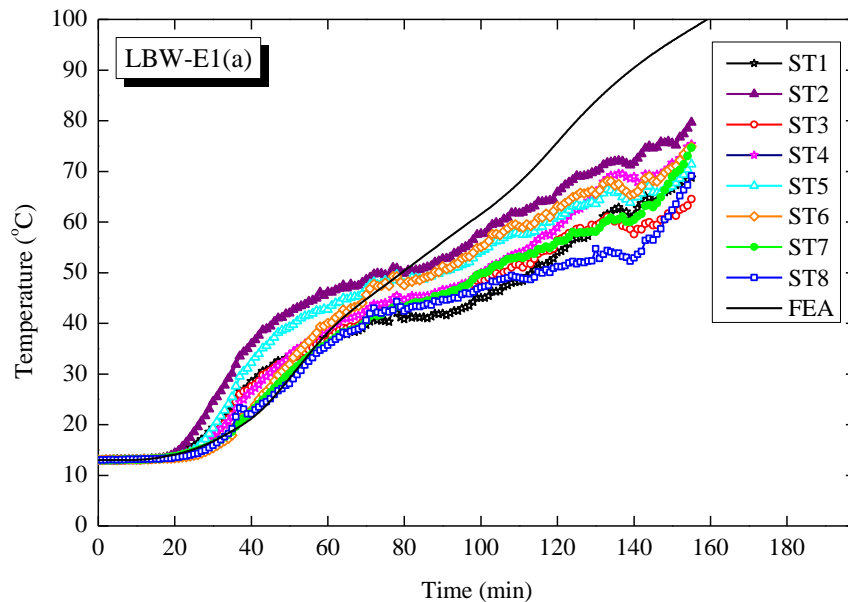
Appendices

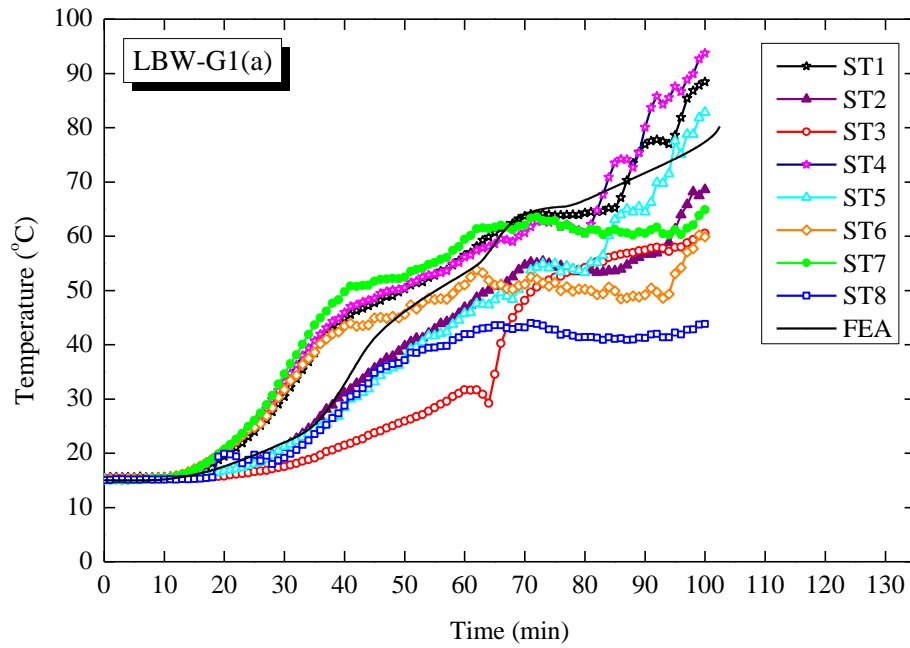
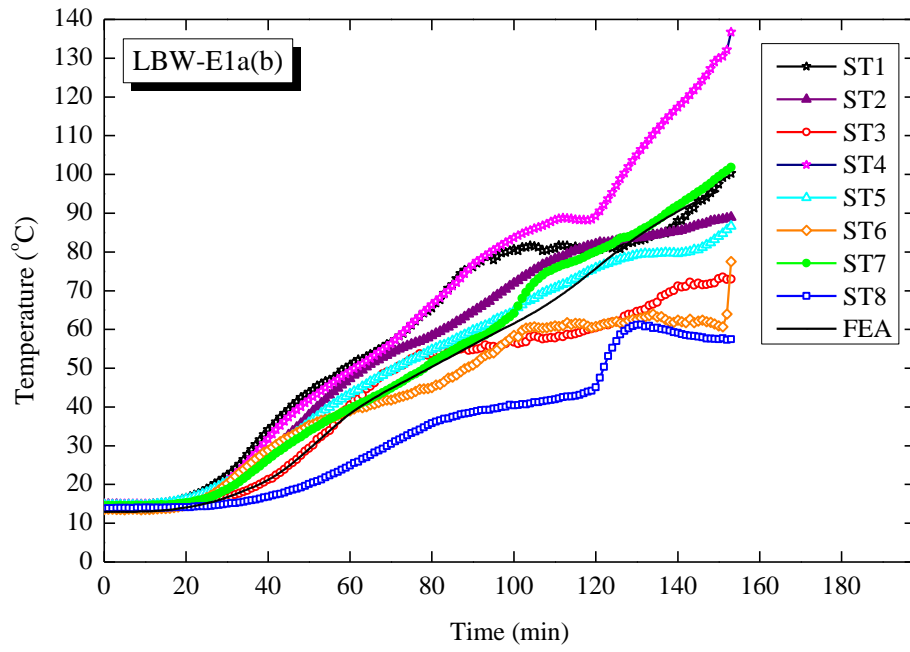
Appendix A Comparison of gypsum board surface temperature on the fire-unexposed side between FEA and full-scale fire tests

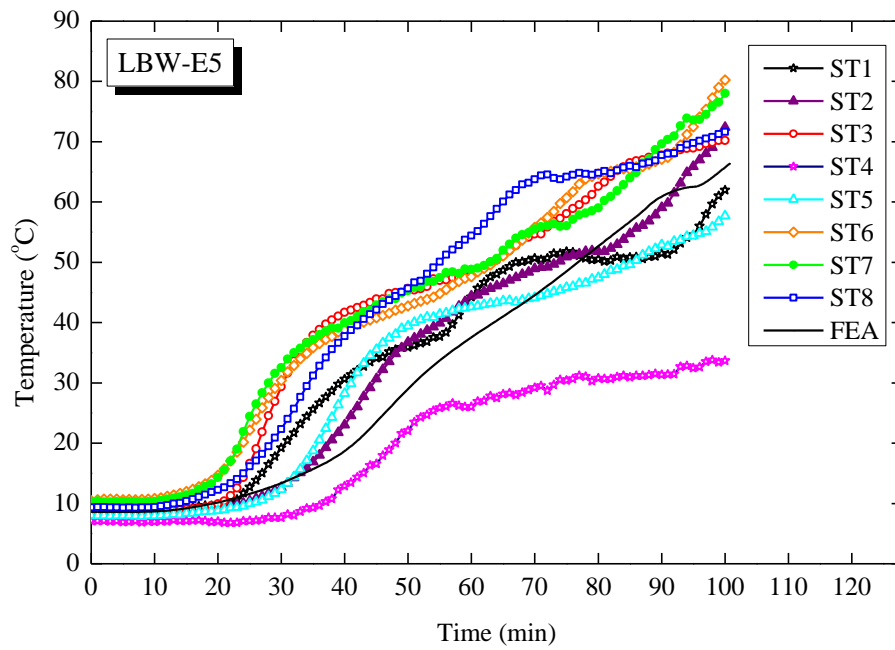
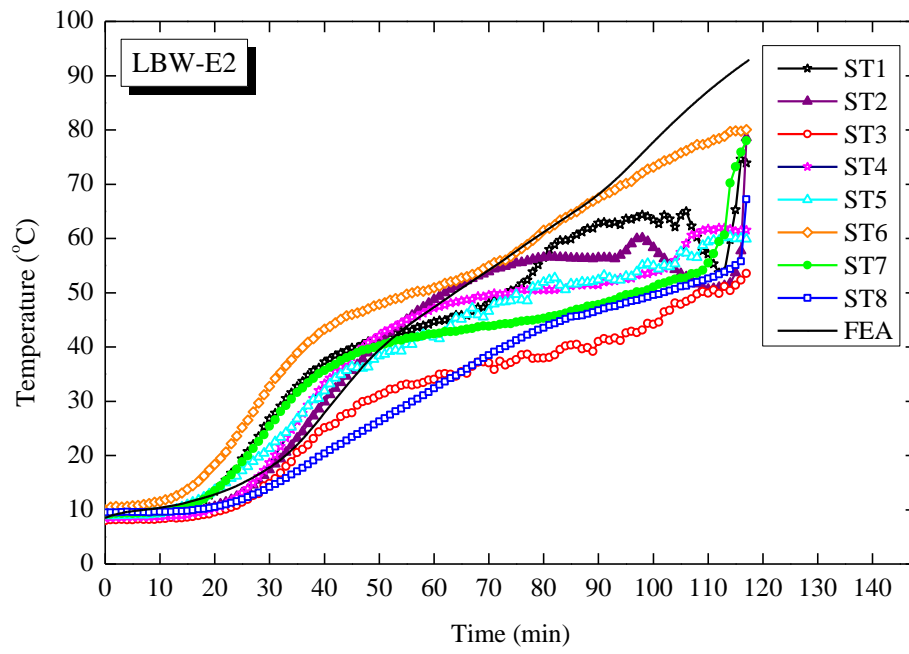
Presented in this Appendix is a comparison of time-dependent temperature profiles obtained from FEA and data measured during the fire tests conducted by (Xu, 2011). The numbers from 1 to 8 indicate the locations where thermocouples were placed throughout the test, as shown in Figure 5.2. The measured data by these thermocouples are named as ST1 to ST8 in the time-temperature curves below. The curve FEA represents the predicted average temperature of the sheathing surface on the fire-unexposed side.

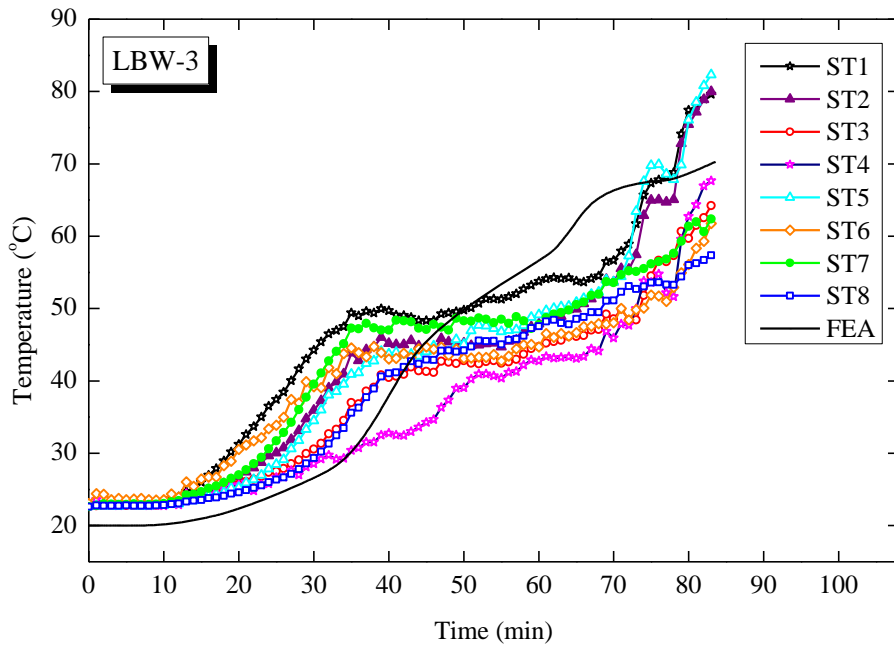
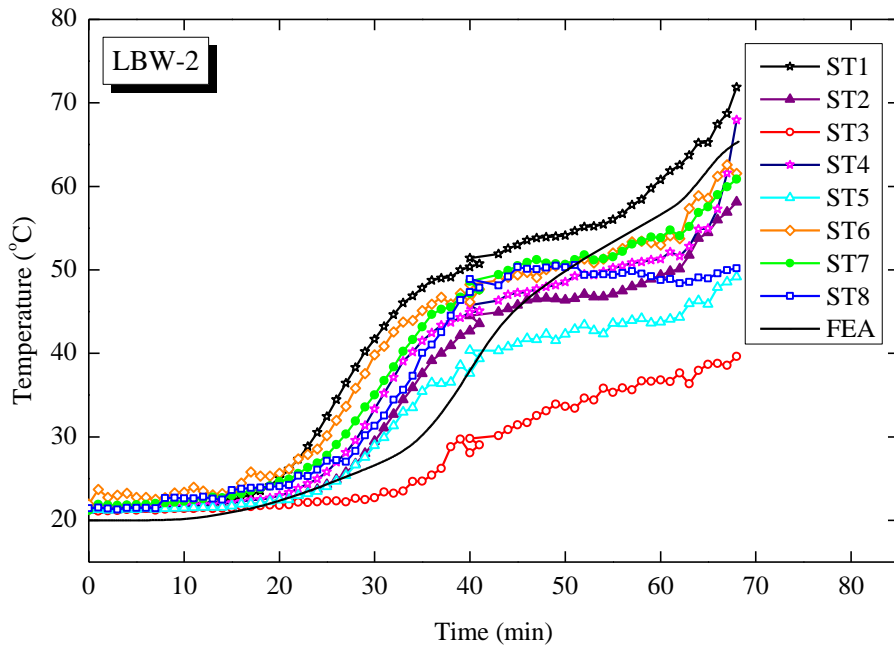


Figure 5.2. Experimental setup









Appendix B FEA results for parametric study (section 6.2)

Failure time (min)	Applied load $\bar{P}_{L_n=0mm}$ (kN)	$\frac{\bar{P}_{L_n=0mm}}{P_{FEA,20^\circ C, L_n=0mm}}$
3.0	82.5	0.997
4.1	82	0.991
5.0	81.5	0.985
5.9	81	0.979
7.7	80	0.967
9.5	79	0.955
11.9	78	0.943
14.9	77	0.931
19.3	76	0.919
23.0	75	0.907
25.8	74	0.895
28.8	73	0.883
31.3	72	0.870
35.2	71	0.858
39.8	70	0.846
43.5	69	0.834
45.8	68	0.822
47.2	67	0.810
49.3	66	0.798
50.7	65	0.786
52.3	64	0.774
54.2	63	0.762
56.2	62	0.750
58.0	61	0.737
60.0	60	0.725
72.5	55	0.665
83.3	50	0.605
93.5	45	0.544
100.2	40	0.484
104.5	35	0.423
110.0	30	0.363
117.3	25	0.302
126.7	20	0.242

Failure time (min)	Applied load $\bar{P}_{L_n=75mm}$ (kN)	$\frac{\bar{P}_{L_n=75mm}}{P_{FEA,20^\circ C, L_n=0mm}}$
2.2	81	0.979
5.0	80.5	0.973
6.3	80	0.967
7.4	79	0.955
9.3	78	0.943
13.3	77	0.931
15.5	76	0.919
19.2	75	0.907
23.0	74	0.895
26.0	73	0.883
28.8	72	0.870
32.0	71	0.858
36.8	70	0.846
41.2	69	0.834
44.5	68	0.822
46.5	67	0.810
48.3	66	0.798
50.0	65	0.786
51.8	64	0.774
53.7	63	0.762
55.8	62	0.750
58.0	61	0.737
60.0	60	0.725
63.0	59	0.713
65.8	58	0.701
73.7	55	0.665
83.7	50	0.605
93.8	45	0.544
100.2	40	0.484
104.5	35	0.423
110.0	30	0.363
117.5	25	0.302
127.7	20	0.242

129.0	19	0.230
131.5	18	0.218
134.8	17	0.206
140.0	16	0.193
147.8	15	0.181
160.5	14	0.169
178.3	13	0.157

130.2	19	0.230
133.0	18	0.218
137.2	17	0.206
143.5	16	0.193
153.2	15	0.181
166.7	14	0.169
185.0	13	0.157

Failure time (min)	Applied load $\bar{P}_{L_h=114mm}$ (kN)	$\frac{\bar{P}_{L_h=114mm}}{P_{FEA,20^\circ C, L_h=0mm}}$
3.0	82.5	0.997
4.1	82	0.991
5.0	81.5	0.985
5.9	81	0.979
7.7	80	0.967
9.5	79	0.955
11.9	78	0.943
14.9	77	0.931
19.3	76	0.919
23.0	75	0.907
25.8	74	0.895
28.8	73	0.883
31.3	72	0.870
35.2	71	0.858
39.8	70	0.846
43.5	69	0.834
45.8	68	0.822
47.2	67	0.810
49.3	66	0.798
50.7	65	0.786
52.3	64	0.774
54.2	63	0.762
56.2	62	0.750
58.0	61	0.737
60.0	60	0.725
72.5	55	0.665

Time (min)	Applied load $\bar{P}_{L_h=130mm}$ (kN)	$\frac{\bar{P}_{L_h=130mm}}{P_{FEA,20^\circ C, L_h=0mm}}$
2.2	81	0.979
5.0	80.5	0.973
6.3	80	0.967
7.4	79	0.955
9.3	78	0.943
13.3	77	0.931
15.5	76	0.919
19.2	75	0.907
23.0	74	0.895
26.0	73	0.883
28.8	72	0.870
32.0	71	0.858
36.8	70	0.846
41.2	69	0.834
44.5	68	0.822
46.5	67	0.810
48.3	66	0.798
50.0	65	0.786
51.8	64	0.774
53.7	63	0.762
55.8	62	0.750
58.0	61	0.737
60.0	60	0.725
63.0	59	0.713
65.8	58	0.701
73.7	55	0.665

83.3	50	0.605	83.7	50	0.605
93.5	45	0.544	93.8	45	0.544
100.2	40	0.484	100.2	40	0.484
104.5	35	0.423	104.5	35	0.423
110.0	30	0.363	110.0	30	0.363
117.3	25	0.302	117.5	25	0.302
126.7	20	0.242	127.7	20	0.242
129.0	19	0.230	130.2	19	0.230
131.5	18	0.218	133.0	18	0.218
134.8	17	0.206	137.2	17	0.206
140.0	16	0.193	143.5	16	0.193
147.8	15	0.181	153.2	15	0.181
160.5	14	0.169	166.7	14	0.169
178.3	13	0.157	185.0	13	0.157

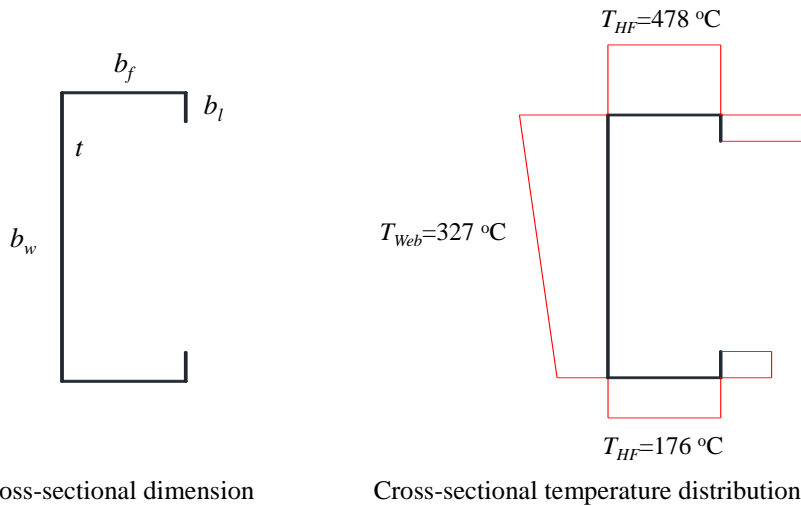
Failure time (min)	Applied load $\bar{P}_{L_n=250mm}$ (kN)	$\frac{\bar{P}_{L_n=250mm}}{P_{FEA,20^\circ C, L_n=0mm}}$
4.4	71	0.858
7.3	70	0.846
10.0	69	0.834
13.5	68	0.822
18.3	67	0.810
23.3	66	0.798
26.8	65	0.786
30.2	64	0.774
34.7	63	0.762
40.0	62	0.750
43.8	61	0.737
46.2	60	0.725
48.3	59	0.713
50.3	58	0.701
52.5	57	0.689
54.8	56	0.677
57.3	55	0.665
60.2	54	0.653
63.2	53	0.641

Failure time (min)	Applied load $\bar{P}_{L_n=380mm}$ (kN)	$\frac{\bar{P}_{L_n=380mm}}{P_{FEA,20^\circ C, L_n=0mm}}$
2.18	66	0.798
5.35	65	0.786
7.63	64	0.774
10.18	63	0.762
13.78	62	0.750
18.83	61	0.737
23.83	60	0.725
27.50	59	0.713
30.83	58	0.701
35.67	57	0.689
40.83	56	0.677
44.17	55	0.665
46.50	54	0.653
48.67	53	0.641
50.83	52	0.629
53.17	51	0.617
55.67	50	0.605
58.50	49	0.592
61.50	48	0.580

66.7	52	0.629
70.2	51	0.617
73.2	50	0.605
76.0	49	0.592
78.5	48	0.580
80.7	47	0.568
82.7	46	0.556
85.2	45	0.544
87.0	44	0.532
89.7	43	0.520
92.0	42	0.508
95.2	41	0.496
98.0	40	0.484
101.2	39	0.472
105.3	36	0.435
106.2	35	0.423
107.0	34	0.411
109.2	32	0.387
111.2	30	0.363
112.5	29	0.351
113.8	28	0.339
115.3	27	0.326
118.3	25	0.302
120.2	24	0.290
123.8	22	0.266
128.0	20	0.242
151.2	15	0.181
164.5	14	0.169
203.3	12	0.145

65.00	47	0.568
68.67	46	0.556
72.00	45	0.544
74.67	44	0.532
77.50	43	0.520
79.83	42	0.508
82.00	41	0.496
84.33	40	0.484
96.33	35	0.423
99.17	34	0.411
102.50	33	0.399
105.33	32	0.387
108.17	31	0.375
111.50	30	0.363
112.67	29	0.351
115.33	27	0.326
118.50	25	0.302
120.17	24	0.290
123.83	22	0.266
127.83	20	0.242
151.33	15	0.181
164.83	14	0.169
183.33	13	0.157

Appendix C Design example using proposed design method



Given:

1. Steel: $F_{y,20} = 345 \text{ N / mm}^2$; $E_{20} = 2.03 \times 10^5 \text{ N / mm}^2$ at room temperature

Eurocode 3 Part 1.2 (BS EN 1993-1-2, 2005) at elevated temperature

2. Section: C150×40×15×1.5

$$b_w = 148.5 \text{ mm}; b_f = 38.5 \text{ mm}; b_l = 14.25 \text{ mm}; t = 1.5 \text{ mm}$$

$$d_h = 38 \text{ mm}; L_h = 130 \text{ mm}; h_A = h_B = (b_w - d_h) / 2 = 55.25 \text{ mm}$$

3. Simply supported at ends, and concentrically loaded

$$4. K_x = K_y = K_t = 1.0; L_x = 3000 \text{ mm}; L_y = L_t = 300 \text{ mm}$$

5. Temperature distribution in the cross-section: $T_{CF} = 176^\circ \text{C}$; $T_{Web} = 327^\circ \text{C}$; $T_{HF} = 478^\circ \text{C}$

T_{CF} - cold flange temperature; T_{Web} - average web temperature; T_{HF} - hot flange temperature.

Required: calculate required applied load

1. Sectional properties of full section (using software CUFSM)

$$A_g = 381 \text{ mm}^2$$

$$I_x = 1239448.5 \text{ mm}^4$$

$$I_y = 81138.6 \text{ mm}^4$$

$$x_{cg} = 10.156 \text{ mm}$$

$$y_{cg} = 74.25 \text{ mm}$$

$$C_w = 371990314 \text{ mm}^6$$

$$J = 285.75 \text{ mm}^4$$

$$x_o = -27.276 \text{ mm}$$

$$y_o = 0.00 \text{ mm}$$

$$r_x = \sqrt{I_x / A_g} = 57.036 \text{ mm}$$

$$r_y = \sqrt{I_y / A_g} = 14.593 \text{ mm}$$

$$r_o = \sqrt{r_x^2 + r_y^2 + x_o^2 + y_o^2} = 64.885 \text{ mm}$$

$$F_{y,176} = 294.395 \text{ N / mm}^2; F_{y,327} = 193.507 \text{ N / mm}^2; F_{y,478} = 128.754 \text{ N / mm}^2$$

$$E_{176} = 187572 \text{ N / mm}^2; E_{327} = 156919 \text{ N / mm}^2; E_{478} = 126266 \text{ N / mm}^2$$

$$\bar{F}_{y,T} = (F_{y,176}(b_f + b_l)t + F_{y,327}b_w t + F_{y,478}(b_f + b_l)t) / A_g = 201.012 \text{ N / mm}^2$$

$$\bar{E}_T = (E_{176}(b_f + b_l)t + E_{327}b_w t + E_{478}(b_f + b_l)t) / A_g = 156919 \text{ N / mm}^2$$

$$\bar{G}_T = \frac{E_T}{2(1 + \mu)} = \frac{156919}{2(1 + 0.3)} = 60353.462 \text{ N / mm}^2$$

2. Nominal axial strength, P_n

a) Check flexural buckling.

$$\frac{K_x L_x}{r_x} = \frac{1.0(3000)}{57.04} = 52.598$$

$$\frac{K_y L_y}{r_y} = \frac{1.0(300)}{14.59} = 20.557$$

Since $\frac{K_y L_y}{r_y} > \frac{K_x L_x}{r_x}$, Euler buckling about the x axis will control.

$$F_e = \frac{\pi^2 \bar{E}_T}{(K_x L_x / r_x)^2} = \frac{\pi^2 (156919)}{((1.0)(3000)/(57.04))^2} = 559.804 \text{ N / mm}^2$$

b) Check flexural-torsional buckling.

$$F_e = \frac{1}{2\beta} \left[(\sigma_{ex} + \sigma_t) - \sqrt{(\sigma_{ex} + \sigma_t)^2 - 4\beta\sigma_{ex}\sigma_t} \right]$$

$$\beta = 1 - (x_o / r_o)^2 = 1 - (27.276 / 64.885)^2 = 0.823$$

$$\sigma_{ex} = \frac{\pi^2 \bar{E}_T}{(K_x L_x / r_x)^2} = \frac{\pi^2 (156919)}{((1.0)(3000)/(57.04))^2} = 559.804 \text{ N / mm}^2$$

$$\begin{aligned} \sigma_t &= \frac{1}{A_g r_o^2} \left[\bar{G}_T J + \frac{\pi^2 \bar{E}_T C_w}{(K_t L_t)^2} \right] \\ &= \frac{1}{(381)(64.885)^2} \left[(60353.462)(285.75) + \frac{\pi^2 (156919)(371990314)}{[(1.0)(300)]^2} \right] \\ &= 4001.440 \text{ N / mm}^2 \end{aligned}$$

$$\begin{aligned} F_e &= \frac{1}{(2)(0.823)} \left[(559.804 + 4001.444) - \sqrt{(559.804 + 4001.444)^2 - (4)(0.823)(559.804)(4001.444)} \right] \\ &= 544.640 \text{ N / mm}^2 \end{aligned}$$

c) Determine controlling buckling mode.

$544.640 \text{ N / mm}^2 < 559.804 \text{ N / mm}^2$, therefore flexural-torsional buckling governs

$$F_e = 544.640 \text{ N / mm}^2$$

$$\lambda_c = \sqrt{\frac{\bar{F}_{y,T}}{F_e}} = \sqrt{\frac{201.012}{544.640}} = 0.608 < 1.5; \text{ therefore,}$$

$$\begin{aligned} F_n &= (0.658^{\lambda_c^2}) \bar{F}_{y,T} \\ &= (0.658^{0.608^2}) (201.012) = 172.240 \text{ N / mm}^2 \end{aligned}$$

d) Compute effective area at $f = F_n = 172.240 \text{ N} / \text{mm}^2$

Hot flange: uniformly compressed element with an edge stiffener.

$$w = 38.5 \text{ mm}$$

$$w/t = 38.5/1.5 = 25.667$$

$$S = 1.28 \sqrt{E_{478} / f}$$

$$= 1.28 \sqrt{126266 / 172.240} = 34.657$$

therefore, $w/t \geq 0.328S \Rightarrow$ Check effective width of flange

Compute flange k based on stiffener lip properties

$$I_a = 399t^4 \left[\frac{w/t}{S} - 0.328 \right] 3 \leq t^4 \left[115 \frac{w/t}{S} + 5 \right]$$

$$= 399(1.5)^4 \left[\frac{38.5/1.5}{34.657} - 0.328 \right]^3 \leq (1.5)^4 \left[115 \left(\frac{38.5/1.5}{34.657} \right) + 5 \right]$$

$$= 141.880 \text{ mm}^4 < 456.480 \text{ mm}^4; \text{ therefore, } I_a = 141.880 \text{ mm}^4$$

$$d = 14.25 \text{ mm}$$

$$\theta = 90 \text{ degrees}$$

$$I_s = (d^3 t \sin^2 \theta) / 12$$

$$= (14.25)^3 (1.5) \sin^2(90^\circ) / 12 = 361.705 \text{ mm}^4$$

$$R_l = I_s / I_a \leq 1$$

$$= 361.705 / 141.880 = 2.549 > 1; \text{ therefore, } R_l = 1.0$$

$$D/w = 15 / 38.5 = 0.390$$

$0.25 < D/w \leq 0.8$; therefore,

$$k = \left(4.82 - \frac{5D}{w} \right) (R_l)^n + 0.43 \leq 4$$

$$= \left(4.82 - \frac{5(15)}{38.5} \right) (1.0)^n + 0.43 = 3.302 \leq 4 \text{ OK}$$

$$F_{cr} = k \frac{\pi^2 \bar{E}_{478}}{12(1-\mu^2)} \left(\frac{t}{w} \right)^2$$

$$= 3.302 \frac{\pi^2 (126266)}{12(1-0.3^2)} \left(\frac{1.5}{38.5} \right)^2 = 571.998 N / mm^2$$

$$\lambda = \sqrt{\frac{f}{F_{cr}}} = \sqrt{\frac{172.240}{571.998}} = 0.549 < 0.673; \text{ therefore, the flange is fully effective.}$$

$$b_{eff1,hf} = b_{eff2,hf} = \frac{38.5}{2} = 19.25 mm$$

Cold flange: the calculation is similar to that of hot flange, but replace E_{478} with E_{176} . The calculated values are listed below:

w	w/t	S	w/t-0.328S>0	d	D	I _a	R _t	k	F _{cr}	λ	ρ	b
38.5	25.667	42.240	11.812	14.25	15	44.168	1	3.302	849.721	0.450	1	38.5

$$b_{eff1,cf} = b_{eff2,cf} = \frac{38.5}{2} = 19.25 mm$$

Hot lip:

$$f = 172.240 N / mm^2$$

$$k = 0.43$$

$$F_{cr} = k \frac{\pi^2 E_{176}}{12(1-\mu^2)}$$

$$= 0.43 \frac{\pi^2 (187572)}{12(1-0.3^2)} \left(\frac{1.5}{14.25} \right)^2 = 543.732 N / mm^2$$

$$\lambda = \sqrt{\frac{f}{F_{cr}}} = \sqrt{\frac{172.240}{543.732}} = 0.563 < 0.673 \quad \therefore \text{ lip is fully effective.}$$

$$c_{eff,hf} = 14.25 mm$$

Cold lip: the calculation is similar to that for the hot flange, but E_{478} is replaced with E_{176} . The calculated values are listed below:

d	k	F_{cr}	λ	ρ	d_s'	d_s	$C_{eff,cf}$
14.25	0.43	807.730	0.462	1.0	14.25	14.25	14.25

Web with perforation:

$$L_h = 130mm; \quad d_h = 38mm$$

$i = A$ or B

$$h_i = \frac{148.5 - 38}{2} - 2.5(1.5) = 51.5mm$$

$$k_i = \begin{cases} 0.425 + \frac{0.2}{(L_h / h_i)^{0.95} - 0.6} & \text{if } L_h / h_i \geq 1 \\ 0.925 & \text{if } L_h / h_i < 1 \end{cases}$$

$$L_h / h_i = \frac{130}{51.5} = 2.524 \geq 1; \text{ therefore,}$$

$$k_i = 0.425 + \frac{0.2}{(2.524)^{0.95} - 0.6} = 0.535$$

$$\begin{aligned} F_{cri} &= k \frac{\pi^2 E_{327}}{12(1 - \mu^2)} \left(\frac{t}{w} \right)^2 \\ &= 0.535 \frac{\pi^2 (156919)}{12(1 - 0.3^2)} \left(\frac{1.5}{51.5} \right)^2 = 64.428 N / mm^2 \end{aligned}$$

$$\lambda = \sqrt{\frac{f}{F_{cri}}} = \sqrt{\frac{172.240}{64.428}} = 1.635 > 0.673$$

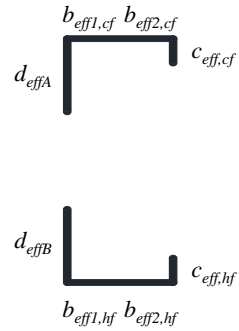
$$\begin{aligned} \rho &= (1 - 0.22 / \lambda) / \lambda \\ &= (1 - 0.22 / 1.635) / 1.635 = 0.529 \end{aligned}$$

$$d_{eff} = \rho h_i + 2.5t = 0.529(51.5) + 2.5(1.5) = 31.010mm$$

$$A_e = 224.21 \text{ mm}^2$$

Sum of the effective widths of the elements

Element	l (mm)
d_{effA}	31.010
d_{effB}	31.010
$b_{eff1,cf}$	19.25
$b_{eff1,hf}$	19.25
$b_{eff2,cf}$	19.25
$b_{eff2,hf}$	19.25
$c_{eff,cf}$	14.25
$c_{eff,hf}$	14.25
sum Σ	167.52



Effective area of pure compression member at elevated temperature A_e

$$A_e = t \Sigma l = 1.5(167.52) = 251.28 \text{ mm}^2$$

Nominal axial strength P_n

$$P_n = A_e F_n = 251.280(172.240) = 43280.145 \text{ N}$$

Thermal bowing $e_{\Delta T}$

Thermal expansion coefficient α_T

$$T_{avg} = 327^\circ C$$

$$\alpha_T = \begin{cases} 1.2 \times 10^{-5} + 0.8 \times 10^{-8}(T - 20) & 20^\circ C \leq T < 750^\circ C \\ 0 & 750^\circ C \leq T \leq 860^\circ C \\ 2 \times 10^{-5} & 860^\circ C < T < 1200^\circ C \end{cases}$$

$$= 1.446 \times 10^{-5} \quad (T = T_{avg})$$

$$e_{\Delta T} = \frac{\alpha_T (T_{HF} - T_{CF}) L^2}{8b_w}$$

$$= \frac{1.446 \times 10^{-5} (478 - 176) (3000)^2}{8(148.5)} = 33.074 mm$$

Neutral axis shift about the major axis $e_{\Delta E}$

$$\bar{Y}_{eff} = \left\{ \begin{array}{l} E_{176} c_{eff,cf} t (b_w - c_{eff,cf} / 2) + E_{176} b_{eff,2,cf} t b_w + E_{176} b_{eff,1,cf} t b_w \\ + E_{327} d_{eff,1} t (b_w - d_{eff,1} / 2) + E_{327} d_{eff,2} t d_{eff,2} / 2 \\ + E_{478} c_{eff,hf} t c_{eff,hf} / 2 \end{array} \right\} / (\bar{A}_e \bar{E}_T)$$

$$= \left\{ \begin{array}{l} (187572) 14.25 (1.5) (148.5 - 14.25 / 2) + (187572) 19.25 (1.5) 148.5 \\ + (187572) 19.25 (1.5) 148.5 + (156919) 31.010 (1.5) (148.5 - 31.010 / 2) \\ + (156919) 31.010 (1.5) 31.010 / 2 + (126266) 14.25 (1.5) 14.25 / 2 \end{array} \right\} / \{(224.21)(156919)\}$$

$$= 82.503 mm$$

$$e_{\Delta E} = \bar{Y}_{eff} - b_w / 2 = 82.503 - 148.5 / 2 = 8.253 mm$$

3. Nominal flexural strength, M_{nx}

The web perforation in the cross-section is not accounted for when calculating the effective widths under pure bending.

Effective area at elevated temperature for pure bending

Web: under stress gradient

$$f = F_n = 172.240 \text{ N} / \text{mm}^2$$

$$w = 148.5 \text{ mm}; \quad w / t = 148.5 / 1.5 = 99$$

$$\psi = 1$$

$$k = 4 + 2(1 + \psi)^3 + 2(1 + \psi) = 24$$

$$F_{cr} = k \frac{\pi^2 E_{Web}}{12(1 - \mu^2)} \left(\frac{t}{w} \right)^2 = 24 \frac{\pi^2 (156919)}{12(1 - 0.3^2)} \left(\frac{1.5}{148.5} \right)^2 = 347.291 \text{ N} / \text{mm}^2$$

$$\lambda = \sqrt{\frac{f}{F_{cr}}} = \sqrt{\frac{172.240}{347.291}} = 0.704 > 0.673$$

$$\begin{aligned} \rho &= (1 - 0.22 / \lambda) / \lambda \\ &= (1 - 0.22 / 0.704) / 0.704 = 0.976 \end{aligned}$$

$$b_e = \rho w = (0.976)(148.5) = 144.990 \text{ mm}$$

$$h_o / b_o = 150 / 40 = 3.750 < 4.0; \text{ therefore,}$$

$$b_1 = b_e / (3 + \psi) = 144.990 / (3 + 1) = 36.248 \text{ mm}$$

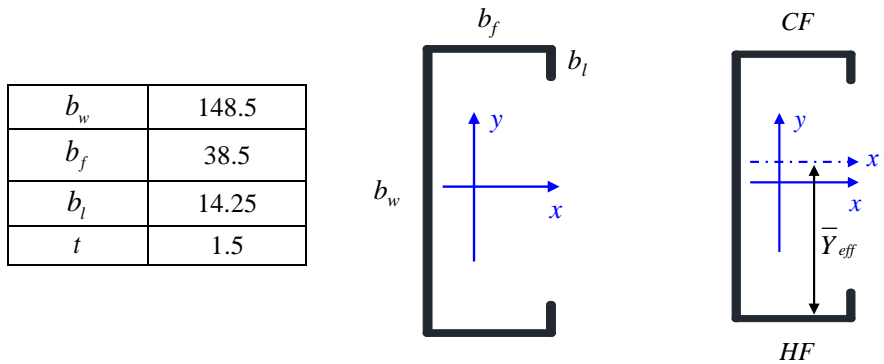
$$\text{for } \psi > 0.236, \quad b_2 = b_e / 2 = 144.990 / 2 = 72.496 \text{ mm}$$

$$b_1 + b_2 = 36.248 + 72.496 = 108.745 \text{ mm}$$

$> w / 2 = 74.250 \text{ mm}$; therefore, the web is fully effective.

Therefore,

- The web is fully effective in this case
- Effective flange and lip widths on the cold side are the same as under uniform compression (fully effective in this case)
- The flange and lip on the hot side are in tension (do not buckle)



$$\begin{aligned}\bar{A}_e &= \left\{ E_{478} t (b_f + b_l) + E_{327} t b_w + E_{176} t (b_f + b_l) \right\} / \bar{E}_T \\ &= \left\{ (126266)(1.5)(38.5 + 14.25) + (156919)(1.5)(148.5) + (187572)(1.5)(38.5 + 14.25) \right\} / 156919 \\ &= 381.000 \text{ mm}\end{aligned}$$

$$\begin{aligned}\bar{Y}_{eff} &= \left\{ \begin{aligned} &E_{176} b_l t (b_w - b_l / 2) + E_{176} b_f t b_w \\ &+ E_{327} b_w t (b_w / 2) + E_{478} b_l t (b_l / 2) \end{aligned} \right\} / (\bar{A}_e \bar{E}_T) \\ &= \left\{ \begin{aligned} &(187572)(14.25)(1.5)(148.5 - 14.25 / 2) + (187572)(38.5)(1.5)(148.5) \\ &+ (156919)(148.5)(1.5)(148.5 / 2) + (126266)(14.25)(1.5)(14.25 / 2) \end{aligned} \right\} / \left\{ (381)(156919) \right\} \\ &= 80.118 \text{ mm}\end{aligned}$$

Nominal flexural strength M_{nx}

$$\bar{I}_{eff.T} = \left\{ \begin{aligned} &E_{176} \left\{ (1/12)tb_l^3 + (1/12)b_f t^3 + b_l t (b_w - \bar{Y}_{eff} - b_l / 2)^2 + b_f t (b_w - \bar{Y}_{eff})^2 \right\} \\ &+ E_{327} \left\{ (1/12)tb_w^3 + b_w t (b_w / 2 - \bar{Y}_{eff})^2 \right\} \\ &+ E_{478} \left\{ (1/12)b_f t^3 + (1/12)tb_l^3 + b_f t \bar{Y}_{eff}^2 + b_l t (\bar{Y}_{eff} - b_l / 2)^2 \right\} \end{aligned} \right\} / \bar{E}_T$$

$$= \frac{\left\{ \begin{aligned} &(187572) \left\{ (1/12)(1.5)(14.25)^3 + (1/12)(38.5)(1.5)^3 \right. \\ &\quad \left. + (14.25)(1.5)(148.5 - 80.118 - 14.25 / 2)^2 + (38.5)(1.5)(148.5 - 80.118)^2 \right\} \\ &+ (156919) \left\{ (1/12)(1.5)(38.5)^3 + (148.5)(1.5)(148.5 / 2 - 80.118)^2 \right\} \\ &+ (126266) \left\{ (1/12)(38.5)(1.5)^3 + (1/12)(1.5)(14.25)^3 \right. \\ &\quad \left. + (38.5)(1.5)(80.118)^2 + (14.25)(1.5)(80.118 - 14.25 / 2)^2 \right\} \end{aligned} \right\}}{156919}$$

$$= 1226062 mm^4$$

$$y_{max} = \max \left\{ \bar{Y}_{eff}, (b_w - \bar{Y}_{eff}) \right\}$$

$$= \max \left\{ 80.118, (148.5 - 80.118) \right\} = 80.118 mm$$

At the mid-height

$$M_{nx,eff} = \frac{\bar{I}_{eff.T} \bar{F}_{y,T}}{y_{max}}$$

$$= \frac{(1266062)(201.012)}{80.118} = 3076112 N \cdot mm$$

At the support

$$M_{nx,eff} = \frac{\bar{I}_{eff.T} F_{y,HF}}{y_{max}}$$

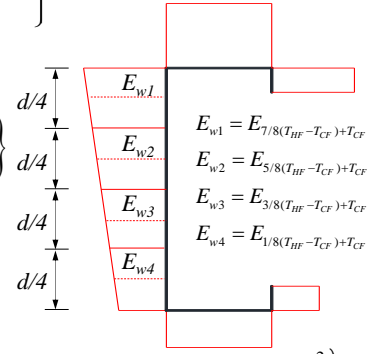
$$= \frac{(1266062)(128.754)}{80.118} = 1970344 N \cdot mm$$

Euler buckling load P_{Ex}

$$\bar{Y} = \left\{ \begin{aligned} &E_{176} b_l t (b_w - b_l / 2) + E_{176} b_f t b_w + E_{w1} \frac{b_w}{4} t \frac{7b_w}{8} + E_{w2} \frac{b_w}{4} t \frac{5b_w}{8} \\ &+ E_{w3} \frac{b_w}{4} t \frac{3b_w}{8} + E_{w4} \frac{b_w}{4} t \frac{b_w}{8} + E_{478} b_l t (b_l / 2) \end{aligned} \right\} / \{A_g \bar{E}_T\}$$

$$= \left\{ \begin{aligned} &(187572)(14.25)(1.5)(148.5 - 14.25 / 2) + (187572)(38.5)(1.5)(148.5) \\ &+ (179908.75) \frac{148.5}{4} (1.5) \frac{7(148.5)}{8} + (164582.25) \frac{148.5}{4} (1.5) \frac{5(148.5)}{8} \\ &+ (149255.75) \frac{148.5}{4} (1.5) \frac{3(148.5)}{8} + (133929.25) \frac{148.5}{4} (1.5) \frac{(148.5)}{8} \\ &+ (126266)(14.25)(1.5)(14.25 / 2) \end{aligned} \right\} / \{381(156919)\}$$

$$= 82.768 \text{ mm}$$



$$\Sigma E_T I = E_{CF} \left\{ (1/12) t b_l^3 + b_l t (b_w - \bar{Y} - b_l / 2)^2 + (1/12) b_f t^3 + b_f t (b_w - \bar{Y})^2 \right\}$$

$$+ E_{w1} \left\{ (1/12) t (b_w / 4)^3 + (b_w / 4) t (b_w - \bar{Y} - b_w / 8)^2 \right\}$$

$$+ E_{w2} \left\{ (1/12) t (b_w / 4)^3 + (b_w / 4) t (b_w - \bar{Y} - 3b_w / 8)^2 \right\}$$

$$+ E_{w3} \left\{ (1/12) t (b_w / 4)^3 + (b_w / 4) t (\bar{Y} - 3b_w / 8)^2 \right\} + E_{w4} \left\{ (1/12) t (b_w / 4)^3 + (b_w / 4) t (\bar{Y} - b_w / 8)^2 \right\}$$

$$+ E_{HF} \left\{ (1/12) t b_l^3 + b_l t (\bar{Y} - b_l / 2)^2 + (1/12) b_f t^3 + b_f t (\bar{Y})^2 \right\}$$

$$= 187572 \left\{ (1/12) 1.5 (14.25)^3 + 14.25 (1.5) (148.5 - 82.768 - 14.25 / 2)^2 \right\}$$

$$+ 179908.75 \left\{ (1/12) 1.5 (148.5 / 4)^3 + (148.5 / 4) 1.5 (148.5 - 82.768 - 148.5 / 8)^2 \right\}$$

$$+ 164582.25 \left\{ (1/12) 1.5 (148.5 / 4)^3 + (148.5 / 4) 1.5 (148.5 - 82.768 - 3(148.5) / 8)^2 \right\}$$

$$+ 149255.75 \left\{ (1/12) 1.5 (148.5 / 4)^3 + (148.5 / 4) 1.5 (82.768 - 3(148.5) / 8)^2 \right\}$$

$$+ 133929.25 \left\{ (1/12) 1.5 (148.5 / 4)^3 + (148.5 / 4) 1.5 (82.768 - 148.5 / 8)^2 \right\}$$

$$+ 126266 \left\{ (1/12) 1.5 (14.25)^3 + 14.25 (1.5) (82.768 - 14.25 / 2)^2 \right\} = 1.885 \times 10^{11} \text{ mm}^4$$

$$P_{Ex} = \frac{\pi^2 \Sigma E_T I}{L^2} = \frac{\pi^2 (1.885 \times 10^{11})}{3000^2} = 206671.913 \text{ N}$$

Interaction of compression and bending

At mid-height

$$e = e_{\Delta T} - e_{\Delta E} = 33.074 - 8.253 = 24.821 \text{ mm}$$

$$C_{mx} = 1$$

Assuming $\bar{P} = 0$ for initial step

$$\alpha_x = \left(1 - \frac{\bar{P}}{P_{Ex}}\right) = \left(1 - \frac{0}{206671.913}\right) = 1$$

$$\frac{\bar{P}}{P_{Ex}} + \frac{C_{mx} \bar{P} e}{\alpha_x M_{nx,eff}} = \frac{\bar{P}}{206671.913} + \frac{1 \cdot \bar{P} \cdot 24.821}{1 \cdot 3076112} = 1$$

By iteration, the solution converges to:

$$\bar{P} = 30679 \text{ N}$$

At support

$$e = e_{\Delta E} = 8.253 \text{ mm} \quad C_{mx} = 1$$

Assuming $\bar{P} = 0$ for initial step

$$\alpha_x = \left(1 - \frac{\bar{P}}{P_{Ex}}\right) = \left(1 - \frac{0}{206671.913}\right) = 1$$

$$\frac{\bar{P}}{P_{Ex}} + \frac{C_{mx} \bar{P} e}{\alpha_x M_{nx,eff}} = \frac{\bar{P}}{206671.913} + \frac{1 \cdot \bar{P} \cdot 8.253}{1 \cdot 1970344} = 1$$

By iteration, the solution converges to:

$$\bar{P} = 35496 \text{ N}$$

Therefore, the ultimate strength of CFS stud in walls under standard fire =30.679 kN. The failure occurs at the mid-height.

Appendix D Calculation results using proposed design method

Studs ($L_h=0$ mm)

Results: $\bar{P}_{L_h=0mm} = \min(\bar{P}$ at mid-height, \bar{P} at support)

$\bar{P}_{n,20^\circ C, L_h=0mm}$ = nominal axial strength calculated at 20 °C under pure compression for studs without web perforation

								mid-height	support	mid-height	support	Results			
Time (min)	T_{HF} (°C)	T_{CF} (°C)	e_{AT} (mm)	e_{AE} (mm)	$(e_{AT} - e_{AE}) / \alpha_x$	P_n (kN)	P_{Ex} (kN)	$M_{nx,eff}$ (kN·m)	$M_{nx,eff}$ (kN·m)	\bar{P} (kN)	\bar{M}_x (kN·m)	\bar{P} (kN)	\bar{M}_x (kN·m)	\bar{P} (kN)	$\frac{\bar{P}_{L_h=0mm}}{P_{n,20^\circ C, L_h=0mm}}$
0.0	20	20	0.000	0.000	0.000	73	261	5.76	5.76	73.12	0.00	73.12	0.00	73.12	1.00
0.5	20	20	0.000	0.000	0.000	73	261	5.76	5.76	73.12	0.00	73.12	0.00	73.12	1.00
0.6	20	20	0.000	0.000	0.000	73	261	5.76	5.76	73.12	0.00	73.12	0.00	73.12	1.00
0.8	20	20	0.000	0.000	0.000	73	261	5.76	5.76	73.12	0.00	73.12	0.00	73.12	1.00
0.9	20	20	0.000	0.000	0.000	73	261	5.76	5.76	73.12	0.00	73.12	0.00	73.12	1.00
1.0	20	20	0.000	0.000	0.000	73	261	5.76	5.76	73.12	0.00	73.12	0.00	73.12	1.00
1.1	20	20	0.000	0.000	0.000	73	261	5.76	5.76	73.12	0.00	73.12	0.00	73.12	1.00
1.3	20	20	0.000	0.000	0.000	73	261	5.76	5.76	73.12	0.00	73.12	0.00	73.12	1.00
1.4	20	20	0.000	0.000	0.000	73	261	5.76	5.76	73.12	0.00	73.12	0.00	73.12	1.00
1.6	20	20	0.000	0.000	0.000	73	261	5.76	5.76	73.12	0.00	73.12	0.00	73.12	1.00
1.8	21	20	0.091	0.000	0.126	73	261	5.76	5.76	73.01	0.01	73.12	0.00	73.01	1.00
2.3	21	20	0.091	0.000	0.126	73	261	5.76	5.76	73.01	0.01	73.12	0.00	73.01	1.00
4.0	25	20	0.455	0.000	0.630	73	261	5.76	5.76	72.54	0.05	73.12	0.00	72.54	0.99
4.5	26	20	0.547	0.000	0.756	73	261	5.76	5.76	72.43	0.05	73.12	0.00	72.43	0.99
7.2	36	21	1.371	0.000	1.887	73	261	5.76	5.76	71.41	0.13	73.12	0.00	71.41	0.98
9.7	47	23	2.204	0.000	3.016	73	261	5.76	5.76	70.43	0.21	73.12	0.00	70.43	0.96
15.0	66	28	3.517	0.000	4.777	73	261	5.76	5.76	68.94	0.33	73.12	0.00	68.94	0.94

19.7	80	33	4.377	0.000	5.916	73	261	5.76	5.76	68.01	0.40	73.12	0.00	68.01	0.93
20.8	83	34	4.569	0.000	6.170	73	261	5.76	5.76	67.81	0.42	73.12	0.00	67.81	0.93
26.0	103	40	5.924	0.066	7.857	73	261	5.74	5.72	66.42	0.52	73.12	0.01	66.42	0.91
34.7	142	54	8.416	0.933	9.973	72	256	5.58	5.22	63.96	0.64	70.94	0.09	63.96	0.87
38.4	155	60	9.140	1.230	10.505	71	254	5.49	5.06	62.79	0.66	69.70	0.12	62.79	0.86
43.3	174	68	10.285	1.671	11.368	70	251	5.34	4.84	60.88	0.69	67.70	0.15	60.88	0.83
46.4	193	73	11.731	2.120	12.594	69	248	5.20	4.61	58.85	0.74	65.80	0.19	58.85	0.80
49.8	221	80	13.933	2.798	14.445	67	244	5.00	4.28	55.92	0.81	62.99	0.24	55.92	0.76
52.6	243	86	15.648	3.344	15.842	65	240	4.84	4.03	53.70	0.85	60.75	0.27	53.70	0.73
54.0	253	89	16.410	3.596	16.444	64	239	4.77	3.91	52.72	0.87	59.71	0.29	52.72	0.72
55.4	263	91	17.273	3.850	17.166	64	237	4.70	3.79	51.71	0.89	58.71	0.30	51.71	0.71
56.8	273	94	18.046	4.108	17.769	63	235	4.62	3.68	50.74	0.90	57.66	0.31	50.74	0.69
59.6	293	100	19.610	4.631	18.975	62	232	4.48	3.45	48.85	0.93	55.56	0.34	48.85	0.67
64.4	322	110	21.791	5.180	20.834	59	226	4.24	3.12	45.90	0.96	52.52	0.35	45.90	0.63
70.1	349	123	23.504	5.627	22.221	57	221	4.01	2.82	43.21	0.96	49.57	0.36	43.21	0.59
71.9	357	127	24.004	5.759	22.617	56	219	3.94	2.73	42.42	0.96	48.67	0.36	42.42	0.58
73.6	365	132	24.409	5.871	22.921	55	218	3.87	2.65	41.63	0.95	47.76	0.36	41.63	0.57
75.4	374	136	25.026	6.034	23.412	54	216	3.79	2.55	40.76	0.95	46.76	0.36	40.76	0.56
77.2	383	141	25.549	6.176	23.811	54	214	3.71	2.45	39.89	0.95	45.73	0.36	39.89	0.55
78.9	393	145	26.288	6.372	24.396	53	212	3.63	2.34	38.94	0.95	44.61	0.36	38.94	0.53
81.6	410	152	27.536	6.710	25.383	51	209	3.51	2.23	37.46	0.95	43.00	0.36	37.46	0.51
84.2	432	159	29.376	7.211	26.859	50	204	3.37	2.14	35.71	0.96	41.23	0.37	35.71	0.49
86.8	454	166	31.244	7.727	28.332	48	200	3.23	2.06	34.01	0.96	39.49	0.38	34.01	0.47
90.2	478	176	33.074	8.253	29.718	47	195	3.08	1.97	32.17	0.96	37.57	0.38	32.17	0.44
93.5	501	187	34.711	8.800	30.847	45	190	2.91	1.88	30.42	0.94	35.64	0.39	30.42	0.42
96.8	523	200	36.049	10.567	30.315	43	180	2.66	1.62	28.70	0.87	31.87	0.41	28.70	0.39
100.1	546	214	37.425	12.535	29.613	40	169	2.40	1.37	26.89	0.80	27.89	0.42	26.89	0.37

100.9	552	218	37.752	13.063	29.387	40	165	2.33	1.30	26.41	0.78	26.83	0.42	26.41	0.36
101.8	558	221	38.183	13.625	29.249	39	162	2.27	1.24	25.94	0.76	25.79	0.42	25.79	0.35
102.1	560	223	38.224	13.791	29.106	39	161	2.25	1.21	25.77	0.75	25.43	0.42	25.43	0.35
102.3	562	224	38.368	13.982	29.057	39	159	2.22	1.19	25.62	0.74	25.08	0.42	25.08	0.34
103.9	573	231	39.009	15.025	28.633	37	153	2.11	1.08	24.82	0.71	23.18	0.41	23.18	0.32
105.3	582	236	39.612	15.950	28.345	37	147	2.04	0.99	24.36	0.69	21.68	0.41	21.68	0.30
107.4	596	244	40.533	17.454	27.819	36	139	1.93	0.84	23.64	0.66	19.28	0.39	19.28	0.26
109.4	608	252	41.210	18.982	26.904	35	132	1.85	0.76	23.03	0.62	17.36	0.38	17.36	0.24
111.2	618	258	41.847	20.120	26.377	34	128	1.79	0.71	22.52	0.59	16.04	0.37	16.04	0.22
114.7	634	271	42.515	21.821	25.271	32	120	1.70	0.62	21.70	0.55	14.05	0.35	14.05	0.19
118.0	648	283	43.037	23.169	24.411	31	113	1.61	0.55	20.97	0.51	12.45	0.32	12.45	0.17
121.0	658	295	43.043	23.937	23.582	30	108	1.55	0.49	20.47	0.48	11.39	0.30	11.39	0.16
122.5	663	300	43.153	24.353	23.259	29	105	1.51	0.47	20.21	0.47	10.87	0.30	10.87	0.15
124.9	670	309	43.090	24.895	22.598	29	102	1.47	0.43	19.87	0.45	10.13	0.28	10.13	0.14
128.1	679	322	42.851	25.594	21.546	28	97	1.40	0.39	19.39	0.42	9.20	0.26	9.20	0.13
129.1	681	325	42.785	25.850	21.176	27	96	1.38	0.38	19.22	0.41	8.96	0.26	8.96	0.12
130.9	685	331	42.652	26.378	20.417	27	93	1.34	0.36	18.89	0.39	8.48	0.25	8.48	0.12
132.3	688	336	42.496	26.786	19.763	26	91	1.30	0.35	18.64	0.37	8.11	0.24	8.11	0.11
136.1	695	347	42.203	27.786	18.261	25	86	1.23	0.31	18.06	0.33	7.29	0.22	7.29	0.10
142.8	703	365	41.256	28.785	15.920	23	80	1.13	0.29	17.36	0.28	6.56	0.21	6.56	0.09
157.6	714	398	38.992	29.731	11.883	20	74	0.99	0.28	16.34	0.19	6.03	0.20	6.03	0.08
162.7	716	408	38.117	30.010	10.446	20	72	0.96	0.28	16.22	0.17	5.91	0.19	5.91	0.08
179.0	724	444	35.025	31.264	4.811	17	73	0.85	0.27	15.91	0.08	5.47	0.18	5.47	0.07
182.5	725	452	34.224	31.503	3.579	17	66	0.83	0.27	15.86	0.06	5.37	0.18	5.37	0.07

Studs ($L_h=75$ mm)

Results:

$$\bar{P}_{L_h=75mm} = \min(\bar{P} \text{ at mid-height, } \bar{P} \text{ at support})$$

$\bar{P}_{n,20^\circ C, L_h=0mm}$ = nominal axial strength calculated at 20 °C under pure compression for studs without web perforation

Time (min)	T_{HF} (°C)	T_{CF} (°C)	e_{AT} (mm)	e_{AE} (mm)	$(e_{AT} - e_{AE}) / \alpha_x$	P_n (kN)	P_{Ex} (kN)	$M_{nx,eff}$ (kN·m)	$M_{nx,eff}$ (kN·m)	mid-height		support		Results	
										\bar{P} (kN)	\bar{M}_x (kN·m)	\bar{P} (kN)	\bar{M}_x (kN·m)	\bar{P} (kN)	$\frac{\bar{P}_{L_h=75mm}}{P_{n,20^\circ C, L_h=0mm}}$
0.0	20	20	0.000	0.000	0.000	70	261	5.757	5.757	70.493	0.000	70.493	0.000	70.49	0.96
0.5	20	20	0.000	0.000	0.000	70	261	5.757	5.757	70.493	0.000	70.493	0.000	70.49	0.96
0.6	20	20	0.000	0.000	0.000	70	261	5.757	5.757	70.493	0.000	70.493	0.000	70.49	0.96
0.8	20	20	0.000	0.000	0.000	70	261	5.757	5.757	70.493	0.000	70.493	0.000	70.49	0.96
0.9	20	20	0.000	0.000	0.000	70	261	5.757	5.757	70.493	0.000	70.493	0.000	70.49	0.96
1.0	20	20	0.000	0.000	0.000	70	261	5.757	5.757	70.493	0.000	70.493	0.000	70.49	0.96
1.1	20	20	0.000	0.000	0.000	70	261	5.757	5.757	70.493	0.000	70.493	0.000	70.49	0.96
1.3	20	20	0.000	0.000	0.000	70	261	5.757	5.757	70.493	0.000	70.493	0.000	70.49	0.96
1.4	20	20	0.000	0.000	0.000	70	261	5.757	5.757	70.493	0.000	70.493	0.000	70.49	0.96
1.6	20	20	0.000	0.000	0.000	70	261	5.757	5.757	70.493	0.000	70.493	0.000	70.49	0.96
1.8	21	20	0.091	0.000	0.124	70	261	5.757	5.757	70.385	0.009	70.493	0.000	70.39	0.96
2.3	21	20	0.091	0.000	0.124	70	261	5.757	5.757	70.385	0.009	70.493	0.000	70.39	0.96
4.0	25	20	0.455	0.000	0.622	70	261	5.757	5.757	69.960	0.043	70.493	0.000	69.96	0.96
4.5	26	20	0.547	0.000	0.746	70	261	5.757	5.757	69.855	0.052	70.493	0.000	69.85	0.96
7.2	36	21	1.371	0.000	1.862	70	261	5.757	5.757	68.921	0.128	70.493	0.000	68.92	0.94
9.7	47	23	2.204	0.000	2.979	70	261	5.757	5.757	68.012	0.203	70.493	0.000	68.01	0.93
15.0	66	28	3.517	0.000	4.720	70	261	5.757	5.757	66.642	0.315	70.493	0.000	66.64	0.91

19.7	83	34	4.569	0.000	6.100	70	261	5.757	5.757	65.594	0.400	70.493	0.000	65.59	0.90
20.8	103	40	5.924	0.066	7.772	70	261	5.745	5.718	64.301	0.500	70.348	0.006	64.30	0.88
26.0	142	54	8.416	0.933	9.867	70	256	5.582	5.217	61.952	0.611	68.407	0.087	61.95	0.85
34.7	155	60	9.140	1.230	10.391	69	255	5.490	5.061	60.829	0.632	67.219	0.112	60.83	0.83
38.4	174	68	10.285	1.671	11.239	67	253	5.343	4.838	58.998	0.663	65.306	0.147	59.00	0.81
43.3	193	73	11.731	2.120	12.448	66	250	5.204	4.614	57.056	0.710	63.488	0.180	57.06	0.78
46.4	221	80	13.933	2.798	14.272	64	247	5.001	4.284	54.252	0.774	60.803	0.226	54.25	0.74
49.8	243	86	15.648	3.344	15.646	63	244	4.840	4.026	52.120	0.815	58.658	0.258	52.12	0.71
52.6	253	89	16.410	3.596	16.239	62	243	4.767	3.910	51.174	0.831	57.667	0.272	51.17	0.70
54.0	263	91	17.273	3.850	16.949	61	241	4.696	3.793	50.206	0.851	56.705	0.285	50.21	0.69
55.4	273	94	18.046	4.108	17.542	61	240	4.622	3.678	49.282	0.865	55.707	0.298	49.28	0.67
56.8	293	100	19.610	4.631	18.727	59	237	4.476	3.447	47.463	0.889	53.699	0.321	47.46	0.65
59.6	322	110	21.791	5.180	20.561	57	232	4.243	3.121	44.614	0.917	50.771	0.337	44.61	0.61
64.4	349	123	23.504	5.627	21.930	55	227	4.012	2.822	42.006	0.921	47.918	0.342	42.01	0.57
70.1	357	127	24.004	5.759	22.320	54	226	3.943	2.733	41.235	0.920	47.055	0.342	41.23	0.56
71.9	365	132	24.409	5.871	22.621	53	224	3.869	2.646	40.469	0.915	46.172	0.341	40.47	0.55
73.6	374	136	25.026	6.034	23.105	52	223	3.794	2.547	39.624	0.916	45.209	0.342	39.62	0.54
75.4	383	141	25.549	6.176	23.498	51	221	3.714	2.449	38.772	0.911	44.216	0.341	38.77	0.53
77.2	393	145	26.288	6.372	24.075	51	219	3.633	2.339	37.856	0.911	43.140	0.342	37.86	0.52
78.9	410	152	27.536	6.710	25.048	49	216	3.509	2.225	36.427	0.912	41.583	0.346	36.43	0.50
81.6	432	159	29.376	7.211	26.502	48	212	3.371	2.142	34.740	0.921	39.888	0.354	34.74	0.48
84.2	454	166	31.244	7.727	27.953	46	209	3.235	2.059	33.095	0.925	38.212	0.361	33.10	0.45
86.8	478	176	33.074	8.253	29.316	45	204	3.076	1.970	31.314	0.918	36.360	0.365	31.31	0.43
90.2	501	187	34.711	8.800	30.424	43	200	2.915	1.878	29.619	0.901	34.493	0.367	29.62	0.41
93.5	523	200	36.049	10.567	29.864	41	190	2.663	1.623	27.934	0.834	30.899	0.390	27.93	0.38
96.8	546	214	37.425	12.535	29.132	38	180	2.403	1.366	26.172	0.762	27.103	0.400	26.17	0.36
100.1	552	218	37.752	13.063	28.898	38	176	2.335	1.301	25.698	0.743	26.097	0.400	25.70	0.35

100.9	558	221	38.183	13.625	28.722	37	173	2.271	1.236	25.248	0.726	25.102	0.400	25.10	0.34
101.8	560	223	38.224	13.791	28.542	37	172	2.246	1.215	25.080	0.717	24.756	0.399	24.76	0.34
102.1	562	224	38.368	13.982	28.454	37	171	2.224	1.193	24.930	0.712	24.423	0.398	24.42	0.33
102.3	573	231	39.009	15.025	27.806	36	164	2.110	1.078	24.148	0.679	22.600	0.394	22.60	0.31
103.9	582	236	39.612	15.950	27.304	35	159	2.039	0.985	23.702	0.659	21.178	0.390	21.18	0.29
105.3	596	244	40.533	17.447	26.418	34	150	1.929	0.845	23.011	0.628	18.888	0.377	18.89	0.26
107.4	608	252	41.210	19.607	24.474	33	143	1.851	0.761	22.584	0.579	16.777	0.373	16.78	0.23
109.4	618	258	41.847	21.189	23.247	32	138	1.795	0.705	22.207	0.547	15.357	0.366	15.36	0.21
111.2	634	271	42.515	23.659	21.008	30	129	1.699	0.619	21.613	0.489	13.243	0.349	13.24	0.18
114.7	648	283	43.037	25.551	19.333	29	121	1.613	0.545	21.051	0.445	11.599	0.328	11.60	0.16
118.0	658	295	43.043	26.478	18.227	28	116	1.546	0.494	20.596	0.415	10.581	0.308	10.58	0.14
121.0	663	300	43.153	26.990	17.738	28	113	1.514	0.469	20.369	0.401	10.072	0.298	10.07	0.14
122.5	670	309	43.090	27.677	16.855	27	109	1.466	0.434	20.058	0.378	9.369	0.284	9.37	0.13
124.9	679	322	42.851	28.590	15.520	26	104	1.400	0.390	19.652	0.345	8.466	0.263	8.47	0.12
128.1	681	325	42.785	28.917	15.074	26	103	1.379	0.380	19.510	0.334	8.230	0.259	8.23	0.11
129.1	685	331	42.652	29.592	14.161	25	100	1.336	0.361	19.231	0.311	7.769	0.249	7.77	0.11
130.9	688	336	42.496	30.119	13.397	25	98	1.303	0.347	19.020	0.292	7.423	0.242	7.42	0.10
132.3	695	347	42.203	31.427	11.611	23	92	1.227	0.314	18.550	0.250	6.634	0.225	6.63	0.09
136.1	703	365	41.256	32.705	9.184	22	86	1.130	0.288	17.963	0.194	5.950	0.209	5.95	0.08
142.8	714	398	38.992	33.779	5.599	19	79	0.988	0.278	17.009	0.113	5.475	0.199	5.48	0.07
157.6	716	408	38.117	34.087	4.328	19	78	0.957	0.276	16.921	0.087	5.367	0.196	5.37	0.07
162.7	724	444	35.025	35.496	-0.505	17	73	0.851	0.269	16.366	0.010	4.956	0.189	4.96	0.07
179.0	725	452	34.224	35.757	-1.644	16	72	0.830	0.269	15.547	0.030	4.884	0.187	4.88	0.07
182.5	725	452	34.224	31.503	3.579	17	66	0.83	0.27	15.86	0.06	5.37	0.18	5.37	0.07

Studs ($L_h=114$ mm)

Results:

$$\bar{P}_{L_h=114mm} = \min(\bar{P} \text{ at mid-height, } \bar{P} \text{ at support}) \quad \bar{P}_{L_h=114mm} = \min(\bar{P} \text{ at mid-height, } \bar{P} \text{ at support})$$

$\bar{P}_{n,20^\circ C,L_n=0mm}$ = nominal axial strength calculated at 20 °C under pure compression for studs without web perforation

Time (min)	T_{HF} (°C)	T_{CF} (°C)	e_{AT} (mm)	e_{AE} (mm)	$(e_{AT} - e_{AE}) / \alpha_x$	P_n (kN)	P_{Ex} (kN)	$M_{nx,eff}$ (kN·m)	$M_{nx,eff}$ (kN·m)	mid-height		support		Results	
										\bar{P} (kN)	\bar{M}_x (kN·m)	\bar{P} (kN)	\bar{M}_x (kN·m)	\bar{P} (kN)	$\frac{\bar{P}_{L_h=114mm}}{P_{n,20^\circ C,L_n=0mm}}$
0.0	20	20	0.000	0.000	0.000	69	261	5.757	5.757	68.795	0.000	68.795	0.000	68.79	0.94
0.5	20	20	0.000	0.000	0.000	69	261	5.757	5.757	68.795	0.000	68.795	0.000	68.79	0.94
0.6	20	20	0.000	0.000	0.000	69	261	5.757	5.757	68.795	0.000	68.795	0.000	68.79	0.94
0.8	20	20	0.000	0.000	0.000	69	261	5.757	5.757	68.795	0.000	68.795	0.000	68.79	0.94
0.9	20	20	0.000	0.000	0.000	69	261	5.757	5.757	68.795	0.000	68.795	0.000	68.79	0.94
1.0	20	20	0.000	0.000	0.000	69	261	5.757	5.757	68.795	0.000	68.795	0.000	68.79	0.94
1.1	20	20	0.000	0.000	0.000	69	261	5.757	5.757	68.795	0.000	68.795	0.000	68.79	0.94
1.3	20	20	0.000	0.000	0.000	69	261	5.757	5.757	68.795	0.000	68.795	0.000	68.79	0.94
1.4	20	20	0.000	0.000	0.000	69	261	5.757	5.757	68.795	0.000	68.795	0.000	68.79	0.94
1.6	20	20	0.000	0.000	0.000	69	261	5.757	5.757	68.795	0.000	68.795	0.000	68.79	0.94
1.8	21	20	0.091	0.000	0.123	69	261	5.757	5.757	68.693	0.008	68.795	0.000	68.69	0.94
2.3	21	20	0.091	0.000	0.123	69	261	5.757	5.757	68.693	0.008	68.795	0.000	68.69	0.94
4.0	25	20	0.455	0.000	0.616	69	261	5.757	5.757	68.292	0.042	68.795	0.000	68.29	0.93
4.5	26	20	0.547	0.000	0.739	69	261	5.757	5.757	68.192	0.050	68.795	0.000	68.19	0.93
7.2	36	21	1.371	0.000	1.847	69	261	5.757	5.757	67.309	0.124	68.795	0.000	67.31	0.92
9.7	47	23	2.204	0.000	2.955	69	261	5.757	5.757	66.449	0.196	68.795	0.000	66.45	0.91
15.0	66	28	3.517	0.000	4.684	69	261	5.757	5.757	65.148	0.305	68.795	0.000	65.15	0.89

20.8	80	33	4.377	0.000	5.806	69	261	5.757	5.757	64.332	0.373	68.795	0.000	64.33	0.88
26.0	83	34	4.569	0.000	6.055	69	261	5.757	5.757	64.153	0.388	68.795	0.000	64.15	0.88
34.7	103	40	5.924	0.066	7.718	69	261	5.745	5.718	62.921	0.486	68.656	0.006	62.92	0.86
38.4	142	54	8.416	0.933	9.802	68	256	5.582	5.217	60.659	0.595	66.791	0.084	60.66	0.83
43.3	155	60	9.140	1.230	10.324	67	255	5.490	5.061	59.568	0.615	65.641	0.109	59.57	0.81
46.4	174	68	10.285	1.671	11.169	66	253	5.343	4.838	57.786	0.645	63.787	0.143	57.79	0.79
49.8	193	73	11.731	2.120	12.374	64	250	5.204	4.614	55.901	0.692	62.025	0.175	55.90	0.76
52.6	221	80	13.933	2.798	14.192	63	247	5.001	4.284	53.178	0.755	59.423	0.219	53.18	0.73
54.0	243	86	15.648	3.344	15.564	61	244	4.840	4.026	51.104	0.795	57.344	0.251	51.10	0.70
55.4	253	89	16.410	3.596	16.155	60	243	4.767	3.910	50.184	0.811	56.383	0.264	50.18	0.69
56.8	263	91	17.273	3.850	16.864	60	241	4.696	3.793	49.242	0.830	55.450	0.277	49.24	0.67
59.6	273	94	18.046	4.108	17.456	59	240	4.622	3.678	48.343	0.844	54.483	0.290	48.34	0.66
64.4	283	97	18.825	4.368	18.048	58	239	4.549	3.562	47.451	0.856	53.510	0.301	47.45	0.65
70.1	293	100	19.610	4.631	18.639	58	237	4.476	3.447	46.568	0.868	52.533	0.313	46.57	0.64
71.9	322	110	21.791	5.180	20.471	56	232	4.243	3.121	43.791	0.896	49.687	0.327	43.79	0.60
73.6	349	123	23.504	5.627	21.840	53	227	4.012	2.822	41.241	0.901	46.907	0.333	41.24	0.56
75.4	357	127	24.004	5.759	22.230	52	226	3.943	2.733	40.487	0.900	46.067	0.333	40.49	0.55
77.2	365	132	24.409	5.871	22.531	52	224	3.869	2.646	39.737	0.895	45.206	0.332	39.74	0.54
78.9	374	136	25.026	6.034	23.015	51	223	3.794	2.547	38.911	0.896	44.267	0.333	38.91	0.53
81.6	383	141	21.269	5.185	19.465	48	217	3.525	2.474	37.665	0.733	42.317	0.273	37.67	0.52
84.2	393	145	26.288	6.372	23.986	49	219	3.633	2.339	37.181	0.892	42.251	0.334	37.18	0.51
86.8	410	152	27.536	6.710	24.958	48	216	3.509	2.225	35.778	0.893	40.733	0.337	35.78	0.49
90.2	432	159	29.376	7.211	26.412	47	212	3.371	2.142	34.137	0.902	39.083	0.345	34.14	0.47
93.5	454	166	31.009	7.664	27.673	45	209	3.244	2.067	32.664	0.904	37.584	0.351	32.66	0.45
96.8	478	176	33.074	8.253	29.227	44	204	3.076	1.970	30.787	0.900	35.642	0.356	30.79	0.42
100.1	501	187	34.711	8.800	30.336	42	200	2.915	1.878	29.125	0.884	33.818	0.358	29.13	0.40
100.9	523	200	36.049	10.567	29.779	40	190	2.663	1.623	27.469	0.818	30.327	0.381	27.47	0.38

101.8	546	214	37.425	12.535	29.049	37	180	2.403	1.366	25.736	0.748	26.635	0.392	25.74	0.35
102.1	552	218	37.752	13.063	28.816	37	176	2.335	1.301	25.270	0.728	25.655	0.392	25.27	0.35
102.3	558	221	38.183	13.625	28.642	36	173	2.271	1.236	24.828	0.712	24.687	0.392	24.69	0.34
103.9	560	223	38.224	13.791	28.463	36	172	2.246	1.215	24.663	0.703	24.349	0.391	24.35	0.33
105.3	562	224	38.368	13.982	28.377	36	171	2.224	1.193	24.516	0.698	24.025	0.391	24.03	0.33
107.4	573	231	39.009	15.025	27.738	35	164	2.110	1.078	23.746	0.666	22.255	0.387	22.25	0.30
109.4	582	236	39.612	15.950	27.242	34	159	2.039	0.985	23.308	0.646	20.864	0.383	20.86	0.29
111.2	596	244	40.533	17.447	26.367	33	150	1.929	0.845	22.631	0.615	18.633	0.371	18.63	0.25
114.7	608	252	41.210	19.607	24.433	32	143	1.851	0.761	22.198	0.568	16.564	0.367	16.56	0.23
118.0	618	258	41.847	21.189	23.212	31	138	1.795	0.705	21.817	0.535	15.171	0.361	15.17	0.21
121.0	634	271	42.515	23.659	20.981	30	129	1.699	0.619	21.216	0.479	13.094	0.345	13.09	0.18
122.5	648	283	43.037	25.551	19.311	28	121	1.613	0.545	20.653	0.435	11.478	0.324	11.48	0.16
124.9	658	295	43.043	26.478	18.210	27	116	1.546	0.494	20.199	0.405	10.478	0.305	10.48	0.14
128.1	663	300	43.153	26.990	17.722	27	113	1.514	0.469	19.974	0.392	9.974	0.295	9.97	0.14
129.1	670	309	43.090	27.677	16.841	26	109	1.466	0.434	19.662	0.369	9.282	0.281	9.28	0.13
130.9	679	322	42.851	28.590	15.508	25	104	1.400	0.390	19.255	0.337	8.389	0.261	8.39	0.11
132.3	681	325	42.785	28.917	15.063	25	103	1.379	0.380	19.114	0.326	8.159	0.256	8.16	0.11
136.1	685	331	42.652	29.592	14.151	24	100	1.336	0.361	18.834	0.303	7.704	0.247	7.70	0.11
142.8	688	336	42.496	30.119	13.387	24	98	1.303	0.347	18.622	0.285	7.362	0.240	7.36	0.10
157.6	695	347	42.203	31.427	11.604	23	92	1.227	0.314	18.149	0.243	6.582	0.223	6.58	0.09
162.7	703	365	41.256	32.705	9.179	21	86	1.130	0.288	17.556	0.188	5.905	0.207	5.91	0.08
179.0	714	398	38.992	33.779	5.596	19	79	0.988	0.278	16.598	0.109	5.433	0.197	5.43	0.07
182.5	716	408	38.117	34.087	4.326	18	78	0.957	0.276	16.500	0.084	5.325	0.195	5.33	0.07
179.0	724	444	35.025	35.496	-0.504	16	73	0.851	0.269	15.923	0.010	4.917	0.187	4.92	0.07
182.5	725	452	34.224	35.757	-1.643	16	72	0.830	0.269	15.140	0.029	4.845	0.186	4.85	0.07

Studs ($L_h=130$ mm)

Results:

$$\bar{P}_{L_h=130mm} = \min(\bar{P} \text{ at mid-height, } \bar{P} \text{ at support})$$

$\bar{P}_{n,20^\circ C, L_h=0mm}$ = nominal axial strength calculated at 20 °C under pure compression for studs without web perforation

Time (min)	T_{HF} (°C)	T_{CF} (°C)	e_{AT} (mm)	e_{AE} (mm)	$(e_{AT} - e_{AE}) / \alpha_x$	P_n (kN)	P_{Ex} (kN)	mid-height	support	mid-height		support		Results	
								$M_{nx,eff}$ (kN·m)	$M_{nx,eff}$ (kN·m)	\bar{P} (kN)	\bar{M}_x (kN·m)	\bar{P} (kN)	\bar{M}_x (kN·m)	\bar{P} (kN)	$\frac{\bar{P}_{L_h=130mm}}{P_{n,20^\circ C, L_h=0mm}}$
0.0	20	20	0.000	0.000	0.000	68	261	5.757	5.757	68.456	0.000	68.456	0.000	68.46	0.94
0.5	20	20	0.000	0.000	0.000	68	261	5.757	5.757	68.456	0.000	68.456	0.000	68.46	0.94
0.6	20	20	0.000	0.000	0.000	68	261	5.757	5.757	68.456	0.000	68.456	0.000	68.46	0.94
0.8	20	20	0.000	0.000	0.000	68	261	5.757	5.757	68.456	0.000	68.456	0.000	68.46	0.94
0.9	20	20	0.000	0.000	0.000	68	261	5.757	5.757	68.456	0.000	68.456	0.000	68.46	0.94
1.0	20	20	0.000	0.000	0.000	68	261	5.757	5.757	68.456	0.000	68.456	0.000	68.46	0.94
1.1	20	20	0.000	0.000	0.000	68	261	5.757	5.757	68.456	0.000	68.456	0.000	68.46	0.94
1.3	20	20	0.000	0.000	0.000	68	261	5.757	5.757	68.456	0.000	68.456	0.000	68.46	0.94
1.4	20	20	0.000	0.000	0.000	68	261	5.757	5.757	68.456	0.000	68.456	0.000	68.46	0.94
1.6	20	20	0.000	0.000	0.000	68	261	5.757	5.757	68.456	0.000	68.456	0.000	68.46	0.94
1.8	21	20	0.091	0.000	0.123	68	261	5.757	5.757	68.355	0.008	68.456	0.000	68.36	0.93
2.3	21	20	0.091	0.000	0.123	68	261	5.757	5.757	68.355	0.008	68.456	0.000	68.36	0.93
4.0	25	20	0.455	0.000	0.615	68	261	5.757	5.757	67.958	0.042	68.456	0.000	67.96	0.93
4.5	26	20	0.547	0.000	0.738	68	261	5.757	5.757	67.860	0.050	68.456	0.000	67.86	0.93
7.2	36	21	1.371	0.000	1.844	68	261	5.757	5.757	66.987	0.124	68.456	0.000	66.99	0.92
9.7	47	23	2.204	0.000	2.951	68	261	5.757	5.757	66.168	0.195	68.456	0.000	66.17	0.90
15.0	66	28	3.517	0.000	4.677	68	261	5.757	5.757	64.849	0.303	68.456	0.000	64.85	0.89

19.7	80	33	4.377	0.000	5.797	68	261	5.757	5.757	64.041	0.371	68.456	0.000	64.04	0.88
20.8	83	34	4.569	0.000	6.046	68	261	5.757	5.757	63.864	0.386	68.456	0.000	63.86	0.87
26.0	103	40	5.924	0.066	7.707	68	261	5.745	5.718	62.644	0.483	68.318	0.006	62.64	0.86
34.7	142	54	8.416	0.933	9.789	68	256	5.582	5.217	60.399	0.591	66.468	0.084	60.40	0.83
38.4	155	60	9.140	1.230	10.310	67	255	5.490	5.061	59.314	0.612	65.325	0.108	59.31	0.81
43.3	174	68	10.285	1.671	11.155	65	253	5.343	4.838	57.543	0.642	63.483	0.142	57.54	0.79
46.4	193	73	11.731	2.120	12.359	64	250	5.204	4.614	55.669	0.688	61.732	0.174	55.67	0.76
49.8	221	80	13.933	2.798	14.176	62	247	5.001	4.284	52.956	0.751	59.151	0.218	52.96	0.72
52.6	243	86	15.648	3.344	15.549	61	244	4.840	4.026	50.918	0.792	57.087	0.249	50.92	0.70
54.0	253	89	16.410	3.596	16.139	60	243	4.767	3.910	49.991	0.807	56.125	0.263	49.99	0.68
55.4	263	91	17.273	3.850	16.764	60	246	4.696	3.793	49.087	0.823	55.220	0.274	49.09	0.67
56.8	273	94	18.046	4.108	17.440	59	240	4.622	3.678	48.160	0.840	57.087	0.308	48.16	0.66
59.6	293	100	19.610	4.631	18.622	57	237	4.476	3.447	46.393	0.864	52.301	0.311	46.39	0.63
64.4	322	110	21.791	5.180	20.453	55	232	4.243	3.121	43.625	0.892	49.469	0.326	43.62	0.60
70.1	349	123	23.504	5.627	21.823	53	227	4.012	2.822	41.096	0.897	46.701	0.331	41.10	0.56
71.9	357	127	24.004	5.759	22.213	52	226	3.943	2.733	40.340	0.896	45.865	0.331	40.34	0.55
73.6	365	132	24.409	5.871	22.513	51	224	3.869	2.646	39.589	0.891	45.011	0.331	39.59	0.54
75.4	374	136	25.026	6.034	22.997	51	223	3.794	2.547	38.767	0.892	44.078	0.332	38.77	0.53
77.2	383	141	25.549	6.176	23.391	50	221	3.714	2.449	37.941	0.887	43.116	0.331	37.94	0.52
78.9	393	145	26.288	6.372	23.968	49	219	3.633	2.339	37.045	0.888	42.073	0.332	37.05	0.51
81.6	410	152	27.536	6.710	24.941	48	216	3.509	2.225	35.654	0.889	40.564	0.335	35.65	0.49
84.2	432	159	29.376	7.211	26.394	46	212	3.371	2.142	34.014	0.898	38.921	0.344	34.01	0.47
86.8	454	166	31.244	7.727	27.844	45	209	3.235	2.059	32.411	0.902	37.290	0.351	32.41	0.44
90.2	478	176	33.074	8.253	29.208	43	204	3.076	1.970	30.676	0.896	35.494	0.355	30.68	0.42
93.5	501	187	34.711	8.800	30.318	42	200	2.915	1.878	29.025	0.880	33.681	0.357	29.03	0.40
96.8	523	200	36.049	10.567	29.762	39	190	2.663	1.623	27.374	0.815	30.211	0.379	27.37	0.37
100.1	546	214	37.425	12.535	29.032	37	180	2.403	1.366	25.648	0.745	26.540	0.390	25.65	0.35

100.9	552	218	37.752	13.063	28.799	37	176	2.335	1.301	25.183	0.725	25.566	0.391	25.18	0.34
101.8	558	221	38.183	13.625	28.652	36	173	2.271	1.236	24.743	0.709	24.603	0.391	24.60	0.34
102.1	560	223	38.224	13.791	28.507	36	172	2.246	1.215	24.578	0.701	24.267	0.390	24.27	0.33
102.3	562	224	38.368	13.982	28.458	36	171	2.224	1.193	24.443	0.696	23.945	0.389	23.94	0.33
103.9	573	231	39.009	15.025	28.016	35	164	2.110	1.078	23.663	0.663	22.177	0.385	22.18	0.30
105.3	582	236	39.612	15.950	27.717	34	159	2.039	0.985	23.229	0.644	20.801	0.382	20.80	0.28
107.4	596	244	40.533	17.447	27.179	33	150	1.929	0.845	22.553	0.613	18.580	0.370	18.58	0.25
109.4	608	252	41.210	19.607	25.557	32	143	1.851	0.761	22.126	0.565	16.527	0.366	16.53	0.23
111.2	618	258	41.847	21.189	24.524	31	138	1.795	0.705	21.738	0.533	15.133	0.360	15.13	0.21
114.7	634	271	42.515	23.659	22.541	29	129	1.699	0.619	21.137	0.476	13.059	0.344	13.06	0.18
118.0	648	283	43.037	25.551	21.053	28	121	1.613	0.545	20.572	0.433	11.453	0.323	11.45	0.16
121.0	658	295	43.043	26.478	20.040	27	116	1.546	0.494	20.118	0.403	10.455	0.304	10.45	0.14
122.5	663	300	43.153	26.990	19.602	27	113	1.514	0.469	19.893	0.390	9.954	0.295	9.95	0.14
124.9	670	309	43.090	27.677	18.770	26	109	1.466	0.434	19.582	0.368	9.264	0.280	9.26	0.13
128.1	679	322	42.851	28.590	17.473	25	104	1.400	0.390	19.175	0.335	8.375	0.260	8.38	0.11
129.1	681	325	42.785	28.917	17.018	25	103	1.379	0.380	19.033	0.324	8.144	0.256	8.14	0.11
130.9	685	331	42.652	29.592	16.079	24	100	1.336	0.361	18.753	0.302	7.690	0.247	7.69	0.11
132.3	688	336	42.496	30.119	15.281	24	98	1.303	0.347	18.541	0.283	7.350	0.239	7.35	0.10
136.1	695	347	42.203	31.427	13.399	23	92	1.227	0.314	18.067	0.242	6.572	0.222	6.57	0.09
142.8	703	365	41.256	32.705	10.721	21	86	1.130	0.288	17.474	0.187	5.896	0.207	5.90	0.08
157.6	714	398	38.992	33.779	6.581	19	79	0.988	0.278	16.514	0.109	5.424	0.197	5.42	0.07
162.7	716	408	38.117	34.087	5.107	18	78	0.957	0.276	16.415	0.084	5.317	0.195	5.32	0.07
179.0	724	444	35.025	35.496	-0.601	16	73	0.851	0.269	15.833	0.010	4.908	0.187	4.91	0.07